



UNIVERSITAT<sub>DE</sub>  
BARCELONA

**PPRHs against undruggable *KRAS* and *MYC*  
oncogenes and for the diagnosis  
and treatment of SARS-CoV-2**

Simonas Valiuska



Aquesta tesi doctoral està subjecta a la llicència **Reconeixement- NoComercial – Compartir Igual 4.0. Espanya de Creative Commons.**

Esta tesis doctoral está sujeta a la licencia **Reconocimiento - NoComercial – Compartir Igual 4.0. España de Creative Commons.**

This doctoral thesis is licensed under the **Creative Commons Attribution-NonCommercial-ShareAlike 4.0. Spain License.**



UNIVERSITAT DE BARCELONA

FACULTAT DE FARMÀCIA I CIÈNCIES DE L'ALIMENTACIÓ

DEPARTAMENT DE BIOQUÍMICA I FISIOLOGIA  
SECCIÓ DE BIOQUÍMICA I BIOLOGIA MOLECULAR

Programa de Doctorat en Biotecnologia

**PPRHs against undruggable *KRAS* and *MYC* oncogenes and for the  
diagnosis and treatment of SARS-CoV-2**

Simonas Valiuska

Barcelona, 2023







UNIVERSITAT DE BARCELONA

FACULTAT DE FARMÀCIA I CIÈNCIES DE L'ALIMENTACIÓ

DEPARTAMENT DE BIOQUÍMICA I FISIOLOGIA  
SECCIÓ DE BIOQUÍMICA I BIOLOGIA MOLECULAR

Programa de Doctorat en Biotecnologia

**PPRHs against undruggable *KRAS* and *MYC* oncogenes and for the  
diagnosis and treatment of SARS-CoV-2**

Memòria presentada per Simonas Valiuska per optar al títol de Doctor per la  
Universitat de Barcelona

Firma manuscrita de Carlos J. Ciudad Gómez.

Dr. Carlos J. Ciudad Gómez  
Director

Firma manuscrita de Dra. Verònica Noé Mata.

Dra. Verònica Noé Mata  
Directora

Firma manuscrita de Simonas Valiuska.

Simonas Valiuska  
Barcelona, 2023



## **ABBREVIATIONS**



4T	Four-thymidine
A	Adenine
AAV	Adeno-associated viruses
ADC	Antibody-drug-conjugates
APRT	Adenine phosphoribosyltransferase
ASO	Antisense oligonucleotide
BCL-2	B-cell CLL/lymphoma 2
bHLHLZ	Basic helix-loop-helix leucine zipper
BSA	Bovine serum albumin
C	Cytosine
CP	Convalescent Plasma
CAM	Chorioallantoic membrane
CAR	Chimeric antigen receptor
CHO	Chinese Hamster Ovary
CNS	Central nervous system
CRC	Colorectal cancer
CRISPR	Clustered regularly interspaced short palindromic repeats
DC-Chol	3- $\beta$ -[N-(N,N'-dimethylaminoethane) carbamoyl]
cholesterol	
DHFR	dihydrofolate reductase
DMSO	Dimethyl sulfoxide
DOTAP	1,2-bis(oleoyloxy)-3-(trimethylammonio)propane
DOPE	Dioleoylphosphatidylethanolamine
DOSPA	2,3-dioleyloxy-N-[2(sperminecarboxamido)ethyl]-N,N-dimethyl-1-propanammonium trifluoroacetate
DOPY	1,3-bis[(4-oleyl-1-pyridinio)methyl]benzene dibromide
Dpi	days post-infection
cDNA	Complementary DNA
dsDNA	Double-stranded DNA
dsRNA	Double-stranded RNA
ECL	Enhanced chemiluminescence
ELISA	Enzyme-Linked Immunosorbent Assay
EMA	European Medicines Agency
EMSA	Electrophoretic Mobility Shift Assay
FBS	Fetal bovine serum
FDA	Food and drug administration
FET	Field-Effect Transistor
G	Guanine

G4	G-quadruplex
G4FS	G4 forming sequences
H1N1	Influenza virus A
HER-2	Epidermal growth factor receptor 2
hpi	hours post-infection
HRP	Horseradish peroxidase
HRSV	Human respiratory syncytial virus
IP	Propidium iodide
JET-PEI	Jet-Polyethyleneimine
QGRS	Quadruplex forming G-Rich Sequences
Kd	Dissociation constant
KRAS	Kirsten rat sarcoma viral oncogene homolog
LAMP	Loop-Mediated Isothermal Amplification
MAX	MYC-associated factor X
mTOR	Mammalian target of rapamycin kinase
MTT	3-(4,5-dimethylthiazol-2-yl)-2,5-diphenyltetrazolium bromide
miRNA	microRNA
mRNA	Messenger RNA
MTX	Methotrexate
nt	Nucleotide
NEP	Nuclear Export protein
NHE III <sub>1</sub>	Nuclease Hypersensitive Element
NSCLC	Non-small-cell lung cancer
ORF	Open reading frame
PEI	Polyethyleneimine
PCR	Polymerase chain reaction
PD-1	Programmed cell death 1
PD-L1	Programmed cell death 1 ligand 1
PDAC	Pancreatic ductal adenocarcinoma
PFU	Plaque forming units
PLL	Polylysine
PO	Parallel orientation
PPIA	Peptidylprolyl isomerase A
PPRH	PolyPurine Reverse Hoogsteen hairpin
PVDF	Polyvinylidene difluoride
ROS	Reactive oxygen species
SCR	Scramble
SARS-CoV-2	Severe Acute Respiratory Syndrome Coronavirus 2

SBA	Small Bowel adenocarcinoma
SDS	Sodium dodecyl sulfate
siRNA	Small interfering RNA
SPR	Plasmon Resonance
ssDNA	Single-stranded DNA
ssRNA	Single-stranded RNA
ssPPY	Single-stranded polypyrimidine
ssPPU	Single-stranded polypurine
T	Thymine
T <sub>M</sub>	Melting Temperature
ThT	Thioflavin T
TYMS	Thymidylate synthase
TOP1	DNA topoisomerase 1
TSS	Transcription start site
TROPY	1,3,5-tris[(4-oelyl-1-pyridinio)methyl]benzene tribromide
TFO	Triplex-forming oligonucleotide
TUO	Tumor of unknown origin
WC	Watson-Crick
WHO	World Health Organization





# TABLE OF CONTENTS



<b>PRESENTATION</b>	<b>1</b>
<b>1. INTRODUCTION</b>	<b>5</b>
1.1 <i>Therapeutic oligonucleotides</i>	7
1.2 <i>PPRHs</i>	8
1.2.1 Triple helix formation	10
1.2.2 PPRHs as gene silencing tool	11
1.2.3 Other PPRHs applications	12
1.3 <i>Delivery of nucleic acids</i>	13
1.3.1 Chemical nonviral delivery systems	16
1.4 <i>DNA secondary structures</i>	20
1.4.1 G-quadruplex	21
1.5 <i>Undruggable cancer targets</i>	23
1.5.1 The <i>KRAS</i> gene	24
1.5.2 The <i>MYC</i> gene	26
1.5.3 <i>KRAS</i> and <i>MYC</i> interactions	28
1.6 <i>SARS-CoV-2</i>	29
1.6.1 Diagnostic	31
1.6.2 SARS-CoV-2 therapeutic agents	34
<b>2. OBJECTIVES</b>	<b>39</b>
<b>3. MATERIALS AND METHODS</b>	<b>43</b>
3.1 <i>General design of PPRHs</i>	45
3.2 <i>DNA-PPRH binding analyses</i>	46
3.3 <i>RNA-PPRH binding analyses</i>	47
3.4 <i>Strand displacement assays</i>	47
3.5 <i>Melting Temperature Assay</i>	48
3.6 <i>Western blot analyses for KRAS, MYC, Cyclin D1 and GAPDH detection</i>	48
3.7 Internalization of PPRHs (Flow cytometry)	49
<b>4. RESULTS</b>	<b>51</b>
<b>5. DISCUSSION</b>	<b>173</b>
5.1 <i>PPRHs as gene silencing tools</i>	175
5.1.1 PPRHs targeting <i>KRAS</i>	175
5.1.2 PPRHs targeting <i>MYC</i>	178
5.1.3 Combinatorial effects of PPRHs against <i>KRAS</i> and <i>MYC</i>	180

<i>5.2 Detection of SARS-CoV-2 using PPRH as a diagnostic tool</i>	182
<i>5.3 PPRHs therapeutic properties for SARS-CoV-2</i>	184
<i>5.4 Conclusion remarks</i>	186
<b>6. CONCLUSIONS</b>	189
<b>7. BIBLIOGRAPHY</b>	193

# **PRESENTATION**



This thesis is focused on the study of Polypurine Reverse Hoogsteen (PPRH) hairpins as a gene silencing strategy against undruggable cancer targets and as a diagnostic and therapeutic tool against SARS-CoV-2.

PPRHs are therapeutic oligonucleotides with hairpin-like structure developed in our laboratory. They are non-modified single stranded DNA molecules formed by two antiparallel polypurine repeats linked by a four-thymidine loop that interact through reverse Hoogsteen bonds. PPRHs bind in a sequence-specific manner with their corresponding polypyrimidine target in dsDNA or RNA, by Watson-Crick bonds, allowing a triplex formation and displacing the complementary strand in the case of a dsDNA target. This triplex formation allows gene silencing, previously demonstrated in *in vitro* and *in vivo* studies targeting *survivin* (de Almagro et al., 2009; Rodríguez et al., 2013) *ERBB2/NEU* (López-Aguilar et al., 2023) and against a wide array of targets involved in cancer progression (Noé et al., 2021).

A major part of this thesis consists in expanding our knowledge of PPRHs as a gene silencing tool. We explored the usage of PPRHs against G-quadruplex (G4) forming sequences (G4FS) within *KRAS* and *MYC* oncogenes. The effects of the PPRHs directed against the complementary sequence of a G4 region was previously demonstrated in the *Thymidylate synthase* (*TYMS*) gene, achieving an enhanced gene silencing by allowing G4 formation (Aubets, Félix, et al., 2020). In this direction, we designed PPRHs targeting *KRAS* and *MYC* especially aiming the complementary strand of G4FS to facilitate the formation of a G4 structure and to decrease gene expression in cancer cell lines that have these genes deregulated. The analyses demonstrated that downregulation of gene expression had consequences in cell growth and proliferation that critically affected cell viability. We found that this effect could be incremented in combination with G4-stabilizing molecules in a synergistic manner. Furthermore, our investigation revealed a noteworthy synergy when combining PPRHs targeting both *KRAS* and *MYC* in a sensitive PC-3 prostate cancer cell line. The combination of PPRHs decreased both, oncogene transcription and translation resulting in cell death.

A second significant aspect of this project was dedicated to expand our understanding of the applications of PPRHs as a diagnostic and therapeutic tool in viral infections. Given the profound impact of the COVID-19 pandemic, we focused on the diagnosis and therapy of SARS-CoV-2. Previously, the potential of PPRHs as a diagnostic tool for determining the hypermethylation status of



PAX-5 and detecting *Pneumocystis pneumonia* in human samples was investigated and validated (Calvo-Lozano et al., 2020; Huertas et al., 2018). In the present study, we focused on the design of different PPRHs and DNA oligonucleotides targeting SARS-CoV-2. Two forms of PPRHs were synthesized: an unmodified version to perform binding assays and a modified form as a viral capture probe for various biodevices. These designs and the confirmed bindings served as a basis for the development of the biosensors to detect SARS-CoV-2.

Lastly, we investigated the protective and therapeutic properties of PPRHs both *in vitro* and *in vivo*. The most efficient designs in previous studies were selected, and dissociation constants for the PPRHs with their respective targets were determined. *In vitro*, PPRHs exhibited a higher affinity and efficacy to inhibit SARS-CoV-2 proliferation as compared to their therapeutic oligonucleotide competitors, antisense oligonucleotides. These protective properties of PPRHs were further validated *in vivo* to protect mice from SARS-CoV-2 spread and disease.

# **1. INTRODUCTION**



## 1.1 Therapeutic oligonucleotides

Gene therapy has emerged as a strong therapeutic tool for cancer and other diseases that have been considered untreatable for a long period of time, due to its ability to specifically modulate genes of interest. Cancer is currently the most frequent disease treated by gene therapy (Lin & Qi, 2023). Gene therapy is primarily based on nucleic acids, DNA and RNA, that can be applied for gene augmentation, removal, or replacement of genetic material to treat/rectify diseases related to gene alterations. Therapeutic oligonucleotides, which represent a very powerful tool in gene therapy can also influence cellular behavior by activating, suppressing, or supplementing gene expression in specific cells and tissues (Dunbar et al., 2018; Orkin & Reilly, 2016; Piotrowski-Daspi et al., 2020; L. Wu et al., 2022).

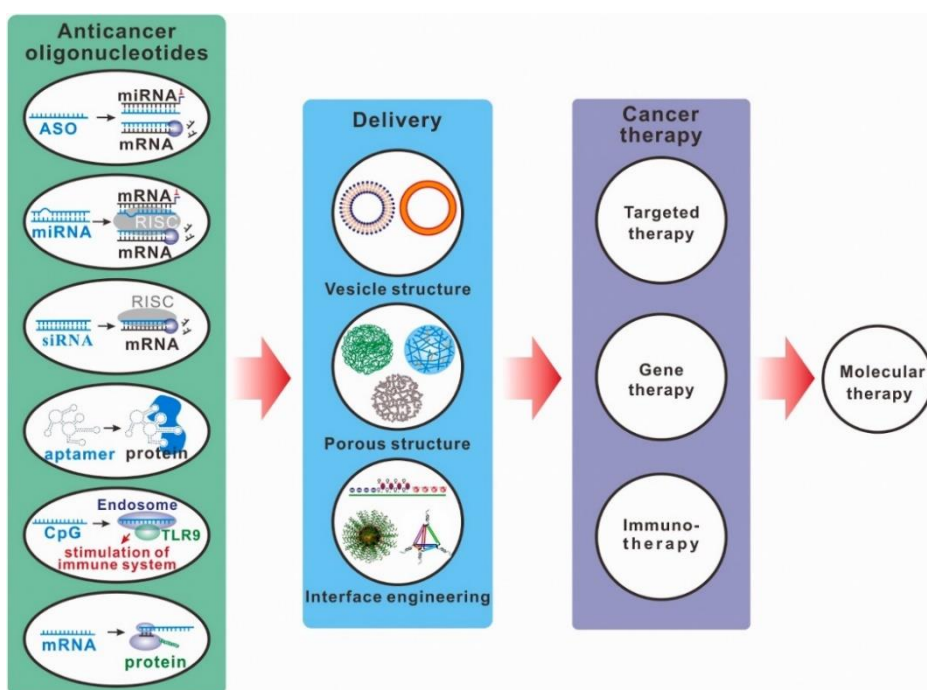


**Figure 1.** Nanocarrier-Based Approaches for Oligonucleotide Delivery in Cancer Molecular Therapy. Adapted from (L. Wu et al., 2022).

Therapeutic oligonucleotides have been actively used since the 90s and during this period of time significant advancements in chemistry, delivery systems, and understanding of molecular biology have been achieved (Crooke,

2017). As a result of these advancements various types of therapeutic oligonucleotides have been developed such as antisense oligonucleotides (ASOs), Triplex forming oligonucleotides (TFOs) small interfering RNA (siRNA), microRNA (miRNA), messenger RNA (mRNA), plasmids, Polypurine Reverse Hoogsteen (PPRH) hairpins, Clustered Regularly Interspaced Short Palindromic Repeats (CRISPR)-based systems, aptamers, ribozymes and decoys (Piotrowski-Daspić et al., 2020). Some of them have been approved by the Food and Drug administration (FDA) or the European Medicines Agency (EMA) and are currently used for disease treatments. One example of therapeutic nucleic acid approved by FDA and EMA, is the Pfizer-BioNTech COVID-19 mRNA-based vaccine that protects against SARS-CoV-2 virus (EMA, 2020; FDA, 2021; Fortner & Schumacher, 2021).

## 1.2 PPRHs

PPRHs are single-stranded (ss) nonmodified DNA (ssDNA) molecules that are formed by two polypurine strands linked by a four-thymidine loop (4T) running in antiparallel orientation. The strands interact with each other intramolecularly by Hoogsteen bonds. The strands of these molecules are designed to specifically bind to their polypyrimidine DNA or RNA target sequence by Watson-Crick bonds (WC), maintaining the hairpin structure, and producing a triplex DNA formation. This triplex conformation arises from the ability of purines to establish Reverse Hoogsteen base pairing interactions with another purine, and simultaneously, WC base pairing interactions with a pyrimidine. This triplex structure provokes the strand displacement of the polypurine strand of the genomic DNA that leads to the inhibition of gene expression of the targeted gene (Coma et al., 2005; de Almagro et al., 2009; Noé et al., 2021).

Polypyrimidines are mainly found in intronic sequences and gene promoters, especially in the upstream region of the transcription start site (TSS) since they can have transcriptional regulatory properties. They are also present in exons, varying their frequency depending on the gene and species (Brahmachari et al., 1997; Goñi et al., 2006). Although it might seem unusual, stretches of polypyrimidine sequences are frequent in many gene sequences. In addition, it is not mandatory to find a pure homopyrimidine track in the DNA target sequence since it can contain up to three purine interruptions and the



efficient in inhibiting gene expression at very low concentrations, much lower than ASOs or TFOs, and with higher affinity (de Almagro et al., 2009; Rodríguez et al., 2015). Also, PPRHs do not provoke immune response, since these are DNA-based molecules with relatively short length, less than 100 nucleotides (nt), and the immune system typically detects longer DNA molecules as foreign or potentially harmful (Villalobos et al., 2014).

### 1.2.1 Triple helix formation

Triplex helix formation refers to a specific DNA or RNA secondary structure in which three strands of nucleic acids come together to form a stable helical complex. This complex appears when a single DNA strand binds through Hoogsteen or reverse Hoogsteen bonds to a purine strand of the major-groove of a Watson-Crick duplex. Triplex formation manifests through diverse modes, including intramolecular and intermolecular configurations, featuring purine or pyrimidine motifs, and adopting either parallel or anti-parallel orientations (Frank-Kamenetskii & Mirkin, 1995). Parallel triplexes form when a pyrimidine single strand binds in a parallel alignment to a purine of the target duplex. This interaction involves Hoogsteen hydrogen bonding, when a thymine (T) of the single strand binds to adenine (A) bound to its corresponding T of the duplex by WC bonds. This triplex formation is indicated as T·AT and for cytosine (C) of the single strand with a guanine (G) bound to its corresponding C it would be C·GC triplets. In contrast, antiparallel structures emerge when a purine-rich third strand binds in an antiparallel manner to a purine-rich domain, facilitated by reverse-Hoogsteen hydrogen bonds encompassing G·GC, A·AT, and T·AT triplets (Figure 3). Although parallel triplexes exhibit greater stability than antiparallel ones, they require low pH conditions to protonate cytosines, potentially limiting their physiological stability. In contrast, antiparallel triplexes are pH-independent (Goñi et al., 2004; Gowers & Fox, 1999).

Triplex formation has a considerable biotechnological and therapeutic potential (Duca et al., 2008; Faria & Giovannangeli, 2001) and has been extensively studied for usage in several applications, such as transcription modulation and site-directed recombination as well as mutagen delivery (Besch et al., 2004; G. Wang et al., 1996).

### Triplex structure

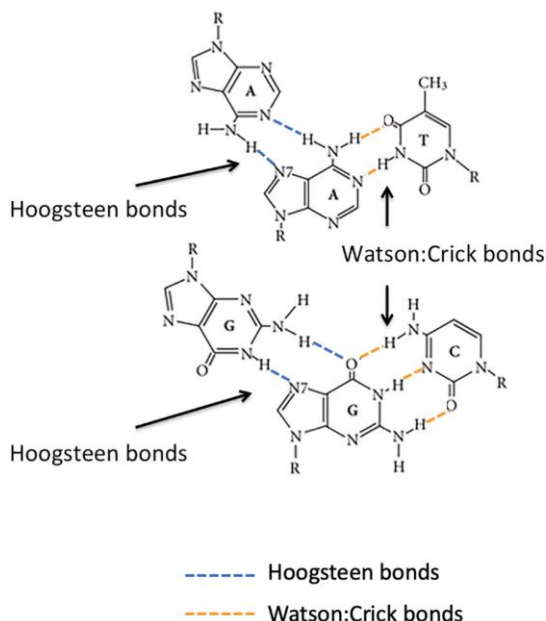


**Figure 3.** The chemical depiction of Hoogsteen and Watson-Crick base pairing involved in triplex formation. Adapted from (Noé et al., 2021).

#### 1.2.2 PPRHs as gene silencing tool

In recent years, PPRHs have demonstrated their versatility for many applications. Among these, one widely explored area is the use of PPRHs as gene silencing tool. Their demonstrated efficacy against a wide range of targets highlights their success in this role. These include genes that play a key role in tumor progression or therapy such as *dihydrofolate reductase (DHFR)* (De Almagro et al., 2011) *telomerase* (de Almagro et al., 2009), *mammalian target of rapamycin kinase (mTOR)*, *topoisomerase (TOP1)*, *c-MYC* and *MDM2* (Villalobos et al., 2015). The PPRHs designed against these targets have been tested in pancreatic, prostate, breast, and colon cancer cell lines and have been shown to decrease target mRNA and protein levels, leading to cell death.

PPRHs have also been used against *WEE1* and *CHK1* genes, involved in the replication stress response. Inhibition of both targets led to reduction of their respective mRNA and protein levels and to an increase of cell death that correlated with the degree of apoptosis. Additional experiments showed a



synergistic effect of *WEE1* and *CHK1* targeting PPRHs when cells were incubated with 5-FU or methotrexate (MTX) (Aubets, Noé, et al., 2020).

The effectiveness of PPRHs for gene silencing was also evaluated on antiapoptotic genes including *survivin* or *BIRC5* (Rodríguez et al., 2013), and *B-cell CLL/lymphoma 2 (BCL-2)* (Villalobos et al., 2015). Both *survivin* and *BCL-2*-targeting PPRHs showed an increased apoptosis and cell death in PC-3 prostate cancer and MIA-PaCa-2 and pancreatic cancer lines, respectively. The PPRH which demonstrated the highest effectiveness in targeting *survivin* (named HpsPr-C), which was effective using low concentrations of PPRH, was chosen for *in vivo* experimentation in mice carrying a subcutaneous xenograft tumor derived from PC-3 prostate cancer cells. This specific PPRH exhibited the ability to reduce tumor growth, lowering the levels of *survivin* protein, and inhibiting the formation of blood vessels. Consequently, these results served as evidence for the potential application of PPRHs as gene silencing tools in an *in vivo* context (Rodríguez et al., 2013).

PPRH gene silencing properties were also demonstrated in a recent study against the *ERBB2/NEU* oncogene (López-Aguilar et al., 2023). The *ERBB2/NEU* oncogene encodes for HER-2 protein participating in cell differentiation, proliferation, and survival. PPRHs targeting HER-2 caused a significant cell survival to decrease in SKBR3 and MDA-MB-453 human breast cancer cells. Furthermore, when these PPRHs were tested in an *in vivo* chick embryo chorioallantoic membrane (CAM) xenograft model, a significant decrease in tumor growth size and weight, as well as lower HER-2 protein relative to control tumors was observed (López-Aguilar et al., 2023). This study expanded the PPRHs use in *in vivo* models.

### 1.2.3 Other PPRHs applications

In addition to their capacity for gene silencing, the capability of PPRHs to bind to precise sequences and create triplex structures has been used for diverse biomedical applications. These applications include gene repair, gene editing, and their usage as biosensors. In the context of gene repair, repair-PPRHs have been employed to accurately correct point mutations within the DNA. This involves using PPRHs with a structure that includes a 5' extension carrying the corrected nucleotide. Repair-PPRHs showed their capacity to correct specific mutations at the endogenous *locus* of two different sets of

Chinese Hamster Ovary (CHO) cell lines: one with mutations in the *DHFR* (Solé et al., 2016) *locus* and a second in the *adenine phosphoribosyltransferase* (*APRT*) *locus* (Félix et al., 2020). Regarding gene editing, our research team also successfully demonstrated the capacity of editing-PPRHs to induce exon skipping at the DNA level. This led to the restoration of the correct DHFR reading frame within a cellular model carrying an additional DHFR exon 2. In a similar way to repair-PPRHs, editing-PPRHs bear an extension in 5' end, but in this case the 5' end is homologous to the sequences adjacent to the exon to be skipped forcing the skipping process to occur (Noé & Ciudad, 2021). Lastly, the triplex formation by PPRHs has been used for the development of biosensors for cancer detection, to analyze the hypermethylation status of PAX-5, and for microbiological detection for the diagnosis of *Pneumocystis pneumonia* in human samples. This system uses a PPRH probe, where its core sequence binds to the target to be studied or analyzed, and it has a 5' extension fixed in a gold sensor surface of a biosensor (Calvo-Lozano et al., 2020; Huertas et al., 2018).

During the COVID-19 pandemic our research group became interested in developing a methodology to efficiently detect SARS-CoV-2 using the ability of the PPRHs to generate triplex structures. In this project we aimed to design specific PPRHs targeting the SARS-CoV-2 RNA to detect the presence of the virus in human samples. The part that was performed by our research group is presented in the Results section of this thesis as a published research article from the collaborative effort among members of the CSIC and our team in the UB.

### 1.3 Delivery of nucleic acids

Nucleic acids are a powerful tool to treat various diseases, but the pathway of these molecules to reach their intended targets present several difficulties since these must surpass many obstacles. The introduction of foreign nucleic acids in circulation could activate blood nucleases. It could also trigger the immune system and lead to degradation of these molecules and thus loss of the therapeutic effect (Judge et al., 2005).

Another aspect to consider is that nucleic acids struggle to trespass biological membranes because of their high molecular weight, hydrophilicity, and massive negative charge, that limits their passive diffusion (Duvall et al., 2014;

Lin & Qi, 2023). Even if nucleic acids are successfully taken up by cells, they may become trapped in endosomes diminishing both their therapeutic effectiveness and availability (Nelson et al., 2013; Sahay et al., 2013) (Figure 4). If the therapeutic oligonucleotide must be delivered to the central nervous system (CNS), it encounters an extra challenge due its difficulty to penetrate the blood-brain barrier (Lin & Qi, 2023).

One approach to improve nucleic acid delivery involves making modifications to their structure, such as chemical, backbone, stereochemistry, or terminal modifications. These changes increase the stability of oligonucleotides or delivery systems, making easier for them to be taken up by cells, or helping them to overcome barriers (Roberts et al., 2020; Torres-Vanegas et al., 2021).

There are several approaches to deliver nucleic acids usually divided into two big categories, viral and nonviral delivery systems. Viral vectors such as adenoviruses (types 2 and 5), adeno-associated viruses (AAV), herpes simplex virus, pox virus, human foamy virus and lentiviruses have shown great success for gene therapy. The viral delivery systems have been shown to be very effective in *in vitro* and *in vivo* trials (Y. Huang et al., 2011). Viral vector genomes have undergone modifications through the selective removal of specific genomic segments. These alterations make the delivery safer, although they can provoke immune response triggering inflammation, toxin production, mortality, or their limitation in transgenic capacity, and they are very cost-effective (Gardlík et al., 2005; Nayerossadat et al., 2012).

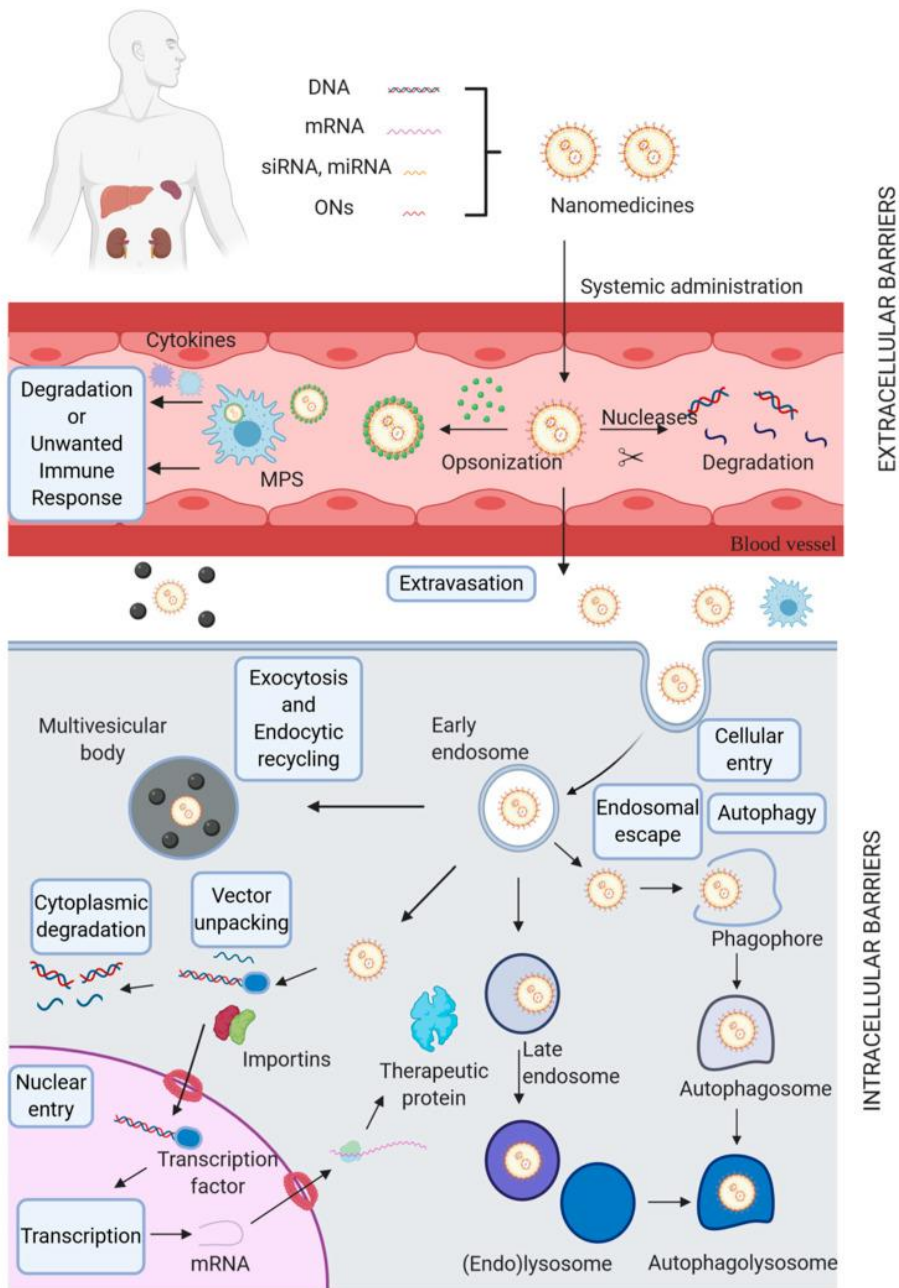


**Figure 4:** Schematic representation of biological barriers for non-viral gene delivery systems. Adapted from (Torres-Vanegas et al., 2021)

Nonviral delivery systems include both physical and chemical approaches. While these systems generally exhibit lower efficiency compared to viral counterparts, they offer advantages such as cost-effectiveness, wider accessibility, and reduced immune responses. Moreover, nonviral systems do not have limitations on transgenic DNA size, a limitation prevalent in viral delivery systems. These attributes have contributed to positioning nonviral delivery systems as more efficient for gene delivery than existing nonviral alternatives (Hirai et al., 1997; Robertson et al., 1996; Suda & Liu, 2007).

Physical delivery systems are based on the transfer of RNA or DNA through transient pores in the membrane of the cells. These pores are created by mechanical, electrical, ultrasonic, hydrodynamic, or laser-based energy so that DNA entrance into the targeted cells is facilitated. This mechanism can be applied to a specific tissue with the drawback that provokes local tissue damage. These processes require time to be optimized and change depending on the tissue. Another aspect to consider is that specialized instruments may be required for the process (Y. Liu et al., 2015; Nayerossadat et al., 2012).

### 1.3.1 Chemical nonviral delivery systems

Chemical nonviral delivery systems are generally nanomeric complexes that compact negatively charged nucleic acid by cationic liposomes or polymers. These compounds typically exhibit sufficient stability and possess the capability to transport nucleic acids into cells via endocytosis (Scherer et al., 2002). They offer enhanced safety profiles compared to viral vectors, are much easier to manufacture and are susceptible to modifications (L. Zhu & Mahato, 2010). Compared to other nonviral delivery systems and especially viral vectors, these are less toxic and lower immunogenic effect since these are made of biological lipids. A primary limitation, however, lies in the relatively lower efficacy (Nayerossadat et al., 2012). Among the frequently employed chemical nonviral delivery systems, it can be found:

- **Cationic liposomes (lipoplexes):** these are the most important nonviral polycationic systems. They consist of a positively charged head group, a hydrophobic segment, and a connecting region or linker, which dictates the chemical stability and degradability of the lipid. The positively charged head engages with the negatively charged DNA, resulting in the formation of lipoplexes (Figure 5). Liposomes have the capacity to transport both

hydrophilic and hydrophobic molecules, demonstrating minimal toxicity and lacking the ability to trigger immune system activation. Liposome rapid degradation and the inability to achieve sustained drug delivery are their main drawbacks (Nayerossadat et al., 2012). Since the first cationic liposome, 1,2-bis(oleoyloxy)-3-(trimethylammonio)propane (DOTAP) was synthesized, numerous types of cationic liposomes have been documented. The most used liposomes include N-[1-dioleoyloxy)propyl]-N,N,N-trimethylammonium (DOTMA), dioleoylphosphatidylethanolamine (DOPE), 2,3-dioleoyloxy-N-[2(sperminecarboxamido)ethyl]-N,N-dimethyl-1-propanammonium trifluoroacetate (DOSPA or LipofectAMINE®) or 3- $\beta$ -[N-(N,N'-dimethylaminoethane) carbamoyl] cholesterol (DC-Chol) (Immordino et al., 2006). Most of our *in vitro* research has involved the formation of complexes between PPRHs and DOTAP. (Aubets, Félix, et al., 2020; de Almagro et al., 2009; De Almagro et al., 2011; Villalobos et al., 2015). Additionally, our research group has collaborated in the obtention of brand-new liposome-based molecules, 1,3-bis[(4-oleyl-1-pyridinio)methyl]benzene dibromide (DOPY) (Aubets et al., 2021) and 1,3,5-tris[(4-oleyl-1-pyridinio)methyl]benzene tribromide (TROPY) (Delgado et al., 2023) and successfully validated PPRH-DOPY and PPRH-TROPY complexes in transfection of *in vitro* cell models.

- **Cationic polymers (polyplexes):** these polymers are formed by positively charged groups along their molecular chains and are referred to as polyplexes. For polyplexes there is a relationship between the length of the polymer, gene delivery efficiency and toxicity. As the length of the polymer increases, so does its efficiency and its toxicity. The first polyplex was polylysine (PLL), lately improved as Polyethyleneimine (PEI) (Nayerossadat et al., 2012). In earlier investigations, our research team successfully administered PPRHs complexed with *in vivo* JET-Polyethylenimine (JET-PEI) through intravenous and intratumoral injections in mice models (Rodríguez et al., 2013). In this work, in collaboration with the Animal Health Research Centre (CISA-INIA-CSIC), it was administered intranasally SARS-CoV-2 targeting PPRHs complexed with *in vivo* JET-PEI in mice.

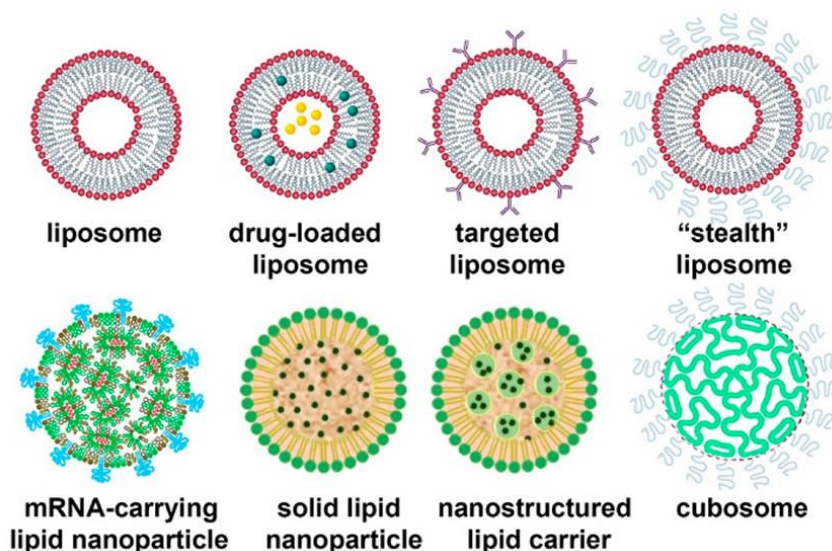


**Figure 5.** Schematic representation of different lipid nanoparticles. Image adapted from (Tenchov et al., 2021).

- Inorganic nanoparticles:** non-carbon-based materials are also used as a delivery system. These compounds can be customized to possess precise dimensions, forms, and surface attributes, facilitating the encapsulation of diverse therapeutic agents enabling them to a controlled release. Certain nanoparticles might lack biocompatibility, potentially triggering immune responses. Nanoparticles may be cost-elevated due to their constituent materials or intricate synthesis procedures. Furthermore, some nanoparticles exhibit non-biodegradability, raising concerns regarding their long-term presence within the body. These materials include gold nanoparticles, magnetic nanoparticles, quantum dots, silica nanoparticles, copper or silver among other nanoparticles (Figure 6) (Luther et al., 2020; Navya et al., 2019).

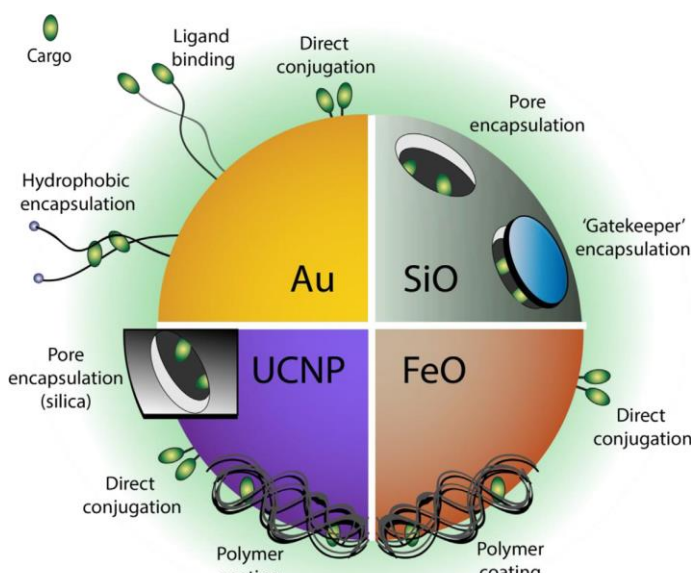


**Figure 6.** Inorganic nanoparticle delivery system. Adapted from (Luther et al., 2020).

- **Exosomes:** these are small, membrane-bound vesicles that are secreted by various types of cells into the extracellular space. Exosomes are a subtype of extracellular vesicles, which also include microvesicles and apoptotic bodies. These molecules can be released from one cell to another to transfer molecules such as nucleic acids, proteins, or lipids by membrane vesicle trafficking. Since these molecules have biological origin, usually isolated from biofluids, these are non-invasive and non-toxic. Exosomes have limited cargo capacity, restricting the number of nucleic acids that can be delivered. These have heterogeneity, varying in size and they can be difficult to isolate, due to the presence of other extracellular vesicles or contaminants present in the biofluids (Butreddy et al., 2021; Elsharkasy et al., 2020).
- **Bioconjugates:** these complexes are molecular assemblies resulting from a covalent connection of two or more different biomolecules. These molecules can include proteins, peptides, nucleic acids, lipids, carbohydrates, or other biologically relevant molecules. As a delivery system, bioconjugates are designed to enhance targeting, stability, and efficiency of therapeutic agents. These can be directed to a specific cell, tissue, or receptors by attaching antibodies or peptides. This approach reduces off-target effects and optimizes delivery (Elzahhar et al., 2019). Some examples include antibody-drug-conjugates (ADCs), GalNAc,



aptamers, lipid conjugates, and peptide-conjugates (Tong & Benjamin Chun-Kit Tong, 2017).

ADCs are monoclonal antibodies linked to a nucleic acid, that act as a personalized medicine since these use a specific antibody. This kind of bioconjugate is already a clinical success since it has been approved for the treatment of cancers such as Hodgkin lymphoma, HER2-positive metastatic breast cancer and bladder cancer (Papachristos et al., 2016).

GalNAc conjugates consist of three molecules of N-acetylgalactosamine that bind to the asialoglycoprotein receptor 1 mainly present in hepatocytes (Figure 7). This delivery system is specific towards liver tissue, with low off-target effects, and works at low doses. It is easy to couple GalNAc ligands to oligonucleotides as the ligand conjugation step can be incorporated in the process of solid-phase synthesis of oligonucleotides (Benizri et al., 2019; Springer & Dowdy, 2018).

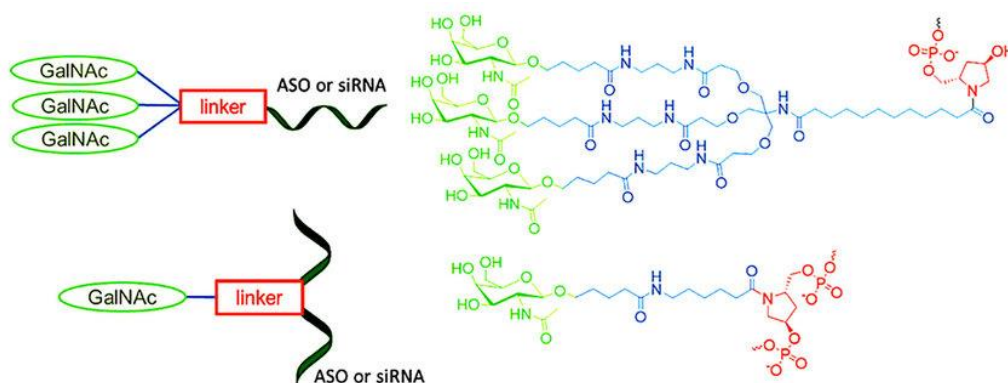


**Figure 7.** Molecular structure of GalNAc conjugates. Oligonucleotide coupled to GalNAc (left) and molecular structure (right). Adapted from (Benizri et al., 2019).

## 1.4 DNA secondary structures

Apart from the canonical B-form described by Watson and Crick, DNA has the capacity to adopt various secondary structures that play crucial roles in essential cellular processes like replication, transcription, recombination, and repair (Watson & Crick, 1953). Within eukaryotic cells, DNA assumes a supercoiled configuration, which relaxes during biological events like

transcription or replication. Consequently, DNA exhibits a capacity to adopt secondary structures beyond the B-form. This diverse structural variability arises from factors such as nucleotide sequence, hydration, solution conditions, ions, proteins, and the presence of super helical stress (Kaushik et al., 2016). The extensively studied DNA structures include the A, B, and Z forms, whereas additional conformations such as hairpin, cruciform, parallel-stranded DNA, DNA bubble or bulge duplex, triplex, quadruplex, and i-motif have attracted research attention. These alternative structures have relevance in DNA damage, repair, and genetic stability. They play distinct roles in the assembly of nucleosomes and other higher-order supramolecular formations involving DNA (G. Wang & Vasquez, 2014).

### 1.4.1 G-quadruplex

Sequences rich in guanines can fold into four-stranded, noncanonical secondary structures called G-quadruplexes (G4s). These are formed in a planar arrangement, stacking on top of each other, through Hoogsteen hydrogen bonds leading to a G4 formation (Figure 8) (Bochman et al., 2012; Varshney et al., 2020). G4s can exhibit different arrangements, which includes both parallel and antiparallel orientations. The parallel orientation refers to guanine strands running in the same direction, while the antiparallel orientation involves strands in opposite directions. Furthermore, these can be either intramolecular or intermolecular in nature. Intramolecular G4s form within a single-strand DNA or RNA (ssRNA), while intermolecular G4s emerge between distinct strands. These arrangements depend on guanine-rich sequences, the presence of monovalent cations ( $\text{Na}^+$ ,  $\text{K}^+$ ) and the specific structural context of the DNA or RNA (Karsisiotis et al., 2013).

The distribution of G4s is not arbitrary, instead they exhibit enrichment in particular genomic regions. To date, with over 370,000 predicted sequences, G4 are found in regions such as telomeres, TSS, as well as sites associated with mitotic and meiotic double-strand breaks (Linke et al., 2021; Spiegel et al., 2020). These guanine-rich DNA sequences show their relevance in several biological processes and are present across a wide range of species. For instance, in yeast, telomeric G4s serve a protective role at the end of the telomeres, preventing them from degradation. However, their presence and functions in other organisms remain unexplored (Bryan, 2020). These structural configurations are abundant in the promoters, scattered across the human genome, exerting regulatory control over gene expression through modulation

of transcription factor binding and interaction with other regulatory entities. This can result in the modulation of gene transcription, either by inhibiting or enhancing the process (Huppert & Balasubramanian, 2007). G4s can also participate in DNA replication acting as barriers and blocking DNA synthesis (Sarkies et al., 2010). G4 conformations can engage and form interactions with proteins implicated in DNA repair processes. This structural configuration holds significant therapeutic value, and many research groups are actively pursuing drug discovery to find specific stabilizers for G4s. However, achieving pronounced selectivity for a particular G4 structure has proven challenging (Kosiol et al., 2021; Linke et al., 2021; Zyner et al., 2019).

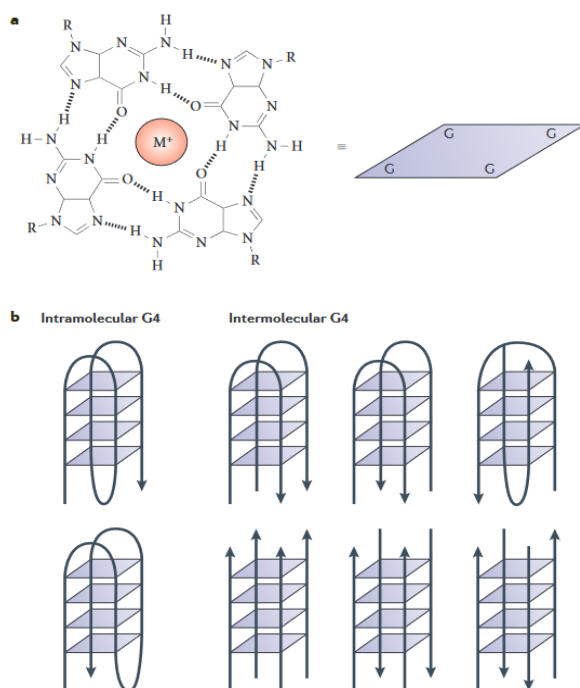


**Figure 8. A.** Representation of a G-quadruplex structure alongside their monovalent cation ( $M^+$ ) associate. On the right site, the square symbolizes the interaction among four guanine molecules. **B.** Illustration of intramolecular (left) and intermolecular (right) configurations, the latter can involve either two strands (upper) or four strands (lower). Adapted from (Bochman et al., 2012).

G4 structure formation and/or stabilization properties are currently studied as a potential anticancer tool that could enhance genome instability and

modulate transcription and telomere homeostasis. Additionally, most oncogene promoters contain a higher number of G4 motifs compared to the promoters of regulatory or tumor suppressor genes. Some studies revealed that changes within the G4 sequences correlated with a reduction of gene expression (Brooks & Hurley, 2010; Cogoi & Xodo, 2006; Dexheimer et al., 2006; Kosiol et al., 2021). An innovative strategy employed distinct G4 ligands designed to target tumor cells and induce high production of reactive oxygen species (ROS) upon photo-irradiation, leading to a cytotoxic impact on tumor cells (Salvati et al., 2007).

Our research group has previously worked on predicted G4 sequences using PPRHs. In this case, they identified and targeted the complementary strands of *Thymidilate synthase* (*TYMS*) G4 forming sequences (G4FS) situated in the 5'UTR of *TYMS* gene (Aubets, Félix, et al., 2020). This work offered new perspectives on developing approaches to enhance the anticancer effectiveness using PPRHs and combining them with conventional *TYMS* inhibitors. It demonstrated that targeting the G4FS with a template-PPRH inhibited transcriptional activity by capturing the template strand of the DNA and forming a G4 structure in the coding strand of the duplex DNA.

In the present work, we have selected and described putative sequences predicted to form G4 structures, to enhance silencing of oncogenes *KRAS* and *MYC* which are considered undruggable cancer targets.

## 1.5 Undruggable cancer targets

Over the last six decades, the field of cancer therapeutics has witnessed the development of various drugs and therapies. Some of the early drugs yielded notable responses interfering in growth and spread of cancer cells but were often accompanied by significant side-effects. The 1990s marked a new era for cancer treatment, with the development of targeted therapies such as monoclonal antibodies, precision medicine (tumor profiling), immunotherapies (using chimeric antigen receptors (CAR) T cells), angiogenesis inhibitors, hormonal or radiation therapies (Schirrmacher, 2019).

Even with the considerable progress in its treatment, cancer remains a significant global health concern. One major obstacle, is the difficulty to effectively use traditional small-molecule drugs to target certain cancer types, considered “undruggable” or difficult to drug. However, many cancer targets that

in the past were called undruggable, have been successfully targeted. *BCL-2*, an anti-apoptotic protein, is a good example of a previously considered undruggable target which now can be targeted by Venetoclax, approved by FDA in 2019 (Dang et al., 2017; FDA, 2019).

Many targets in cancer are considered undruggable due to their large protein-protein interactions, the absence of well-defined or suitable binding sites or their intracellular or nuclear localization (McCormick, 2015; Whitfield et al., 2017). There are two primary categories identified as undruggable cancer targets. One category involves transcription factors such as MYC, MYB, and nuclear factor- $\kappa$ B (NF- $\kappa$ B), which are crucial for cell proliferation and developmental processes (Baud & Karin, 2009; Dang, 2012). The second category, includes RAS oncogene products (KRAS, NRAS and HRAS) which are the most studied proteins, since their mutations are present in approximately 30% of human cancers with KRAS having the highest mutation rate among all cancers (Cox et al., 2014).

### 1.5.1 The *KRAS* gene

Kirsten rat sarcoma viral oncogene homolog (*KRAS*), is a human gene that encodes for a membrane-bound regulatory protein that belongs to RAS family GTPases. This protein acts as a switch, cycling between active GTP-bound state and inactive GDP-bound state. When activated, *KRAS* downstream pathways control cell survival, proliferation, and differentiation (Adjei, 2001; Colicelli, 2004). Mutations involving a single alteration in the *KRAS* gene disrupt its natural GTP hydrolysis process, leading to a persistent activation of the protein. This constitutive activity is associated with elevated tumorigenicity and is linked to an unfavorable prognosis (Friday & Adjei, 2005). Also, it is related to the development of aggressive diseases including pancreatic ductal adenocarcinoma (PDAC), non-small-cell lung cancer (NSCLC), and colorectal cancer (CRC) (L. Huang et al., 2021).

Numerous drug discovery initiatives are currently in progress, concentrating on specific mutant *KRAS* isoforms. Sotorasib, which targets the *KRAS*<sup>G12C</sup> mutant protein, received the FDA approval for lung cancer treatment in May 2021 (Nakajima et al., 2022). Although this brightens the future for cancers with *KRAS* alterations, G12C is not the only common mutation, and it does not benefit patients with overexpressed or other *KRAS* variants. *KRAS*<sup>G12D</sup>

and  $KRAS^{G12V}$  are the most frequently mutated alleles found in patients with pancreatic and colorectal cancer (figure 9) (Dang et al., 2017; Neumann et al., 2009; Salem et al., 2022). For this reason, the strategy of creating treatments for individual  $KRAS$  mutations requires the development of a range of drugs. Importantly, reducing transcription has proven to be fatal for tumor cells with abnormal  $KRAS$  signaling, exposing their dependency on  $KRAS$ , regardless of their mutational state, and offers a broad potential for therapeutic intervention. The technique of stabilizing complex genomic structures is a recognized method for influencing transcription (Ali et al., 2012; Hu et al., 2012; Singh et al., 2009).

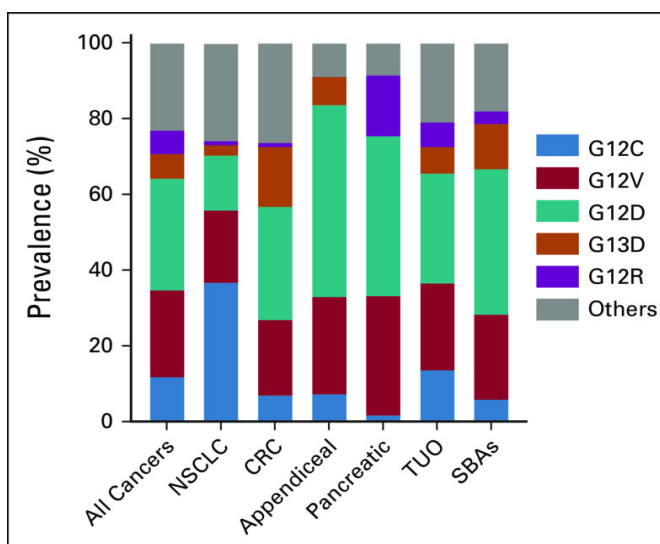


**Figure 9.**  $KRAS$  variants prevalence varies among tumor subtypes including colorectal cancer (CRC), appendiceal, pancreatic, non-small-cell lung cancer (NSCLC), small bowel adenocarcinoma (SBA), and tumors of unknown origin (TUO). Adapted from (Salem et al., 2022).

Within the promoter region of  $KRAS$ , there are segments rich in G/C content, that can form G4s. Some known G4 structures in  $KRAS$ , like 32R, recruit transcription factors like MAZ, PARP-1 and hnRNP A1 forming a complex that pre-initiates transcription (Marquevielle et al., 2020). Other structures, such as  $G4_{mid}$  described by Morgan et al., 2016, are related to transcriptional silencing. Targeting the complementary strand of G4s can enable G4 formation and diminish or suppress  $KRAS$  transcription (Marquevielle et al., 2020). Following this therapeutic interest, we selected some of the known G4FS and new putative

ones to apply the PPRHs technology as a possible treatment to suppress KRAS expression.

### 1.5.2 The *MYC* gene

Commonly known as *MYC*, *c-MYC* belongs to an extensive family of basic helix-loop-helix leucine zipper (bHLHLZ) DNA binding proteins including *L-MYC* and *N-MYC* (Beaulieu et al., 2020; Duffy et al., 2021). To be transcriptionally functional, *MYC* heterodimerizes with its obligate partner *MYC*-associated factor X (*MAX*) (Madden et al., 2021; Nie et al., 2020). *MYC* serves as a transcription factor in numerous signal transduction pathways that stimulate cell growth and other cellular functions including metabolism, differentiation, and apoptosis. Notably, *MYC* controls the expression of up to 15% of human genes (Armelin et al., 1984; Dang, 2012; L. Shen et al., 2015). Aberrant *MYC* expression serves as a catalyst for both the initiation and maintenance of tumors, and it is associated with all the emblematic hallmarks of cancer (Figure 10) (Llombart & Mansour, 2021).

*MYC* expression is very low in quiescent cells and increases with cell division and development signals (Meyer & Penn, 2008). The regulation of *MYC* expression involves a meticulous interplay of transcription regulatory motifs found in the promoter region including H-triplex, G-quadruplex, i-motif-DNA, and a far upstream element, transcription factors and chromatin components (Levens, 2008). Furthermore, *MYC* protein is fragile, since it presents a general instability, a short half-life, and it is quickly degraded by the ubiquitin-linked proteasome, as a mechanism to protect against *MYC* excessive activity (Herrick & Ross, 1994). Other causes, such as chromosomal translocations, viral insertions, amplification, deletions, insertions, and/or cis-element mutations can disrupt *MYC* regulation. In normal cells, *MYC* proto-oncogene is strictly regulated, and if some of the mentioned regulatory mechanisms fail, the presence of abnormal *MYC* mRNA and/or protein can culminate in the emergence of malignancies (Levens, 2008).

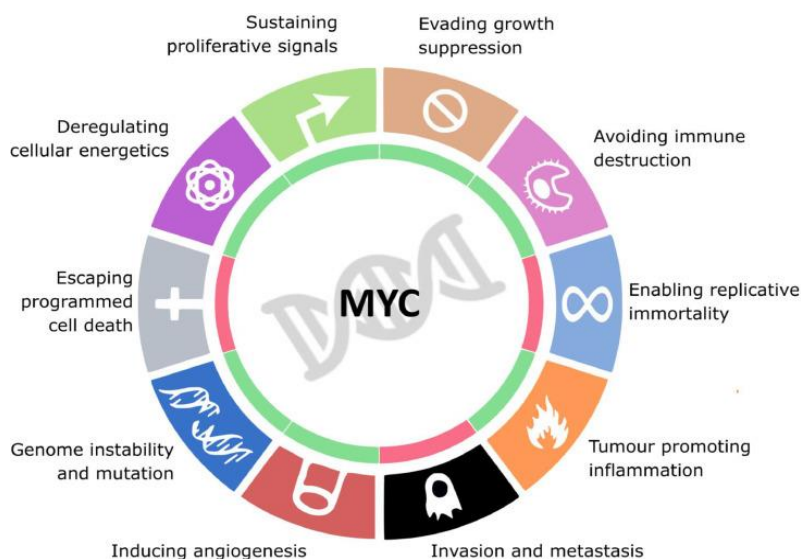


**Figure 10.** *MYC* governs all fundamental aspects of cancer traits. Adapted from (Llombart & Mansour, 2021).

*MYC* is known to be one of the oncogenes undergoing a process of amplification across a wide array of human cancers (Beroukhi et al., 2010). Approximately 70% of human cancer types, including breast, bone, brain, B-cell lymphoma, colon, cervix, lung, pancreatic, and prostate tumors, exhibit various *MYC* alterations that align with unfavorable prognoses and elevated disease aggressiveness (Mossafa et al., 2006; Tabernero et al., 2013). Experimental models illustrating *MYC*-associated tumorigenesis suggest that well-developed tumors become dependent or addicted to *MYC* (Dang, 2012).

*MYC* protein instability and lack of druggable binding pockets have been the main reasons to consider indirect targeting as a strategy for this oncogene. Some strategies considered targeting MAX to disrupt transcription (Adhikary & Eilers, 2005). Other strategies have considered targeting *MYC* target genes, like targeting the *MYC*-regulated miRNA, miR-26, in liver cancer that showed remarkable response in this type of cancer (Frenzel et al., 2010). As *KRAS* and many other oncogenes, *MYC* has well-known G4 structures, especially in its upstream promoter region, within the nuclease hypersensitive element (NHE III<sub>1</sub>) region, where a G4 forms with silencing properties. These G4 regulatory sequences have been considered as a possible therapeutic target. In 2011, Brown et al., identified a potent G4 stabilizer which provoked alterations in mRNA and protein expression of *MYC* with induced cytotoxicity. However,



achieving significant selectivity for a specific G4 structure has proven to be challenging.

Previously, in our laboratory we designed a MYC targeting PPRH against its intron 1, that successfully reduced cell viability and MYC mRNA expression in different cancer cell lines (Villalobos et al., 2015). In the present work, we considered the utilization of PPRHs to precisely target distinct segments of known and putative G4FS of the MYC gene.

### 1.5.3 *KRAS* and *MYC* interactions

In 1983, Land et al. demonstrated that mutant HRAS could induce growth transformation of rodent fibroblasts, but this process relied on the simultaneous overexpression of MYC. This provided the initial evidence that MYC can enhance RAS-driven oncogenic transformation. Following investigations in mouse models, it was revealed that MYC played a crucial role in KRAS-driven oncogenesis (Soucek et al., 2013). The expression of the *MYC* gene is influenced by downstream signaling of KRAS (Figure 11). As a result, the presence of oncogenic KRAS mutations leads to continuous expression of MYC (Hashimoto et al., 2021; Waters et al., 2021). MYC amplifies the pro-proliferative signals initiated by KRAS, promoting rapid cell cycle progression and resistance to apoptosis. This cooperation often results in more aggressive and treatment-resistant cancer phenotypes. Recent studies found that *MYC* is important for many KRAS-mutant cancer cells lines such as pancreatic MIA PaCa-2 and AsPC-1, demonstrating that KRAS suppression causes polyubiquitination and proteasomal degradation of MYC protein (Vaseva et al., 2018).

The interconnection between *KRAS* and *MYC* presents significant challenges in the development of targeted therapies. Disrupting one without affecting the other can lead to compensatory mechanisms, limiting treatment efficacy. Therefore, strategies that simultaneously target both *KRAS* and *MYC* have gained attention as potential solutions. Such therapies may hold the key to achieve durable treatment responses and overcome resistance (Donati & Amati, 2022). Now, we wanted to study how specifically designed PPRHs against both *MYC* and *KRAS*, would affect expression and cancer cell viability in KRAS and MYC-dependent cells.

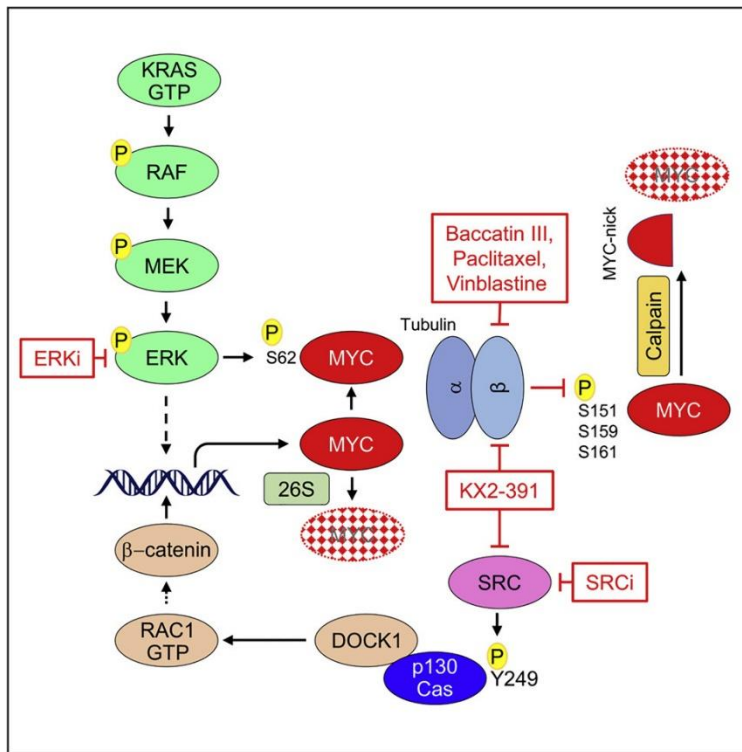


**Figure 11.** KRAS signaling pathway impacts the expression of the MYC gene. Adapted from (Waters et al., 2021).

## 1.6 SARS-CoV-2

Severe Acute Respiratory Syndrome Coronavirus 2 (SARS-CoV-2) is classified within the coronavirus family alongside viruses causing common colds such as severe pathogens like SARS-CoV, and MERS-CoV. SARS-CoV-2 transmits more rapidly and causes much higher fatality rate (Jackson et al., 2021). It is responsible for the COVID-19 pandemic that began in 2019 in Wuhan, China. Three years later, on the 5<sup>th</sup> of May of 2023, the World Health Organization (WHO) declared that COVID-19 was no longer a public health emergency of international concern. SARS-CoV-2 had infected more than 769.3 million people and caused more than 6.95 million deaths around the world by August 2023 (WHO, 2023) although it is estimated that this number might have been much higher due to many non-detected asymptomatic cases. As a preventive measure to stop the virus spreading, almost 3 billion individuals faced lockdown, that had several direct and indirect effects on the environment, economy, and social well-being of people (Hammad et al., 2023).

SARS-CoV-2 genome is a non-segmented large positive (+) single-stranded RNA with a length of 30kb (C. rong Wu et al., 2022). This genetic material carries instructions for producing both structural and non-structural proteins (Figure 12). It contains different open reading frames (ORF) including ORF 1a and ORF 1b that are translated into two polyproteins (pp1a and pp1ab). SARS-CoV-2 encodes for spike protein that interact with human ACE2 receptors, allowing the virus to bind and merge its envelope with the host membrane. Then it uses the host mechanisms to transcribe RNA and to synthesize structural proteins (spike, membrane, envelope and nucleocapsid) and accessory proteins. The generated viral RNA and proteins are then organized into new virus particles within the host cells cytoplasm. These particles are moved to the cell surface enclosed in vesicles and subsequently discharged, frequently resulting in the host cells death (Jackson et al., 2021; Jamison et al., 2022; Michel et al., 2020).

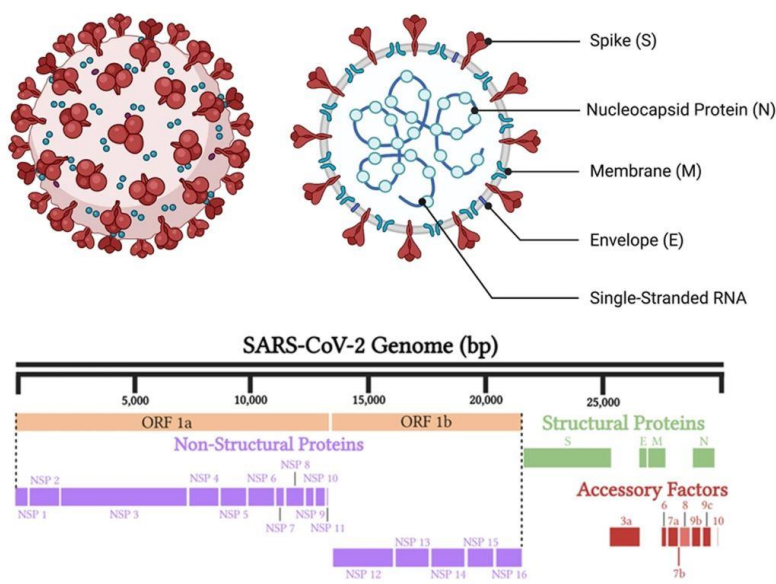


**Figure 12.** Structure elements of the SARS-CoV-2 genome (above) and its components (below). Adapted from (Jamison et al., 2022).

### 1.6.1 Diagnostic

The COVID-19 pandemic led to the rapid development and implementation of various diagnostic methods. The urgency of preventing or containing the virus spread and diagnosing cases quickly prompted researchers, scientists, and medical professionals around the world to innovate and create new diagnostic techniques (Rong et al., 2023). Of these methods, polymerase chain reaction (PCR)-based assays are considered the reference standard for virus detection due to their exceptional sensitivity and specificity (M. Shen et al., 2020). Nevertheless, it does come with some limitations including the necessity of high pure samples, expensive laboratory equipment such as thermocyclers, trained specialists, and extended processing time (Corman et al., 2020). Other strategies considered include (Figure 13):

- **Clustered Regularly Interspaced Short Palindromic Repeats (CRISPR)-based tests:** CRISPR-based tests offer the potential for rapid and highly accurate detection of SARS-CoV-2. They have advantages such as speed (30 to 40 minutes), sensitivity (concentrations below 10 nM), and the potential for point-of-care testing. However, the CRISPR technology has limitations related to the specificity of target sequences, and its potential for interference and cross-reactivity when detecting multiple targets in a single reaction. Furthermore, their development and implementation require careful optimization, validation, and regulatory approval (Li et al., 2019; Nouri et al., 2021).
- **Gene sequencing:** it is a complex technology that gives a detailed sequence of the virus that can help to understand the patterns of transmission, its origins or behavior and its responses to treatments or vaccines. Although it is a good tool for the discovery of new diseases, or virus variants, it requires specialized equipment and trained personnel. It is also time-consuming, making it less useful for real-time diagnosis (Lam et al., 2020; Ren et al., 2020).
- **Loop-Mediated Isothermal Amplification (LAMP):** these tests are like PCR tests but operate at a constant temperature, making them easier to use in some settings. They bring results within 30 minutes, and they are suitable for field or resource-limited settings. Although it is promising, this method

presents development and implementation challenges, as well as equipment and reagent requirements (James & Alwneh, 2020).

- **Antigen testing:** this method detects specific proteins on the surface of the virus. They single use, lateral flow, that can be visually read using a small portable device. The detection is much faster (15 to 20 minutes) and less expensive, suitable for mass testing and screening. Their main drawback is the lower sensitivity; it may produce false negatives during early infection and false positives due to cross-reactivity with other antigens (Lv et al., 2020; Peeling et al., 2021).
- **Serological testing:** these assays identify antibodies against SARS-CoV-2 present in blood and tissue samples. They encompass techniques such as enzyme-linked immunosorbent assay (ELISA) and immunochromatography. They indicate if a person has been previously infected and presents an immune response. It helps to understand the prevalence of the virus in the population. However, they are not typically used for diagnosing acute infections, it takes time to develop antibodies after infection and there is a variability in antibody response between individuals (W. Liu et al., 2020; Rong et al., 2023; Zhang et al., 2020).
- **Computed tomography or chest imaging:** this approach is employed to detect lung irregularities linked to COVID-19 infection. It involves capturing multiple X-ray images of the patient's chest from various angles. While these techniques can offer insights when other diagnostic tests have inconclusive results, they are not sufficient on their own to definitively diagnose COVID-19. The main drawbacks are the requirement for expertise and interpretation as well as expensive equipment that have limited availability (Bernheim et al., 2020; E. Y. P. Lee et al., 2020; Rong et al., 2023).
- **Microarray based methods:** they use immobilized oligonucleotides cDNA probes produced through reverse transcriptase of the viral RNA (Q. Chen et al., 2010). Fluorescence or chemiluminescence methods are used to identify the bound sequences, indicating the presence of the virus. It can be used to detect multiple virus variants since this method is very specific. Microarrays are suitable for screening many samples in a relatively short time and at very low concentrations. However, their complexity, equipment requirements, and potential for technical challenges should be considered when designing and

implementing these methods for SARS-CoV-2 detection (Eftekhari et al., 2021; Rong et al., 2023).

- **Biosensor-based methods:** the array of biosensor methods is wide, such as Plasmon Resonance (SPR), Field-Effect Transistor (FET), electro-chemical, nucleic acid, or antibody biosensors (Rong et al., 2023). SPR method measures changes in the refractive index of a surface as viral particles bind, enabling the detection with extreme sensibility (G. Qiu et al., 2020). FET biosensors detect changes in electrical conductivity upon viral binding, producing a signal (Seo et al., 2020). Nucleic acid-based biosensors use specific DNA or RNA probes, that bind to viral genetic material and antibody-based sensors use specific antibodies that hybridize to viral antigens. These methods, when bound to the viral material, trigger signals indicating the virus presence. Biosensor-based methods offer rapid and sensitive detection of SARS-CoV-2, with the potential for multiplexing and point-of-care use. However, challenges related to specificity, validation, and technical expertise should be carefully addressed during development and implementation (Pandey et al., 2022).

In this study, we investigated a novel analytical method centered around the concept of sandwich oligonucleotide hybridization, using designed PPRH hairpins that form high-affinity triplexes with viral polypyrimidine target sequences to efficiently capture the viral genome. The goal was to explore this approach in customized biosensing tools, such as thermal lateral flow devices, electrochemical devices, and fluorescent microarrays.

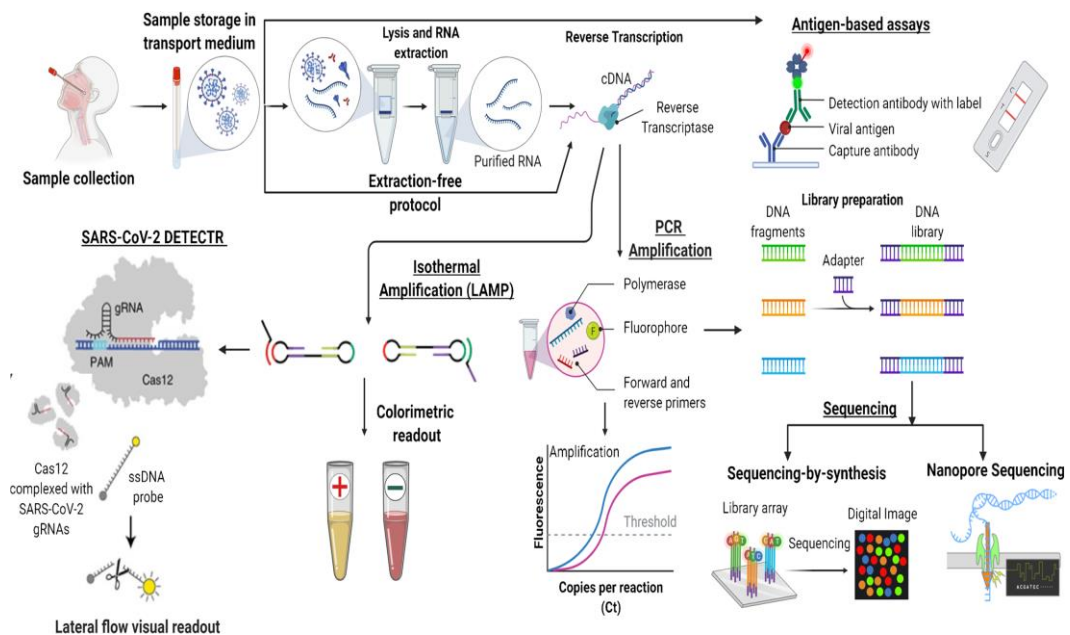


**Figure 13.** Outline of the diagnostic process for COVID-19. Adapted from (Jayamohan et al., 2021).

### 1.6.2 SARS-CoV-2 therapeutic agents

Aside from advancing in the diagnostic methods, during the pandemics, the scientific community worked hard to develop a wide array of therapies against SARS-CoV-2 while waiting for a vaccine capable of to effectively prevent COVID-19 severity and reduce transmission (Scavone et al., 2020). These methods include a diverse range of medications with distinct modes of action:

- **Antiviral drugs:** aimed to inhibit viral replication and spread within the body. These include molecules involved in life cycle and/or pathogenesis of SARS-CoV-2. There are several antiviral approaches, including polymerase or protease inhibitors, immune modulators, viral entry inhibitors or neuraminidase Inhibitors (Tao et al., 2021). RNA polymerase inhibitors, like the FDA approved drug, Redemsivir (FDA, 2020), target RNA-dependent RNA polymerase which virus needs for transcription and replication. Another strategy considered are protease inhibitors, since viruses often require protease of host cells to process viral proteins, inhibiting hosts proteases can prevent the virus from producing necessary proteins for replication (Huff et al., 2022). Entry inhibitors have also been explored as potential therapeutic strategy, these stop the virus from gaining access to host cells, preventing

initial stages of infection. This could have a broad-spectrum potential that could make them useful against a wide range of virus. Administered in the early course of infection, they could help to reduce severity of the disease, or even prevent it (Chitsike & Duerksen-Hughes, 2021).

- **Therapeutic oligonucleotides:** they consist of short sequences of nucleotides of DNA or RNA, designed in a natural or modified version for therapeutic purposes. These molecules can bind to viral genes and repress replication. Some strategies studied against SARS-CoV-2 include aptamers (Amini et al., 2022), ASOs (Qiao et al., 2023; C. Zhu et al., 2022), miRNAs (Ergün et al., 2023), siRNAs (Idris et al., 2021; Y. R. Lee et al., 2023; Supramaniam et al., 2023; Traube et al., 2022) and CRISPR-based methods (Cui et al., 2022; Nguyen et al., 2020).
- **Convalescent Plasma (CP) Therapy:** it consists of plasma from individuals who have recovered from SARS-CoV-2 infection, since it contains antibodies that may provide temporary protection (Ye et al., 2020). These antibodies have the potential to reduce the viral entry. It is generally used to prevent infection and shorten duration and severity of illness. However, CP has limited availability, patients may show adverse reactions and the antibody levels variate in donated plasma (Izda et al., 2021). Based on randomized trials, its current usage is not recommended (Simonovich et al., 2021).
- **Monoclonal Antibody or Antibody cocktail Therapy:** these are laboratory made specific antibodies against SARS-CoV-2 spike protein. They can neutralize the virus and mitigate symptom severity, particularly among high-risk individuals. However, challenges related to production and administration, along with potential limitations in effectiveness against emerging variants, are important factors to consider (Baum et al., 2020).
- **Corticosteroids:** These anti-inflammatory drugs aid in modulating the immune response during severe cases. They can alleviate cytokine storms and lung inflammation in critically ill patients. However, they come with several adverse effects, such as metabolic disturbances, heightened infection susceptibility, and bone irregularities, among other concerns (Fardet & Fève, 2014).



- **Vaccines:** Since the start of the pandemic, the primary approach was to develop a vaccine, both effective and that could be produced on a large scale. Traditional vaccines are developed during 10 to 15 years, instead COVID-19 vaccines were developed between 12 to 16 months through emergency use authorization (Kashte et al., 2021). Vaccines have proven to be very effective in preventing severe illness and reducing transmission. However, their global availability is limited, and some individuals need booster shots, of two or more doses. SARS-CoV-2 mutated in multiple variants during the pandemic, for this reason more than one or two doses were necessary. In fact, antibody responses showed to be more effective after a third dose of the Covaxin vaccine against Delta, Beta and Omicron variants (Deshpande et al., 2022). Although most of COVID-19 vaccines are well tolerated, some individuals present rare complications such as myocarditis with the mRNA COVID-19 vaccines and association with increased thrombocytopenia and cerebral thrombotic events with Janssen and AstraZeneca Vaccines (Oster et al., 2022; Sharifian-Dorche et al., 2021). There are many types of vaccines including non-replicating viral vectors (like adenoviral based vectors), mRNA vaccines, self-amplifying mRNA vaccines, DNA vaccines, inactivated viruses, and protein subunits vaccines (Izda et al., 2021). The available vaccines are shown in Table 1. The most widely used vaccines include mRNA Pfizer/BioNTech's "BNT 162b2" and Moderna's "mRNA-1273" vaccines, the non-replicating viral vector Janssen/Johnson and Johnson "Ad26.COV2.S", and AstraZeneca's "ChAdOx1 nCoV-19/AZD1222" vaccines (Sadoff et al., 2021; Thompson et al., 2021; Voysey et al., 2021; Yadav et al., 2023).

	<b>Mechanism of action</b>	<b>Dose</b>	<b>Side effects</b>
<b>Moderna (mRNA-1273)</b>	mRNA vaccine delivered in lipid nanoparticles to express the spike protein	Two divided doses of 100 mcg each 28 days apart, intramuscularly Booster of 50 mcg 5 months after primary series	Myalgia, fatigue, injection site pain, fevers and chills; myocarditis, pericarditis and myopericarditis have been reported
<b>Pfizer (BNT 162b2 “Cominarty”)</b>	mRNA vaccine in lipid nanoparticle	Two divided doses of 30 mcg, 21 days apart; booster of 30 mcg 5 months after primary series	
<b>Janssen/Johnson and Johnson (Ad26.COV2.S)</b>	Replication of incompetent adenovirus vector vaccine	0.5 mL single-dose vaccine Booster: available booster, which is also 0.5 mL given 2 months after the primary	Headache, fatigue and injection site pain, tachycardia, dizziness and syncope, thrombosis with thrombocytopenia, and Guillain-Barre syndrome
<b>AztraZeneca (ChAdOx1 nCoV-19/AZD1222)</b>	Replication of incompetent virus vector vaccine	Two divided doses, intramuscularly, 4–12 weeks apart; unfortunately, there is no booster dose available at this moment	Fatigue, headache, fever, thrombosis with thrombocytopenia
<b>Covaxin (BBV 152)</b>	Inactivated virus	Two doses 29 days apart	Injection site pain, fatigue, headache and muscle aches
<b>Novovax (NVX-cov2373)</b>	Recombinant protein nanoparticle vaccine	Two doses (0.5 mL), intramuscularly, at an interval of 3–4 weeks	Headache, fever, fatigue, muscle aches, nausea, pain, irritation, redness and injection site swelling
<b>Sinovac</b>	Inactivated vaccine	Two doses 28 days apart	Nausea and a rare neurological disorder
<b>Sinopharm (WIV04 and HB02)</b>	Inactivated vaccine	Two doses 28 days apart	Injection site pain, fatigue and headache
<b>Sputnik V</b>	Replication incompetent adenovirus vector vaccine (uses two separate vectors) developed by Gamaleya institute in Russia	First dose with the adenovirus 26 vector dose, second dose with adenovirus 5 vector 21 days to 3 months after the first dose	Fatigue (70%), headache (64%), muscle pain (61%), joint pain (46%), chills, nausea and vomiting
<b>Cansino biologics Ad5-based COVID-19 vaccine</b>	Replication of incompetent adenovirus vector	Single intramuscular dose	Redness, fatigue, fever, nausea, headaches and muscle pains

**Table 1.** Available vaccinations for COVID-19. Adapted from (Chinta et al., 2023).



## **2. OBJECTIVES**



This work is divided into two main parts, one exploring the effects PPRHs against undruggable cancer targets, and a second centered in the usage of the PPRHs both as a tool for the diagnosis of COVID-19 and as a therapeutic agent against the viral infection caused by SARS-CoV-2. Therefore, we set up these two main goals:

1. To study the effects of PPRHs as a gene silencing tool against the undruggable cancer targets *KRAS* and *MYC*.
  - To identify G-quadruplex forming sequences in the *KRAS* gene, to target their complementary regions with PPRHs and to inhibit the expression of this oncogene.
  - To determine the modulatory effects of the complementary G4 forming sequences in cancer cells overexpressing *MYC*.
  - To evaluate the combinatorial effect of the most effective PPRHs targeting *KRAS* and *MYC*.
2. To determine the PPRH properties to detect SARS-CoV-2 and to use them as a therapeutic tool.
  - To study and validate the ability of PPRHs as a diagnostic tool for SARS-CoV-2.
  - To explore the therapeutic properties of PPRHs to decrease SARS-CoV-2 proliferation in VERO-E6 cells.
  - To test the protective effect of PPRHs targeting SARS-CoV-2 RNA in transgenic mice bearing the humanized ACE2 receptor.



### **3. MATERIALS AND METHODS**





Materials and methods are already described within the articles presented in the “Results” section of this thesis. However, additional materials or methodologies that are not included in the manuscripts are described within this section.

### 3.1 General design of PPRHs

To find polypurine sequences capable of binding to the polypyrimidine-specific region in a target gene, we employed the Triplex-Forming Oligonucleotide Target Sequence Search software (TFO searching tool). This software was developed at the MD Anderson Cancer Center, University of Texas, Houston, TX, USA (Gaddis et al., 2006).

The design of the specific molecules was guided by specific criteria to ensure the best PPRH properties:

- A length per arm of the PPRH ranging between 20-25 nt.
- A minimum G content of 40-45 %.
- A maximum of 3 pyrimidine interruptions within the purine stretch.
- A four-thymidine connector between the two arms of the PPRH.

All these design considerations are crucial to ensure stability and effectiveness of the PPRHs in their intended applications.

Then, the selected PPRHs were analyzed by the software contained in the QGRS mapper to check for putative G-quadruplex forming sequences (G4FS). This tool uses an algorithm to recognize and depict possible G-quadruplex elements within a specific sequence providing a G-score. The greater the value of this score, the more likely the formation of a G-quadruplex structure is. We chose the polypurine sequences with the highest G-score and analyzed them by BLAST to ensure that they do not exhibit similarities or matches with unintended targets.

The following PPRHs were designed:

- Against MYC, six different PPRHs: (HpMYC-G4-PR-C, HpMYC-G4-I1-T, HpMYC-Pr-Distal-T, HpMYC-Pr-Prox-T, HpMYC-I1-T, HpMYC-I1\_short-T and HpMYC-I2-C).

- Against KRAS, five PPRHs: (HpKRAS-PrEF-C [PPRH1], HpKRAS-PrBC-C [PPRH 2], HpKRAS-I1-T, HpKRAS-E5-C).
- Against SARS-CoV-2, three different PPRHs: (CC1-PPRH, CC2-PPRH and CC3-PPRH).

A polypurine scrambled hairpin (HpSc9) was used as a negative control. The designed PPRHs were synthesized as non-modified oligodeoxynucleotides by Merck-Sigma (Haverhill, UK). Hairpins were resuspended at a concentration of 100  $\mu$ M with Tris-EDTA buffer (1 mM EDTA and 10 mM Tris-HCl, pH 8.0) (Sigma-Aldrich, Madrid, Spain) and stored at -20°C. The corresponding sequences for each PPRH used in this work and the negative control are shown in the corresponding articles.

### 3.2 DNA-PPRH binding analyses

The binding capability of MYC, KRAS and SARS-CoV-2 targeting PPRHs against their targets was analyzed by electrophoretic mobility shift assays (EMSA).

Binding reactions were performed by incubation of the PPRHs using two approaches (i) with a polypyrimidine ssDNA probe or (ii) with a dsDNA probe. Both ssDNA and dsDNA had the polypyrimidine strand labeled with fluorescein (6-FAM) and were synthesized by Merck-Sigma (Haverhill, UK). The dsDNA was obtained by mixing equimolecular amounts of each single-stranded oligodeoxynucleotide in a 150 mM NaCl solution, hybridized at 95 °C for 5 min, and cooled down to RT.

Binding reactions were performed using binding buffer (5% glycerol, 100 mM NaCl, 10 mM MgCl<sub>2</sub>, 40 mM HEPES, pH 7.2; all from Sigma-Aldrich, Madrid, Spain). For ssDNA binding reactions, as an unspecific competitor, tRNA was added, whereas for dsDNA Poly(dI:dC) (1:1 ratio for both cases) was used. The corresponding amounts of ssDNA and dsDNA (ranging between 100 and 200 ng) with their corresponding PPRHs (ranging from 12.5 to 2000 ng) are shown in the scientific articles.

Binding mixtures with ssDNA were incubated at 37°C whereas dsDNA binding reactions were incubated at 65 °C. In both cases, binding reactions were

incubated for 10 min without the probe and then for a 20 min period with the probe. As a negative control Hp-Sc9 was used.

Binding products were electrophoretically resolved in 7 or 8 % polyacrylamide non-denaturing gels containing 5 % glycerol, 10 mM  $\text{MgCl}_2$ , 50 mM HEPES, pH 7.2 using a running buffer containing 10 mM  $\text{MgCl}_2$  and 50 mM HEPES (pH 7.2) and run at a fixed 190 V and 4 °C. ImageLab software v5.2 was used to visualize the results (GE Healthcare, Barcelona, Spain). Specific ssDNA, dsDNA, PPRHs, and gel percentages are shown in the articles.

### 3.3 RNA-PPRH binding analyses

The capacity of the RNA-PPRH to bind to its target sequence in SARS-CoV-2 regions was analyzed using EMSA assays as described in section 3.2. DNA-PPRH binding analyses were performed with the conditions for ssDNA binding reactions (at 37 °C) using DEPC  $\text{H}_2\text{O}$ .

### 3.4 Strand displacement assays

The capacity of PPRHs to bind to their dsDNA targets, displacing the complementary strand, and allowing G4 formation for KRAS and MYC, was explored by Strand Displacement Assays.

We used 1.5  $\mu\text{g}$  of each oligonucleotide ssDNA (single-strand polypyrimidine [ssPPY] labeled with FAM or single-strand polypurine [ssPPU]) or dsDNA labeled with FAM with increasing amounts of PPRH. dsDNA probes were prepared as described in section 3.2.

The mixes of the oligonucleotides with the PPRHs were prepared in a 100 mM KCl and 100 mM Tris-HCl, pH 7.4 buffer, incubated at 90°C for 5 min in a water bath and slowly cooled down to RT. The resulting structures were resolved in non-denaturing 12 % polyacrylamide and 10 mM KCl gels in 1x TBE buffer at a fixed 150 V.

Once electrophoresed, bands were detected under a UV light lamp. Then, gels were stained with 5  $\mu\text{M}$  Thioflavin T (ThT) (Sigma Aldrich, Madrid, Spain) for 15 min with shaking and washed in water for 2 min. Images were taken under a UV light lamp or using the Gel Doc<sup>TM</sup> EZ with the Image Lab

Software, Version 6.0. Target sequences for each KRAS and MYC PPRHs, ssDNA or dsDNA, are described in the corresponding articles.

### **3.5 Melting Temperature Assay**

To determine melting temperatures ( $T_{Ms}$ ) of MYC and KRAS, we used a ssPPY probe and the PPRH at a ratio of 1:1 in a final concentration of 1  $\mu$ M in buffer solution with 100 mM NaCl, 10 mM  $MgCl_2$ , and 40 mM HEPES, pH 7.2.

Before performing the experiments, the mix was heated to 65 °C for 15 min and slowly cooled down to RT. Melting studies were performed using a V-730BIO UV-Vis spectrophotometer (Jasco, Madrid, Spain), connected to a controller that increased the temperature from 10 to 90 °C and then decreased it from 90 to 10 °C at a 1 °C/min rate. Absorbance was recorded at 260 nm in a 1 cm pathlength quartz cuvette and monitored every 0.5 °C.

### **3.6 Western blot analyses for KRAS, MYC, Cyclin D1 and GAPDH detection**

PC-3 cells (60,000) were plated in 6-well dishes and transfected 24 h after with different concentrations of PPRHs, described in the corresponding articles.

Total extracts were obtained 72 or 120 h after transfection in RIPA buffer (1 % Igepal CA-630, 0.5 % sodium deoxycholate, 0.1 % SDS, 150 mM NaCl, 10 mM NaF, 1 mM PMSF, 1 mM EDTA, 50 mM of Tris-HCl, pH 8.0 and containing Protease Inhibitor (P8340-5ML); all purchased from Sigma Aldrich, Madrid, Spain, with the exception of Tris-HCl, which was from PanReac AppliChem, Barcelona, Spain).

Cell extract was centrifuged at 13,000 x g for 10 min at 4 °C. Supernatants were collected and their protein level were quantified using the Bio-Rad protein assay based on the Bradford method using Bovine serum albumin (BSA) as standard (Sigma-Aldrich, Madrid, Spain).

Protein extracts were electrophoresed in 4-12 % SDS-polyacrylamide gels and transferred to polyvinylidene difluoride (PVDF) membranes (immobilon

P, Milipore, Madrid, Spain) using a semi-dry electroblotter. Membranes were blocked using 5 % Blotto.

Membranes were probed with either MYC (1:1500 dilution; ab205818, Abcam, Cambridge, UK) or KRAS (1:1,500 dilution; LS-C211371; LifeSpan BioSciences, Washington, USA) antibodies conjugated with horseradish peroxidase (HRP), with a primary antibody against cyclin D1 (1:100 dilution; M-20, sc-718, Santa Cruz Biotechnology, Heidelberg, Germany), or a primary antibody against GAPDH (1:200 dilution; sc-47724, Santa Cruz Biotechnology, Heidelberg, Germany) overnight at 4 °C with slow agitation. Cyclin D1 protein levels were detected using a secondary HRP-conjugated anti-rabbit antibody (1:1,200 dilution, P0399, Agilent Technologies, Singapore). GAPDH protein was detected using a secondary HRP-conjugated anti-mouse antibody (1:1,500 dilution, sc-516102, Santa Cruz Biotechnology, Heidelberg, Germany) and used to normalize the results.

Signals of KRAS, MYC, Cyclin D1 and GAPDH proteins were detected using enhanced chemiluminescence (ECL), as recommended by the manufacturer (Amersham, Arlington Heights, IL). ImageQuant LAS 4000 mini-imager (GE Healthcare, Barcelona, Spain) was used to visualize the protein bands and quantification was performed using the ImageQuant 10.1 software or Image J2 2.3.0 (FIJI).

### **3.7 Internalization of PPRHs (Flow cytometry)**

PC-3, MCF-7 and SW480 Cells (100,000) were plated in well-dishes in F12 + 10% FBS serum. The day after, cells were transfected with a 100 µl mix of N-[1-(1,2-Di-(9Z-octadecenoyl)-3- trimethylammoniumpropane methyl sulfate (DOTAP; Biontex, Germany) or 1,3-bis[(4-oleyl-1-pyridinio)methyl]benzene dibromide (DOPY, synthesized in house, UB) with a scrambled 6-FAM-labeled PPRH (HpSC9-FAM) in F12 serum-free medium.

One day after transfection, cells were trypsinized, collected in PBS and centrifuged at 1,200 x g at 4 °C for 5 min. Cell pellet was resuspended in 400 µL of PBS.

Propidium Iodide (IP) was added to a final concentration of 5 µg/mL (Sigma Aldrich, Madrid, Spain). Flow cytometry analyses were performed in a Gallios flow cytometer (Beckman Coulter, Inc., Barcelona, Spain) at the CCiT.



## **4. RESULTS**





## Informe dels directors

Els Drs. Carlos J. Ciudad Gómez i Verónica Noé Mata, directors de la tesi doctoral titulada *“PPRHs against undruggable KRAS and MYC oncogenes and for the diagnosis and treatment of SARS-CoV-2.”*.

## INFORMEN

Del factor d'impacte de les revistes de publicació dels articles inclosos en aquesta tesi doctoral.

Que els articles I i II són treballs en co-autoria, en què ambdós primers coautors han compartit els projectes i han realitzat els experiments per igual, i que no s'han utilitzat per la realització de cap tesi doctoral prèvia.

Que l'article III està en preparació, que el doctorant n'és el primer autor i que no s'ha utilitzat per la realització de cap tesi doctoral prèvia.

Que l'article IV és un treball en col·laboració, que el doctorand ha participat en la part de disseny i en els assajos de unió (assajos de canvi de mobilitat electroforètica), i no s'ha utilitzat per la realització de cap tesi doctoral prèvia.

Que l'article V està en preparació i és un treball en col·laboració amb altres autors. El doctorand ha realitzat assajos de unió i no s'ha utilitzat per la realització de cap tesi doctoral prèvia.

## Llistat de publicacions

- **Article I.** Targeting KRAS Regulation with PolyPurine Reverse Hoogsteen Oligonucleotides.

Alexandra Maria Psaras<sup>#</sup>, Simonas Valiuska<sup>#</sup>, Véronique Noé, Carlos J. Ciudad and Tracy A. Brooks.

<sup>#</sup>Both authors contributed equally.

International Journal of Molecular Sciences. 2022, 23(4), 2097. (Impact factor: 6.208)

- **Article II.** Targeting MYC Regulation with Polypurine Reverse Hoogsteen Oligonucleotides.

Simonas Valiuska<sup>#</sup>, Alexandra Maria Psaras<sup>#</sup>, Véronique Noé, Tracy A. Brooks, and Carlos J. Ciudad

<sup>#</sup>Both authors contributed equally.

International Journal of Molecular Sciences. 2023, 24(1), 378. (Impact factor: 5.6)

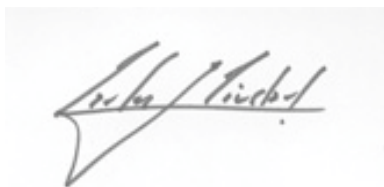
- **Article III (manuscrit en preparació).** Combinatorial effect of Polypurine Reverse Hoogsteen hair-pins against *KRAS* and *MYC* targeting in PC-3 cell line.

- **Article IV.** Detection of SARS-CoV-2 Virus by Triplex Enhanced Nucleic Acid Detection Assay (TENADA).

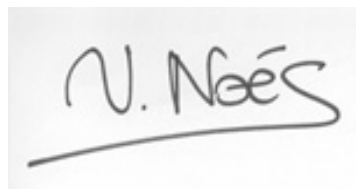
Anna Aviñó, Carlos Cuestas-Ayllón, Manuel Gutiérrez-Capitán, Lluïsa Vilaplana, Valeria Grazu, Véronique Noé, Eva Balada, Antonio Baldi, Alex J. Félix, Eva Aubets, Simonas Valiuska, Arnau Domínguez, Raimundo Gargallo, Ramon Eritja, M.-Pilar Marco, César Fernández-Sánchez, Jesús Martínez de la Fuente and Carlos J. Ciudad

International Journal of Molecular Sciences. 2022, 23(23), 15258 (Impact factor: 5.6)

- **Article V (manuscript en preparació).** Polypurine Reverse Hoogsten hairpins as a therapeutic tool for SARS-CoV-2 infection.

A handwritten signature in black ink, appearing to read 'Carlos J. Ciudad Gómez', written over a horizontal line.

Dr. Carlos J. Ciudad Gómez

A handwritten signature in black ink, appearing to read 'V. Noé Mata', written over a horizontal line.

Dra. Verónica Noé Mata



## 4.1. ARTICLE I

### Targeting KRAS Regulation with PolyPurine Reverse Hoogsteen Oligonucleotides

Alexandra Maria Psaras<sup>#</sup>, Simonas Valiuska<sup>#</sup>, Véronique Noé, Carlos J. Ciudad and Tracy A. Brooks

<sup>#</sup> Both authors contributed equally to this work

International Journal of Molecular Sciences. 2022, 23(4), 2097. (Impact factor: 6.208)

**Background:** The *KRAS* gene (Kirsten rat sarcoma viral oncogene homolog) is a proto-oncogene encoding a small GTPase protein that participates in the signaling of several growth factors. It plays a pivotal role in intracellular signal transduction, relaying signals from cell surface receptors to the nucleus (Colicelli, 2004; Cox & Der, 2010). However, when *KRAS* is mutated and becomes constitutively active, it can drive uncontrolled cell proliferation and tumorigenesis. *KRAS* mutational activation is widely distributed across diverse cancer types, exhibiting a broad range of occurrences (Prior et al., 2012; Pylayeva-Gupta et al., 2011). However, it is particularly prominent in lung, colorectal and pancreatic cancers, where it is detected in over 95% of cases (Adjei, 2001). For many years, *KRAS* has been considered a undruggable target due to its lack of targetable pockets for possible drugs, its highly dynamic conformation when activated, and because the GDP/GTP cycle exchange is highly regulated. Although some drugs are being developed against *KRAS*, they are usually designed for rare *KRAS* mutations, and thus the development of anti-*KRAS* drug is required (Nakajima et al., 2022). *KRAS* contains known G-quadruplex sequences that form G4 structures which have a role in *KRAS* expression regulation. For this reason, *KRAS* G4-rich sequences have been considered potential targets for *KRAS* gene silencing (Cogoi & Xodo, 2006; D'Aria et al., 2020; Shalaby et al., 2013).

**Objectives:** To discover previously unknown G-quadruplex forming sequences (G4FS) in the *KRAS* gene and to develop specific PPRHs that can target and interact with these G4FS, along with a known G-quadruplex region. Our main aim was to investigate the effects and the therapeutic implications of these designed PPRHs on *KRAS* gene regulation.

**Results:** A total of five different PPRHs were designed, two against the *KRAS* promoter G4<sub>mid</sub> (HpKRas-Pr-EF-C, HpKRas-Pr-BC-C, referred as PPRH 1 and PPRH 2, respectively) and three others against putative G4FS in the distal promoter (HpKRas-Pr-C), intron 1 (HpKRas-I1-T) and exon 5 (HpKRas-E5-C).

We investigated the formation of higher-order DNA structures in three specific regions of the *KRAS* gene that had not been previously explored. These regions are found in the distal promoter (Pr-C), an intronic region (I1) and an exonic region (E5). The latter region was confirmed to be a G4FS with a parallel topology.

We verified that the interaction of the PPRHs with their corresponding targets displaces the complementary strand allowing the formation of secondary structures.

We also analyzed the cytotoxic effect of the PPRHs in ovarian and pancreatic cancer *KRAS* dependent cell lines. PPRHs displayed different levels of effectiveness in pancreatic and ovarian cancer cells. However, we consistently observed that when targeting *KRAS* promoter with PPRHs (HpKRas-Pr-C, PPRH 1 and PPRH 2), there was a significant inhibition of cellular growth and viability in both cancer cell types.

*KRAS* transcription levels were affected in cells transfected with PPRHs 1 and 2. PPRH 2 was the most effective in decreasing *KRAS* transcription activity. We also analyzed the transcription modulation mediated by PPRH 1 and PPRH 2 with a *KRAS* promoter selective G4-stabilizing compound, NSC 317605, observing synergistic activities that improved the transcriptional downregulation and the reduction of cell viability.

**Conclusions:** In this study, we have identified and integrated two therapeutic approaches: PPRHs and NSC 317605. These two strategies effectively stabilize the G-quadruplex (G4) structure present in the middle (G4mid) region of the *KRAS* promoter. As a result, transcription of the *KRAS* gene is reduced, leading to a synergistic modulation of *KRAS*-dependent AsPc-1 pancreatic cancer cells viability.







## Article

## Targeting KRAS Regulation with PolyPurine Reverse Hoogsteen Oligonucleotides

Alexandra Maria Psaras <sup>1</sup>, Simonas Valiuska <sup>2</sup>, Véronique Noé <sup>2</sup>, Carlos J. Ciudad <sup>2</sup> and Tracy A. Brooks <sup>1,\*</sup><sup>1</sup> Department of Pharmaceutical Sciences, School of Pharmacy and Pharmaceutical Sciences, Binghamton University, Binghamton, NY 13902, USA; apsaras@binghamton.edu<sup>2</sup> Department of Biochemistry and Physiology, School of Pharmacy and Food Sciences, & IN2UB, University of Barcelona, 08028 Barcelona, Spain; simonasvaliuska13@gmail.com (S.V.); vnoe@ub.edu (V.N.); cciudad@ub.edu (C.J.C.)

\* Correspondence: tbrooks@binghamton.edu; Tel.: +1-607-777-5842



Citation: Psaras, A.M.; Valiuska, S.; Noé, V.; Ciudad, C.J.; Brooks, T.A. Targeting KRAS Regulation with PolyPurine Reverse Hoogsteen Oligonucleotides. *Int. J. Mol. Sci.* **2022**, *23*, 2097. <https://doi.org/10.3390/ijms23042097>

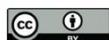
Academic Editor: Vincenza Barresi

Received: 31 December 2021

Accepted: 9 February 2022

Published: 14 February 2022

**Publisher's Note:** MDPI stays neutral with regard to jurisdictional claims in published maps and institutional affiliations.



**Copyright:** © 2022 by the authors. Licensee MDPI, Basel, Switzerland. This article is an open access article distributed under the terms and conditions of the Creative Commons Attribution (CC BY) license (<https://creativecommons.org/licenses/by/4.0/>).

**Abstract:** KRAS is a GTPase involved in the proliferation signaling of several growth factors. The KRAS gene is GC-rich, containing regions with known and putative G-quadruplex (G4) forming regions. Within the middle of the G-rich proximal promoter, stabilization of the physiologically active G<sub>4mid</sub> structure downregulates transcription of KRAS; the function and formation of other G<sub>4s</sub> within the gene are unknown. Herein we identify three putative G<sub>4</sub>-forming sequences (G<sub>4FS</sub>) within the KRAS gene, explore their G<sub>4</sub> formation, and develop oligonucleotides targeting these three regions and the G<sub>4mid</sub> forming sequence. We tested Polypurine Reverse Hoogsteen hairpins (PPRHs) for their effects on KRAS regulation via enhancing G<sub>4</sub> formation or displacing G-rich DNA strands, downregulating KRAS transcription and mediating an anti-proliferative effect. Five PPRHs were designed, two against the KRAS promoter G<sub>4mid</sub> and three others against putative G<sub>4FS</sub> in the distal promoter, intron 1 and exon 5. PPRH binding was confirmed by gel electrophoresis. The effect on KRAS transcription was examined by luciferase, FRET Melt<sup>2</sup>, qRT-PCR. Cytotoxicity was evaluated in pancreatic and ovarian cancer cells. PPRHs decreased activity of a luciferase construct driven by the KRAS promoter. PPRH selectively suppressed proliferation in KRAS dependent cancer cells. PPRH demonstrated synergistic activity with a KRAS promoter selective G<sub>4</sub>-stabilizing compound, NSC 317605, in KRAS-dependent pancreatic cells. PPRHs selectively stabilize G<sub>4</sub> formation within the KRAS mid promoter region and represent an innovative approach to both G<sub>4</sub>-stabilization and to KRAS modulation with potential for development into novel therapeutics.

**Keywords:** KRAS; PPRH; G-quadruplex; pancreatic cancer; ovarian cancer

## 1. Introduction

KRAS is a 21-kD GTPase that plays a role in cell survival, proliferation, and differentiation [1,2]. It is constitutively expressed, but active only when GTP-bound. Normal functioning KRAS has a relatively short, and inducible, GTP-bound life. Mutations in RAS proteins are found in approximately one-third of all human tumors, with KRAS being the most frequently mutated isoform [3,4]. Single point mutations of the KRAS gene abolish inherent GTP hydrolysis; these mutations render the protein constitutively active. The highest incidence of mutational activation occurs in lung, colorectal, and >95% of pancreatic cancers [1,4,5]. KRAS mutations are associated with increased tumorigenicity and poor prognosis [3]. Mutation of the KRAS gene has been identified as a transforming oncogenic event, where it creates an unstable environment allowing for more mutational selection and increasingly aggressive disease [5]. In the absence of a mutation, increased KRAS activity in human tumors is the result of gene amplification, overexpression, or increased upstream activation [3]. The genomic amplification of KRAS, in particular, is associated with metastatic disease and poor prognosis in hormone-related cancers such as ovarian cancer [6–21].

KRAS is a well validated anti-cancer therapeutic target. Many active drug discovery programs are ongoing, with a focus on individual mutant KRAS isoforms. Sotorasib targets the G12C mutant protein and was FDA-approved for lung cancer in late May of 2021 [22,23]. While this drug's development, clinical activity, and approval is remarkable, G12C is not a common mutation in pancreatic and colorectal cancers with KRAS mutations and sotorasib does not benefit patients with amplified or overexpressed KRAS. The approach of developing agents for each KRAS mutation necessitates an array of drugs to be developed and does not address cancers with dysregulation of non-mutant KRAS. Notably, transcriptional down-regulation has been demonstrated to be lethal to tumor cells with aberrant KRAS signaling, irrespective of mutational status, and to potentially have a wide therapeutic window [1,24–27]. Stabilization of higher order genomic structures is an established approach to modulating transcription.

Within the proximal promoter region of KRAS lies a GC-rich region of DNA capable of forming non-canonical G-quadruplex (G4) structures. G4s are secondary structures made of four guanine bases associated by Hoogsteen hydrogen bonds and a stack of a minimum two of these structures forming helical composition. G4 structures have an important role in controlling different biological processes such as DNA replication [28] telomere homeostasis [29] and mRNA transcription and regulation, processing and translation [30,31]. Since they are present in biological key functions, these formations can be considered as potential therapeutic targets. G4 formation in both DNA and RNA has been demonstrated in live cells [28] in an inducible manner [32]. Moreover, G4-positive nuclei are significantly increased in cancer cells, as compared to surrounding non-neoplastic tissue, from patient-derived solid tumor tissue biopsies [33]. G4s are attractive therapeutic targets as they are more globular than B-DNA, enabling more selective gene interactions. The core promoter region of *KRAS* is highly G/C-rich (~75%) and putatively capable of forming higher order non-B-DNA structures [34–36]. The proximal promoter region contains several G4-forming sequences, including G4<sub>near</sub> (32r) and G4<sub>mid</sub>. Previous work from our collaborative group described the predominant G4 isoform formed by G4<sub>mid</sub>, and ascribed G4-mediated silencing within this region to G4<sub>mid</sub> formation [37]. Several other putative G4-forming regions exist within the promoter and the gene itself whose formation and function have yet to be described.

In this work we targeted the G-rich, putative G4-forming regions with PolyPurine Reverse Hoogsteen hairpins (PPRHs), which are two polypurine strands linked by a four-thymidine loop (4T) running in antiparallel directions and bound by intramolecular Hoogsteen bonds, forming a hairpin structure. These molecules can hybridize in a specific sequence-dependent manner to single- or double-stranded DNA (dsDNA) by Watson-Crick bonds forming a triplex structure and displacing the fourth strand of the dsDNA which can lead to a knockdown of the targeted gene [38]. We classify the PPRHs depending on the strand of the DNA they target. If the polypyrimidine stretch is found in the template strand they are called Template-PPRHs [39] and if the stretch is found in the coding strand, they are called Coding-PPRHs [40]. The latter can also target mRNA, where it can modulate post-transcriptional events, since it has the same orientation as the coding strand. PPRHs have already been shown to inhibit gene expression of cancer related genes [41] in immunotherapy [42–44] or in replication stress [45]. In addition, they can be used for gene repair to correct point mutations [46,47] and very recently have also been used as the sensor component of biodelectors [48,49].

Previously, we observed that targeting the complementary strand of G4 forming sequences (G4FS) in the 5'-UTR of the thymidylate synthase (TYMS) gene was very effective in reducing the viability, mRNA, and protein levels of this target [50]. Here we designed and used PPRHs against polypyrimidine tracts in the promoter and gene coding region of *KRAS*, making them complementary to G4FS to promote possible G4 folding and related gene silencing or post-transcriptional modifications. We targeted the promoter region of this gene, including proximal and distal segments and an intronic part within the 5'-UTR. Additionally, we designed a PPRH targeting exon 5 in the 3'-UTR of the gene.

## 2. Results

### 2.1. Identification of Putative PPRHs Target Sequences in KRAS Promoter and Gene Region

G4's formed within the proximal KRAS promoter have been previously described [37,51], including the physiologically active KRAS G4<sub>mid</sub> sequence. We included this region and searched for other G4FS within the KRAS gene sequence using both the TFO searching tool and the QGRS mapper (Figure 1A,B), and then selected sequences that could form triplexes with the highest G-Score. Notably, the QGRS identified portions of the G4<sub>mid</sub> sequence with G-scores of 20–21; inputting only the G4<sub>mid</sub> sequence containing seven G-tracts, the mapper identified a wide array of putative G4s with G-scores ranging up to 39. The predicted G4 with the highest G-score encompasses the second (termed B) through fifth (termed E) G-tracts, in agreement with the structure identified previously [37], and is targeted by two of the PPRHs designed below. We further designed the PPRHs targeting the polypyrimidine stretches complementary to the known G4<sub>mid</sub> or the G4FS (Figure 1C). The KRAS sequence with the designed hairpin target regions is shown in Figure 1D. Figure 1E represents PPRHs mechanism of action with the example of HpKRasPrEF-C (PPRH 1).

### 2.2. G4 Formation within Newly Identified G4FS-PR, I1 and E5

While the G4 formation within the proximal promoter region has been previously explored and described, it is unknown for the newly identified sequences within the distal promoter (KRasPr-C, PR), intron 1 (KRasI1-T, I1) and exon 5 (KRasE5-C, E5). Using electronic circular dichroism, we examined the induction of G4 sequences upon the addition of 100 mM KCl (Figure 2A). The distal promoter sequence did not demonstrate any secondary structure in either the absence or presence of KCl, whereas the intron 1 sequence formed a structure without variation in the absence or presence of KCl that is consistent with a hairpin loop. Only the sequence within exon 5 demonstrated the induction of a parallel G4 upon the addition of KCl. All sequences were melted from 20–100 °C; mdeg were recorded every 1 °C at 262 nm and full spectra were recorded every 10 °C (Figure S1). With no apparent formation of a secondary structure within the PR region, no melting profile was able to be described. Both the I1 and the E5 sequences, however, were probed without and with 100 mM KCl to examine their thermal stability ( $T_M$ ). The  $T_M$  of I1 increased from 46 to 51 °C upon the addition of KCl, whereas the  $T_M$  of E5 markedly increased from 45 to 75 °C under the same conditions (Figure 2A, right). The inter- versus intra-molecular tendencies of the E5 G4 was explored through the examination of dose dependent G4 formation and thermal stability in the presence of 100 mM KCl (Figure 2B). G4 formation and thermal stability increased in a dose dependent manner, with maximal mdeg at 264 nM increasing from 1 to 14 theta and  $T_M$ s increasing from 58 to 70 °C, consistent with an interstrand G4.

### 2.3. PPRHs Binding to KRAS Target Sequences and Polupurine Strand Displacement

To evaluate the binding of the designed PPRHs to their corresponding target regions, we performed different electrophoretic mobility shift assays (EMSA; Figure 3) in a native gel testing the PPRHs with dsDNA of KRAS target sequences (Table 1). In the case of PPRH 1 and HpKRasBC-C (PPRH 2) we designed a sole dsDNA target probe spanning the entire KRAS G4<sub>mid</sub> sequence, encompassing the binding sites for both PPRHs. However, for PR, I1 and E5, we designed a dsDNA target probe corresponding to their sequences. For each of the PPRHs tested, we observed one main shifted band that corresponds to the binding of the hairpin with the probe. In contrast, the negative control, Hp-Sc9 (SCR), did not show any shifted band for any of the probes.

In order to assess whether the binding of the targeting PPRHs mediated the displacement of the G-rich strand, we performed a strand displacement assay using incubations of the dsDNA-KRAS-I1 probe with increasing concentrations of HpKRAS-I1 and staining with thioflavin T (ThT) [52,53] after resolving the structures by native gel electrophoresis (Figure 3B). The Hp-KRAS-I1 was able to displace the polypurine strand in a concentration-dependent manner.



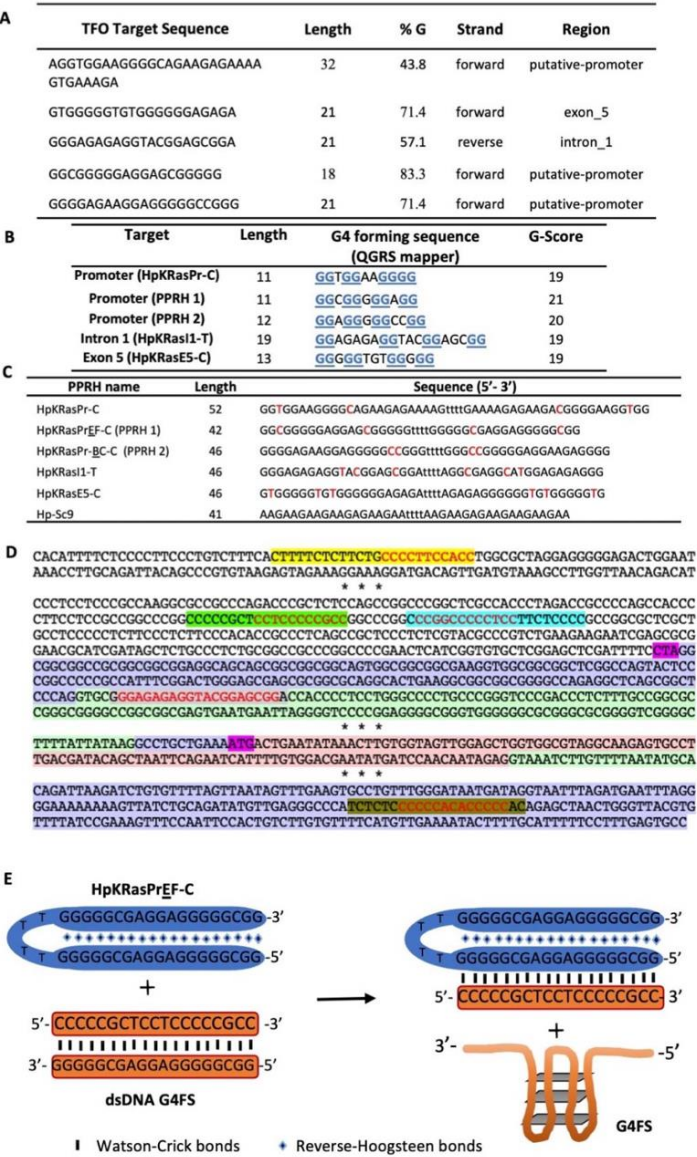


**Figure 1.** (A) Putative target regions of K-Ras using the TFO searching tool and searching the sequence in the Promoter Database. (B) QGRS mapper results of the selected sequences. Guanines marked in blue and underlined are involved in G4 formation. (C) Design of the PPRHs targeting K-Ras specific G4FS (HpKRasPr-C, HpKRasPrEF-C, HpKRasPrBC-C, HpKRasI1-T, HpKRasE5-C) and a scramble hairpin, Hp-Sc9 as a negative control. Pyrimidine interruptions are marked in red.

(D) Location of the target regions of the selected PPRHs: four of them belong to the coding category (HpKRasPr-C highlighted in yellow, HpKRasPr-EF-C in light green, HpKRasPr-BC-C in cyan, and HpKRas-E5-C in brown) and HpKRas-I1-T in grey which is a template-PPRH. The putative G4FS, or its complementary sequence, are marked in red. Three PPRHs have targets in the promoter sequence (white zone). Another PPRH binds to intron 1 (green) which is within the 5'-UTR (purple). The beginning of transcription (CTA) and translation (ATG) are indicated in magenta, right before the first coding region (pink). The last PPRH is designed towards a sequence within the 3'-UTR in Exon 5. Asterisks indicate gaps in the sequence of K-Ras. (E) Putative mechanism of PPRH 1 (HpKRasPrEF-C) strand displacement of the dsDNA G4FS target sequence, facilitating G4-formation and subsequent gene regulation.

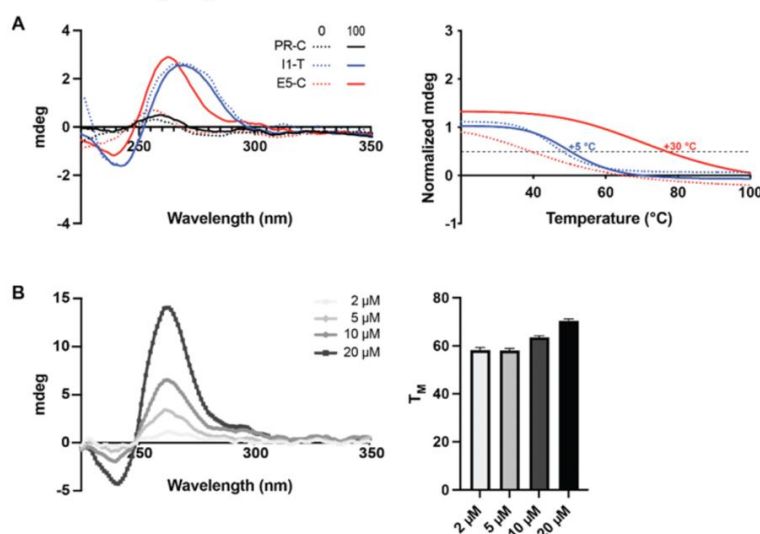


**Figure 2.** G4 formation within newly identified G4FS. (A) Indicated DNA strands were annealed in the absence (dotted lines) or presence (solid lines) of 100 mM KCl and their spectra were recorded from 225–350 nm (left). Thermal stability of the I1 and E5 structures were determined in the absence (dotted lines) and presence (solid lines) of 100 mM KCl (right). Only the E5 sequence demonstrated induction of a G4 structure (with parallel topology) with increased thermal stability in the presence of KCl. (B) E5's G4 formation (left) and thermal stability (right) were further examined over a range of concentrations (2–20 M) in the presence of 100 mM KCl as an indicator of inter- versus intra-strand G4 formation. Both G4 formation and thermal stability increased as a function of concentration, indicating inter-strand G4 formation.

A single polypurine strand, and Hp-KRAS-I1, are able to form non-canonical structures, such as a G4 [52] or hairpin [53], since these bands stained with ThT presenting a cyan band. Combination of dsDNA-KRAS-I1 with Hp-KRAS-I1, led to a formation of several bands, the upper corresponds to the intron 1 dsDNA-PPRH triplex, the second upper band corresponds to HpKRAS-I1 excess, the third band coincides with dsDNA-KRAS-I1 as we observe a decrease of this band with the increase of HpKRAS-I1. The lower band corresponds with the displaced ssPPU band of the triplex formed as we observe a higher cyan fluorescence of this band with a higher amount of PPRH per dsDNA. Incubation of dsDNA-KRAS-I1 with the scrambled PPRH (Hp-Sc9), lane 8, did not show any displaced

band. The independency of KCl for structured formations in the intron 1 probe is shown in (Figure S2), in agreement with the ECD results; similar displacement results for the distal promoter probe were also noted (Figure S3). Notably, all PPRH sequences were examined by ECD for their secondary structure formation (Figure S4). In the absence of KCl, sequences were either single-stranded or noted to form hairpin structures (data not shown). Except for the scrambled sequence (HpSc9), they each formed structures that facilitate ThT binding as noted in Figure 3. Specifically, PPRH1, PPRH2, and Hp-KRAS-E5-C formed inducible G4 structures, Hp-KRAS-PR-'s maxima at 266 nm sits somewhere in between a G4 and a hairpin and Hp-KRAS-I1-T forms an apparent hairpin structure.

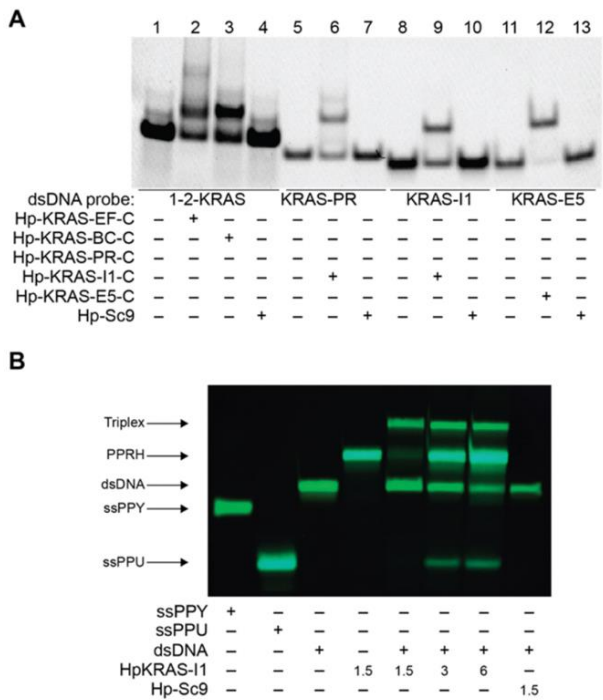


**Figure 3.** (A) Bindings of K-RAS PPRHs and Hp-Sc9 (1 µg) to the complementary polypyrimidine G4FS target sequence dsDNA (200 ng) marked with FAM. Lane 1, dsDNA-1-2-KRAS probe alone; lane 2, dsDNA-1-2-KRAS probe plus HpKRasPrEF-C; lane 3, dsDNA-1-2-KRAS probe plus HpKRasPrBC-C; lane 4 dsDNA-1-2-KRAS probe plus Hp-Sc9; lane 5, dsDNA-KRAS-PR-UP probe alone; lane 6, dsDNA-KRAS-PR-UP probe plus HpKRAS-PR-C; lane 7, dsDNA-KRAS-PR-UP probe plus Hp-Sc9; lane 8, dsDNA-KRAS-I1 probe alone; lane 9, dsDNA-KRAS-I1 probe plus Hp-KRAS-I1-T; lane 10, dsDNA-KRAS-I1 probe plus Hp-Sc9; lane 11, dsDNA-KRAS-E5 probe alone; lane 12, dsDNA-KRAS-E5 probe plus Hp-KRAS-E5-C; lane 13, dsDNA-KRAS-E5 probe plus Hp-Sc9. The image is representative of at least three different EMSAs performed at different times. (B) Displacement analysis of the Polypurine (PPU) strand in Intron 1 probe. Bindings were performed using 1.5 µg of dsDNA labelled with FAM (green) in the polypyrimidine (PPY) strand only, then incubated with the indicated amounts of KRAS-I1 PPRH or 1.5 µg of the negative control HpSc9. The resulting structures were resolved by native polyacrylamide (12%) gel electrophoresis. PPRHs, ssPPU and displaced PPU were visualized after Thioflavin-T staining (cyan bands).

**Table 1.** Name and nucleotide sequences used in the Electronic Circular Dichroism assays.

Name	Sequence (5'-3')
I1	CGGGAGAGAGGTACGGAGCGGAC
E5	GTGGGGGTGTGGGGGA
PR	CAGGTGAAGGGCA

#### 2.4. Effect of KRAS-Targeting PPRHs on Cell Viability and Growth

We examined the dose-dependent effects of KRAS-targeting PPRHs (144 h) on the viability of KRAS mutant expression pancreatic cancer cell lines AsPc-1 (G12D, highly addicted to KRAS) and MiaPaCa-2 (G12C, moderately addicted to KRAS) and KRAS overexpressing ovarian cancer SKOV-3 cell lines (Figure 4A). All effects on viability were compared to untreated control, and vehicle (N-[1-(1,2-Di-(9Z-octadecenoyl))-3-trimethylammoniumpropane methyl sulfate, DOTAP) and scrambled (Sc9, SCR) sequences were included as negative controls. All KRAS-targeting PPRHs significantly decreased the viability of AsPc-1 cells in a dose-dependent manner, but surprisingly none had lone efficacy in the moderately addicted MiaPaCa-2 cells. Targeting the promoter region with PPRH 1 or HpKRAS-PR-C (PR), or intron 1 with HpKRAS-I1-T (I1), significantly decreased cell viability in SKOV-3 cells as well. We further explored the effects of each PPRH at 100 nM over time in the three cell lines using live cell microscopy over time and evaluating percent confluency in the wells. In accordance with the viability effects, all the PPRHs modulated the growth of AsPc-1 cells and targeting the promoter with PPRH 1 or PR had the most marked effects on SKOV-3 growth. The effect of DOTAP on the growth of SKOV-3 cells within 16–96 h occurred consistently ( $n = 3$  with 25 images taken per well every 8 h) and normalized after 96 h; cells incubated with scramble DNA in DOTAP did not exert any stimulation of growth. Interestingly, targeting the promoter also decreased the growth of MiaPaCa-2 cells, despite there being no significant change in the viability of the remaining cells. One key difference in the viability and the cell growth studies is the well size (96 well versus 6 well), so we also monitored viability in the larger plates used for cell growth. In the 6 well plate, PPRH 1 mediated a decrease in MiaPaCa-2 viability by 35%, and PR decreases viability by 13%; while the magnitude and significance does not match the findings with cell growth alone, the general trends are in agreement. Overall, targeting transcription of KRAS with PPRHs targeting either the distal or proximal promoter region modulated the growth of cells with mutant or overexpressed KRAS.

To assess the possible additive or synergistic effects of combining PPRHs targeting different parts of the KRAS gene, we examined the effects of PPRH 2 (50 nM) plus each other PPRH (50 nM). DOTAP and SCR DNA (50 and 100 nM) were used as comparative controls. SCR DNA (50 nM) was also combined with either PPRH1 or PPRH2 (50 nM) and the effects on cell viability were comparable to PPRH1 or PPRH2 at 50 nM alone (data not shown). All other combinations of SCR + PPRH at 50 nM each were not examined, but were rather compared to 100 nM of SCR DNA alone. PPRH2 was chosen for all combinations as targeting the KRAS G<sub>4mid</sub> region was efficacious at decreasing cell viability and growth in the cell lines tested; it demonstrated promoter-related decreases in activity (see below), and its activity was moderate in all cell lines, allowing for enhancement or inhibition to be noted. One-way ANOVAs with Tukey post-hoc analyses were utilized to evaluate effects that were more than their constitutive parts, and all were compared to the negative controls of SCR DNA or DOTAP alone (Figure 5). While significant effects were noted with 100 nM of combined effects in SKOV-3 cells as compared to either negative control, the effects were apparently additive. No combinatorial effects were noted in the MiaPaCa-2 cells. Notably, in the cell line which has been reported to be the most sensitive to KRAS modulation, AsPc-1, apparent synergistic effects were noted with most PPRH combinations. PPRH 2 at 50 nM alone decreased viability of AsPc-1 cells by 14%, and the other agents decreased viability by 13–28%, whereas all combinations containing PPRH 2 decreased cell viability by 73–88%.



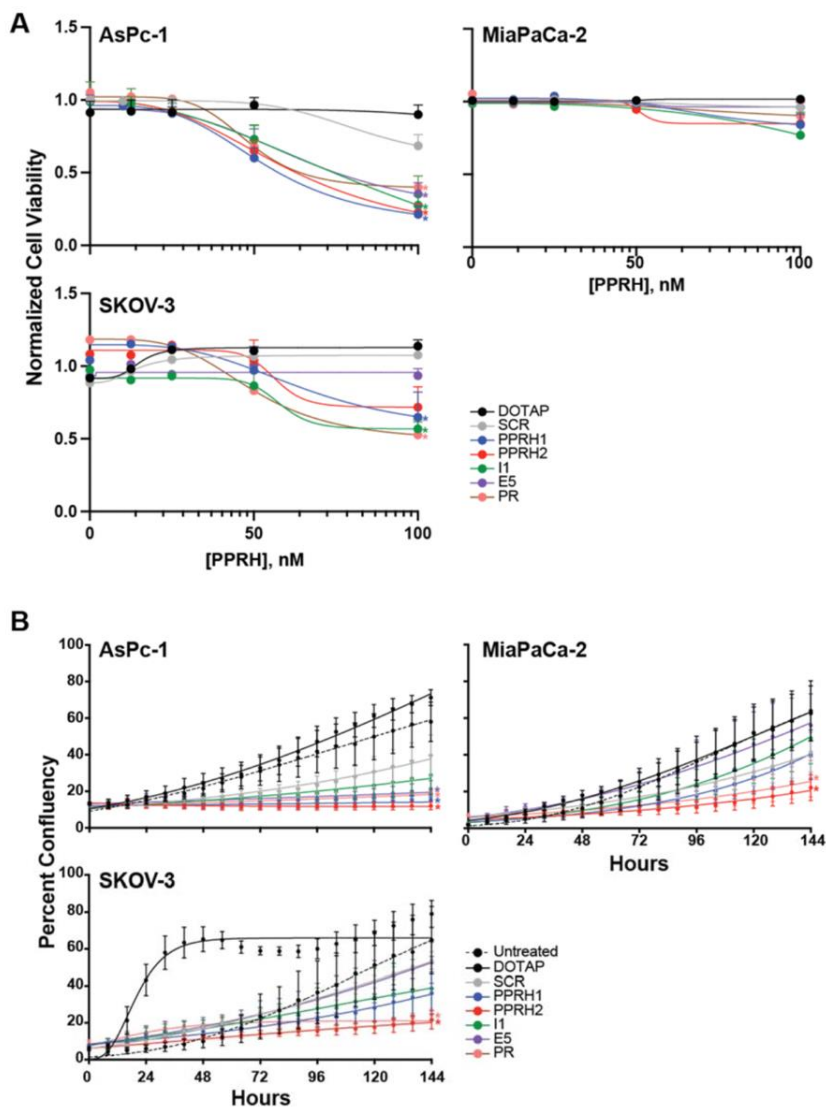


**Figure 4.** Effect of KRAS-targeting PPRHs on pancreatic cell lines expressing mutant KRAS, AsPc-1 and MiaPaCa-2, and ovarian cancer KRAS overexpressing SKOV-3 cells. (A) All cells were incubated with a dose-range (up to 100 nM) of the indicated sequences for 144 h. (B) The effects of 100 nM of each sequence on cancer cell line growth was measured overtime. Color coded \*  $p < 0.05$  versus DOTAP and SCR controls as determined by two-way ANOVA with Tukey post-hoc testing, all experiments were performed minimally in triplicate with internal triplicate data for the cellular viability studies and 25 images per time point for the live cell microscopy cellular growth studies.

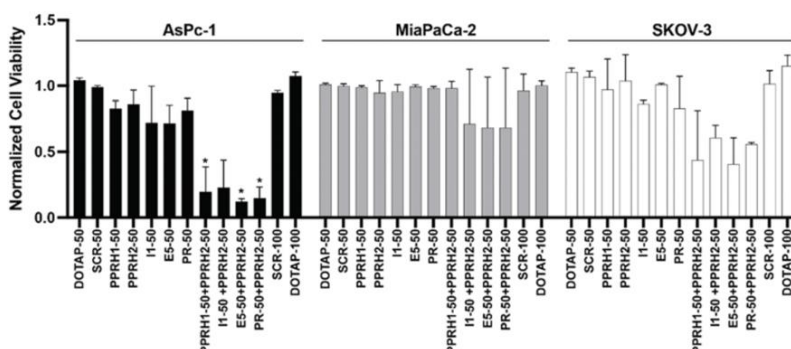


**Figure 5.** Combinations of PPRHs targeting the KRAS gene in AsPc-1 and MiaPaCa-2 pancreatic cancer cells and ovarian cancer SKOV-3 cells. Each PPRH was examined alone or in combination at 50 nM in the indicated cell lines for 144 h, and changes in cell viability were noted. Vehicle (DOTAP) and scramble DNA (SCR) controls were examined at both 50 and 100 nM. \*  $p < 0.05$  in the combinations, as compared to either component alone, as determined by one-way ANOVA with Tukey post-hoc testing. All experiments were performed minimally in triplicate with internal triplicate data.

### 2.5. Combined Effect of Targeting KRAS Promoter G4s with PPRH and Small Molecules

Finally, we sought to understand the effect of the combined targeting of the KRAS promoter G4 with PPRHs and small molecules. As only PPRH 1 and PPRH 2 target the confirmed G4 within the KRAS gene, this final study focused only on this region and these PPRHs. The regulation of KRAS promoter activity by PPRH 1 and PPRH 2 (100 nM, each) was first examined utilizing the KRAS promoter-driven luciferase cassette previously described [37] as compared to a promoterless empty vector (EV). Both PPRH moieties decreased KRAS promoter activity in a time-dependent manner, with PPRH 2 demonstrating significant decreases within 48 h of transfection.

NSC 317605 (hereafter referred to as 317605) is an indoloquinoline compound identified through screening the NCI DTP Diversity Set III's 1600 compounds by the FRET Melt<sup>2</sup> assay [54] for stabilizers of the KRAS G4<sub>mid</sub> structure. The thermal stability of the KRAS G4<sub>mid</sub> structure was increased by 8 °C, whereas there was no effect on the KRAS G4<sub>near</sub> structure ( $\Delta T_M < 0.5$  °C) (Figure 6B, left). This is notable as both G4s have been described in the literature; however, the biologically silencing function of G4-modulation on KRAS has been identified within the mid region and notably the mid region is the target of the designed PPRH 1 and PPRH 2 oligonucleotides. 317605's activity on the other KRAS sequences described in the current work, in the presence of KCl (100 mM), was also examined and there was no induction of a G4 structure within the PR or I1 sequences. E5's G4 was retained, but there was no increase in G4 formation as evidenced by increased theta, and there was no increase in thermal stability ( $\Delta T_M = 0.5$  °C) (data not shown).

In cells, 317605 (1  $\mu$ M) significantly decreased KRAS promoter activity within 48 h of transfection and treatment (Figure 6B, middle). In vitro potency of this compound is moderate, with a 72 h IC<sub>50</sub> in the AsPc-1 cell line of 21  $\mu$ M, but KRAS expression is significantly decreased (by 50%) at the [IC<sub>50</sub>]. As PPRH 1 and PPRH 2 both target the same G4-forming region stabilized by 317605, combinations of SCR, PPRH 1 or PPRH 2 and the small molecule were examined in the AsPc-1 cell line (Figure 6C). Both PPRH 1 and PPRH 2, but not SCR, dose-dependently enhanced the cytotoxic effects of 317605 at concentrations up to 50 nM. Notably, as described above, these are concentrations of the PPRH moieties that are not markedly cytotoxic in the AsPc-1 cells, highlighting the synergistic activities of the small molecule/PPRH approach to KRAS modulation.

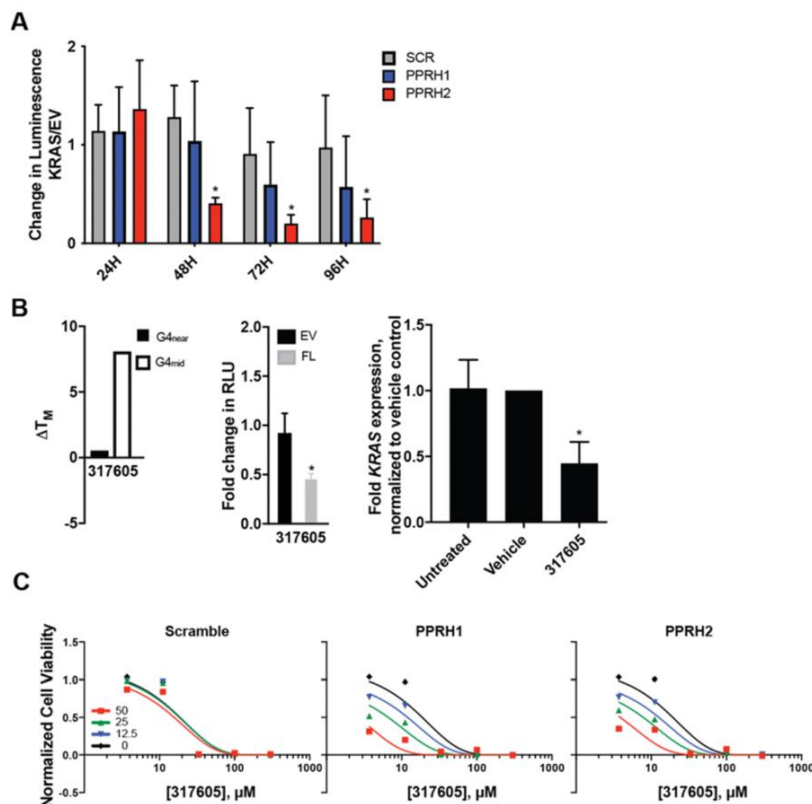


**Figure 6.** Combinatorial effects of targeting the KRAS promoter G4<sub>mid</sub> structure with small molecules and PPRHs. (A) PPRHs significantly decreased KRAS promoter activity within 48 h, and extended through 96 h in HEK-293 cells stably transfected with the KRAS FL promoter, but not the promoterless EV. (B) 317605 was identified as a KRAS G4<sub>mid</sub> selective stabilizer, versus G4<sub>near</sub>, from the NCI DTP Diversity Set III. FRET Melt<sup>2</sup> (left) demonstrated a marked increase in thermal stability of G4<sub>mid</sub> with correlations in decreased KRAS promoter activity (middle) and KRAS gene expression in AsPc-1 cells at the 72 h [IC<sub>50</sub>]. (C) AsPc-1 cells were exposed to dose-ranges of both 317605 and the designated PPRHs for 144 h. PPRH1 and PPRH2, but not scramble oligonucleotides, sensitize the pancreatic cancer cells to 317605, showing a synergistic effect. \*  $p < 0.05$  as compared to relevant scramble or untreated controls. All experiments were completed minimally in duplicate, with internal replicates as indicated in the materials and methods.

### 3. Discussion

In the present study, we sought to develop a novel means of modulating KRAS expression and/or function by targeting gene regulation with PolyPurine Reverse Hoogsteen hairpins (PPRH) targeting putative G4-forming DNA sequences within the KRAS gene. PPRHs are novel therapeutic tools that can be used for gene silencing [55], gene repair [46,47] to validate new targets and for diagnostic purposes [48,49]. PPRHs target polypyrimidine tracts, and in this work, we selected stretches of polypyrimidines that had

putative G4 forming sequence (G4FS) in the complementary strand. PPRHs have multiple applications and exhibit several advantages. Since these hairpins are non-modified oligonucleotides, they are very economical to synthesize. Due to the hairpin conformation made of deoxynucleotides, PPRHs present high stability and, because their length is less than 100 nucleotides, the absence of immunogenicity [56]. Additionally, these moieties inhibit gene activity at low concentrations, and they are sequence specific. Recently, we described the use of a PPRH targeting the complementary strand of a G4FS in the 5'UTR region of the Thymidylate synthase which produced a great reduction in viability, mRNA, and protein levels in PC3 and HeLa cells [50]. Following the same philosophy, in the present work we designed 5 PPRHs—4 coding and 1 template-directed against various G4FS in the *KRAS* gene.

We identified and examined higher order DNA formation in three previously unexplored regions of *KRAS*—one distal promoter, one intronic and one exonic. Of those, we identified one region capable of forming interstrand G4 structures which have the potential to form in the pre-transcriptionally modified mRNA. PPRHs were further designed to target these three novel G-rich DNA regions independent of their G4-forming capabilities, in addition to the previously identified and described G4-forming region within the proximal promoter, G4<sub>mid</sub> [54]. The PPRH oligonucleotides interacted with their target DNA in a sequence-specific manner. Since the binding of PPRHs to their targets provokes strand displacement, the aim of our approach was to either facilitate G4 formation or to displace the G-rich strand to disrupt transcription factor binding. Independent of G4 formation, G-rich DNA strand displacement could inhibit transcription to downregulate gene expression or alter post-transcriptional modification to interfere with functional *KRAS* protein expression, either of which would decrease proliferation of *KRAS* dependent ovarian and pancreatic cancer cells. We found that PPRHs have varying efficacy in pancreatic and ovarian cancer cells, but consistently that targeting the promoter with PPRHs inhibits cellular growth and viability. The PPRHs demonstrated synergistic activity in AsPc-1 cells, and additivity in SKOV3 cells. We further identified and described a G4<sub>mid</sub>-selective small molecule, NSC 317605, and demonstrated the synergistic activities with enhanced selectivity for the *KRAS* promoter G4<sub>mid</sub>, improved transcriptional downregulation and correlating effects on *KRAS*-dependent AsPc-1 pancreatic cancer cells. This combinatorial approach has the potential to enhance the selectivity and activity of G4-stabilizing small molecules and is a novel means to G4-stabilization and gene control.

G4s are globular constructs that form from a single strand of guanine-rich DNA that folds on itself to form a higher order, non-canonical, four-stranded structure. DNA intramolecular G4 formation occurs in telomeres, promoter regions, at origins of replication, regions of DNA breaks and at locations of DNA repair [28,57–60]. G4 formation within promoter regions requires opening of the double-stranded (ds) DNA, which occurs under the negative torsional stress induced by transcription. Genes with higher transcription rates have a greater potential for promoter G4 formation [61]. This underscores the role of most promoter G4s as negative regulators of gene expression, as their formation mediates a local negative feedback loop that regulates transcription rates. G4 formation in both DNA and RNA has been demonstrated in live cells [28] in an inducible manner [32]. Moreover, G4-positive nuclei are significantly increased in cancer cells, as compared to the surrounding non-neoplastic tissue, from patient-derived solid tumor tissue biopsies [33]. G4 formation is also inducible by small molecules, and endogenous levels of G4s can predict tumor sensitivity to G4-targeted ligands [62].

Within the core of *KRAS* promoter (+50 to −510 bp from the transcription start site) it has been reported that there are transcription factor (TF) binding sites for Sp1, E2F-1, STAT4, MAZ, WT1 or P53. Notably, the target sequences of the PPRHs contain binding sites of TFs such as Sp1 and E2F-1 and therefore the hairpins could impair the interaction between the TFs and the promoter independent of G4 formation, thus decreasing transcription [54]. The results obtained in the luciferase experiments corroborate that there was indeed a decrease



in transcription provoked by the promoter targeting PPRHs, alone and in combination with the small molecule, indoloquinoline NSC 317605.

Pancreatic cancer overall, and aggressive ovarian cancers in particular, harbor aberrant KRAS signaling correlating with more metastatic and progressive disease and poorer response to chemotherapies [6,17,63–65]. Pancreatic cancer is the ninth most common cancer in terms of incidence, and the fourth most common cause of cancer-related deaths in the United States. While ovarian cancer incidence is less common, it is the third most common genital system malignancy and the fifth most common cause of cancer related deaths in women. Decreased KRAS expression is a validated therapeutic approach for these and other cancers harboring additions to aberrant KRAS signaling [1,9,26,28]. Stabilization of higher order genomic structures—such as the G4—is an established approach to modulating transcription. The work described herein identifies and combines two therapeutic strategies—PPRHs and the small molecule NSC 317605—capable of stabilizing the KRAS promoter G4<sub>mid</sub> structure, decreasing transcription and synergistically modulating KRAS addicted AsPc-1 pancreatic cancer cells.

PPRHs, a new type of therapeutic oligonucleotide, are DNA molecules composed of two symmetrical stretches of polypurines separated and connected by four thymidines, forming a hairpin structure wherein Hoogsteen base-pairing facilitates G:G and A:A bonds. These structures further utilize Watson-Crick base-pairing to form triplex structures with cytosine-rich regions of DNA, freeing the guanine-rich complementary strand to facilitate G4 formation, displace TF binding, and modulate post-transcriptional events [41,66–70]. PPRH ODNs binding to the mid-G4-forming region of the KRAS promoter enhance G4 structures in vitro, mediating KRAS downregulation and subsequent cytotoxicity. Moreover, PPRH ODNs demonstrate synergistic activity with small molecules in KRAS-dependent pancreatic cell lines. The binding of PPRHs to their targets is sequence-specific and decreases transcriptional activity, viability and confluency. Therapeutic development for selective stabilization of individual promoter G4s is an active area of research, and our approach of combining PPRH moieties with small molecules to stabilize particular promoter G4s is novel and has strong potential for enhanced selectivity and anti-cancer activity.

#### 4. Materials and Methods

##### 4.1. Design of Polypurine Reverse Hoogsteen Hairpins

Putative KRAS targets of PPRH hairpins were searched using the Triplex-Forming Oligonucleotide Target Sequence Search software (TFO) (Triplex-Forming Oligonucleotide Target Sequence Search. Available online: <http://utw10685.utweb.utexas.edu/tfo/> (accessed on 10 February 2021)), MD Anderson Cancer Center, University of Texas, Houston, TX, USA). From a list of putative KRAS targets in the TFO searching tool, we selected the polypurine stretches that follow the best criteria according to our previous results: a minimum of 40% G, a length between 20 and 25 nucleotides per strand of PPRH and allowing no more than three pyrimidine interruptions.

Within the selected KRAS PPRHs hairpins target sequences we searched for putative G4FS using the QGRS mapper (<http://bioinformatics.ramapo.edu/QGRS/index.php> (accessed on 10 February 2021)), a computational tool that uses algorithms to map putative G-quadruplex elements in mammalian genes. Next, we selected the sequences with the highest G-score that represents the best candidates to form G4FS. To confirm the specificity of the designed PPRHs and avoid unintended targets, the final candidate sequences were analyzed using BLAST.

The final design of the PPRH hairpins consists of two polypurine strands linked by a four-thymidine loop in a mirror repeat fashion, thus running in antiparallel orientations. As negative control we designed a scramble hairpin (Hp-Sc9). All the designed sequences were synthesized as non-modified oligodeoxynucleotides by Sigma-Aldrich (Haverhill, UK) resuspended in sterile Tris-EDTA buffer (10 mM Tris and 1 mM EDTA, pH 8.0) (Sigma-Aldrich, Madrid, Spain) and stored at −20 °C.

#### 4.2. Electronic Circular Dichroism (ECD)

DNA sequences (Table 1) were purchased from Integrated DNA technologies (IDT, Coralville, IA, USA) as desalted oligonucleotides. Upon arrival, they were solvated in double-distilled water overnight, they were heated to 95 °C for 5 min and their A260 was determined at temp using a Nanodrop3000 (Thermo Scientific, Waltham, MA, USA) and their concentrations were determined using the nearest neighbor technique. On the experimental day, oligonucleotides were diluted to ~5 (range 2–20) mM in 10 mM Tris Acetate buffer (pH 7.4), in the absence or presence of 100 mM KCl; experimental concentrations were confirmed as described above by heating to 95 °C for 5 min and measuring the A260 at temperature, DNA was rapidly cooled on ice for 10 min. Spectra and thermal stability of the putative G4 forming regions were evaluated on a Jasco J-1500 spectrophotometer (Jasco, Easton, MD, USA). Spectra were recorded from 225–350 nm in triplicate for each experiment using a 1 cm quartz cuvette and a 1 mm bandwidth; the triplicate reads were averaged. Full spectra were recorded over increasing temperature from 20–100 °C, with recordings of the Cotton effect at 262 nm at each temperature. Millidegrees (mdeg, theta) were reported as experimentally determined, or normalized for the thermal melt determinations;  $T_M$ s were calculated using the data at 262 nm over temperature using non-linear regression analysis with GraphPad Prism software (San Diego, CA, USA).

#### 4.3. Electrophoretic Mobility Shift Assay (EMSA)

To perform EMSA analyses, we used fluorescently labeled dsDNA probes, corresponding to the target regions of each PPRH (Table 2), obtained by hybridizing (95 °C for 5 min and cool down at RT) equimolecular amounts of single-stranded oligodeoxynucleotide (Table 2) in a 150 mM NaCl solution. The probes were labeled in the 5'-end with 6-FAM (fluorescein) in the polypyrimidine ssDNA and were synthesized by Sigma-Aldrich (Haverhill, UK). Binding reactions were performed using binding buffer (5% glycerol, 36 mM KCl, 25 mM Tris-HCl, 4 mM MgCl<sub>2</sub>, 0.5 mM DTT, 0.5 mM EDTA, pH 8.0; all reagents were from Sigma-Aldrich). The different PPRHs (1 µg) were mixed with 200 ng of Poly(dI:dC) as a nonspecific competitor and incubated at 65 °C for 10 min. Afterwards, 200 ng of dsDNA probe were added to the mix at 65 °C for an additional period of time of 20 min. The products of the binding were electrophoretically resolved in 7% polyacrylamide and 5% glycerol native gels in 0.5× TBE buffer, at a fixed of 190 V and 4 °C. ImageLab software v5.2 was used to visualize the results (GE Healthcare, Barcelona, Spain).

**Table 2.** Name and sequence of the DNA probes used in the EMSA.

Name	Sequence (5'-3')
Probe-1-2-PY-KRAS	5'-[6FAM]-CCCCGCTCCTCCCCGCGCCGCCGCGCCCGCCCTCTTCTCCCC-3'
Probe 1-PPU-KRAS	5'-GGGGAGAAGGAGGGGCGGGCCGG-3'
Probe 2-PPU-KRAS	5'-GCCGCGGGGGAGGAGCGGGGG-3'
Probe-PPY-KRAS-PR-UP	5'-[6FAM]-CTTTTCTCTCTGCCCTTCCACC-3'
Probe-PPU-KRAS-PR-UP	5'-GGTGAAGGGGAGAGAGAGAAAAG-3'
Probe-PPY-KRAS-I1	5'-[6FAM]-TCCGCTCCGTACCTTCTCCCC-3'
Probe-PPU-KRAS-I1	5'-GGGAGAGAGGTACGGAGCGGA-3'
Probe-PPY-KRAS-E5	5'-[6FAM]-TCTCTCCCCCACACCCAC-3'
Probe-PPU-KRAS-E5	5'-GTGGGGGTGTGGGGGAGAGA-3'

#### 4.4. Strand Displacement Assay upon PPRH Incubation

To detect G4 Structures, 1.5 µg of each oligonucleotide alone (Table 2) or in combination with the indicated amounts of PPRH were mixed in 60 µL of buffer containing 100 mM Tris-HCl (pH 7.4) and 100 mM KCl and then incubated at 90 °C for 5 min in water and slowly cooled down to room temperature (90 min). dsDNA probes were prepared by hybridizing the two strands where the polypyrimidine one was labeled with FAM following the same protocol as in 4.3 of M & M. The resulting structures were resolved in native polyacrylamide gels (12%) containing 10 mM KCl in 1× TBE buffer and electrophoresed for 1–2 h at 150 V.

After electrophoresis, gels were stained with 5  $\mu$ M of Thyoflavin T solution for 15 min under agitation and washed in water for 2 min. Images were captured under a UV light lamp or using the Gel DocTM EZ with the Image Lab Software, Version 6.0.

#### 4.5. Cell Cultures

All cell lines were purchased from American Tissue Culture Collection (Manassas, VA, USA) and stored in liquid nitrogen until use. Low passage cells (<20) were maintained for the duration of these experiments. Pancreatic cancer AsPc-1 and MiaPaCa-2 cell lines were grown in RPMI 1640 and Dulbecco's Modified Eagle's Medium (DMEM) media, respectively, ovarian cancer SKOV-3 cells were maintained in McCoy's 5A media, and HEK293 cells were maintained in Eagle's Minimum Essential Media (EMEM); media were supplemented with 10% fetal bovine serum (Sigma Aldrich, St Louis, MO, USA) and penicillin/streptomycin (Sigma Aldrich). All cells were maintained in exponential growth at 37 °C in a humidified 5% CO<sub>2</sub> incubator.

#### 4.6. Cellular Viability and Cell Growth Studies

One day before transfection, cells were seeded in 96 or 12 well plates at  $0.5\text{--}2.5 \times 10^3$  and  $8\text{--}20 \times 10^4$  cells per well in 90 or 900 mL of corresponding media, respectively. PPRHs were incubated with N-[1-(1,2-Di-(9Z-octadecenoyl)-3-trimethylammoniumpropane methyl sulfate (DOTAP; Sigma Aldrich) in a 1:100 ratio at 10x solutions in OptiMEM media for 20 min at room temperature to form micelles. Micelles or compounds were diluted over a 5–6 log range in OptiMEM media and 10 or 100 mL were added to the 96- or 6-well cell plates, respectively. Cells were incubated with the PPRHs for up to 144 h, or with NSC317605 for 72 or 144 h, at 37 °C in a humidified 5% CO<sub>2</sub> incubator. The combined effect of PPRHs and NSC317605 was examined by exposing the cells to a 5–6 log range of NSC317605 in the absence or presence of 0–50 nM of PPRH's. Only 5 mL of the PPRH of compound were added to the plated cells, thus the stocks were 20x rather than the 10x described above. To determine effects on cellular viability, Cell Titer AQueous (MTS) reagent (Promega; Madison, WI, USA) was activated with 5% phenazine methosulfate (Sigma Aldrich), and 20 or 200 mL of the activated reagent was added to the 96- or 12-well plates and incubated for 2–4 h. Absorbance was measured at 490 nm on a SpectraMax i3x (Molecular Devices; San Jose, CA, USA). Background absorbance (media and all reagents) was subtracted from all experimental values and normalized to untreated controls. Non-linear regression was performed with GraphPad Prism software for the dose-response studies, and a two-way ANOVA with a post-hoc Tukey analysis was utilized to evaluate statistical significance for all experimental groups. Additionally, live-cell images were captured of all 12-well plates every 8 h after transfection utilizing the CellCyte X Live imaging system (Cytena; Boston, MA, USA). Twenty-five images per well were captured every 8 h; analysis software was trained to accurately determine the shape and volume of each cell line, and the “masks” created by training were applied to determine percent confluency within each images' surface area. Gompertzian growth was analyzed by GraphPad Prism and two-way ANOVAs with Tukey post hoc analyses was performed. Cell viability and cell confluency/growth studies were all performed in triplicate.

#### 4.7. FRET Melt<sup>2</sup>

5'FAM and 3'TAMRA labeled G4<sub>mid</sub> (5'-GGCGGGGAGAAGGAGGGGCCGGGCC GGGCCGGCGGGGAGGAGCGGGGCCGGGCCG-3') or G4<sub>near</sub> (5'-TGAGGGCGGTGT GGGGAAGAGGGAAGAGGGGGAGG-3') DNA (consecutive guanines underlined, guanines involved in resolved predominant G4 isoforms italicized [38]) was diluted to 0.5 mM in 10 mM sodium cacodylate (pH 7.4) with 90 mM LiCl, 10 mM KCl and 10% glycerol [54]. The G4 was annealed by heating the DNA to 95 °C for 5 min and rapidly cooled on ice for 10 min, twice. Annealing was done in either the absence or presence of 2 mM of NSC317605. Fluorescence was then recorded from 20–95 °C, at every degree with a hold for 10 s on a Bio-Rad CFX96 real-time PCR machine (BioRad Laboratories; Hercules, CA,



USA). Fluorescence for each sample at each temperature was normalized to the values determined at 20 °C, and non-linear regression was performed using GraphPad Prism to determine the  $T_M$ . Experiments were performed in triplicate with internal duplicates.

#### 4.8. Luciferase Assays

HEK-293 cells were stably transfected with either the pGL4.17 promoterless luciferase plasmid (Promega) or the KRAS promoter containing KRAS-324 luciferase plasmid (FL; [37]), selected by neomycin resistance. HEK-293-EV or -FL cells were seeded in 24 well plates at  $8 \times 10^4$  cells/well and allowed to attach overnight. Cells were treated with 100 nM PPRH, 1 mM NSC317605, or vehicle control (DOTAP or DMSO), for 48 h. Cells were lysed in passive lysis buffer, frozen to  $-20$  °C, thawed, and refrozen before measuring firefly luciferase activity with the Dual Luciferase Assay kit (Promega) using a Lumat LB9507 luminometer. The Pierce BCA assay (Thermo Fisher) was used to determine the protein concentration from each sample, and luciferase was normalized to protein content, and normalized again to untreated control. Luciferase assays were performed minimally in triplicate; one-way ANOVAs with Tukey post-doc analyses were used to determine significance.

#### 4.9. RT-qPCR

To determine *KRAS* mRNA levels in AsPc-1 cells at the  $[IC_{50}]$ , cells were plated at  $3-4 \times 10^5$  cells/well in a 6 well plate and allowed to attach overnight. Cells were treated with 21 mM NSC 317605 for 72 h, lysed and RNA was harvested with the Roche GeneJet RNA isolation kit (Thermo Fisher). 500 ng of RNA was reversed transcribed into cDNA, and 1/5 of the resultant cDNA was mixed with  $1 \times$  TaqMan PerfeCTa qPCR SuperMix (QuantaBio; Beverly, MA, USA), 1  $\mu$ L of FAM-labeled *KRAS* probe (ABI, Thermo Fisher Hs00364282\_m1 and 1  $\mu$ L of primer-limited VIC-labeled *GAPDH* probe (ABI, Thermo Fisher Hs02758991\_g1). PCR cycling conditions were 3 min denaturation at 95 °C, followed by 40 cycles of 10 s at 95 °C and 30 s at 60 °C. Relative expression of *KRAS* was determined using the  $DDC_T$  method from regression modeled  $C_T$  values; experiments were performed in triplicate with minimally duplicate qPCR samples. One-way ANOVA with post-hoc Tukey analysis was used to determine statistical significance.

#### 4.10. Statistical Analyses

Statistical analyses were carried out using GraphPad Prism 9 (GraphPad Software, San Diego, CA, USA) using the tests described in the corresponding text. All data, with a minimum of three independent experiments, are shown as the mean  $\pm$  SEM.

**Supplementary Materials:** The following supporting information can be downloaded at: <https://www.mdpi.com/article/10.3390/ijms23042097/s1>.

**Author Contributions:** Conceptualization, T.A.B., V.N. and C.J.C.; methodology, A.M.P., S.V. and T.A.B.; formal analysis, C.J.C. and T.A.B.; investigation A.M.P., S.V. and T.A.B.; writing—original draft preparation, A.M.P., S.V., C.J.C. and T.A.B.; writing—review and editing, C.J.C., V.N. and T.A.B.; funding acquisition, V.N. and T.A.B. All authors have read and agreed to the published version of the manuscript.

**Funding:** This research was funded by Plan Nacional de Investigación Científica (Spain), grant number RTI2018-093901-B-I00, PID2021-122271OB-I00, and by start up funding from Binghamton University.

**Institutional Review Board Statement:** Not applicable.

**Informed Consent Statement:** Not applicable.

**Data Availability Statement:** Not applicable.

**Conflicts of Interest:** The authors declare that they have no conflict of interest.



## References

- Adjei, A.A. Blocking oncogenic Ras signaling for cancer therapy. *J. Natl. Cancer Inst.* **2001**, *93*, 1062–1074. [\[CrossRef\]](#)
- Colicelli, J. Human RAS superfamily proteins and related GTPases. *Sci. STKE* **2004**, *2004*, RE13. [\[CrossRef\]](#) [\[PubMed\]](#)
- Friday, B.B.; Adjei, A.A. K-ras as a target for cancer therapy. *Biochim. Biophys. Acta* **2005**, *1756*, 127–144. [\[CrossRef\]](#) [\[PubMed\]](#)
- Young, A.; Lyons, J.; Miller, A.L.; Phan, V.T.; Alarcon, I.R.; McCormick, F. Ras signaling and therapies. *Adv. Cancer Res.* **2009**, *102*, 1–17. [\[PubMed\]](#)
- Hingorani, S.R.; Petricoin, E.F.; Maitra, A.; Rajapakse, V.; King, C.; Jacobetz, M.A.; Ross, S.; Conrads, T.P.; Veenstra, T.D.; Hitt, B.A.; et al. Preinvasive and invasive ductal pancreatic cancer and its early detection in the mouse. *Cancer Cell* **2003**, *4*, 437–450. [\[CrossRef\]](#)
- Birkeland, E.; Wik, E.; Mjos, S.; Hoivik, E.A.; Trovik, J.; Werner, H.M.J.; Kusonmano, K.; Petersen, K.; Raeder, M.B.; Holst, F.; et al. KRAS gene amplification and overexpression but not mutation associates with aggressive and metastatic endometrial cancer. *Br. J. Cancer* **2012**, *107*, 1997–2004. [\[CrossRef\]](#)
- The Cancer Genome Atlas Research Network. Integrated genomic analyses of ovarian carcinoma. *Nature* **2011**, *474*, 609–615. [\[CrossRef\]](#)
- Chen, Y.; McGee, J.; Chen, X.; Doman, T.N.; Gong, X.; Zhang, Y.; Hamm, N.; Ma, X.; Higgs, R.E.; Bhagwat, S.V.; et al. Identification of druggable cancer driver genes amplified across TCGA datasets. *PLoS ONE* **2014**, *9*, e98293. [\[CrossRef\]](#)
- Craig, D.W.; O'Shaughnessy, J.A.; Kiefer, J.A.; Aldrich, J.; Sinari, S.; Moses, T.M.; Wong, S.; Dinh, J.; Christoforides, A.; Blum, J.L.; et al. Genome and transcriptome sequencing in prospective metastatic triple-negative breast cancer uncovers therapeutic vulnerabilities. *Mol. Cancer Ther.* **2013**, *12*, 104–116. [\[CrossRef\]](#)
- Giltane, J.M.; Balko, J.M. Rationale for targeting the Ras/MAPK pathway in triple-negative breast cancer. *Discov. Med.* **2014**, *17*, 275–283.
- Goddard, N.C.; McIntyre, A.; Summersgill, B.; Gilbert, D.; Kitazawa, S.; Shipley, J. KIT and RAS signalling pathways in testicular germ cell tumours: New data and a review of the literature. *Int. J. Androl.* **2007**, *30*, 337–348, discussion 349; discussion 49. [\[CrossRef\]](#) [\[PubMed\]](#)
- Huang, R.Y.; Chen, G.B.; Matsumura, N.; Lai, H.-C.; Mori, S.; Li, J.; Wong, M.K.; Konishi, I.; Thiery, J.-P.; Goh, L. Histotype-specific copy-number alterations in ovarian cancer. *BMC Med. Genom.* **2012**, *5*, 47. [\[CrossRef\]](#) [\[PubMed\]](#)
- Mackenzie, R.; Kommoss, S.; Winterhoff, B.J.; Kipp, B.R.; Garcia, J.J.; Voss, J.; Halling, K.; Karnezis, A.; Senz, J.; Yang, W.; et al. Targeted deep sequencing of mucinous ovarian tumors reveals multiple overlapping RAS-pathway activating mutations in borderline and cancerous neoplasms. *BMC Cancer* **2015**, *15*, 415. [\[CrossRef\]](#)
- McIntyre, A.; Gilbert, D.; Goddard, N.; Looijenga, L.; Shipley, J. Genes, chromosomes and the development of testicular germ cell tumors of adolescents and adults. *Genes Chromosomes Cancer* **2008**, *47*, 547–557. [\[CrossRef\]](#) [\[PubMed\]](#)
- Podo, F.; Buydens, L.M.; Degani, H.; Hilhorst, R.; Klipp, E.; Gribbestad, I.S.; Huffel, S.V.; van Laarhoven, H.W.M.; Luts, J.; Monleon, D.; et al. Triple-negative breast cancer: Present challenges and new perspectives. *Mol. Oncol.* **2010**, *4*, 209–229. [\[CrossRef\]](#) [\[PubMed\]](#)
- Pulciani, S.; Santos, E.; Long, L.K.; Sorrentino, V.; Barbacid, M. ras gene Amplification and malignant transformation. *Mol. Cell. Biol.* **1985**, *5*, 2836–2841.
- Rahman, M.T.; Nakayama, K.; Rahman, M.; Katagiri, H.; Katagiri, A.; Ishibashi, T.; Ishikawa, M.; Sato, E.; Iida, K.; Nakayama, N.; et al. KRAS and MAPK1 gene amplification in type II ovarian carcinomas. *Int. J. Mol. Sci.* **2013**, *14*, 13748–13762. [\[CrossRef\]](#)
- Roelofs, H.; Mostert, M.C.; Pompe, K.; Zafarana, G.; van Oorschot, M.; van Gurp, R.J.H.L.M.; Gillis, A.J.M.; Stoop, H.; Beverloo, B.; Oosterhuis, J.W.; et al. Restricted 12p amplification and RAS mutation in human germ cell tumors of the adult testis. *Am. J. Pathol.* **2000**, *157*, 1155–1166. [\[CrossRef\]](#)
- Ross, J.S.; Ali, S.M.; Wang, K.; Palmer, G.; Yelensky, R.; Lipson, D.; Miller, V.A.; Zajchowski, D.; Shawver, L.K.; Stephens, P.J. Comprehensive genomic profiling of epithelial ovarian cancer by next generation sequencing-based diagnostic assay reveals new routes to targeted therapies. *Gynecol. Oncol.* **2013**, *130*, 554–559. [\[CrossRef\]](#)
- Wang, Y.; Yang, D.; Cogdell, D.; Hu, L.; Xue, F.; Broadus, R.; Zhang, W. Genomic characterization of gene copy-number aberrations in endometrial carcinoma cell lines derived from endometrioid-type endometrial adenocarcinoma. *Technol. Cancer Res. Treat.* **2010**, *9*, 179–189. [\[CrossRef\]](#)
- Yang-Feng, T.L.; Li, S.B.; Leung, W.Y.; Carcangiu, M.L.; Schwartz, P.E. Trisomy 12 and K-ras-2 amplification in human ovarian tumors. *Int. J. Cancer* **1991**, *48*, 678–681. [\[CrossRef\]](#) [\[PubMed\]](#)
- Sotorasib Edges Closer to Approval. *Cancer Discov.* **2021**, *11*, OF2. [\[CrossRef\]](#) [\[PubMed\]](#)
- Hong, D.S.; Fakih, M.G.; Strickler, J.H.; Desai, J.; Durm, G.A.; Shapiro, G.I.; Falchook, G.S.; Price, T.J.; Sacher, A.; Denlinger, C.S.; et al. KRAS(G12C) Inhibition with Sotorasib in Advanced Solid Tumors. *N. Engl. J. Med.* **2020**, *383*, 1207–1217. [\[CrossRef\]](#) [\[PubMed\]](#)
- Ali, S.; Ahmad, A.; Aboukameel, A.; Bao, B.; Padhye, S.; Philip, P.A.; Sarkar, F.H. Increased Ras GTPase activity is regulated by miRNAs that can be attenuated by CDF treatment in pancreatic cancer cells. *Cancer Lett.* **2012**, *319*, 173–181. [\[CrossRef\]](#)
- Duursma, A.M.; Agami, R. Ras interference as cancer therapy. *Semin. Cancer Biol.* **2003**, *13*, 267–273. [\[CrossRef\]](#)
- Hu, Y.; Ou, Y.; Wu, K.; Chen, Y.; Sun, W. miR-143 inhibits the metastasis of pancreatic cancer and an associated signaling pathway. *Tumour Biol.* **2012**, *33*, 1863–1870. [\[CrossRef\]](#)
- Wickstrom, E. Oligonucleotide treatment of ras-induced tumors in nude mice. *Mol. Biotechnol.* **2001**, *18*, 35–55. [\[CrossRef\]](#)

28. Hansel-Hertsch, R.; Di Antonio, M.; Balasubramanian, S. DNA G-quadruplexes in the human genome: Detection, functions and therapeutic potential. *Nat. Rev. Mol. Cell Biol.* **2017**, *18*, 279–284. [\[CrossRef\]](#)
29. Rhodes, D.; Lipps, H.J. G-quadruplexes and their regulatory roles in biology. *Nucleic Acids Res.* **2015**, *43*, 8627–8637. [\[CrossRef\]](#)
30. Huppert, J.L. Four-stranded nucleic acids: Structure, function and targeting of G-quadruplexes. *Chem. Soc. Rev.* **2008**, *37*, 1375–1384. [\[CrossRef\]](#)
31. Huppert, J.L.; Balasubramanian, S. G-quadruplexes in promoters throughout the human genome. *Nucleic Acids Res.* **2007**, *35*, 406–413. [\[CrossRef\]](#) [\[PubMed\]](#)
32. Biffi, G.; Tannahill, D.; McCafferty, J.; Balasubramanian, S. Quantitative visualization of DNA G-quadruplex structures in human cells. *Nat. Chem.* **2013**, *5*, 182–186. [\[CrossRef\]](#) [\[PubMed\]](#)
33. Biffi, G.; Tannahill, D.; Miller, J.; Howat, W.J.; Balasubramanian, S. Elevated levels of G-quadruplex formation in human stomach and liver cancer tissues. *PLoS ONE* **2014**, *9*, e102711. [\[CrossRef\]](#) [\[PubMed\]](#)
34. Jordano, J.; Perucho, M. Chromatin structure of the promoter region of the human c-K-ras gene. *Nucleic Acids Res.* **1986**, *14*, 7361–7378. [\[CrossRef\]](#)
35. Jordano, J.; Perucho, M. Initial characterization of a potential transcriptional enhancer for the human c-K-ras gene. *Oncogene* **1988**, *2*, 359–366.
36. Yamamoto, F.; Perucho, M. Characterization of the human c-K-ras gene promoter. *Oncogene Res.* **1988**, *3*, 125–130.
37. Morgan, R.K.; Batra, H.; Gaerig, V.C.; Hockings, J.; Brooks, T.A. Identification and characterization of a new G-quadruplex forming region within the KRAS promoter as a transcriptional regulator. *Biochim. Biophys. Acta* **2016**, *1859*, 235–245. [\[CrossRef\]](#)
38. Coma, S.; Noe, V.; Eritja, R.; Ciudad, C.J. Strand displacement of double-stranded DNA by triplex-forming antiparallel purine hairpins. *Oligonucleotides* **2005**, *15*, 269–283. [\[CrossRef\]](#)
39. De Almagro, M.C.; Coma, S.; Noe, V.; Ciudad, C.J. Polypurine hairpins directed against the template strand of DNA knock down the expression of mammalian genes. *J. Biol. Chem.* **2009**, *284*, 11579–11589. [\[CrossRef\]](#)
40. De Almagro, M.C.; Mencia, N.; Noe, V.; Ciudad, C.J. Coding polypurine hairpins cause target-induced cell death in breast cancer cells. *Hum. Gene Ther.* **2011**, *22*, 451–463. [\[CrossRef\]](#)
41. Villalobos, X.; Rodriguez, L.; Sole, A.; Lliberós, C.; Mencia, N.; Ciudad, C.J.; Noé, V. Effect of Polypurine Reverse Hoogsteen Hairpins on Relevant Cancer Target Genes in Different Human Cell Lines. *Nucleic Acid Ther.* **2015**, *25*, 198–208. [\[CrossRef\]](#) [\[PubMed\]](#)
42. Bener, G.; A, J.F.; Sanchez de Diego, C.; Pascual Fabregat, I.; Ciudad, C.J.; Noe, V. Silencing of CD47 and SIRPalpha by Polypurine reverse Hoogsteen hairpins to promote MCF-7 breast cancer cells death by PMA-differentiated THP-1 cells. *BMC Immunol.* **2016**, *17*, 32. [\[CrossRef\]](#) [\[PubMed\]](#)
43. Ciudad, C.J.; Medina Enriquez, M.M.; Felix, A.J.; Bener, G.; Noe, V. Silencing PD-1 and PD-L1: The potential of PolyPurine Reverse Hoogsteen hairpins for the elimination of tumor cells. *Immunotherapy* **2019**, *11*, 369–372. [\[CrossRef\]](#)
44. Medina Enriquez, M.M.; Felix, A.J.; Ciudad, C.J.; Noe, V. Cancer immunotherapy using PolyPurine Reverse Hoogsteen hairpins targeting the PD-1/PD-L1 pathway in human tumor cells. *PLoS ONE* **2018**, *13*, e0206818. [\[CrossRef\]](#) [\[PubMed\]](#)
45. Aubets, E.; Noe, V.; Ciudad, C.J. Targeting replication stress response using polypurine reverse hoogsteen hairpins directed against WEE1 and CHK1 genes in human cancer cells. *Biochem. Pharmacol.* **2020**, *175*, 113911. [\[CrossRef\]](#)
46. Felix, A.J.; Ciudad, C.J.; Noe, V. Correction of the aprt Gene Using Repair-Polypurine Reverse Hoogsteen Hairpins in Mammalian Cells. *Mol. Ther. Nucleic Acids* **2020**, *19*, 683–695. [\[CrossRef\]](#)
47. Sole, A.; Ciudad, C.J.; Chasin, L.A.; Noe, V. Correction of point mutations at the endogenous locus of the dihydrofolate reductase gene using repair-Polypurine Reverse Hoogsteen hairpins in mammalian cells. *Biochem. Pharmacol.* **2016**, *110–111*, 16–24. [\[CrossRef\]](#)
48. Huertas, C.S.; Avino, A.; Kurachi, C.; Piqué, A.; Sandoval, J.; Eritja, R.; Esteller, M.; Lechuga, L.M. Label-free DNA-methylation detection by direct ds-DNA fragment screening using poly-purine hairpins. *Biosens. Bioelectron.* **2018**, *120*, 47–54. [\[CrossRef\]](#)
49. Noe, V.; Aubets, E.; Felix, A.J.; Ciudad, C.J. Nucleic acids therapeutics using PolyPurine Reverse Hoogsteen hairpins. *Biochem. Pharmacol.* **2020**, *189*, 114371. [\[CrossRef\]](#)
50. Aubets, E.; Chillón, M.; Ciudad, C.J.; Noe, V. PolyPurine Reverse Hoogsteen Hairpins Work as RNA Species for Gene Silencing. *Int. J. Mol. Sci.* **2021**, *22*, 10025. [\[CrossRef\]](#)
51. Cogoi, S.; Xodo, L.E. G-quadruplex formation within the promoter of the KRAS proto-oncogene and its effect on transcription. *Nucleic Acids Res.* **2006**, *34*, 2536–2549. [\[CrossRef\]](#)
52. Renaud de la Faverie, A.; Guedin, A.; Bedrat, A.; Yatsunyk, L.A.; Mergny, J.L. Thioflavin T as a fluorescence light-up probe for G4 formation. *Nucleic Acids Res.* **2014**, *42*, e65. [\[CrossRef\]](#)
53. Trinh, K.H.; Kadam, U.S.; Rampogu, S.; Cho, Y.; Yang, K.-A.; Kang, C.H.; Lee, K.-W.; Chung, W.S.; Hong, J.C. Development of novel fluorescence-based and label-free noncanonical G4-quadruplex-like DNA biosensor for facile, specific, and ultrasensitive detection of fipronil. *J. Hazard. Mater.* **2022**, *427*, 127939. [\[CrossRef\]](#) [\[PubMed\]](#)
54. Morgan, R.K.; Psaras, A.M.; Lassiter, Q.; Raymer, K.; Brooks, T.A. G-quadruplex deconvolution with physiological mimicry enhances primary screening: Optimizing the FRET Melt(2) assay. *Biochim. Biophys. Acta Gene Regul. Mech.* **2020**, *1863*, 194478. [\[CrossRef\]](#) [\[PubMed\]](#)



55. Rodríguez, L.; Villalobos, X.; Dakhel, S.; Padilla, L.; Hervás, R.; Hernández, J.L.; Ciudad, C.J.; Noé, V. Polypurine reverse Hoogsteen hairpins as a gene therapy tool against survivin in human prostate cancer PC3 cells in vitro and in vivo. *Biochem. Pharmacol.* **2013**, *86*, 1541–1554. [\[CrossRef\]](#) [\[PubMed\]](#)
56. Villalobos, X.; Rodríguez, L.; Prevot, J.; Oleaga, C.; Ciudad, C.J.; Noe, V. Stability and immunogenicity properties of the gene-silencing polypurine reverse Hoogsteen hairpins. *Mol. Pharm.* **2014**, *11*, 254–264. [\[CrossRef\]](#) [\[PubMed\]](#)
57. Spiegel, J.; Cuesta, S.M.; Adhikari, S.; Hansel-Hertsch, R.; Tannahill, D.; Balasubramanian, S. G-quadruplexes are transcription factor binding hubs in human chromatin. *Genome Biol.* **2021**, *22*, 117. [\[CrossRef\]](#)
58. Krafcikova, M.; Dzatko, S.; Caron, C.; Granzhan, A.; Fiala, R.; Loja, T.; Teulade-Fichou, M.-P.; Fessl, T.; Hänsel-Hertsch, R.; Mergny, J.-L.; et al. Monitoring DNA-Ligand Interactions in Living Human Cells Using NMR Spectroscopy. *J. Am. Chem. Soc.* **2019**, *141*, 13281–13285. [\[CrossRef\]](#) [\[PubMed\]](#)
59. Hansel-Hertsch, R.; Spiegel, J.; Marsico, G.; Tannahill, D.; Balasubramanian, S. Genome-wide mapping of endogenous G-quadruplex DNA structures by chromatin immunoprecipitation and high-throughput sequencing. *Nat. Protoc.* **2018**, *13*, 551–564. [\[CrossRef\]](#) [\[PubMed\]](#)
60. Hansel-Hertsch, R.; Beraldi, D.; Lensing, S.V.; Marsico, G.; Zyner, K.; Parry, A.; Antonio, M.D.; Pike, J.; Kimura, H.; Narita, M.; et al. G-quadruplex structures mark human regulatory chromatin. *Nat. Genet.* **2020**, *52*, 878–883. [\[CrossRef\]](#)
61. Balasubramanian, S.; Hurley, L.H.; Neidle, S. Drug targeting of transcriptional control via G-quadruplexes. *Nat. Rev. Drug Discov.* **2010**. submitted.
62. Hansel-Hertsch, R.; Simeone, A.; Shea, A.; Hui, W.W.I.; Zyner, K.G.; Marsico, G.; Rueda, O.M.; Bruna, A.; Martin, A.; Zhang, X.; et al. Landscape of G-quadruplex DNA structural regions in breast cancer. *Nat. Genet.* **2020**, *52*, 878–883. [\[CrossRef\]](#) [\[PubMed\]](#)
63. Deramaudt, T.; Rustgi, A.K. Mutant KRAS in the initiation of pancreatic cancer. *Biochim. Biophys. Acta* **2005**, *1756*, 97–101. [\[CrossRef\]](#) [\[PubMed\]](#)
64. Ostrem, J.M.; Shokat, K.M. Direct small-molecule inhibitors of KRAS: From structural insights to mechanism-based design. *Nat. Rev. Drug Discov.* **2016**, *15*, 771–785. [\[CrossRef\]](#)
65. Wang, Y.; Kaiser, C.E.; Frett, B.; Li, H.Y. Targeting Mutant KRAS for Anticancer Therapeutics: A Review of Novel Small Molecule Modulators. *J. Med. Chem.* **2013**, *56*, 5219–5230. [\[CrossRef\]](#)
66. Avino, A.; Eritja, R.; Ciudad, C.J.; Noe, V. Parallel Clamps and Polypurine Hairpins (PPRH) for Gene Silencing and Triplex-Affinity Capture: Design, Synthesis, and Use. *Curr. Protoc. Nucleic Acid Chem.* **2019**, *77*, e78. [\[CrossRef\]](#)
67. Ciudad, C.J.; Rodríguez, L.; Villalobos, X.; Felix, A.J.; Noe, V. Polypurine Reverse Hoogsteen Hairpins as a Gene Silencing Tool for Cancer. *Curr. Med. Chem.* **2017**, *24*, 2809–2826. [\[CrossRef\]](#)
68. Noe, V.; Ciudad, C.J. Polypurine Reverse-Hoogsteen Hairpins as a Tool for Exon Skipping at the Genomic Level in Mammalian Cells. *International journal of molecular sciences. Int. J. Mol. Sci.* **2021**, *22*, 3784. [\[CrossRef\]](#)
69. Rodríguez, L.; Villalobos, X.; Sole, A.; Lliberos, C.; Ciudad, C.J.; Noe, V. Improved design of PPRHs for gene silencing. *Mol. Pharm.* **2015**, *12*, 867–877. [\[CrossRef\]](#)
70. Sole, A.; Delagoutte, E.; Ciudad, C.J.; Noe, V.; Alberti, P. Polypurine reverse-Hoogsteen (PPRH) oligonucleotides can form triplexes with their target sequences even under conditions where they fold into G-quadruplexes. *Sci. Rep.* **2017**, *7*, 39898. [\[CrossRef\]](#)

## Supplementary

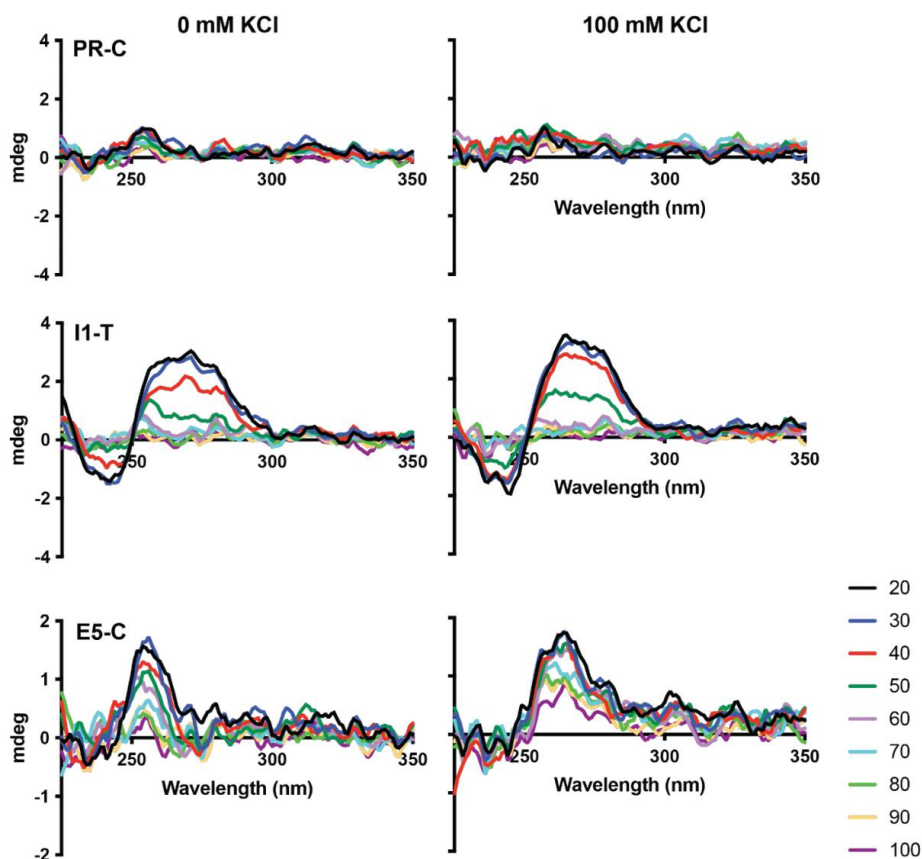


**Figure S1.** ECD Spectra for three novel G4FS as a function of temperature. PR-C formed no discernible secondary DNA structure at any temperature in either the absence (left) or presence (right) of 100 mM KCl (top). I1-T formed hairpin structures with comparable thermal stability in the absence or presence of KCl (middle), and E5-C demonstrated an induction of the G4 sequence, as evidenced by a right shift in spectral maxima towards 262 nm, with the addition of KCl, and also an increase in thermal stability.

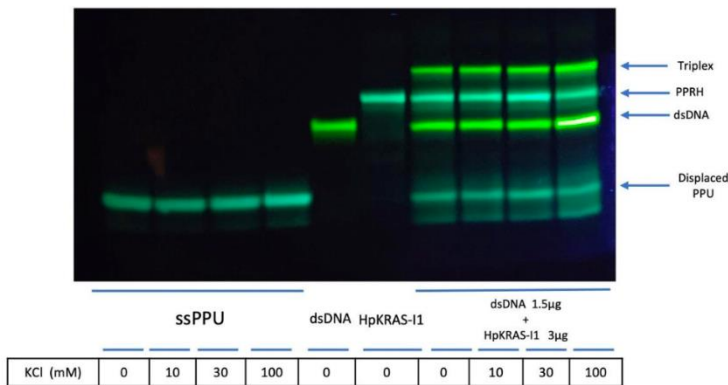


**Figure S2.** Displacement analysis of the Polypurine (PPU) strand in Intron 1 probe with increasing concentrations of KCl. Bindings were performed using 1.5 μg of dsDNA labelled with FAM (green) in the polypyrimidine (PPY) strand only, then incubated as described in M&M with 3μg of Hp-KRAS-I1. The mobility of the ssPPU, dsDNA and PPRH was checked by loading 1.5μg in the corresponding tracks. The resulting structures were resolved by native polyacrylamide (12%) gel electrophoresis. PPRHs, ssPPU and displaced PPU were visualized after Thioflavin-T staining (cyan bands).

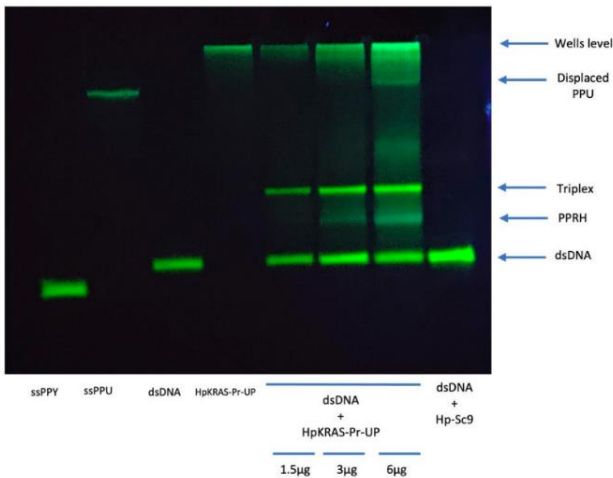


**Figure S3.** Displacement analysis of the Polypurine (PPU) strand in the distal promoter probe. Bindings were performed using 1.5 μg of dsDNA labelled with FAM (green) in the polypyrimidine (PPY) strand only, then incubated as described in M&M with the indicated amounts of Hp-KRAS-Pr-Up PPRH or 1.5 μg of the negative control HpSc9. The resulting structures were resolved by native polyacrylamide (12%) gel electrophoresis. PPRHs, ssPPU and displaced PPU were visualized after Thioflavin-T staining (cyan bands).

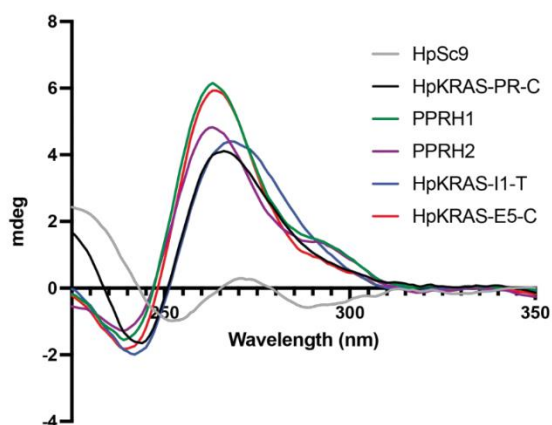


**Figure S4.** ECD spectra of PPRH sequences. Spectra were recorded from 225-350 nm at room temperature for all PPRH sequences in the presence of 100 mM KCl.



### 4.1.1 Additional results to Article I

In addition to the binding assays, we conducted melting temperature ( $T_M$ ) measurements to assess the affinity of each PPRH for its respective target (Table 2). We compared the differences in  $T_M$  between each PPRH with its target, as well as between each target with a negative control, HpSc9. HpKRAS-Pr-C, one of the most effective PPRHs, exhibited the lowest  $T_M$ , indicating a lower affinity, whereas HpKRAS-PR-EF presented the strongest affinity with its target.

KRAS region	$T_M$ (°C)	$\Delta T_M$ (°C)	Complex (PPY+)
I1	71.65	43.73	HpKRAS-I1
	27.92		HpSc9
E5	78.2	50.14	HpKRAS-E5
	28.06		HpSc9
PR-EF	87.75	59.83	HpKRAS-Pr-EF-C (PPRH 1)
	27.92		HpSc9
PR-BC	83.78	56.02	HpKRAS-Pr-BC-C (PPRH 2)
	28.26		HpSc9
PR-C	71.40	36.76	HpKRAS-Pr-C
	34.64		HpSc9

**Table 2.** Melting temperatures ( $T_{Ms}$ ) of the different KRAS polypyrimidine single-stranded targets (PPY) with their corresponding PPRHs and HpSc9.

We also extended the scope of our work to investigate the effects of the PPRHs on various cancer cell lines exhibiting KRAS deregulation (Figure 14). The most effective PPRHs in these cancer cell lines were HpKRAS-E5-C, HpKRAS-PR-C and HpKRAS-I1-T, reducing cell viability by more than 60%. The negative control did not show a significant decrease in cell viability.



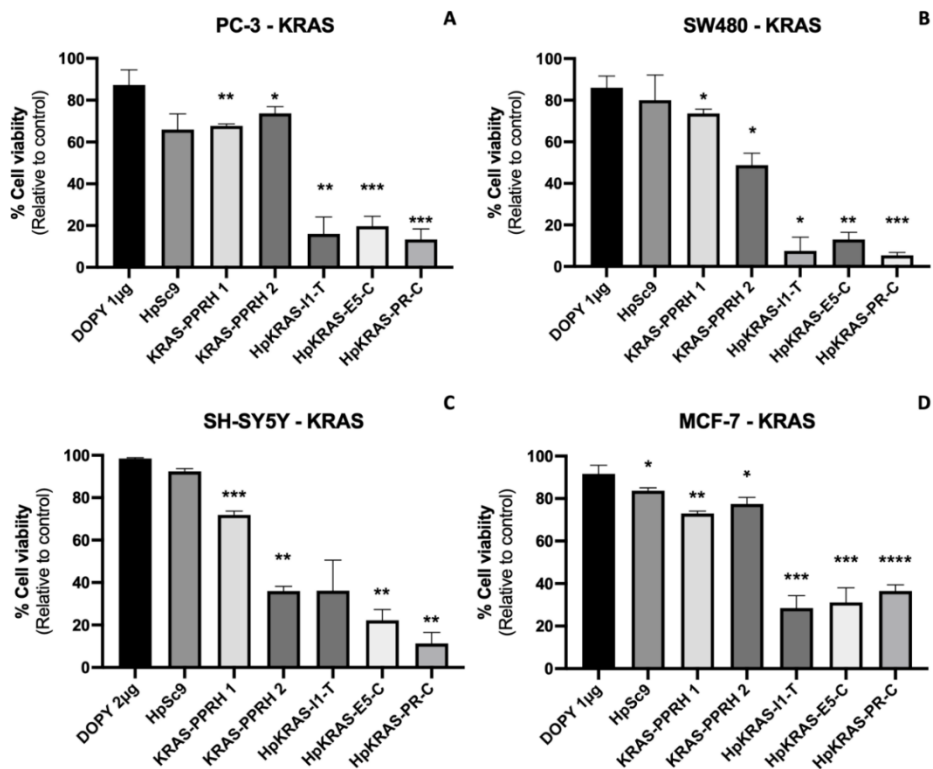


**Figure 14.** Effect of KRAS-targeting PPRHs transfected with DOPY on the viability of various cancer cell lines, prostate PC-3 (A), colorectal SW-480 (B), neuroblastoma SH-Sy5y (C), and breast MCF-7 (D). A 100 nM of PPRHs was transfected with either 2.1 or 4.2 µM of Dioleoyl Pyridinium (DOPY). The effects of the PPRHs were assessed 120 hours after transfection through cell viability assays. Results were normalized to the transfection vehicle (DOPY) control. Experiments were conducted in triplicate with internal duplicates. Statistical significance was determined using one-way ANOVA with a post hoc Dunnett test, comparing the results against the HpSc9 control; \*  $p < 0.05$ , \*\*  $p < 0.01$ , \*\*\*  $p < 0.001$ , \*\*\*\*  $p < 0.0001$ .

## 4.2. ARTICLE II

### Targeting MYC Regulation with Polypurine Reverse Hoogsteen Oligonucleotides

Simonas Valiuska <sup>#</sup>, Alexandra Maria Psaras<sup>#</sup>, Véronique Noé, Tracy A. Brooks <sup>\*</sup> and Carlos J. Ciudad<sup>\*</sup>

<sup>#</sup> Both authors contributed equally to this work

International Journal of Molecular Sciences. 2023, 24(1), 378. (Impact factor: 6.208)

**Background:** *cMYC* (referred as *MYC*) is a proto-oncogene from a large family of regulator gene that encode for transcription factors, that acts as a critical regulator of cell proliferation, differentiation, and apoptosis. It actively regulates the expression of a third of human genes, so its tightly regulated. When MYC control systems fail, it becomes deregulated and can lead to a malignant formation (Conacci-Sorrell et al., 2014; Dang, 2012; L. Shen et al., 2015). Oncogenic *MYC* is abnormally expressed in approximately 70% of human cancers and it is commonly overexpressed or amplified in Burkitt's lymphoma, neuroblastoma, colon, cervix, lung, pancreatic, and prostate cancers (Ala, 2022; Madden et al., 2021; X. Qiu et al., 2022). *MYC* is classically labeled as undruggable since the protein lacks traditional pockets or binding sites accessible to drug interactions, making it difficult to design specific inhibitors. The promoter region of the *MYC* gene contains GC-rich sequences that can form G-quadruplex structures, which have been shown to play a regulatory role in mediating transcription downregulation. The presence of G-quadruplexes in *MYC* promoter region has generated interest in exploring their potential as therapeutic targets for cancer treatment. (Brooks & Hurley, 2010; Eddy et al., 2011; Huppert & Balasubramanian, 2007).

**Objectives:** To study the effects of PPRHs targeting known G-quadruplex forming sequences (G4FS) and other GC-rich sequences present within intronic and promoter regions of the *MYC* gene. We aimed to investigate the effects of different PPRHs in various cell lines with

deregulated *MYC*, including pancreatic, prostate, neuroblastoma, colorectal, ovarian, and breast cancers. The primary focus was to understand the regulatory impact of these PPRHs on *MYC* expression and to explore their potential for cancer treatment.

**Results:** A total of six different PPRHs were designed, three targeting *MYC* promoter regions (HpMYC-G4-PR-C, HpMYC-PR-Distal-T and HpMYC-PR-Prox-T) and intronic regions (HpMYC-I1-T, HpMYC-I1\_short-T and HpMYC-I2-C). Only HpMYC-G4-PR-C and HpMYC-I2-C demonstrated parallel G4 formation whereas HpMYC-Dist-T, HpMYC-Prox-T, and HpMYC-I1-T all formed hairpin structures.

We verified that the interaction of *MYC* PPRHs with their corresponding targets displaced the complementary strand, allowing the formation of G4 secondary structures as visualized by Thioflavin T staining.

HpMYC-G4-PR significantly decreased promoter activity whereas HpMYC-PR-Prox-T increased it. We also analyzed the cytotoxic effects of the PPRHs transfected with DOPY in a collection of *MYC*-overexpressing and -addicted cell lines, including estrogen receptor-positive breast MCF-7, neuroblastoma SH-Sy5y, colorectal SW480, and prostate PC-3 cancer cells. All PPRHs tested decreased cell viability, HpMYC-G4-PR and HpMYC-I1T being the most effective.





We conducted further analyses in pancreatic AsPC-1 and prostate PC-3 cancer cell lines, which exhibited a higher sensitivity to the tested PPRHs. Transfection of PPRHs with DOTAP resulted in a notable inhibition of exponential growth after 72 hours. The effects of PPRHs were ranked based on their impact at a 25 nM concentration, and they correlated with the changes observed in cell viability, HpMYC-G4-PR-C and HpMYC-I1-T, showed the most significant efficacy. We additionally explored the effects on *MYC* mRNA and protein expression produced by HpMYC-G4-PR-C and HpMYC-I1-T in PC-3 cells. Both PPRHs significantly decreased mRNA levels at 72 hours, and protein levels were significantly lowered by both PPRHs where HpMYC-I1-T was the most effective. Cyclin D1 levels were also decreased in these conditions.

**Conclusions:** We explored the formation of G4 structures within *MYC* gene sequences and the effects of PPRHs on these structures. We found that G4 structures were formed within certain *MYC* sequences, and discovered a new G4 forming structure with parallel formation in *MYC* intron 2. PPRHs targeting these sequences were able to induce changes in cell viability. The most effective PPRHs were HpMYC-G4-PR-C and HpMYC-I1-T. These findings provide insights into the potential therapeutic applications of PPRHs directed toward G4 *MYC* structures for cancer treatment.



## Article

# Targeting MYC Regulation with Polypurine Reverse Hoogsteen Oligonucleotides

Simonas Valiuska <sup>1</sup>, Alexandra Maria Psaras <sup>2</sup>, Véronique Noé <sup>1</sup>, Tracy A. Brooks <sup>2,\*</sup> and Carlos J. Ciudad <sup>1,\*</sup>

<sup>1</sup> Department of Biochemistry and Physiology, School of Pharmacy and Food Sciences, University of Barcelona, 08028 Barcelona, Spain

<sup>2</sup> Department of Pharmaceutical Sciences, School of Pharmacy and Pharmaceutical Sciences, Binghamton University, Binghamton, NY 13902, USA

\* Correspondence: cciudad@ub.edu (C.J.C.); tbrooks@binghamton.edu (T.A.B.); Tel.: +34-93-403-4455 (C.J.C.)

**Abstract:** The oncogene MYC has key roles in transcription, proliferation, deregulating cellular energetics, and more. Modulating the expression or function of the MYC protein is a viable therapeutic goal in an array of cancer types, and potential inhibitors of MYC with high specificity and selectivity are of great interest. In cancer cells addicted to their aberrant MYC function, suppression can lead to apoptosis, with minimal effects on non-addicted, non-oncogenic cells, providing a wide therapeutic window for specific and efficacious anti-tumor treatment. Within the promoter of MYC lies a GC-rich, G-quadruplex (G4)-forming region, wherein G4 formation is capable of mediating transcriptional downregulation of MYC. Such GC-rich regions of DNA are prime targets for regulation with Polypurine Reverse Hoogsteen hairpins (PPRHs). The current study designed and examined PPRHs targeting the G4-forming and four other GC-rich regions of DNA within the promoter or intronic regions. Six total PPRHs were designed, examined in cell-free conditions for target engagement and in cells for transcriptional modulation, and correlating cytotoxic activity in pancreatic, prostate, neuroblastoma, colorectal, ovarian, and breast cancer cells. Two lead PPRHs, one targeting the promoter G4 and one targeting Intron 1, were identified with high potential for further development as an innovative approach to both G4 stabilization and MYC modulation.

**Keywords:** MYC; PPRH; G-quadruplex; pancreatic cancer; prostate cancer; neuroblastoma; breast cancer; colon cancer



**Citation:** Valiuska, S.; Psaras, A.M.;

Noé, V.; Brooks, T.A.; Ciudad, C.J.

Targeting MYC Regulation with

Polypurine Reverse Hoogsteen

Oligonucleotides. *Int. J. Mol. Sci.*

**2023**, *24*, 378. <https://doi.org/10.3390/ijms24010378>

10.3390/ijms24010378

Academic Editor: Joon-Hwa Lee

Received: 1 November 2022

Revised: 7 December 2022

Accepted: 20 December 2022

Published: 26 December 2022



**Copyright:** © 2022 by the authors.

Licensee MDPI, Basel, Switzerland.

This article is an open access article

distributed under the terms and

conditions of the Creative Commons

Attribution (CC BY) license (<https://creativecommons.org/licenses/by/4.0/>).

## 1. Introduction

cMYC (hereafter referred to as MYC) is a basic helix–loop–helix zipper (bHLHZ) family transcription factor, from the larger MYC proto-oncogene family, that controls the expression of more than 30% of human genes. It has an important role in several cellular processes, such as cell growth, metabolism, cell differentiation, and cell death [1,2]. The MYC gene is located on chromosome 8q24 and it is composed of three exons, including a non-coding exon 1. MYC has four promoter regions that are independently controlled—P0, P1, P2, and P3. P0 is located 600 bp upstream of the P1 promoter, P1 and P2 are close to Exon 1, and P3 is near to the 3' of intron 1. MYC expression is further regulated by the far upstream element (FUSE) 1.4 kilobases away, contributing to rates of transcription, as opposed to initiation of transcription. The gene encodes for a 439 amino acid protein of 64 to 67 kDa [3–5].

MYC expression is highly regulated by transcription factors, including TFIIH, Sp1 MAZ1, and DNA structures, such as H-triplex, G-quadruplex, i-motif-DNA, and the aforementioned FUSE element [6]. Moreover, the MYC protein has a short half-life (20–30 min), general instability, and is degraded by ubiquitin-linked proteasome mechanisms as safeguards to overactive MYC function. Should these mechanisms and control systems fail, aberrant MYC mRNA and/or protein can lead to a malignant formation [7]. Oncogenic MYC is dysregulated or aberrantly expressed in approximately 70% of human cancers,

including breast, bone, brain, B-cell lymphoma, colon, cervix, lung, pancreatic, and prostate tumors [8–12], with correlating poor prognosis and aggressive disease [13,14]. MYC deregulation can be provoked by many factors, including upregulation due to upstream factors, chromosomal translocation, viral insertions, amplification, deletions, insertions, and/or mutations of cis elements [6].

Of note for the current study, G-quadruplexes (G4s) are non-canonical DNA secondary structures formed from GC-rich regions of DNA. Generally, G4s are conforming to a consensus sequence  $(G_{2-3}X_{1-9})_3G_{2-3}$ , wherein four contiguous sets of two or three continuous guanines are connected by loops of up to nine nucleotides, although a number of alternative isoforms can form from non-confirming DNA sequences. To form a G4, four guanines base pair through Hoogsteen hydrogen bonds to form a tetrad, and two or more tetrads stack with the assistance of monovalent cations, such as  $K^+$  [15]. G4 formation has been shown to regulate several central dogmatic functions, including transcription, splicing, replication forks, telomere homeostasis, and DNA repair [16–21]. Within promoters, a consensus sequence will fold back on itself to form a higher-order structure and generally acts as a silencing element for transcription due to the sequestration of transcription factor binding sites. Just upstream of the P1 promoter of the MYC promoter lies a nuclelease hypersensitivity element (NHE III<sub>1</sub>) with well-established silencing G4 formation [22,23]. This structure is of high therapeutic value, and many groups are pursuing drug discovery efforts to identify selective stabilizers of this parallel G4 [24–26], although gaining strong selectivity for one particular G4 has proven to be a difficult feat.

In the current study, and to mediate specificity for one gene and one G4, we used Polypurine Reverse Hoogsteen hairpins (PPRHs) to target specific regions of the MYC gene, with an initial focus on G4-forming sequences (G4FSs). PPRHs are hairpins formed by two antiparallel polypurine mirror repeats bound through intramolecular Hoogsteen bonds and linked by a four-thymidine loop. These moieties bind to their RNA [27], single-stranded DNA (ssDNA), or double-stranded DNA (dsDNA) target with an affinity in the order of  $6 \times 10^{-7}$  M [28], forming a triplex that, in the case of dsDNA, provokes the displacement of the polypurine strand [29]. PPRHs targeting the complementary sequence of G4-forming regions can facilitate more G4 formation and, thus, transcriptional repression. PPRHs targeting non-G4-forming regions mediate effects either by decreased binding of transcription factors or by interference with RNA polymerase function during transcription. We classify the PPRHs into template (-T) or coding (-C) moieties, based on their targeting, a sequence on the template or the coding strand, respectively [30]. Coding PPRH, apart from targeting and binding DNA, can target mRNA and modify post-transcriptional processes [31]. These hairpin molecules have a broad spectrum of applications and have been previously shown to be used as immunotherapy tools [32,33], biodetectors [34,35], in gene repair [36,37], or to inhibit replication stress [38]. PPRHs have also been shown to be good candidates for gene silencing [27], targeting cancer targets [39], and, more recently, G4FS [40,41].

## 2. Results

### 2.1. PPRH Target Selection and Sequence Design

We detected several potential PPRH targets within the MYC gene using a combination of the Triplex-Forming Oligonucleotide (TFO) search tool and the Quadruplex-forming G-rich sequence (QGRS) mapper. Primarily, we selected target sequences with high G scores, indicating more potential to form G4s (Figure 1, Table 1). Then, we proceeded to design the corresponding PPRHs targeting the complementary sequence of the putative G4 forming sequence (Figure 1, sequences detailed in materials and methods). The region with the highest G score (42) is the previously described promoter G4 [23,42], followed closely by an undescribed region (G-score = 36) in intron 2. Five of the six designed PPRHs target putative G4 forming sequences (G4FS), with the additional PPRH targeting a 54% GC-rich region within the proximal promoter.



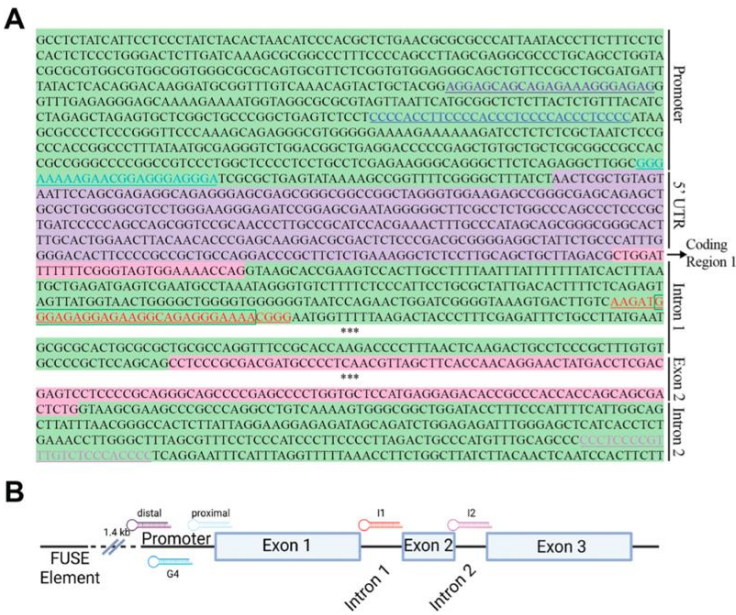


**Figure 1.** MYC sequence and PPRH localization. (A) The MYC sequence, including non-coding (green highlight) promoter and intron regions and coding (pink highlight) exons, is the target of the six designed PPRH moieties—three within the promoter region (HpMYC-PR-Distal-T, purple text; HpMYC-G4-PR-C, dark blue text; and HpMYC-PR-Prox-T, light blue text), two targeting intron 1 (HpMYC-I1-T, red text and HpMYC-I1<sub>short</sub>-T, green box around subset of red text) and one in intron 2 (HpMYC-I2-C, lilac text). Asterisks indicate gaps in the sequence of MYC. A general schema of the MYC sequence and targeting PPRHs is shown in (B).

**Table 1.** PPRHs and their G-rich targets. Name and sequence of the target G-rich forming sequences and their G4 forming potential, complementary to the polypyrimidine target of the PPRH against MYC. Guanines potentially involved in G4 formation are highlighted in bold and the entirety of the G-rich portion of the target sequence is flanked by square brackets in both length and sequence.

MYC Region	Length	G-rich PPRH Target Sequence (5′-3′)	G-Score
G4-Pr-C	46 [31]	GCGCTTAT[GGGGAGGGTGGGGAGGGTGGGGAAGGTGGGG]AGGAGAC	42
I1_T	26 [21]	GAT[GGGAGAGGAGAAGGCAGAGGG]AA	21
PR-distal-T	24	TCCTCGTCGTCTCTTTCCTCTC	0
MYC-PR-prox-T	27 [22]	GC[GGGAAAAAGAACGGAGGGAGGG]ATC	14
MYC-I2-C	30 [27]	TGA[GGGGTGGGAGACAAACGGGGAGGGGGG]	36

2.2. Examination of G4 Formation within the Target Sequences

The ability of the target sequences to form inducible G4 structures was examined by electronic circular dichroism in the absence and presence of 100 mM KCl (Figure 2). Parallel G4s demonstrate maximal Cotton effects in the 262–264 nm range, and antiparallel loops are highlighted with Cotton effects in the 290 nm range. The PR-Prox-T region did not form a G4 structure in either the absence or presence of KCl. This region’s Cotton effects



are consistent with dsDNA, with maxima in the 260–280 nm range, likely forming from the five A's on one strand complementing the 3' series of Gs on a second strand. Interestingly, the structure was destabilized with the addition of KCl, which is a yet-unexplored phenomenon whose exploration, while interesting, lays beyond the scope of the current investigation. While the Cotton effects did increase to a small degree with the addition of 100 mM KCl for the Distal-T and the I1-T sequences, the maxima are neither distinct nor in the parallel or anti-parallel G4-forming ranges. G4-C has been shown extensively to form a strong G4 structure, even in the absence of KCl, which we confirmed. For the first time, a stable and minorly inducible parallel G4 structure was shown to form within intron 2 (I2-C). G4 and hairpin formation was also examined with the PPRH sequences targeting each of these MYC gene sequences (Supplemental Figure S1). HpMYC-G4-C and HpMYC-I2-C were also both found to form parallel G4 sequences, while HpMYC-Dist-T, HpMYC-Prox-T, and HpMYC-I1-T all form hairpin structures. This pattern of G4-targeting PPRHs also forming G4s was noted recently with *KRAS*-gene-targeting PPRHs [41].

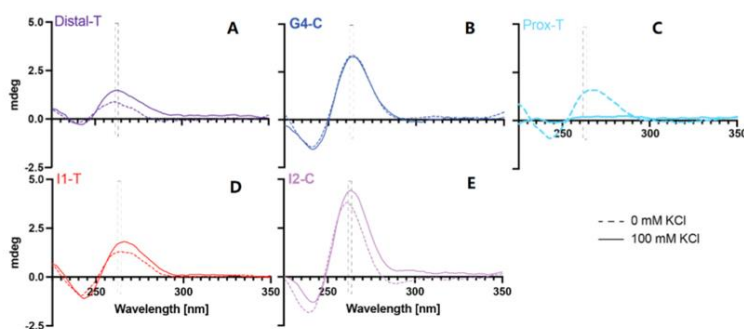


**Figure 2.** G4 formation within GC-rich MYC sequences. G4 formation was monitored by electronic circular dichroism (ECD) for the five putative G4-forming DNA sequences—Distal-T (A), G4-C (B), Prox-T (C), I1-T (D) and I2-C (E). The sequences were annealed in the absence (dashed lines) or presence (solid lines) of 100 mM KCl; spectra were recorded from 225 to 350 nm. Only G4-C and I2-C (both bold) demonstrated parallel G4 formation as noted by maximal Cotton effects in the 262–264 nm range (highlighted in each frame by the dashed box).

### 2.3. PPRHs Binding to MYC Target Sequences

To check the bindings of the designed PPRHs with their target regions, we performed Electrophoretic Mobility Shift Assays (EMSAs) in native gels (Figure 3). Each target sequence was incubated with either the corresponding PPRH or with a scrambled PPRH control (HpSc9). Binding of the target:PPRH sequences was noted for each pair by the supershift in bands 2, 5, 8, 11, and 14, albeit to varying degrees. No binding was noted between any target sequence and the HpSc9 control (bands 3, 6, 9, 12, and 15).

Thermal stability ( $T_M$ ) was also examined via UV-Vis spectrophotometry for the target polypyrimidine (PPY):PPRH pairs and compared to the target:HpSc9 control pairs (Table 2). Stability of the PPYs in the presence of HpSc9 was found to be between 27 and 30 °C, while that of the PPYs plus their target PPRHs, forming a triplex, ranged from 71 to 89 °C.  $\Delta T_M$ s ranged from 41 to 61 °C, with the highest stabilities being identified for the G4-forming PPY sequences and their target PPRHs. Interestingly, the  $T_M$  of the double-stranded (ds) DNA targets of MYC-I2 and MYC-PR-Prox was 70.18 and 74.79 °C. These values are 3.16 and 5.74 °C less than their corresponding PPRH-PPY triplexes, respectively. This shows that the PPY + PPRH had a stronger interaction than the correlating dsDNA formed from PPY + polypurine (PPU) sequences.

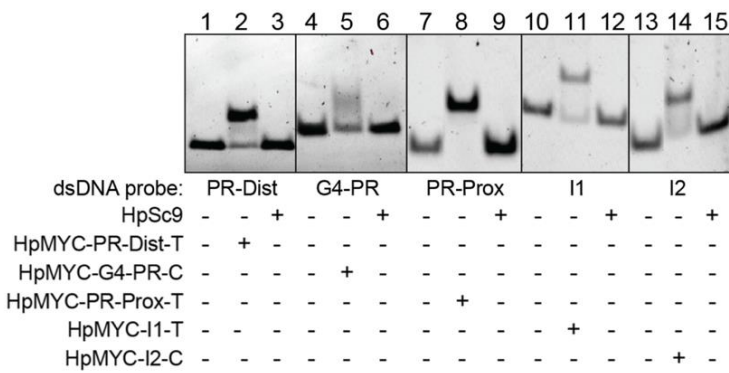


**Figure 3.** PPRH binding to target sequences in the MYC gene. Binding of HpMYC- PR-Dist-T, G4-PR-C, PR-Prox-T, I1-T, I2-C, and HpSc9 (1 µg) to the complementary FAM-labeled polypyrimidine target sequence dsDNA (200 ng). The length of the dsDNA probes was the same as each arm of the PPRHs, that is, ranging between 23 and 34 nucleotides. A supershift is noted for all binding pairs (e.g., dsDNA probes with the matched PPRH), but not scramble controls. The image is representative of at least 3 different EMSAs.

**Table 2.** Melting temperatures ( $T_{Ms}$ ) of the different polypyrimidine single-stranded targets (PPY) with their corresponding PPRH and HpSc9.

MYC Region	$T_M$ (°C)	$\Delta T_M$ (°C)	Complex (PPY+)
PR-Prox	73.34	44.88	HpMYC-PR-Prox
	28.46		HpSc9
G4-PR	88.90	60.92	HpMYC-G4-PR
	27.98		HpSc9
PR-Distal	71.89	41.96	HpMYC-PR-distal
	29.93		HpSc9
I1	78.36	50.00	HpMYC-I1-T
	28.36		HpSc9
I1_short	73.80	46.47	HpMYC-I1_short
	27.33		HpSc9
I2	80.53	52.63	HpMYC-I2
	27.90		HpSc9

2.4. Polypurine Strand Displacement

Strand displacement assays were used to examine the ability of the PPRHs to displace the PPU-rich strands from their dsDNA complexes (Figure 4, Supplemental Figure S2). As an example, HpMYC-PR-Prox-T dose-dependent displacement of the PPU strand from MYC-PR-Prox dsDNA is shown in Figure 4. The PPY strand is FAM labeled, whereas the PPRH strands were visualized with staining by Thioflavin T, a dye that has affinity and stains non-canonical DNA structures [40]. Samples were run on native gels with a fixed concentration of dsDNA and increasing concentrations of HpMYC-PR-Prox-T; banding patterns were visualized with UV light. In lanes 5, 6, and 7, an upper-shifted band corresponding to the triplex could be observed along with slight, but observable, decreases in the dsDNA (Figure 4A). We observed the appearance of both a PPRH and a displaced

ssPPU cyan band in a concentration-dependent manner after the gel was stained with Thioflavin T. Notably, the displacement of the ssPPU strand from the triplex was observed with MYC-PR-Prox-T, but not with HpSc9 (Figure 4B). The strand displacement assay was also performed with HpMYC-I1-T and HpMYC-I2-C and their corresponding DNA regions, showing the same strand displacement behavior as PR-Prox-T (Supplemental Figure S2).

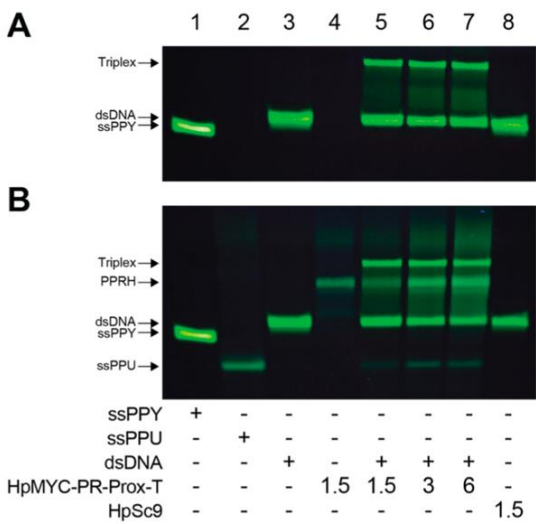


**Figure 4.** Displacement analysis of the Polypurine (ssPPU) strand in the proximal promoter probe. (A) Bindings were performed using 1.5 µg of dsDNA labeled with FAM (green) in the single-stranded (ss) PPY strand only, then incubated with the indicated amounts of HpMYC-Pr-Prox-T or 1.5 µg of HpSc9. The resulting structures were resolved by native polyacrylamide (12%) gel electrophoresis and visualized with UV light (green bands). (B) Visualization of PPRHs, ssPPU, and displaced PPU bands after Thioflavin-T staining (cyan bands). The image is representative of at least 3 different strand displacement assays.

2.5. Effect of MYC-Targeting PPRHs on Promoter Activity, Cell Growth and Viability, and Correlating Changes in Transcription and Translation

The Del4 luciferase plasmid, containing the MYC gene +/− 400 bp around the transcriptional start site (TSS), was co-transfected with a pRL plasmid into HEK-293 cells. A pGL.14 empty vector (EV) was co-transfected with the pRL plasmid into HEK-293 cells as a negative control. The effects of each PPRH (1 µM) on luciferase expression after co-transfection with each plasmid pair were monitored 48 h later (Figure 5). Notably, the Del4 promoter contains the targets for all of the promoter-focused PPRHs (left of the dashed line), but not those in the intronic regions (right of the dashed line). Of the PPRH targeting sequences in the Del4 plasmid, neither HpMYC-PR-Dist-T nor HpMYC-PR-Prox-T demonstrated significant MYC promoter regulation, whereas HpMYC-G4-PR-C significantly decreased promoter activity driven by the Del4 plasmid. Interestingly, HpMYC-G4-PR-C and HpMYC-PR-Prox-T significantly decreases promoter activity driven by the EV vector in a non-specific manner. Significantly different effects were observed for the HpMYC-G4-PR-C and HpMYC-PR-Prox-T PPRHs between the EV and Del4 vectors with related decreased and increased promoter activity, respectively. More markedly, HpMYC-G4-PR-C mediated a 50% greater decrease in promoter activity in the Del4, as compared to the EV plasmid while HpMYC-PR-Prox-T increased the expression of EV. Interestingly,

HpMYC-I2-C mediated a significant decrease in EV, but not Del4 promoter activity, though HpMYC-I1-T and -I1\_short did not change expression from either the EV or Del4 plasmids. Of the PPRHs targeting the promoter, HpMYC-G4-PR-C demonstrated the greatest promise in its significant effects, both from its control and from the EV effects.

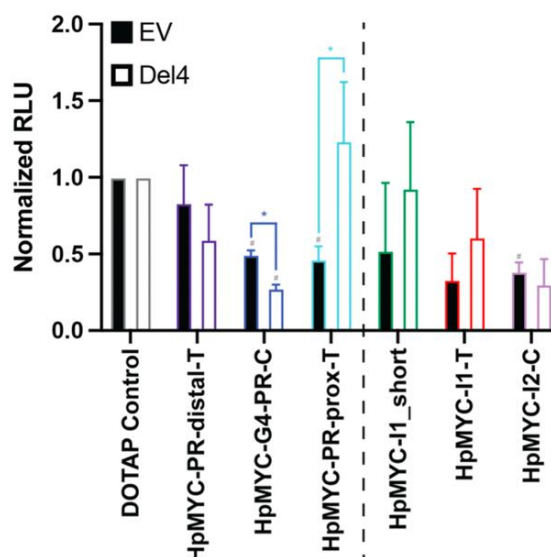


**Figure 5.** PPRH-mediated regulation of MYC promoter activity. Activity from the MYC promoter was measured indirectly via a luciferase assay using the Del4 luciferase plasmid, containing +/− 400 bp around the transcriptional start site. HEK-293 cells were co-transfected with either the Del4 or a promoterless empty vector (EV) control and the pRL plasmid as a transfection efficiency control. The indicated PPRHs (1  $\mu$ M; PR-distal-T, purple; G4-PR-C, blue; PR-prox-T, light blue; I1\_short, green; I1-T, red; and I2-C, lilac) were co-transfected with the luciferase plasmid pairs; 48 h later, cells were lysed and luciferase activity was measured as a correlate to MYC promoter activity. For each plasmid:PPRH pair, effects were normalized to DOTAP vehicle control, and two-way ANOVA with Dunnett's post hoc analysis was performed to determine statistical significance. PPRH targeting elements present in the Del4 plasmid are grouped to the left of the dashed line, and those targeting elements missing in the Del4 plasmid are grouped to the right of the promoter. HpMYC-G4-PR-C demonstrated a significant decrease in the promoter activity of Del4, compared to both its matched DOTAP control and its parallel EV:PPRH pair. Experiments were performed minimally in triplicate; #  $p < 0.05$  as compared to plasmid matched DOTAP control; \*  $p < 0.05$  as compared to PPRH matched EV control.

The effects of PPRHs were examined in an array of MYC-overexpressing and -addicted cell lines, including estrogen receptor-positive breast MCF-7, neuroblastoma SH-Sy5y, colorectal SW480, and prostate PC-3 cancer cells. Cells were transfected with 100 nM of the indicated PPRHs with 2.1 or 4.2  $\mu$ M of Dioleoyl Pyridinium (DOPY) [43], particularly used for the difficult-to-transfect SH-Sy5y cells (Figure 6); all effects were normalized to DOPY controls. Remarkably, all of the PPRHs mediated a significant decrease in the SW480, Sh-Sy5y, and MCF7 cell lines. PC-3 cells are globally more sensitive to DNA transfection, as evidenced by the significant decrease in viability with the non-targeting HpSc9 PPRH; however, HpMYC-G4-PR-C, HpMYC-I1-T and \_short-T, and HpMYC-PR-prox-T significantly decreased PC-3 viability when compared to HpSc9 control.



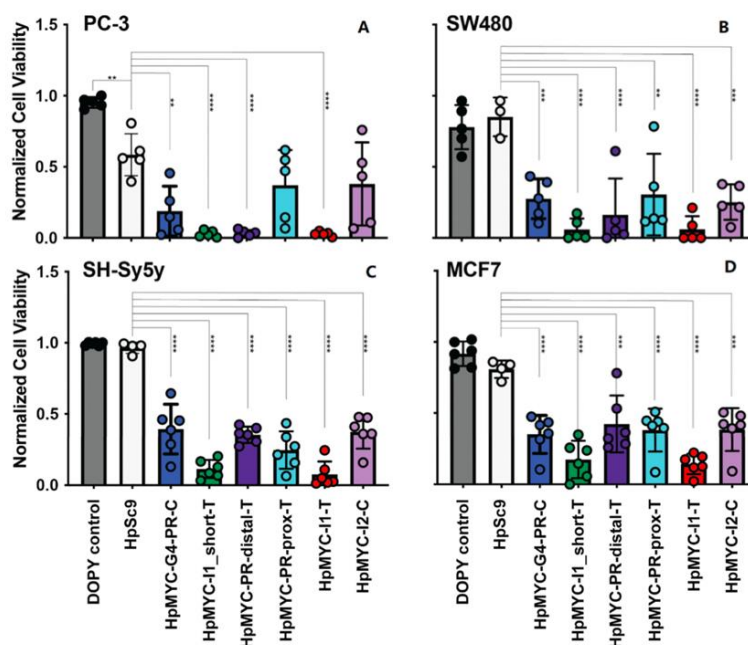


**Figure 6.** Effect of MYC targeting PPRHs on prostate cancer PC-3 (A), colorectal cancer SW-480 (B), neuroblastoma SH-Sy5y (C), and breast cancer MCF-7 (D), cell viability. Thus, 100 nM of PPRHs was transfected with Dioleoyl Pyridinium (DOPY). The effects of the PPRHs were determined 120 h after the transfection by cellular viability assays. PPRH effects were normalized to transfection vehicle (DOPY) control, and experiments were performed in triplicate with internal duplicates. Statistical significance was analyzed by one-way ANOVA with a post hoc Dunnett test comparing groups against the HpSc9 control; \*\*  $p < 0.01$ , \*\*\*  $p < 0.001$ , \*\*\*\*  $p < 0.0001$ .

Dose-dependent effects of the PPRHs were further examined in PC-3 and the MYC-regulation-sensitive AsPc-1 pancreatic cancer cell line (Figure 7A). Both cell lines were remarkably sensitive to the PPRHs and even to transfected DNA at high-enough concentrations, as evidenced by the decreased cell viability with 100 nM HpSc9. The reduction in cell viability at 25 nM of PPRHs ranged from 40 to 60% for AsPc-1 cells and from 40 to 90% for PC-3 cells. The  $IC_{50}$  for most PPU-targeting PPRHs in AsPc-1 cells ranged from 22 to 30 nM, with the exception of HpMYC-PR-distal-T and HpSc9 with  $IC_{50}$ s of 51 and 54 nM, respectively. PC-3 cells were even more susceptible to DNA transfection, with lesser differentials between the scrambled HpSc9 and the targeting PPRHs. HpMYC-PR-distal-T and HpMYC-I1\_short dose-dependent effects were indistinguishable from HpSc9 with  $IC_{50}$  values ranging from 33 to 60 nM, while the cells were most sensitive to HpMYC-PR-G4-C, HpMYC-I1-T, and HpMYC-PR-Prox-T with  $IC_{50}$ s of 5, 8, and 4 nM, respectively.

Monitoring cell growth over time, in addition to the terminal viability assay described above, can be informative to determine the time to onset of PPRH effects [41]. Thus, we visualized the effects of each PPRH at 25, 50, and 100 nM in AsPc-1 pancreatic cancer cells using live cell microscopy over time and evaluating the percent confluency in the wells (Figure 7B); pictures were taken every 8 h post-transfection for 120 h. The cell confluence was determined by using software trained to AsPc-1 cell-specific morphology. As noted in the viability assay, AsPc-1 cells were sensitive to 100 nM HpSc9 and, thus, the lower

doses yielded more informative data. Overall, two conclusions could be inferred from the time- and dose-dependent examination of PPRH effects. The first was that the general onset of differential growth parameters caused by PPRHs was 72 h, as observed by their inhibition of exponential growth. The second observation is that the effect of PPRHs could be further ranked by looking at the effects of 25 nM, and these findings concur with the changes observed in cell viability. In particular, HpMYC-PR-distal-T was the least-effective moiety—in agreement with all data presented thus far, HpMYC-prox-T, I1-T, and I1\_short all clustered as moderately more effective, and the two G4-targeting and G4-forming sequences—HpMYC-G4-PR-C and HpMYC-I2-C—were the most efficacious in these cells.

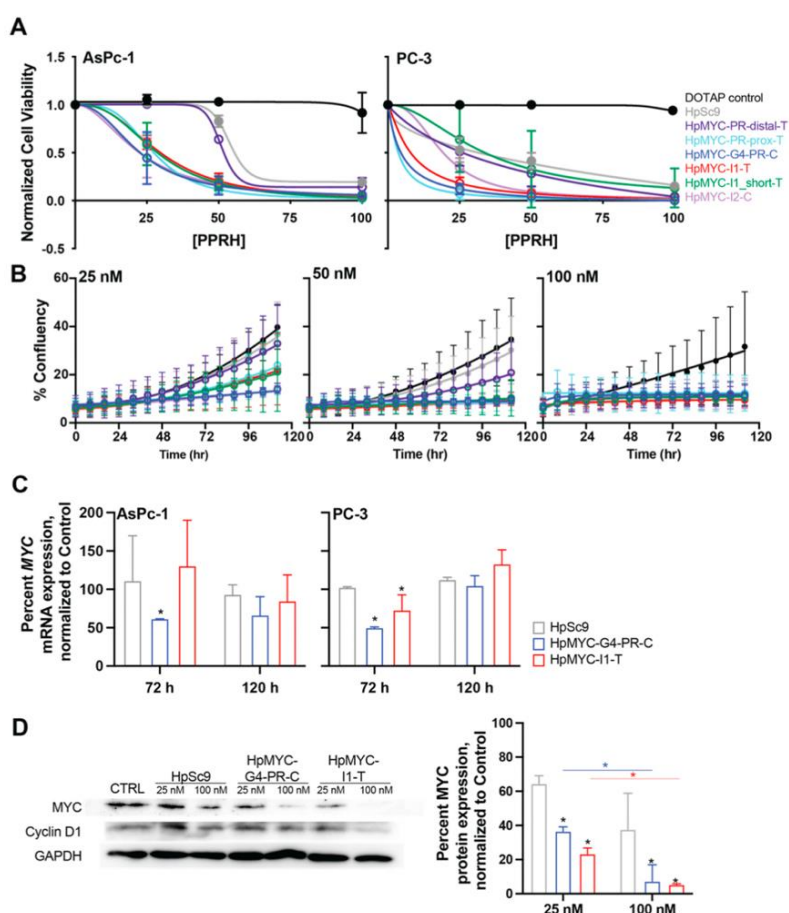


**Figure 7.** Effect of MYC targeting PPRHs on cell viability, growth confluency, mRNA, and protein levels in prostate (PC-3) and pancreatic (AsPc-1) cancer cell lines. (A) Dose-dependent effects of PPRHs on the viability of PC-3 prostate cancer and AsPc-1 pancreatic cancer cell lines were measured after 120 h. (B) The same PPRHs were monitored over time in AsPc-1 pancreatic cancer cells at 25, 50, and 100 nM for their effects on cell growth, as measured by confluency. Notably, changes in confluency

became evident 72 h post-incubation, driving the selection for times to monitor changes in transcription (C) and translation (D). (C) Changes in MYC mRNA, as normalized to GAPDH and again to DOTAP-treated vehicle controls (not shown), were examined in both cell lines at 72 and 120 h post-treatment. Experiments were repeated at least 3 times, with duplicate technical replicates in qPCR experiments. \*  $p < 0.05$  as compared to vehicle-treated controls as determined by one-way ANOVA with post hoc Dunnett analyses. (D) PPRH (HpSc9, HpMYC-G4-PR-C, and HpMYC-I1-T) changes in translation were examined in PC-3 cells, as the more sensitive cell line, in a dose-dependent manner 72 h post-treatment. Representative images of MYC and Cyclin D1 proteins, and GAPDH loading control are shown (left) and semi-quantitation reveals a dose-dependent decrease in MYC expression. Experiments were repeated in duplicate; \*  $p < 0.05$  as compared to HpSc9 control (black) within a dose, or across dose (color coded) as determined by two-way ANOVA with post hoc Dunnett analyses for dose-dependent effects.

Across all of the data observed thus far, and honing in on the sensitive AsPc-1 and PC-3 cells, transcriptional effects of HpMYC-G4-PR-C and HpMYC-I1-T (25 nM) were examined over time (Figure 7C). These two particular PPRHs were selected for their clear physical interactions demonstrated in cell-free systems and their consistent efficacy in both cell lines. Times selected for observation of transcriptional regulation were 72 and 120 h, representing the onset of differential growth and the terminus of the experiment. Thus, 72 h post-transfection, HpMYC-G4-PR-C decreased mRNA expression in both cell lines by 38–50% and HpMYC-I1-T decreased mRNA expression in PC-3 cells by 27%. Unexpectedly, and intriguingly, MYC transcription returned to baseline for both cell lines and both PPRHs by 120 h. While we hypothesize that this is related to a lack of mRNA regulation in the small cell population remaining after 120 h of PPRH treatment, further studies outside the scope of the current work would be required to explore this effect.

The effects of HpMYC-I1-T and HpMYC-G4-PR-C on MYC protein expression were examined in a dose-dependent manner in the more-sensitive-to-transcriptional-regulation PC-3 cells. We performed Western blots 72 h after transfection with 25 and 100 nM of the HpMYC-G4-PR-C, HpMYC-I1-T, and HpSc9 PPRHs (Figure 7D). The qualitative decrease in MYC expression was semi-quantitated using ImageQuant software and normalizing to GAPDH. MYC expression was dose-dependently decreased by the HpSc9 PPRH in PC-3 cells, which correlates with the dose-dependent effects on cell viability as well. HpMYC-G4-PR-C decreased MYC protein expression 43 and 80% more than the scramble PPRH at 25 and 100 nM, respectively. The effects of HpMYC-I1-T were more pronounced, and MYC protein expression was reduced 64 and 86% more than HpSc9 at 25 and 100 nM, respectively. The effects of both PPRHs were significant at both concentrations when compared to untreated and scramble controls. Cyclin D1 is a transcriptional target of MYC, and its protein expression was measured to confirm downstream effects of MYC modulation. Cyclin D1 decreased by 33 and 45% by 25 and 100 nM HpMYC-I1-T, respectively, while no marked effects were observed with HpMYC-G4-PR-C.

### 3. Discussion

The current work focused on the design and examination of a series of Polypurine Reverse Hoogsteen (PPRH) oligonucleotides targeting the MYC gene and its regulatory regions. Six PPRHs were designed against MYC, covering the promoter and intronic regions, both coding (C) and template (T) strands, G-quadruplex (G4) forming sequences (G4FSs), and other regulatory regions. Two of the PPRHs ultimately targeted coding strands complementary to G4 formations—MYC-G4-PR-C and MYC-I2-C—while the other four targeted template strands of non-G4-forming regions. All of the PPRHs formed triplexes with their target sequences, displacing the relevant polypurine strands. In cells, the PPRHs demonstrated regulation of MYC promoter activity and broad anti-cancer activity at 100 nM in breast, brain, colorectal, and prostate cancer cells. Dose-dependent effects were monitored in PC-3 prostate cancer cells, as well as in previously identified PPRH-sensitive AsPc-1 pancreatic cancer cells, where strong dose- and time-dependent



effects on cell viability and growth and MYC transcription and translation were observed. The two lead PPRHs targeting the MYC gene were identified as HpMYC-G4-PR-C and HpMYC-I1-T, both showing promise as novel therapeutics targeting MYC regulation.

MYC has been considered an undruggable target for many years for several reasons, including its lack of enzymatic active site, location in the nuclear compartment, and tight protein–protein interactions with partners, such as MAX. To date, there are no specific drugs targeting it directly [26,44]. MYC, however, is a high-value therapeutic target due to its high prevalence in cancers overexpressing the deregulated protein and the search for possible therapies against this proto-oncogene has persisted. Since it is difficult to directly target MYC, other strategies targeting key factors in transcription, translation, stability, and activation have been considered to modulate MYC's expression [45].

The current project utilized specific polypurine reverse Hoogsteen oligonucleotides (PPRHs) designed against the complementary sequences of different G4FSs or other regulatory elements present in the MYC gene to mediate gene silencing. We previously demonstrated the efficacy of the PPRH approach on the *KRAS* [41] and *TYMS* [40] genes, and the modulation of their expression resulted in a reduction in cancer cell viability. PPRHs have a number of advantages compared to other therapeutic oligonucleotides, including: (i) enhanced stability as DNA, versus RNA, entities enhanced by the hairpin structure they adopt, conferring resistance to degradation; (ii) lack of immunogenicity [46] as DNA molecules shorter than 100 bases usually range from 50 to 55 nucleotides and, therefore, do not activate toll-like receptors (TLRs), as compared again to RNA molecules; (iii) low cost of synthesis; and (iv) efficacy without the required backbone modifications. Notably, the length of the arms for each of the six designed PPRHs ranged from 23 to 31 bp, providing high specificity to their target regions within the MYC gene. Specificity was validated by binding experiments and melting assays were used to verify the PPRHs' strong interaction and, thus, their high affinity, with their corresponding targets.

The PPRHs designed and tested in the presented study were initially focused on complementing G4FS—one of which had been previously characterized thoroughly [23,42] and three newly identified regions; one target sequence within the proximal promoter was not predicted to form a G4 structure. Of the three newly identified G4FSs, only the MYC-I2-C formed a G4 structure—a parallel formation—as defined by electronic circular dichroism. The newly identified G4 is on the coding strand and will, thus, also be present in mRNA with a great likelihood of having nascent functions in splicing and pre-mRNA processing [47]. Further studies are indicated to explore the biological function of this new region, although they are beyond the scope and intent of the current work.

The PPRHs designed demonstrated broad and potent efficacy in MYC-addicted or overexpressing colorectal (SW480), neuroblastoma (SH-Sy5y), breast (MCF-7), prostate (PC-3), and pancreatic cancer cells (AsPc-1). Cytotoxic doses were correlated in the more-sensitive prostate and pancreatic cancer cell lines to changes in promoter activity, transcription, and translation. In particular, PPRHs interfering with promoter activation (HpMYC-G4-PR-C) and transcription (HpMYC-I1-T) dose- and time-dependently regulated these cancer cells and decreased MYC and downstream Cyclin D1 expression at concentrations as low as 25 nM. Direct promoter activity of the promoter-targeting PPRHs, and namely of HpMYC-G4-PR-C, was demonstrated by luciferase experiments with the Del4 luciferase plasmid [48], although this plasmid was unable to decipher the activity of the intronically targeted PPRHs. Targeting the DNA region complementing the promoter G4, and facilitating more G4 formation, likely decreases transcription due to G4 formation sequestering the binding site of transcription factors, such as Sp1 and CNBP, as shown with G4-stabilizing compounds [49]. Additionally, the region forming G4-PR-C also contains binding sites for KLF4 [50], KLF5 [51], or MZF1 [52], as determined by the JASPAR transcription database [53]. Therefore, HpMYC-G4-PR-C could be facilitating G4 formation and interfering with the binding of TF, such as Sp1, CNBP, KLF4, KLF5, and/or MZF1, thus, decreasing transcription. Targeting the template sequence with HpMYC-I1-T will mediate



a hairpin with the template of RNA polymerase and directly interfere with transcription and mRNA elongation, as noted in the study.

Cumulatively, our study successfully identified targets within the *MYC* gene that are susceptible to regulation by PPRH technology and lead therapeutic oligonucleotides were identified and characterized. Although our initial focus was on G4FS, we ultimately identified a lead PPRH facilitating G4 formation in the promoter and another interfering with transcription in a G4-independent manner. Both of these potential therapeutic oligonucleotides demonstrate potent regulation of *MYC* expression in a highly specific manner, with broad applicability to *MYC*-dependent tumors. Further works examining the enhancement of *MYC* promoter G4-stabilizing compounds and other chemotherapeutic regimens are indicated as we explore the full potential of PPRH-mediated regulation of *MYC* in the advancement of the technology presented.

#### 4. Materials and Methods

##### 4.1. Design of Polypurine Reverse Hoogsteen Hairpins

PPRHs against *MYC* were designed using the TFO searching tool software (Triplex-Forming Oligonucleotide Target Sequence Search, available online: <http://utw10685.utweb.utexas.edu/tfo/> (accessed on 10 October 2022)). We searched for triplex-forming sequences in the *MYC* gene with more than 20 nucleotides in length, a maximum of 3 pyrimidine interruptions, and a minimum of 40% of GC content as described [54]. Polypurine sequences in the promoter and intron of the *MYC* gene were analyzed for similarities using the BLAST resource found within the NCBI. Those that were 100% specific with the *MYC* gene and showed dissimilarity or mismatches to other genes were selected.

The selected polypurine sequences were introduced to QGRS mapper to check for putative G4FS (<http://bioinformatics.ramapo.edu/QGRS/index.php> (accessed on 12 October 2022)). This tool uses an algorithm for the recognition and mapping of G-quadruplex elements within a specific sequence and gives a G-score for the putative G4 formations; the higher the score, the more plausible the G-quadruplex formations. The polypurine sequences with the highest G-score were selected and then analyzed with BLAST to avoid any unintended target.

The design of the PPRHs consists of two mirror repeats of the polypurine strands running in antiparallel orientation and linked by a four-thymidine loop. As a negative PPRH control, we used HpSc9 [38]. The designed PPRHs were synthesized as non-modified oligodeoxynucleotides by Sigma-Aldrich (Haverhill, UK) resuspended in sterile Tris-EDTA buffer (10 mM Tris and 1 mM EDTA, pH 8.0) (Sigma-Aldrich, Madrid, Spain) and stored at  $-20^{\circ}\text{C}$ .

##### 4.2. Electronic Circular Dichroism (ECD)

DNA sequences were purchased from Integrated DNA technologies (IDT, Coralville, IA, USA) as desalted oligonucleotides. Upon arrival, they were solvated in double-distilled water overnight, were heated to  $95^{\circ}\text{C}$  for 5 min, then their A260 was determined at temp using a Nanodrop3000 (Thermo Scientific, Waltham, MA, USA) and their concentrations were calculated using the nearest neighbor technique. On the experimental day, the oligonucleotides were diluted to 5  $\mu\text{M}$  final concentration in 50 mM Tris Acetate buffer (pH 7.4), in the absence or presence of 100 mM KCl. Spectra and thermal stability of the putative G4 forming regions were evaluated on a Jasco J-1500 spectrophotometer (Jasco, Easton, MD, USA). Full spectra were recorded from 225 to 350 nm wavelength in triplicate for each experiment using a 1 cm quartz cuvette and a 1 mm bandwidth; the triplicate reads were then averaged. Millidegrees (mdeg, theta) were reported as experimentally determined.

##### 4.3. Melting Temperature Assay

Melting temperatures ( $T_{\text{Ms}}$ ) were determined in a buffer containing 100 mM NaCl, 10 mM  $\text{MgCl}_2$ , and 40 mM HEPES, pH 7.2. The mixture was prepared in a ratio of 1:1

between the polypyrimidine single-stranded target (ssPPY) and the hairpin, in a final concentration of 1  $\mu$ M. Before performing the melting experiments, the mixture was heated to 65 °C for 15 min and slowly cooled down to room temperature.

Melting studies were carried out using a V-730BIO UV-Vis spectrophotometer (Jasco, Madrid, Spain), connected to a temperature controller that increased from 10 to 90 °C and then decreased from 90 to 10 °C at a 1 °C/min rate. Absorbance was measured at 260 nm in a 1 cm pathlength quartz cuvette and monitored every 0.5 °C.

#### 4.4. Electrophoretic Mobility Shift Assay (EMSA)

EMSA analyses were performed with dsDNA probes corresponding to each of the PPRH target sequences. The probes were obtained by mixing equimolecular amounts of each single-stranded oligodeoxynucleotide with 150 mM NaCl solution hybridized at 95 °C for 5 min and cooled down to RT. The polypyrimidine ssDNA was labeled with fluorescein, 6-FAM, in the 5'-end and was synthesized by Sigma-Aldrich (Haverhill, UK). Binding reactions were performed in a binding buffer (5% glycerol, 10 mM MgCl<sub>2</sub>, 100 mM NaCl, 40 mM HEPES, pH 7.2; all reagents were purchased from Sigma-Aldrich). PPRHs (1  $\mu$ g) were mixed with Poly(dI:dC) (200 ng) as a nonspecific competitor and incubated at 65 °C for 10 min. Then, 200 ng of the dsDNA probe was added to the mix for an additional period of 20 min. The resulting products were resolved in a 7% polyacrylamide, 5% glycerol, 10 mM MgCl<sub>2</sub>, 50 mM HEPES, pH 7.2 native gel, at a fixed 190 V and 4 °C, using a running buffer of 10 mM MgCl<sub>2</sub> 50 mM HEPES, pH 7.2. To visualize the results of the electrophoresis, ImageLab software v5.2 was used (GE Healthcare, Barcelona, Spain).

#### 4.5. Strand Displacement Assay upon PPRH Incubation

To detect G4 formation and polypurine strand displacement, we used 1.5  $\mu$ g of each oligonucleotide, alone or in combination with increasing amounts of PPRHs (Table 3). dsDNA probes were prepared following the same protocol described in 4.3 of M & M. dsDNA and PPRH were mixed with 100 mM KCl and 100 mM Tris-HCl, pH 7.4, incubated at 90 °C in a water bath for 5 min, and slowly cooled down to RT. The resulting products were electrophoretically resolved in a non-denaturing 12% polyacrylamide and 10 mM KCl gel running in 1 $\times$  TBE buffer at fixed 150 V. Once electrophoresed, the bands were detected under UV light lamps. Afterwards, the gels were stained with 5  $\mu$ M Thioflavin T solution for 15 min under agitation and washed in water for 2 min. The images were captured with a camera or using Gel DocTM EZ with ImageLab, Version 6.0.

#### 4.6. Cell Cultures

MCF-7, SW-480, SH-Sy5Y, and PC-3 cancer lines were obtained from the cell bank resources of the University of Barcelona (UB). AsPc-1 cells were purchased from American Tissue Culture Collection (ATCC) (Manassas, VA, USA). In all cases, the cells were stored in liquid nitrogen until use. MCF-7, SW-480, SH-Sy5Y, and PC-3 were grown in Ham's F12 medium supplemented with 10% fetal bovine serum (GIBCO, Invitrogen, Barcelona, Spain). AsPc-1 cells were grown in RPMI-1640 medium (ATCC) (Manassas, VA, USA) supplemented with 10% fetal bovine serum (Sigma-Aldrich, St. Louis, MO, USA) and 1 $\times$  penicillin/streptomycin. All cells were maintained at low passages and in exponential growth at 37 °C in a humidified 5% CO<sub>2</sub> incubator.

#### 4.7. Cellular Viability and Cell Growth Studies

One day before transfection, MCF-7, SW-480, SH-Sy5Y, and PC-3 cells (10,000 cells per well) were plated in 6-well dishes in 800  $\mu$ L relevant media. AsPc-1 was plated in 96-well dishes at 2.5  $\times$  10<sup>3</sup> cells per well in 90  $\mu$ L per well of relevant media. The transfection consisted of mixing N-[1-(2-Di-(9Z-octadecenoyl)-3-trimethylammoniumpropane methyl sulfate (DOTAP; Biontex, Germany), or 1,3-bis[(4-oley-1-pyridinio)methyl]benzene dibromide (DOPY, synthesized in house, UB (17)) with the PPRH in serum-free medium, in volumes of 200 or 10  $\mu$ L for 6-well dishes or 96-well plates, respectively. Cells were

transfected using either 2.1 or 4.2  $\mu\text{M}$  of DOPY, as indicated, or 100 $\times$  of DOTAP (the molar ratio of PPRH/DOTAP was 1:100 (100 nM/10  $\mu\text{M}$ )). Then, 20 min after incubation at room temperature, the mixture was added to the cells to obtain a final volume of 1 mL or 100  $\mu\text{L}$  in 6-well dishes or 96-well plates, respectively. Cells were incubated with the PPRHs for up to 120 h at 37  $^{\circ}\text{C}$  in a humidified 5%  $\text{CO}_2$  incubator.

To determine the effects on cellular viability, CellTiter AQueous (MTS) reagent (Promega; Madison, WI, USA) was activated with 5% phenazine methosulfate (Sigma Aldrich), 200  $\mu\text{L}$  or 20  $\mu\text{L}$  of the activated reagent was added to the 6-well dishes or 96-well plates, respectively, and incubated for 2–4 h at 37  $^{\circ}\text{C}$  and 5%  $\text{CO}_2$ . Absorbance was measured at 490 nm on a SpectraMax i3x (Molecular Devices; San Jose, CA, USA). Background absorbance (media and all reagents) was subtracted from all experimental values and normalized to untreated controls. Non-linear regression was performed with GraphPad Prism software for the dose-response studies to determine  $\text{IC}_{50}$  values.

Live-cell images of AsPc-1 cells were captured every 8 h after transfection utilizing the CellCyte X Live imaging system (Cytena; Boston, MA, USA). The analysis software was trained to accurately determine the shape and volume of AsPc-1 cells, and the “mask” created was applied to determine percent confluency within each images’ surface area. Gompertzian growth was analyzed by GraphPad Prism and two-way ANOVAs with Tukey post hoc analyses. Cell viability and cell confluency/growth studies were all performed in triplicate.

Table 3. Design of MYC-targeting PPRHs with their target sequences in italics.

PPRH Name (Location)	Length	Sequence (5’-3’)
HpMYC-G4-PR-C (Promoter)	67	5’-GGGGTGGAAAGGGTGGGAGGGTGGGAGGGG-3’ 5’-GGGGTGGAAAGGGTGGGAGGGTGGGAGGGG-3’ 5’-CCCCACCTTCCCCACCTCCCCACCTCCCC-3’ 3’-GGGGTGGAAAGGGTGGGAGGGTGGGAGGGG-5’
HpMYC-PR-Distal-T (Promoter)	50	3’-AGGAGCAGCAGAGAAAGGGAGAGt 5’-AGGAGCAGCAGAGAAAGGGAGAGt 3’-TCCTCGTCGTCTCTTCCCTCTC-5’ 5’-AGGAGCAGCAGAGAAAGGGAGAG-3’
HpMYC-PR-Prox-T (Promoter)	50	3’-GGGAAAAGAACGGAGGGAGGGAt 5’-GGGAAAAGAACGGAGGGAGGGAt 3’-CCCTTTTCTTGCTCCCTCCCT-5’ 5’-GGGAAAAGAACGGAGGGAGGGGA-3’
HpMYC-I1-T (Intron 1)	72	3’-AAGATGGGAGAGGAGAAGGCAGAGGGAAAACGGGt 5’-AAGATGGGAGAGGAGAAGGCAGAGGGAAAACGGGt 3’-TTCTACCCTCTCTCTTCCGTCTCCCTTTTGGCC-5’ 5’-AAGATGGGAGAGGAGAAGGCAGAGGGAAAACGGG-3’
HpMYC-I1_short-T (Intron 1)	55	3’-GGGAGAGGAGAAGGCAGAGGGAAAAt 5’-GGGAGAGGAGAAGGCAGAGGGAAAAt 3’-CCCTCTCTCTTCCGTCTCCCTTTT-5’ 5’-GGGAGAGGAGAAGGCAGAGGGAAAA-3’
HpMYC-I2-C (Intron 2)	52	5’-GGGAGGGGCAAAACAGAGGTGGGG-3’ 5’-GGGAGGGGCAAAACAGAGGTGGGG-5’ 5’-CCCTCCCGTTTGTCTCCACCCC-3’ 3’-GGGGTGGGAGACAAACGGGGAGGG-5

4.8. Luciferase Assays

Human embryonic kidney cells (HEK-293), purchased from ATCC (Manassas, VA, USA), were cultured in 37  $^{\circ}\text{C}$  and 5%  $\text{CO}_2$  in Eagle’s Minimum Essential Medium (EMEM) (ATCC; Manassas, VA, USA), enriched with 10% fetal bovine serum (FBS) (Sigma Aldrich; St. Louis, MO, USA) and 1 $\times$  penicillin/streptomycin solution. The HEK-293 cells were transiently transfected with either the pGL4.17 promoterless luciferase plasmid (Promega;



Madison, WI, USA) or the MYC promoter region Del4 and the renilla luciferase pRL promoter (Promega). The c-myc promoter (Del 4) was a gift from Bert Vogelstein (Addgene plasmid # 16604; <http://n2t.net/addgene:16604>, accessed on 10 October 2022; RRID:Addgene\_16604). [48] HEK-293 cells were seeded in 24-well plates at  $8 \times 10^4$  cells per well and allowed to attach overnight. Cells were transfected with 250 ng of Del4 or EV plasmid and 100 ng of pRL either alone or with 1  $\mu$ g of PPRHs or vehicle control (DOTAP) for 48 h. Cells were lysed in Passive Lysis Buffer and then frozen to  $-20^\circ\text{C}$ , followed by two freeze and thaw cycles in order to improve cell lysis. Firefly and renilla luciferase expression was then measured with the Dual Luciferase Assay kit (Promega; Madison, WI, USA) using a Lumat LB9507 luminometer. Firefly luciferase was normalized to renilla expression and normalized again to untreated control. Luciferase experiments were performed minimally in triplicate; one-way ANOVAs with Tukey post hoc analyses were used to determine significance.

#### 4.9. RT-qPCR

To determine MYC mRNA levels, PC-3 and AsPc-1 cells (30,000 cells per well) were seeded in 6-well dishes and incubated overnight. The following day, cells were transfected with 25 nM of PPRHs. Total RNA was extracted from cells using TRIzol® (Life Technologies; Barcelona, Spain) or GeneJet RNA isolation kit (ThermoFisher; Waltham, MA, USA) following the manufacturer's specifications. RNA concentrations were determined by measuring their absorbance at 260 nm using a NanoDrop ND-1000 spectrophotometer (Thermo Fisher; Barcelona, Spain). Thus, 0.5–1  $\mu$ g of cDNA was reverse transcribed using either the qScript kit (Quanta Biosciences; Beverly, MA, USA) or with 125 ng of random hexamers (Roche; Spain), 500  $\mu$ M of each dNTP (Bioline; Barcelona, Spain), 20 units of RNase inhibitor, and 200 units of Moloney murine leukemia virus reverse transcriptase (last three from Lucigen; WI, USA) in the retrotranscriptase buffer. qPCR was run with 100–150 ng of cDNA using Taqman assays for MYC (Hs00153408\_m1) and either Adenine Phosphoribosyltransferase (*aprt*) (Hs00975725\_m1) or GAPDH (VIC-labeled for multiplexing, Hs02758991\_g1) (Applied Biosystems; Barcelona, Spain or Waltham, MA, USA). Relative expression of MYC was determined with the  $2^{-\Delta\Delta C_t}$  method. Biological experiments were performed in triplicate, and each qPCR reaction was run with technical duplicates.

#### 4.10. Western Blot Analyses

PC-3 cells (60,000 cells per well) were seeded in 6-well dishes and transfected with 25 and 100 nM of PPRHs. Total protein was extracted 72 h after transfection using RIPA buffer (1% Igepal, 0.5% sodium deoxycholate, 0.1% SDS, 150 mM NaCl, 1 mM EDTA, 1 mM PMSF, 10 mM NaF and 50 mM Tris-HCl, pH 8, and containing a Protease inhibitor cocktail (P8340-5ML); all reagents were purchased from Sigma Aldrich, Madrid, Spain, with the exception of Tris-HCl, which was from PanReac AppliChem, Barcelona, Spain). Cell debris was removed by centrifugation for 10 min at  $13,300 \times g$  and  $4^\circ\text{C}$ . Protein concentrations were determined by using a Bio-Rad protein assay based on the Bradford method using bovine serum albumin (BSA) as a standard (Sigma-Aldrich, Madrid, Spain).

Protein extracts were electrophoresed in 4%/12% SDS-polyacrylamide gels and transferred to polyvinylidene difluoride membranes (immobilon P, Milipore, Madrid, Spain) for 2 and 5 h and 400 mA using a semi-dry electroblotter. Blocking of membranes was performed using 5% Blotto. Membranes were probed with either an antibody against MYC conjugated with horseradish peroxidase (HRP) (1:1500 dilution; ab205818, Abcam, Cambridge, UK), a primary antibody against cyclin D1 (1:100 dilution; M-20, sc-718, Santa Cruz Biotechnology, Heidelberg, Germany), or a primary antibody against GAPDH (1:200 dilution; sc-47724, Santa Cruz Biotechnology, Heidelberg, Germany) overnight at  $4^\circ\text{C}$  with slow agitation. For the detection of cyclin D1 protein levels, a secondary horseradish peroxidase-conjugated anti-rabbit antibody was used (1:1200 dilution, P0399, Agilent Technologies, Singapore). GAPDH protein levels were used to normalize the results and a

secondary horseradish peroxidase-conjugated anti-mouse antibody was then used (1:1500 dilution, sc-516102, Santa Cruz Biotechnology, Heidelberg, Germany).

Signals of MYC, Cyclin D1, and GAPDH proteins were detected using enhanced chemiluminescence (ECL), as recommended by the manufacturer (Amersham, Arlington Heights, IL). To visualize the protein bands, we used ImageQuant LAS 4000 mini imager (GE Healthcare, Barcelona, Spain). Quantification was performed using the ImageQuant 10.1 software.

#### 4.11. Statistical Analyses

Statistical analyses were performed using GraphPad Prism 6 (GraphPad Software, CA, USA). All data are shown as the mean  $\pm$  SEM of at least three independent experiments. The levels of statistical significance were denoted as follows:  $p < 0.05$  (\*),  $p < 0.01$  (\*\*),  $p < 0.001$  (\*\*\*), or  $p < 0.0001$  (\*\*\*\*).

**Supplementary Materials:** The following supporting information can be downloaded at: <https://www.mdpi.com/article/10.3390/ijms24010378/s1>.

**Author Contributions:** Conceptualization, T.A.B., V.N., C.J.C.; methodology, A.M.P., S.V., T.A.B.; formal analysis, C.J.C., T.A.B.; investigation A.M.P., S.V., T.A.B.; writing—original draft preparation, A.M.P., S.V., C.J.C., T.A.B.; writing—review and editing, C.J.C., V.N., T.A.B.; funding acquisition, V.N. and T.A.B. All authors have read and agreed to the published version of the manuscript.

**Funding:** This research was funded by Plan Nacional de Investigación Científica (Spain), grant number RTI2018-093901-B-I00 and by start-up funding from Binghamton University.

**Institutional Review Board Statement:** Not applicable.

**Informed Consent Statement:** Not applicable.

**Data Availability Statement:** Not applicable.

**Conflicts of Interest:** The authors declare no conflict of interest.

## References

- Shen, L.; O'Shea, J.M.; Kaadige, M.R.; Cunha, S.; Wilde, B.R.; Cohen, A.L.; Welm, A.L.; Ayer, D.E. Metabolic reprogramming in triple-negative breast cancer through Myc suppression of TXNIP. *Proc. Natl. Acad. Sci. USA* **2015**, *112*, 5425–5430. [\[CrossRef\]](#) [\[PubMed\]](#)
- Dang, C.V.; O'Donnell, K.A.; Zeller, K.I.; Nguyen, T.; Osthus, R.C.; Li, F. The c-Myc target gene network. *Semin. Cancer Biol.* **2006**, *16*, 253–264. [\[CrossRef\]](#) [\[PubMed\]](#)
- Nair, S.K.; Burley, S.K. X-ray Structures of Myc-Max and Mad-Max Recognizing DNA: Molecular Bases of Regulation by Proto-Oncogenic Transcription Factors. *Cell* **2003**, *112*, 193–205. [\[CrossRef\]](#)
- Nanbru, C.; Lafon, I.; Audigier, S.; Gensac, M.-C.; Vagner, S.; Huez, G.; Prats, A.-C. Alternative Translation of the Proto-oncogene c-myc by an Internal Ribosome Entry Site. *J. Biol. Chem.* **1997**, *272*, 32061–32066. [\[CrossRef\]](#)
- Ro-Choi, T.S.; Choi, Y.C. The Analysis of Structure of c-Myc Gene Transcript. *J. Mol. Genet.* **2019**, *2*, 1–7.
- Levens, D. How the c-myc Promoter Works and Why It Sometimes Does Not. *J. Natl. Cancer Inst. Monogr.* **2008**, *2008*, 41–43. [\[CrossRef\]](#) [\[PubMed\]](#)
- Herrick, D.J.; Ross, J. The half-life of c-myc mRNA in growing and serum-stimulated cells: Influence of the coding and 3' untranslated regions and role of ribosome translocation. *Mol. Cell. Biol.* **1994**, *14*, 2119–2128. [\[CrossRef\]](#) [\[PubMed\]](#)
- Schleger, C.; Verbeke, C.; Hildenbrand, R.; Zentgraf, H.; Bleyl, U. c-MYC Activation in Primary and Metastatic Ductal Adenocarcinoma of the Pancreas: Incidence, Mechanisms, and Clinical Significance. *Mod. Pathol.* **2002**, *15*, 462–469. [\[CrossRef\]](#)
- Madden, S.K.; de Araujo, A.D.; Gerhardt, M.; Fairlie, D.P.; Mason, J.M. Taking the Myc out of cancer: Toward therapeutic strategies to directly inhibit c-Myc. *Mol. Cancer* **2021**, *20*, 1–18. [\[CrossRef\]](#)
- Han, G.; Wang, Y.; Bi, W. c-Myc Overexpression Promotes Osteosarcoma Cell Invasion Via Activation of MEK-ERK Pathway. *Oncol. Res. Featur. Preclin. Clin. Cancer Ther.* **2012**, *20*, 149–156. [\[CrossRef\]](#)
- Ala, M. Target c-Myc to treat pancreatic cancer. *Cancer Biol. Ther.* **2022**, *23*, 34–50. [\[CrossRef\]](#) [\[PubMed\]](#)
- Qiu, X.; Boufaied, N.; Hallal, T.; Feit, A.; de Polo, A.; Luoma, A.M.; Alahmadi, W.; Larocque, J.; Zadra, G.; Xie, Y.; et al. MYC drives aggressive prostate cancer by disrupting transcriptional pause release at androgen receptor targets. *Nat. Commun.* **2022**, *13*, 1–17. [\[CrossRef\]](#)



13. Mossafa, H.; Damotte, D.; Jenabian, A.; Delarue, R.; Vincenneau, A.; Amouroux, I.; Jeandel, R.; Khoury, E.; Martelli, J.M.; Samson, T.; et al. Non-Hodgkin's lymphomas with Burkitt-like cells are associated with c-Myc amplification and poor prognosis. *Leuk. Lymphoma* **2006**, *47*, 1885–1893. [\[CrossRef\]](#) [\[PubMed\]](#)
14. Vita, M.; Henriksson, M. The Myc oncoprotein as a therapeutic target for human cancer. *Semin. Cancer Biol.* **2006**, *16*, 318–330. [\[CrossRef\]](#) [\[PubMed\]](#)
15. Bochman, M.L.; Paeschke, K.; Zakian, V.A. DNA secondary structures: Stability and function of G-quadruplex structures. *Nat. Rev. Genet.* **2012**, *13*, 770–780. [\[CrossRef\]](#) [\[PubMed\]](#)
16. Cahoon, L.A.; Seifert, H.S. An Alternative DNA Structure Is Necessary for Pilin Antigenic Variation in *Neisseria gonorrhoeae*. *Science* **2009**, *325*, 764–767. [\[CrossRef\]](#) [\[PubMed\]](#)
17. Paeschke, K.; Juranek, S.; Simonsson, T.; Hempel, A.; Rhodes, D.; Lipps, H.J. Telomerase recruitment by the telomere end binding protein- $\beta$  facilitates G-quadruplex DNA unfolding in ciliates. *Nat. Struct. Mol. Biol.* **2008**, *15*, 598–604. [\[CrossRef\]](#)
18. Postberg, J.; Tsytlonok, M.; Sparvoli, D.; Rhodes, D.; Lipps, H.J. A telomerase-associated RecQ protein-like helicase resolves telomeric G-quadruplex structures during replication. *Gene* **2012**, *497*, 147–154. [\[CrossRef\]](#)
19. Beaudoin, J.-D.; Perreault, J.-P. Exploring mRNA 3'-UTR G-quadruplexes: Evidence of roles in both alternative polyadenylation and mRNA shortening. *Nucleic Acids Res.* **2013**, *41*, 5898–5911. [\[CrossRef\]](#)
20. Huppert, J.L. Four-stranded nucleic acids: Structure, function and targeting of G-quadruplexes. *Chem. Soc. Rev.* **2008**, *37*, 1375–1384. [\[CrossRef\]](#)
21. Balasubramanian, S.; Hurley, L.H.; Neidle, S. Targeting G-quadruplexes in gene promoters: A novel anticancer strategy? *Nat. Rev. Drug Discov.* **2011**, *10*, 261–275. [\[CrossRef\]](#) [\[PubMed\]](#)
22. Simonsson, T.; Pribylovab, M.; Vorlickova, M. A Nuclease Hypersensitive Element in the Human c-myc Promoter Adopts Several Distinct i-Tetraplex Structures. *Biochem. Biophys. Res. Commun.* **2000**, *278*, 158–166. [\[CrossRef\]](#) [\[PubMed\]](#)
23. Brooks, T.A.; Hurley, L.H. Targeting MYC Expression through G-Quadruplexes. *Genes Cancer* **2010**, *1*, 641–649. [\[CrossRef\]](#)
24. Simonsson, T.; Kubista, M.; Pečinka, P. DNA tetraplex formation in the control region of c-myc. *Nucleic Acids Res.* **1998**, *26*, 1167–1172. [\[CrossRef\]](#)
25. Zyner, K.G.; Mulhearn, D.S.; Adhikari, S.; Cuesta, S.M.; Di Antonio, M.; Erard, N.; Hannon, G.J.; Tannahill, D.; Balasubramanian, S. Genetic interactions of G-quadruplexes in humans. *eLife* **2019**, *8*, e46793. [\[CrossRef\]](#) [\[PubMed\]](#)
26. Wong, K.K.L.; Liao, J.Z.; Verheyen, E.M. A positive feedback loop between Myc and aerobic glycolysis sustains tumor growth in a *Drosophila* tumor model. *eLife* **2019**, *8*, e46315. [\[CrossRef\]](#) [\[PubMed\]](#)
27. Aubets, E.; Chillon, M.; Ciudad, C.J.; Noé, V. PolyPurine Reverse Hoogsteen Hairpins Work as RNA Species for Gene Silencing. *Int. J. Mol. Sci.* **2021**, *22*, 10025. [\[CrossRef\]](#)
28. Aviñó, A.; Cuestas-Ayllón, C.; Gutiérrez-Capitán, M.; Vilaplana, L.; Grazu, V.; Noé, V.; Balada, E.; Baldi, A.; Félix, A.J.; Aubets, E.; et al. Detection of SARS-CoV-2 Virus by Triplex Enhanced Nucleic Acid Detection Assay (TENADA). *Int. J. Mol. Sci.* **2022**, *23*, 15258. [\[CrossRef\]](#)
29. Coma, S.; Noe, V.; Eritja, R.; Ciudad, C. Strand Displacement of Double-Stranded DNA by Triplex-Forming Antiparallel Purine-Hairpins. *Oligonucleotides* **2005**, *15*, 269–283. [\[CrossRef\]](#)
30. de Almagro, M.C.; Coma, S.; Noé, V.; Ciudad, C.J. Polypurine Hairpins Directed against the Template Strand of DNA Knock Down the Expression of Mammalian Genes. *J. Biol. Chem.* **2009**, *284*, 11579–11589. [\[CrossRef\]](#)
31. de Almagro, M.C.; Mencia, N.; Noé, V.; Ciudad, C.J. Coding Polypurine Hairpins Cause Target-Induced Cell Death in Breast Cancer Cells. *Hum. Gene Ther.* **2011**, *22*, 451–463. [\[CrossRef\]](#) [\[PubMed\]](#)
32. Bener, G.; Félix, A.J.; Sánchez de Diego, C.; Fabregat, I.P.; Ciudad, C.J.; Noé, V. Silencing of CD47 and SIRP $\alpha$  by Polypurine reverse Hoogsteen hairpins to promote MCF-7 breast cancer cells death by PMA-differentiated THP-1 cells. *BMC Immunol.* **2016**, *17*, 1–12. [\[CrossRef\]](#) [\[PubMed\]](#)
33. Ciudad, C.J.; Enriquez, M.M.M.; Félix, A.J.; Bener, G.; Noé, V. Silencing PD-1 and PD-L1: The potential of PolyPurine Reverse Hoogsteen hairpins for the elimination of tumor cells. *Immunotherapy* **2019**, *11*, 369–372. [\[CrossRef\]](#) [\[PubMed\]](#)
34. Huertas, C.S.; Aviñó, A.; Kurachi, C.; Piqué, A.; Sandoval, J.; Eritja, R.; Esteller, M.; Lechuga, L.M. Label-free DNA-methylation detection by direct ds-DNA fragment screening using poly-purine hairpins. *Biosens. Bioelectron.* **2018**, *120*, 47–54. [\[CrossRef\]](#)
35. Noé, V.; Aubets, E.; Félix, A.J.; Ciudad, C.J. Nucleic acids therapeutics using PolyPurine Reverse Hoogsteen hairpins. *Biochem. Pharmacol.* **2020**, *189*, 114371. [\[CrossRef\]](#)
36. Solé, A.; Ciudad, C.J.; Chasin, L.A.; Noé, V. Correction of point mutations at the endogenous locus of the dihydrofolate reductase gene using repair-PolyPurine Reverse Hoogsteen hairpins in mammalian cells. *Biochem. Pharmacol.* **2016**, *110–111*, 16–24. [\[CrossRef\]](#)
37. Félix, A.J.; Ciudad, C.J.; Noé, V. Correction of the aprt Gene Using Repair-Polypurine Reverse Hoogsteen Hairpins in Mammalian Cells. *Mol. Ther. -Nucleic Acids* **2019**, *19*, 683–695. [\[CrossRef\]](#)
38. Aubets, E.; Noé, V.; Ciudad, C.J. Targeting replication stress response using polypurine reverse hoogsteen hairpins directed against WEE1 and CHK1 genes in human cancer cells. *Biochem. Pharmacol.* **2020**, *175*, 113911. [\[CrossRef\]](#)
39. Villalobos, X.; Rodríguez, L.; Solé, A.; Lliberós, C.; Mencia, N.; Ciudad, C.; Noe, V. Effect of Polypurine Reverse Hoogsteen Hairpins on Relevant Cancer Target Genes in Different Human Cell Lines. *Nucleic Acid Ther.* **2015**, *25*, 198–208. [\[CrossRef\]](#)

40. Aubets, E.; Félix, A.J.; Garavis, M.; Reyes, L.; Aviñó, A.; Eritja, R.; Ciudad, C.J.; Noé, V. Detection of a G-Quadruplex as a Regulatory Element in *Thymidylate Synthase* for Gene Silencing Using Polypurine Reverse Hoogsteen Hairpins. *Int. J. Mol. Sci.* **2020**, *21*, 5028. [\[CrossRef\]](#)
41. Psaras, A.M.; Valiuska, S.; Noé, V.; Ciudad, C.J.; Brooks, T.A. Targeting KRAS Regulation with PolyPurine Reverse Hoogsteen Oligonucleotides. *Int. J. Mol. Sci.* **2022**, *23*, 2097. [\[CrossRef\]](#) [\[PubMed\]](#)
42. Brooks, T.A.; Hurley, L.H. The role of supercoiling in transcriptional control of MYC and its importance in molecular therapeutics. *Nat. Rev. Cancer* **2009**, *9*, 849–861. [\[CrossRef\]](#) [\[PubMed\]](#)
43. Aubets, E.; Grier, R.; Felix, A.J.; Rigol, G.; Sikorski, C.; Limón, D.; Mastrorosa, C.; Busquets, M.A.; Pérez-García, L.; Noé, V.; et al. Synthesis and validation of DOPY: A new gemini dioleilylbispyridinium based amphiphile for nucleic acid transfection. *Eur. J. Pharm. Biopharm.* **2021**, *165*, 279–292. [\[CrossRef\]](#)
44. Wang, C.; Zhang, J.; Yin, J.; Gan, Y.; Xu, S.; Gu, Y.; Huang, W. Alternative approaches to target Myc for cancer treatment. *Signal Transduct. Target. Ther.* **2021**, *6*, 1–14. [\[CrossRef\]](#)
45. Chen, H.; Liu, H.; Qing, G. Targeting oncogenic Myc as a strategy for cancer treatment. *Signal Transduct. Target. Ther.* **2018**, *3*, 5. [\[CrossRef\]](#) [\[PubMed\]](#)
46. Villalobos, X.; Rodríguez, L.; Prévot, J.; Oleaga, C.; Ciudad, C.; Noé, V. Stability and Immunogenicity Properties of the Gene-Silencing Polypurine Reverse Hoogsteen Hairpins. *Mol. Pharm.* **2013**, *11*, 254–264. [\[CrossRef\]](#)
47. Dumas, L.; Herviou, P.; Dassi, E.; Cammas, A.; Millevoi, S. G-Quadruplexes in RNA Biology: Recent Advances and Future Directions. *Trends Biochem. Sci.* **2020**, *46*, 270–283. [\[CrossRef\]](#)
48. He, T.-C.; Sparks, A.B.; Rago, C.; Hermeking, H.; Zawel, L.; da Costa, L.T.; Morin, P.J.; Vogelstein, B.; Kinzler, K.W. Identification of c-MYC as a Target of the APC Pathway. *Science* **1998**, *281*, 1509–1512. [\[CrossRef\]](#)
49. Brown, R.V.; Danford, F.L.; Gokhale, V.; Hurley, L.H.; Brooks, T.A. Demonstration that Drug-targeted Down-regulation of MYC in Non-Hodgkins Lymphoma Is Directly Mediated through the Promoter G-quadruplex. *J. Biol. Chem.* **2011**, *286*, 41018–41027. [\[CrossRef\]](#)
50. Morales-Martinez, M.; Valencia, A.; Vega, G.; Neri, N.; Nambo, M.J.; Alvarado, I.; Cuadra, I.; Duran-Padilla, M.A.; Martínez-Maza, O.; Huerta-Yepez, S.; et al. Regulation of Krüppel-Like Factor 4 (KLF4) expression through the transcription factor Yin-Yang 1 (YY1) in non-Hodgkin B-cell lymphoma. *Oncotarget* **2019**, *10*, 2173–2188. [\[CrossRef\]](#)
51. Guo, P.; Dong, X.-Y.; Zhao, K.; Sun, X.; Li, Q.; Dong, J.-T. Opposing Effects of KLF5 on the Transcription of MYC in Epithelial Proliferation in the Context of Transforming Growth Factor  $\beta$ . *J. Biol. Chem.* **2009**, *284*, 28243–28252. [\[CrossRef\]](#) [\[PubMed\]](#)
52. Tsai, L.-H.; Wu, J.-Y.; Cheng, Y.-W.; Chen, C.-Y.; Sheu, G.-T.; Wu, T.-C.; Lee, H. The MZF1/c-MYC axis mediates lung adenocarcinoma progression caused by wild-type lkb1 loss. *Oncogene* **2015**, *34*, 1641–1649. [\[CrossRef\]](#) [\[PubMed\]](#)
53. Castro-Mondragon, J.A.; Riudavets-Puig, R.; Rauluseviciute, I.; Lemma, R.B.; Turchi, L.; Blanc-Mathieu, R.; Lucas, J.; Boddie, P.; Khan, A.; Pérez, N.M.; et al. JASPAR 2022: The 9th release of the open-access database of transcription factor binding profiles. *Nucleic Acids Res.* **2021**, *50*, D165–D173. [\[CrossRef\]](#) [\[PubMed\]](#)
54. Aviñó, A.; Eritja, R.; Ciudad, C.J.; Noé, V. Parallel Clamps and Polypurine Hairpins (PPRH) for Gene Silencing and Triplex-Affinity Capture: Design, Synthesis, and Use. *Curr. Protoc. Nucleic Acid Chem.* **2019**, *77*, e78. [\[CrossRef\]](#)

**Disclaimer/Publisher's Note:** The statements, opinions and data contained in all publications are solely those of the individual author(s) and contributor(s) and not of MDPI and/or the editor(s). MDPI and/or the editor(s) disclaim responsibility for any injury to people or property resulting from any ideas, methods, instructions or products referred to in the content.

Supplementary

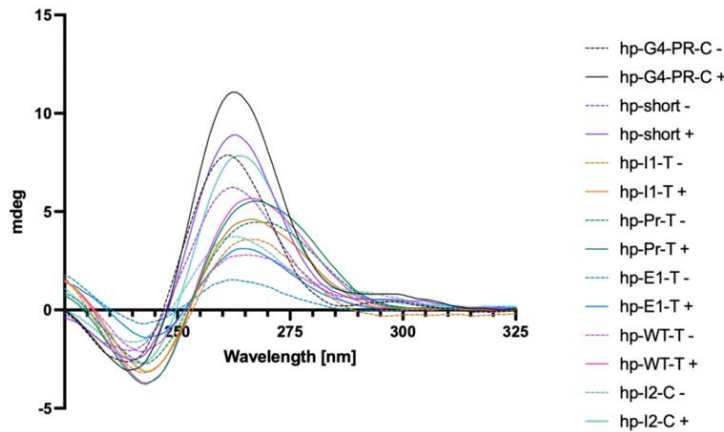


**Figure S1.** G4 and hairpin formation within the PPRH sequences. ECD was used to establish the non-canonical DNA formations, if any, formed from the PPRHs in the absence (-, dashed lines) or presence (+, solid lines) of 100 mM KCl. Parallel G4 formation is identified by a maximal Cotton effect in the 262-264 nm range, as identified with the hp-G4-PR-C and Hp-I2-C sequences, while hairpin formation was identified in all other PPRH sequences by a maximal (and broad) Cotton effect at 270 nM.

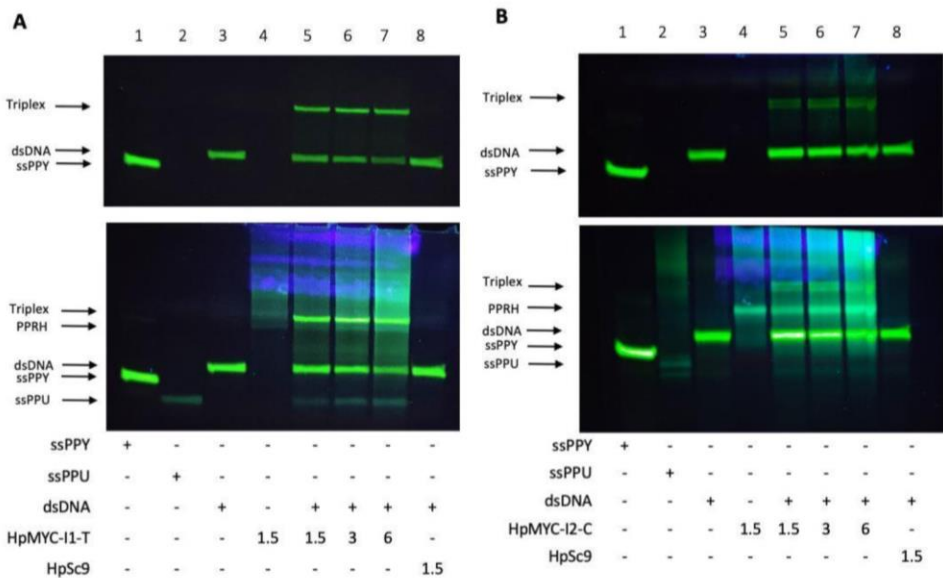


**Figure S2.** Displacement analyses of the Polypurine (ssPPU) strand in intron 1 (A) and Intron 2 (B) probes. (A) Displacement analysis of the Polypurine (PPU) strand in Intron 1 probe. (B) Displacement analysis of the Polypurine (PPU) strand in Intron 2 probe. Bindings were performed using 1.5 µg of dsDNA labeled with FAM (green) in the polypyrimidine (PPY) strand only, then incubated as described in M&M with increased amounts of their PPRH, HpMYC-I1-T, or HpMYC-I2-C.





#### 4.4. ARTICLE III (Manuscript in preparation)

##### Combinatorial effect of KRAS and MYC targeting Polypurine Reverse Hoogsteen hairpins in PC-3 cancer cell lines

**Background:** *MYC* and *KRAS* cancer targets have a tight relationship since *MYC* protein is a downstream effector of *KRAS* and in the presence of mutated *KRAS*, it will be constitutively expressed and stabilized (Kerkhoff et al., 1998; T. Lee et al., 2008), making cells susceptible to DNA damage and apoptosis (Shortt & Johnstone, 2012). It is also suggested that *MYC* plays a crucial role in *KRAS*-driven malignancies (Eilers & Eisenman, 2008). Both oncogenes fall into the category of undruggable cancer targets and the interconnection between *KRAS* and *MYC* present significant challenges in the development of targeted therapies (McCormick, 2015; Whitfield et al., 2017). Disrupting one target without affecting the other can lead to compensatory mechanisms, limiting treatment efficacy and may carry risk of incomplete eradication of cancer. Targeting both *KRAS* and *MYC* has gained attention as potential solutions for cancer treatment. Such therapies may hold the key to achieving durable treatment responses and overcome resistance (Donati & Amati, 2022). In this study, we targeted *KRAS* and *MYC* at the same time in PC-3 prostate cancer cells using previously designed PPRHs against both oncogenes.

**Objectives:** We aimed to study the combinatorial effects of PPRHs against *KRAS* and *MYC*. First, we wanted to select the most efficient PPRHs against both oncogenes. Then we proceeded to analyze several combinations, at the lowest concentrations possible, to test their effects on cell viability and expression of both oncogenes in *KRAS* and *MYC* mutated PC-3 prostate cancer cells.

**Results:** We performed a dose response analysis of previously designed PPRHs against *KRAS* and *MYC* in PC-3 prostate cancer cells. We selected the most efficient PPRHs targeting each gene, HpMYC-PR-G4-C (G4-C), HpMYC-I1-T (I1-T) which are *MYC*-targeting PPRHs and HpKRAS-PR-C (PR-C) and PPRH 2 which target *KRAS* regions. We evaluated the four possible combinations of each *MYC* PPRH (25 nM)

with KRAS PPRHs (25 nM), at a final concentration of 50 nM, and compared them to the treatment with each individual PPRH at 50 nM.

Most PPRH combinations showed a synergic effect on PC-3 cell viability, with a greater cytotoxicity than individual treatments of the PPRHs at 50 nM. Combinations with MYC PPRH G4-C showed to be the most efficient in inducing PC-3 cells death.

We performed time-course experiments with the same individual and combination conditions to monitor KRAS and MYC mRNA expression changes over time. We observed an early increase in mRNA levels and a maximum decrease five days post-treatment.

Lastly, we explored the effect of the PPRHs in the protein levels of both oncogenes at 120 hours after transfection, corresponding to the lowest point of transcription. We observed a similar tendency as in cell viability, where the combinations, especially with G4-C, had the highest impact in reducing both oncogenes protein levels. MYC protein levels showed a more sensitive outcome upon PPRH transfection.

**Conclusions:** This study shows an insight of the effect of PPRH combinations for *in vitro* simultaneous targeting of two oncogenes, *KRAS* and *MYC*, using as a model the PC-3 prostate cancer cell line. The synergy produced by these PPRHs demonstrates their potential to downregulate both oncogenes by using PPRH combinations at low concentrations.



## Article

# Combinatorial effect of Polypurine Reverse Hoogsteen hairpins against *KRAS* and *MYC* targeting in PC-3 cell line

Simonas Valiuska <sup>1,2</sup>, Véronique Noé <sup>1,2</sup> and Carlos J. Ciudad <sup>1,2\*</sup>

<sup>1</sup> Department of Biochemistry and Physiology, School of Pharmacy and Food Sciences, University of Barcelona (UB), 08028 Barcelona, Spain

<sup>2</sup> Instituto de Nanociencia y Nanotecnología (IN2UB), University of Barcelona (UB), 08028 Barcelona, Spain

\* Correspondence: [cciudad@ub.edu](mailto:cciudad@ub.edu) (C.J.C.); Tel.: +34-93-403-4455 (C.J.C.)

**Abstract:** *KRAS* and *MYC* are proto-oncogenes strictly regulated in healthy cells since they have key roles in several processes such as cell growth, proliferation, differentiation, or apoptosis. These genes are tightly interconnected, and their dysregulation can lead to cancer progression. We had previously individually targeted these oncogenes using Polypurine Revers Hoogsteen (PPRH) hairpins, many of them targeting the complementary strand of G-quadruplex forming sequences. We validated them *in vitro* in different cancer cell lines with deregulated *KRAS* and/or *MYC*. In this work we focused on understanding the cooperative dynamics between these oncogenes, by investigating the combined impact of PPRHs targeting *KRAS* and *MYC* in the PC-3 prostate cancer cell line. The used combinations had a modulatory impact in both oncogene expression, downregulating their mRNA and protein levels five days post-treatment. Out of the four tested PPRHs, *MYC*-targeting PPRHs, and especially HpMYC-G4-PR-C, showed a higher effect especially at the protein level. When both *KRAS*- and *MYC*-targeting PPRHs were applied in combination, a synergistic reduction in cell viability was observed. The simultaneous targeting of *KRAS* and *MYC*, demonstrates efficacy in gene modulation, thus in decreasing cell proliferation and viability.

**Keywords:** *KRAS*; *MYC*; PPRH; G-quadruplex; Prostate cancer

## 1. Introduction

The human gene Kirsten rat sarcoma viral oncogene homolog (*KRAS*) encodes a membrane-bound regulatory protein belonging to the RAS family of GTPases. When *KRAS* is activated, it governs downstream cellular pathways responsible for regulating cell survival, proliferation, and differentiation [1,2]. Mutations in *KRAS* disrupt its normal function, resulting in the continuous activation of the protein, which is linked to an increased tumorigenicity, and it is associated with unfavorable prognosis [3]. In the context of aggressive diseases, *KRAS* is overexpressed in about 30% of all human cancers including 95% of pancreatic cancers and 45% of colorectal cancers, pancreatic ductal adenocarcinomas (PDAC) and non-small-cell lung cancers (NSCLC) [4]. In 2013, the National Center Institute (NCI) established “The RAS initiative” to mobilize the community involved in the research of cancers driven by RAS gene family (*KRAS*, *HRAS* and *NRAS*) [5]. Several drug discovery efforts are presently underway, with a focus on targeting distinct mutant *KRAS* isoforms. Sotorasib, targeting the *KRAS*<sup>G12C</sup> mutant protein, obtained the FDA approval for the treatment of lung cancer in May 2021 [6]. While this development holds promise for cancers bearing *KRAS* alterations, it is important to note that the G12C mutation is not the only common mutation, and it does not provide advantages for patients with amplified or other *KRAS* variants. The most prevalent mutated alleles in patients with pancreatic and colorectal cancers are *KRAS*<sup>G12D</sup> and *KRAS*<sup>G12V</sup> [7–9]. Therefore, the approach of developing treatments adapted to specific *KRAS* mutations requires the creation of a diverse array of drugs. Inhibiting transcription in cancers with aberrant *KRAS* expression, has proven to be detrimental to tumor cells,

**Citation:** To be added by editorial staff during production.

Academic Editor: Firstname  
Lastname

Received: date  
Revised: date  
Accepted: date  
Published: date



**Copyright:** © 2023 by the authors. Submitted for possible open access publication under the terms and conditions of the Creative Commons Attribution (CC BY) license (<https://creativecommons.org/licenses/by/4.0/>).

revealing their dependency on *KRAS*, independently of its mutational status and provides a wide scope for therapeutic intervention [10–12].

*c-MYC*, here referred as *MYC*, is a member of a large family of DNA-binding proteins with a basic helix-loop-helix-loop-helix (bHLHLZ) leucine zipper motif, which also includes L-MYC and N-MYC [13–14]. *MYC* operates as a transcription factor, participating in multiple signal transduction pathways that trigger cell growth and various cellular processes such as metabolism, differentiation, and apoptosis. Non-cancer cells have *MYC* tightly regulated and quiescent cells have minimal or hardly detectable levels of *MYC*, that increase in response to signals related to growth and development [15]. Significantly, *MYC* regulates the expression of more than 30% of human genes [16–18]. Its protein is intrinsically fragile, characterized by general instability and a short half-life, making it susceptible to rapid degradation through the ubiquitin-linked proteasome system. This degradation mechanism serves as a safeguard against excessive *MYC* activity [19]. However, when any of these regulatory mechanisms malfunction, it can result in the presence of abnormal *MYC* mRNA and/or protein, which can lead to the development of malignancies. Alterations in *MYC* regulation can also be due to factors such as chromosomal translocations, viral insertions, gene amplification, deletions, insertions and mutations in cis-elements [20]. Deregulated *MYC* expression acts as a driver of both tumor initiation and maintenance and it is linked to all the defining hallmarks of cancer [21]. *MYC* is recognized as one of the most frequently amplified oncogenes [22]. About 70% of human cancers, including breast, bone, brain, B-cell lymphoma, colon, cervix, lung, pancreas, and prostate tumors have various *MYC* alterations that correlate with poor prognosis and increased disease aggressiveness [23–24]. Experimental models demonstrating *MYC*-associated tumorigenesis suggest that established tumors develop *MYC* dependence or addiction [17].

Both *KRAS* and *MYC* have been categorized as undruggable cancer targets. This may be attributed to their extensive protein-protein interactions, lack of clearly defined or appropriate binding sites, or their intracellular or nuclear localization [25,26]. *MYC* expression is downstream of *KRAS* signaling. Consequently, the presence of oncogenic *KRAS* mutations results in sustained *MYC* expression [27,28]. *KRAS*-initiated pro-proliferative signals are potentiated by *MYC*, facilitating rapid cell cycle progression and resistance to apoptosis. This collaboration often leads to the development of more aggressive and therapy-resistant cancers. In some cancer cells with mutated *KRAS* it was found that its suppression causes polyubiquitination and proteasomal degradation of *MYC* protein [29].

Guanine-rich sequences can adopt unique secondary structures known as G-quadruplexes (G4s). These structures consist of four strands and are characterized by a non-canonical arrangement in which the guanine bases are stacked in a planar pattern, held together by Hoogsteen hydrogen bonds, resulting in the formation of a G4 structure [30,31]. They are highly present in the promoter of human genes, modulating their expression through transcription factor binding and interaction with other entities [32,33]. Currently, there are more than 370,000 predicted G4 sequences, typically found in regions such as transcriptional start sites (TSS), telomeres, and sites associated with mitotic and meiotic double-strand breaks [32,34]. G4 structures can also act as barriers to block DNA replication [35] and they can interact with proteins implicated in DNA repair processes [34]. Many oncogene promoters, including *KRAS* and *MYC*, have a greater number of G4 motifs than promoters of regulatory or tumor suppressor genes. Several studies indicated that alterations in G4 sequences are associated with decreased gene expression [36–38].

In this study, we used previously designed Polypurine Reverse Hoogsteen (PPRHs) hairpins against *KRAS* and *MYC*, either individually or as combined treatments to decrease the expression of both oncogenes and provoke cell death in a *KRAS* and *MYC*

dependent prostate cancer cell line (PC-3). PPRHs are unmodified single-stranded DNA molecules made of two polypurine strands connected by a loop of four thymidines in antiparallel orientation. These strands interact intramolecularly with each other via Hoogsteen bonds. PPRHs are designed to bind specifically to a polypyrimidine DNA or RNA sequence by Watson-Crick base pairing, while conserving their hairpin structure. Consequently, PPRH binding results in the formation of a DNA triplex structure that induces the displacement of the polypurine chain in the genomic DNA, leading to the suppression of expression of the target gene [39–41]. PPRHs do not need to be designed as a pure homopurine since they can include up to three pyrimidine interruptions. This flexibility allows the design of PPRHs targeting practically any gene in the genome [42]. PPRHs are classified as coding (-C) or template (-T), depending on the strand that they are targeting. Coding PPRHs can interact with DNA and mRNA of the target gene. This interaction can influence splicing or translation processes [40,43]. We have previously used PPRHs to target genes related to cancer such as *mTOR*, *BCL-2*, *MDM2*, *TOP1*, *MYC* [44], and *HER-2* [45]. We have also designed efficient PPRHs targeting complementary sequences of G4FS in *TYMS* [46], *KRAS* [47] and *MYC* [48] demonstrating PPRH efficacy in reducing cell viability and gene expression.

## 2. Results

### 2.1. PPRH Selection and Individual and Combinatorial effect of PPRHs in PC-3 cell viability.

We performed a dose-response study using previously designed PPRHs against *KRAS* and *MYC* in the sensitive prostate cancer PC-3 cells (Figure 1) [47,48]. Cells were transfected with a mixture of 10  $\mu$ M DOTAP and a range of concentrations between 12.5 and 100 nM of PPRHs targeting *KRAS* and *MYC* determining the effects 120 h after transfection. The *MYC* PPRHs assayed were HpMYC-PR-G4-C (G4-C), HpMYC-I1-T (I1-T), HpMYC-I2-C, HpMYC-PR-Prox-T, and HpMYC-PR-Dist-T. We tested the promoter *KRAS* targeting PPRHs HpKRAS-PR-C (PR-C), HpKRAS-PR-EF-C (PPRH 1) and HpKRAS-PR-BC-C (PPRH 2). As a negative control we used a scrambled PPRH, Hp-Sc9 (SC9). From the dose-response results (data not shown), we selected two of the most efficient PPRHs for each gene, G4-C and I1-T for *MYC*-targeting PPRHs and PR-C and PPRH 2 for *KRAS*-targeting PPRHs. We chose a combination dose of 25 nM and 50 nM since at these concentrations, the individual treatments were not too lethal for PC-3 cells. We performed individual PPRH transfections at 50 nM and combinations of each of the most efficient *MYC*-targeting PPRH with *KRAS*-targeting PPRHs at 25 nM each, with a final concentration of 50 nM (Figure 2). The PPRH effects in PC-3 cell viability were compared to those obtained after incubating with DOTAP only. SC9 did not produce any significant effect in cell viability neither at 25 nor 50 nM. While all the individual PPRH treatments reduced cell viability in a dose-dependent manner, the combinations showed greater effect in reducing cell viability (Figure 2). The calculated Combination Index (CI) showed synergisms for all combinations at 25 nM, excepting for the combinations for I1-T and PR-C that demonstrated to have a slight synergism (Table 1). Among the four PPRHs, G4-C had the most significant impact on cell viability when used in both individual and combined treatments. Individual treatments with G4-C at 25 and 50 nM reduced cell viability by 61 and 85 %, respectively, and combinations with PR-C and PPRH 2, reduced it by 95 and 91 % respectively (Figure 2).

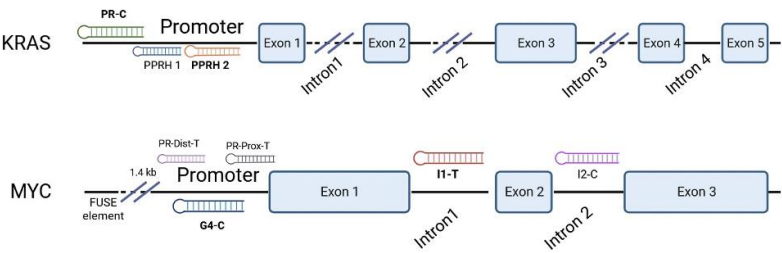


**Figure 1.** Schematic representation of *KRAS* and *MYC* gene structures and the location of targeting PPRHs. The selected PPRHs, PR-C, PPRH 2, G4-C and I1-T, for individual and combinatorial treatments are marked in bold.

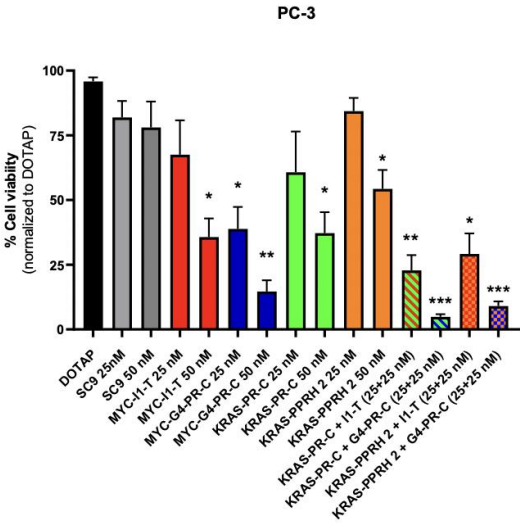


**Figure 2.** Effect on PC-3 prostate cancer cells viability of MYC (I1-T and G4-C) and *KRAS*-targeting (PR-C and PPRH 2) PPRHs. Experiments were performed three times with internal duplicates. Statistical significance was determined using a one-way ANOVA with Dunnett's multiple comparison test comparing groups against DOTAP (\*  $p < 0.05$ , \*\*  $p < 0.01$ , \*\*\*  $p < 0.001$ ).

Dose MYC PPRHs (nM)		Dose KRAS PPRHs (nM)		CI Media	Description
I1-T	G4-C	PR-C	PPRH 2		
25	-	25	-	0.88	Slight synergism
25	-	-	25	0.65	Synergism
-	25	25	-	0.57	Synergism
-	25	-	25	0.41	Synergism

**Table 1.** Analysis of synergy for the combinations of PPRHs in PC-3 cells.

## 2.2. Individual and combinatorial effects of PPRHs on KRAS and MYC mRNA levels in PC-3 cells.

To evaluate the effect of PPRHs in KRAS and MYC mRNA levels, we kept fixed a final concentration of 50 nM, transfecting the PPRHs either alone or in combinations of 25 nM each, and we performed time-course experiments between 24 and 120 h (Figure 3A and Figure 4A). We compared the effects relative to SC9 at 50 nM and observed similar mRNA modulation for both oncogenes. Both MYC and KRAS mRNA expression started increasing, reaching a peak between 24 and 48 h after transfection (Figures 3B and 4B). Afterwards, their expression started decreasing between 48 and 72 h after transfection, reaching the lowest point at 120 h (Figures 3C and 4C). While KRAS mRNA expression presented a more subtle increase at early hours, reaching a maximum of 150% when transfected with G4-C and PR-C, no statistically significant results were observed. However, at 120 h after transfection, KRAS transcription expression decreased at least 25% in all cases and a remarkable 50% when G4-C and PR-C were combined. At 120 h, all the PPRH treatments reduced significantly KRAS mRNA expression except for PPRH 2 (Figure 3C). The modulation of transcription at early times for MYC mRNA was more pronounced, increasing 150% in most of the cases and more than 200% with the combination of I1-T and PPRH 2 at 24 h (Figure 4B). All the PPRH treatments increased significantly MYC mRNA expression at early hours, except for G4-C and the combination of G4-C with PPRH 2. Five days after transfection, all PPRHs reduced MYC mRNA levels by more than 50%, in all cases except for PPRH 2 and the combination of I1-T with PPRH 2, which reduced MYC mRNA by 30 and 40%, respectively (Figure 4C).



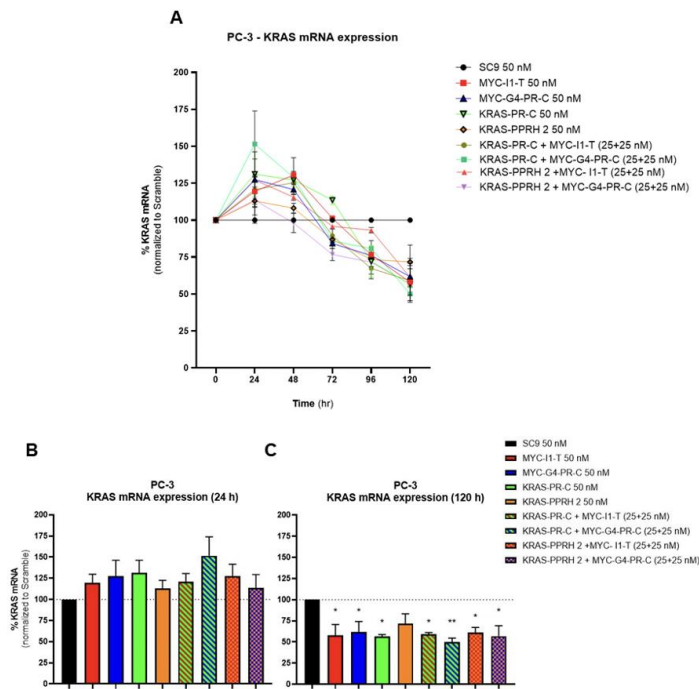


**Figure 3.** Effect of KRAS and MYC-targeting PPRHs, individually and in combination, on KRAS mRNA levels in PC-3 prostate cancer cells. **(A)** Time-course of the PPRHs effect was monitored between 24 and 120 h. mRNA levels are expressed relative to SC9 at 50 nM. **(B)** KRAS mRNA expression 24 h after transfection. **(C)** KRAS mRNA expression after 120 h of PPRH incubation. Experiments were carried out three times with internal duplicates. Statistical significance was determined using a one-way ANOVA with Dunnett's multiple comparison test comparing groups against SC9 (\*  $p < 0.05$ , \*\*  $p < 0.01$ ).

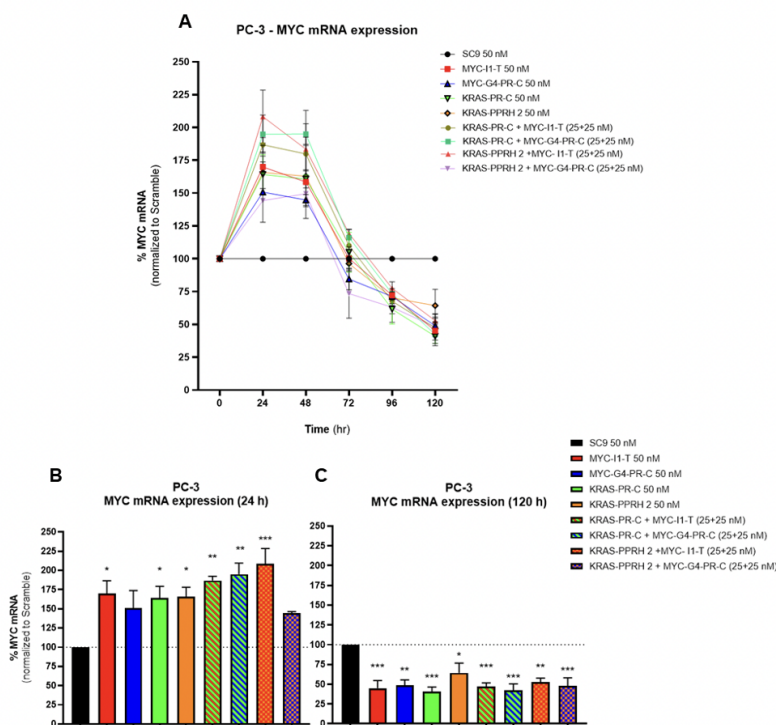


**Figure 4.** Effect of KRAS and MYC-targeting PPRHs, individually and in combination, on MYC transcription in PC-3 prostate cancer cells. (A) Time-course effect of PPRH between 24 and 120 h relative to SC9 at 50 nM. (B) MYC mRNA expression 24 h after transfection. (C) MYC mRNA expression 120 h after PPRH transfection. Experiments were performed three times with internal duplicates. Statistical significance was determined using a one-way ANOVA with Dunnett's multiple comparison test comparing groups against SC9 (\*  $p < 0.05$ , \*\*  $p < 0.01$ , \*\*\*  $p < 0.001$ ).

### 2.3. Individual and Combinatorial Effects of PPRHs on KRAS and MYC protein levels in PC-3 cells

After analyzing the modulatory effects of PPRHs on mRNA levels in time-course experiments, we wanted to study their effects in KRAS and MYC translation at 120 h, where mRNA expression upon PPRH transfection reached its lowest point. We conducted Western blot determinations under the same conditions as the RT-qPCR experiments. This included the use of PPRHs individually at 50 nM, and combinations of 25 nM of MYC-targeting PPRHs with 25 nM of a KRAS-targeting PPRH (Figure 5) and compared the results to SC9. The reduction in KRAS and MYC expression was qualitatively assessed (Figure 5A) and quantified using the ImageQuant software, normalized to GAPDH (Figure 5B). MYC and KRAS expression was reduced upon individual or combinatorial transfection of the PPRHs. For KRAS, individual treatments with MYC-targeting PPRHs had a higher effect in its protein level than KRAS-PPRH. Out of the four possible combinations, those with G4-C were the most potent in KRAS downregulation, with a reduction of 65% when combined with PR-C and a reduction of 60% when G4-C was combined with PPRH 2. The reduction in MYC protein expression was stronger than in

KRAS, and generally similar changes in protein levels as those previously determined in mRNA 120 h after transfection were observed. All the individual PPRHs reduced MYC protein levels by more than 40%, where KRAS-targeting PPRHs, PR-C and PPRH 2, reduced them by 60 and 55%, respectively. Although the reduction of MYC protein levels by MYC-targeting PPRHs was not statistically significant, I1-C and G4-C reduced MYC levels by 42 and 62%, respectively. Generally, MYC protein decreases correlated with the observed reduction in PC-3 cell viability, where all four combinations reduced MYC protein expression by 80 % or more. I1-T combinations with PR-C and PPRH 2 reduced protein levels by 90 and 85%, respectively (Figure 5B).

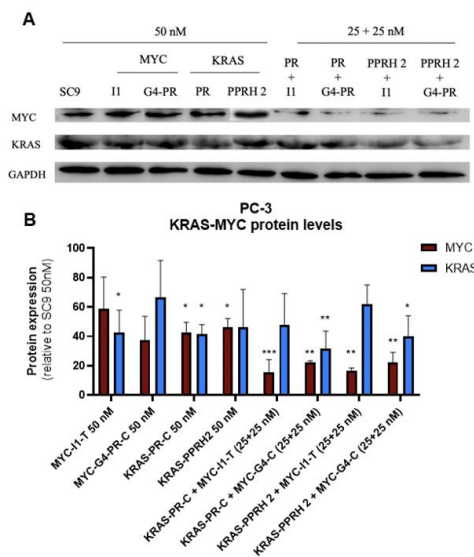


**Figure 5.** KRAS and MYC protein levels after individual or combinatorial treatment with PPRHs targeting KRAS and MYC in PC-3 prostate cancer cells. Effects were monitored 120 hours after transfection. (A) Representative blot of KRAS and MYC protein levels normalized to GAPDH. (B) Quantitation of MYC (red) and KRAS (blue) protein levels. Experiments were performed in triplicate. Statistical significance for each PPRH was determined comparing to SC9 control at 50 nM and using one-way ANOVA with post hoc Dunnett analyses (\* p < 0.05, \*\* p < 0.01, \*\*\* p < 0.001).

### 3. Discussion

KRAS and MYC proto-oncogenes have intricate interactions, where changes in their expression have the potential to initiate tumorigenesis [49]. Current studies propose that MYC plays a crucial role in KRAS-driven cancers [50], although the connection between MYC and drug resistance in these types of cancers remains an unanswered question [51]. It is known that MYC is downstream of KRAS, and in the presence of oncogenic KRAS, it will be constitutively expressed [27-28] and stabilized [52], making cells susceptible to DNA damage and apoptosis [53]. Other hypotheses suggest that MYC protein stabilization intensifies the process of tumorigenesis [54]. The tight relationship between KRAS and MYC presents major challenges in the development of targeted therapies, since

disrupting one target without affecting the other may trigger compensatory mechanisms that limit the efficacy of treatments. Consequently, strategies that simultaneously target *KRAS* and *MYC* have attracted interest as potential solutions. These treatments may hold promise in achieving durable therapeutic responses and overcoming resistance [55].

We had previously validated *KRAS* and *MYC*-targeting PPRHs which provoked gene silencing and the consequent death of cancer cell lines with deregulated *KRAS* and/or *MYC* [47,48]. In this present work, we studied the response to individual and combinatorial *MYC* and *KRAS* targeting PPRHs, in *KRAS* and *MYC*-deregulated, dependent, and sensitive prostate PC-3 cancer cells. To do so, we selected four of the most effective PPRHs, two targeting *MYC* (-II-T and G4-C) and two against *KRAS* (PR-C and PPRH 2). The combinations of PPRHs showed synergism proving the potential of combinations of PPRHs against different oncogenes at very low concentrations. The mRNA levels of both oncogenes were increased at early hours post-transfection following by a reduction with a highest effect five days after PPRH incubation. We hypothesize that an early increase in mRNA levels for both oncogenes is caused by a compensatory effect in increasing transcription after the blockage in expression upon PPRHs binding to their target regions. The reduction observed in *KRAS* and *MYC* mRNA expression demonstrate the intrinsic relation between both oncogenes, where targeting one oncogene affects the other one.

One interesting outcome was that PPRHs targeting *MYC* PPRHs reduced *KRAS* mRNA and protein levels. According to some reports, *MYC* is required for mutant-*KRAS* driven tumor initiation and progression and that *MYC* inhibition has demonstrated to impair the growth of pancreatic cancer [29,48,56]. Since *MYC* is a *KRAS* downstream effector, we expected more relevant effects in *MYC* mRNA and protein levels when targeting *KRAS* with individual PPRHs and combinations. This does not seem to be the case for mRNA levels, but it does for protein. From the two oncogenes studied, *MYC* expression showed to be more sensitive to PPRHs, resulting in a more pronounced downregulation compared to *KRAS*.

Generally, we observed a more notorious downregulation of *KRAS* and *MYC* when PC-3 cells were transfected with PPRHs targeting *MYC* than with those targeting *KRAS*. *MYC*-PPRHs may have a stronger affinity to their targets and thus cause a more pronounced gene silencing in *MYC*, and since both oncogenes tightly interact, it also affects *KRAS* expression. Out of the two *MYC*-PPRHs, G4-C was the most effective in gene silencing when combined with *KRAS*-PPRHs. This PPRH forms a triplex with its target sequence, displacing the complementary strand and allowing the formation of a G-quadruplex structure [48] which enhances *MYC* gene silencing [57]. Previously, our research group validated PPRHs targeting the complementary sequences of G4 forming sequences (G4FS) to enhance G4 formation in *TYMS* [46], *KRAS* [47] and *MYC* [48]. Additional to the fact that HpMYC-G4-PR-C facilitates G4 structure formation, it potentially disrupts the binding of Sp1 and CNBP transcription factor. This might be the reason for HpMYC-G4-PR-C to cause a stronger effect in the protein and cell viability reduction. We hypothesize that the main effect observed in cell viability is the result of the specific translation downregulation produced by PPRHs, especially by the *MYC*-targeting. Further investigations in different *KRAS*-*MYC*-dependent cancer cells and dose-response studies are needed to support PPRH combination effectiveness. Another interesting approach would be to perform combinations of PPRHs with G4 stabilizing molecules, to enhance *KRAS* and *MYC* silencing by facilitating G4 formations.

4. Materials and Methods

4.1. Polypurine Reverse Hoogsteen hairpins

Previously designed PPRHs against *KRAS* [47] and *MYC* [48] were used throughout this work. Table 1 provides the sequences and names of the oligonucleotides utilized in this study. PPRHs were synthesized as non-modified oligodeoxynucleotides by Sigma-Aldrich (Haverhill, UK) resuspended in sterile Tris-EDTA buffer (10 mM Tris and 1 mM EDTA, pH 8.0) (Sigma-Aldrich, Madrid, Spain) and stored at -20 °C.

Gene	PPRH Name (Location)	Length	Sequence (5'-3')
KRAS	HpKRAS-PR-C (Promoter)	52	5'-GGTGAAGGGCAGAAGAGAAAAG 3'-GGTGAAGGGCAGAAGAGAAAAG 5'-CCACCTTCCCGTCTTCTTTTC-3' 3'-GGTGAAGGGCAGAAGAGAAAAG-5'
	HpKRAS-PR-EF-C (PPRH 1) (Promoter)	42	5'- GGCGGGGAGGAGCGGGG 3'- GGCGGGGAGGAGCGGGG 5'- CCGCCCCCTCTCGCCCC-3' 3'- GGCGGGGAGGAGCGGGG-5'
	HpKRAS-PR-BC-C (PPRH 2) (Promoter)	46	3'- GGGGAGAAGGAGGGGCCGGG 5'- GGGGAGAAGGAGGGGCCGGG 3'- CCCCTCTCTCTCCCCGGCCC-5' 5'- GGGGAGAAGGAGGGGCCGGG-3'
MYC	HpMYC-G4-PR-C (Promoter)	67	4T GGGGTGAAGGGGTGGGAGGGGTGGGAGGGG-3' GGGGTGAAGGGGTGGGAGGGGTGGGAGGGG-5' 5'-CCCCACCTTCCCCACCTCCCCACCTCCCC-3' 3'-GGGGTGAAGGGGTGGGAGGGGTGGGAGGGG-5'
	HpMYC-PR-Distal-T (Promoter)	50	3'-AGGAGCAGCAGAGAAAGGAGAG 5'-AGGAGCAGCAGAGAAAGGAGAG 3'- TCCTCGTCGTCTTTCCCTCTC-5' 5'- AGGAGCAGCAGAGAAAGGAGAG-3'
	HpMYC-PR-Prox-T (Promoter)	50	3'- GGGAAAAAGAACGGAGGGAGGGA 5'- GGGAAAAAGAACGGAGGGAGGGA 3'- CCCTTTTCTTGCCTCCCTCCCT-5' 5'-GGGAAAAAGAACGGAGGGAGGGA-3'
	HpMYC-I1-T (Intron 1)	72	3'-AAGATGGGAGAGGAGAAGGCAGAGGAAAAACGGG 5'-AAGATGGGAGAGGAGAAGGCAGAGGAAAAACGGG 3'-TTCTACCTCTCTCTTCCGTCTCCCTTTGCC-5' 5'-AAGATGGGAGAGGAGAAGGCAGAGGAAAAACGGG-3'
	HpMYC-I2-C (Intron 2)	52	4T GGGAGGGGCAACAGAGGTTGGG-3' GGGAGGGGCAACAGAGGTTGGG-5' 5'-CCCTCCCCGTTTGTCTCCACCCC-3' 3'-GGGGTGGGAGACAAACGGGGAGGG-5'

#### 4.2. Cell Culture

PC-3 cancer cells were obtained from the Cell Bank resources at the University of Barcelona (UB). Cells were grown in Ham's F12 medium supplemented with 10% fetal bovine serum (FBS) (GIBCO, Invitrogen, Barcelona, Spain) and maintained in exponential growth at 37 °C in humidified 5% CO<sub>2</sub> incubator. For cell culture and expansion, a 0.05% trypsin solution (Merck Life Science S.L.U. in Madrid, Spain) was used to dissociate the cells.

#### 4.2. Cell transfection

Cells were plated in 6-well dishes in 800 µL of Ham's F12 medium supplemented with 10% FBS. For transfection, a mixture was prepared with a fixed amount of 1,2-Dioleoyl-3-trimethylammonium propane (DOTAP; Biontex, Germany) (10 µM) with variable quantities of PPRHs (from 12.5 to 100 nM, or combinations of 25 nM of each PPRH) in serum-free medium with a final volume of 200 µL. Following a 20-minute incubation at room temperature, the mixture was added to the cells to reach a total volume of 1 mL.

#### 4.3. Cellular Viability with MTT assay

PC-3 cells (10,000 cells per well) were plated and transfected as described in 4.2. For MTT assays, cells were incubated with PPRHs for up to 120 hours at 37°C in a humidified 5% CO<sub>2</sub> incubator. Then, 3-(4,5-dimethylthiazol-2-yl)-2,5-diphenyltetrazolium bromide (MTT) and sodium succinate, to a final concentration of 0.63 mM and 100 µM, respectively, (both from Sigma-Aldrich, Madrid, Spain) were added to the culture medium and then incubated at 37°C for 3 hours. Afterwards, culture medium was discarded, and 1 mL of lysis solution containing 0.57% acetic acid and 10% sodium dodecyl sulfate (SDS) in dimethyl sulfoxide (DMSO) (Sigma-Aldrich, Madrid, Spain) was added. Absorbance at 560 nm was measured using a Varioskan™ Lux multimode microplate reader (Thermo Scientific, Madrid, Spain). Cell viability results were expressed as the percentage relative to cells transfected with the negative control SC9.

The evaluation of the level of synergism between PPRHs using CompuSyn software (version 1.0) [58]. The Combination Index (CI) was computed for each combination, and the resultant effect was categorized based on the following values: CI < 0.3 Strong Synergism, CI 0.3–0.7 Synergism, CI 0.7–0.85 Moderate Synergism, CI 0.85–0.90 Slight Synergism, CI 0.90–1.10 Nearly Additive, and CI > 1.10 Antagonism.

#### 4.4. RNA extraction

PC-3 cells (30,000 cells per well) were initially plated in 6-well dishes and transfected the following day with the PPRHs. After 24, 48, 72, 96 and 120 h of transfection, total RNA was extracted with TRIzol® (Life Technologies; Barcelona, Spain) following the manufacturer's provided instructions. To assess RNA concentrations, absorbance at 260 nm was measured using a NanoDrop ND-1000 spectrophotometer (Thermo Fisher; Barcelona, Spain).

#### 4.5. Reverse transcription

One µg of RNA was reversed transcribed into cDNA. This was accomplished employing 125 ng of random hexamers (Roche; Spain), 500 µM of each dNTP (Bioline;



Barcelona, Spain), 20 units of RNase inhibitor, and 200 units of Moloney murine leukemia virus reverse transcriptase (the last three components were from Lucigen; WI, USA) in the retrotranscriptase buffer. The reaction was incubated at 42 °C for 1 h.

#### 4.6. Real-time qPCR

Quantitative PCR (qPCR) was conducted with Taqman probes for *KRAS* (Hs00364282\_m1), *MYC* (Hs00153408\_m1), and peptidylprolyl isomerase A (*PPIA*) (Hs04194521\_s1) (ThermoFisher Scientific, Madrid, Spain) as the endogenous control. PCR reactions were conducted in a 20 µL volume, which included 1X TaqMan Universal PCR Mastermix (Applied Biosystems, Madrid, Spain), 0.5X TaqMan probe, and 3 µL of the cDNA mixture. PCR amplification was performed in a QuantStudio 3 Real-Time PCR System (Applied Biosystems, Barcelona, Spain). Relative expression of *KRAS* and *MYC* was calculated using the  $2^{-\Delta\Delta Ct}$  method. Experiments were carried out in triplicate, and each qPCR reaction was performed with technical duplicates.

#### 4.6. Western Blot Analyses

PC-3 cells (60,000 cells per well) were plated in 6-well dishes and transfected with individual PPRHs at 50 nM or in combination of 25nM each. Total protein extracts were prepared 120 hours post-transfection using RIPA buffer (comprising 1% Igepal, 0.5% sodium deoxycholate, 0.1% SDS, 150 mM NaCl, 1 mM EDTA, 1 mM PMSF, 10 mM NaF, and 50 mM Tris-HCl, pH 8 supplemented with a Protease inhibitor cocktail (P8340-5ML). All chemicals were purchased from Sigma Aldrich, Madrid, Spain, except for Tris-HCl, which was obtained from PanReac AppliChem, Barcelona, Spain). Cell debris was removed by centrifugation for 10 minutes at 13,300 × g and 4°C. Protein concentrations were determined using the Bio-Rad protein assay based on the Bradford method, employing bovine serum albumin as a standard (Sigma-Aldrich, Madrid, Spain).

Protein extracts were subjected to electrophoresis on 4%/12% SDS-polyacrylamide gels and then transferred to polyvinylidene difluoride membranes (Immobilon P, Milipore, Madrid, Spain) using a semi-dry electroblotter. Membranes were blocked with 5% Blotto, followed by incubation with primary antibodies. For MYC detection, an antibody conjugated to horseradish peroxidase (HRP) was used (dilution 1:1500; ab205818, Abcam, Cambridge, UK). For KRAS detection, a polyclonal rabbit anti human KRAS antibody, conjugated to HRP was used (dilution 1:1200; LS-C211371, Abyntek Biopharma S.L., Biscay, Spain). GAPDH levels were assessed using a primary antibody (dilution 1:500; sc-47724, Santa Cruz Biotechnology, Heidelberg, Germany). Primary antibody incubations were carried out overnight at 4°C with gentle agitation. For GAPDH, a secondary horseradish peroxidase-conjugated anti-mouse antibody was used (dilution 1:1500, sc-516102, Santa Cruz Biotechnology, Heidelberg, Germany).

KRAS, MYC and GAPDH protein levels were detected using enhanced chemiluminescence (ECL) in accordance with the manufacturer's instructions (Amersham, Arlington Heights, IL). Protein bands were visualized using the ImageQuant LAS 4000 mini-imager (GE Healthcare, Barcelona, Spain), and quantification was performed using the ImageQuant 10.1 software.

#### 4.7. Statistical Analyses

Statistical analyses were conducted utilizing GraphPad Prism 6 (GraphPad Software, CA, USA). Data represent the mean value along with the standard error of the mean (SEM) from a minimum of three independent experiments. Statistical significance levels were indicated as follows:  $p < 0.05$  (\*),  $p < 0.01$  (\*\*),  $p < 0.001$  (\*\*\*), or  $p < 0.0001$  (\*\*\*\*).

## References

- Adjei, A. A. Blocking oncogenic Ras signaling for cancer therapy. *Journal of the National Cancer Institute*, **2001**, *93*(14), 1062–1074. <https://doi.org/10.1093/NCI/93.14.1062>
- Colicelli, J. Human RAS Superfamily Proteins and Related GTPases. Science's STKE: Signal Transduction Knowledge Environment, **2004**, (250), RE13. <https://doi.org/10.1126/STKE.2502004RE13>
- Friday, B. B., & Adjei, A. A. K-ras as a target for cancer therapy. *Biochimica et Biophysica Acta*, **2005**, *1756*(2), 127–144. <https://doi.org/10.1016/j.BBCAN.2005.08.001>
- Huang, L., Guo, Z., Wang, F., & Fu, L. KRAS mutation: from undruggable to druggable in cancer. *Signal Transduction and Targeted Therapy*, **2021**, *6*(1), 1–20. <https://doi.org/10.1038/s41392-021-00780-4>
- Nissley, D. V., & McCormick, F. RAS at 40: Update from the RAS Initiative. *Cancer Discovery*, **2022**, *12*(4), 895–898. <https://doi.org/10.1158/2159-8290.CD-21-1554>
- Nakajima, E. C., Drezner, N., Li, X., Mishra-Kalyani, P. S., Liu, Y., Zhao, H., Bi, Y., Liu, J., Rahman, A., Wearne, E., Ojofeitimi, I., Hotaki, L. T., Spillman, D., Pazdur, R., Beaver, J. A., & Singh, H. FDA Approval Summary: Sotorasib for KRAS G12C Mutated Metastatic NSCLC. *Clinical Cancer Research: An Official Journal of the American Association for Cancer Research*, **2022**, *28*(8), 1482–1486. <https://doi.org/10.1158/1078-0432.CCR-21-3074>
- Dang, C. V., Reddy, E. P., Shokat, K. M., & Soucek, L. Drugging the ‘undruggable’ cancer targets. *Nature Reviews. Cancer*, **2017**, *17*(8), 502–508. <https://doi.org/10.1038/NRC.2017.36>
- Neumann, J., Zeindl-Eberhart, E., Kirchner, T., & Jung, A. Frequency and type of KRAS mutations in routine diagnostic analysis of metastatic colorectal cancer. *Pathology, Research and Practice*, **2009**, *205*(12), 858–862. <https://doi.org/10.1016/j.PR.2009.07.010>
- Salem, M. E., El-Refai, S. M., Sha, W., Puccini, A., Grothey, A., George, T. J., Hwang, J. J., O’Neil, B., Barrett, A. S., Kadakia, K. C., Musselwhite, L. W., Raghavan, D., Cutsem, E. Van, Tabernero, J., & Tie, J. Landscape of KRASG12C, Associated Genomic Alterations, and Interrelation With Immuno-Oncology Biomarkers in KRAS-Mutated Cancers. *JCO Precision Oncology*, **2022**, *6*, e2100245. <https://doi.org/10.1200/PO.21.00245>
- Singh, A., Greninger, P., Rhodes, D., Koopman, L., Violette, S., Bardeesy, N., & Settleman, J. A gene expression signature associated with “K-Ras addiction” reveals regulators of EMT and tumor cell survival. *Cancer Cell*, **2009**, *15*(6), 489–500. <https://doi.org/10.1016/j.CCR.2009.03.022>
- Ali, S., Ahmad, A., Aboukameel, A., Bao, B., Padhye, S., Philip, P. A., & Sarkar, F. H. Increased Ras GTPase activity is regulated by miRNAs that can be attenuated by CDF treatment in pancreatic cancer cells. *Cancer Letters*, **2012**, *319*(2), 173–181. <https://doi.org/10.1016/j.canlet.2012.01.013>
- Hu, Y., Ou, Y., Wu, K., Chen, Y., & Sun, W. miR-143 inhibits the metastasis of pancreatic cancer and an associated signaling pathway. *Tumour Biology: The Journal of the International Society for Oncodevelopmental Biology and Medicine*, **2012**, *33*(6), 1863–1870. <https://doi.org/10.1007/s13277-012-0446-8>
- Duffy, M. J., O’Grady, S., Tang, M., & Crown, J. MYC as a target for cancer treatment. *Cancer Treatment Reviews*, **2021**, *94*, 102154. <https://doi.org/10.1016/j.ctrv.2021.102154>
- Beaulieu, M. E., Castillo, F., & Soucek, L. Structural and Biophysical Insights into the Function of the Intrinsically Disordered Myc Oncoprotein. *Cells*, **2020**, *9*(4), 1038. <https://doi.org/10.3390/CELLS9041038>
- Meyer, N., & Penn, L. Z. Reflecting on 25 years with MYC. *Nature Reviews Cancer*, **2008**, *8*(12), 976–990. <https://doi.org/10.1038/nrc2231>
- Armelin, H. A., Armelin, M. C. S., Kelly, K., Stewart, T., Leder, P., Cochran, B. H., & Stiles, C. D. Functional role for c-myc in mitogenic response to platelet-derived growth factor. *Nature*, **1984**, *310*(5979), 655–660. <https://doi.org/10.1038/310655A0>
- Dang, C. V. MYC on the Path to Cancer. *Cell*, **2012**, *149*(1), 22–35. <https://doi.org/10.1016/j.CELL.2012.03.003>
- Shen, L., O’Shea, J. M., Kaadige, M. R., Cunha, S., Wilde, B. R., Cohen, A. L., Welm, A. L., & Ayer, D. E. Metabolic reprogramming in triple-negative breast cancer through Myc suppression of TXNIP. *Proceedings of the National Academy of Sciences of the United States of America*, **2015**, *112*(17), 5425–5430. <https://doi.org/10.1073/PNAS.1501555112/-DCSUPPLEMENTAL>
- Herrick, D. J., & Ross, J. The half-life of c-myc mRNA in growing and serum-stimulated cells: influence of the coding and 3’ untranslated regions and role of ribosome translocation. *Molecular and Cellular Biology*, **1994**, *14*(3), 2119–2128. <https://doi.org/10.1128/MCB.14.3.2119>
- Levens, D. L. How the c-myc Promoter Works and Why It Sometimes Does Not. *Journal of the National Cancer Institute. Monographs*, **2008**, *39*, 41–43. <https://doi.org/10.1093/NCIMONOGRAPH/MLN004>
- Llombart, V., & Mansour, M. R. Therapeutic targeting of “undruggable” MYC. *EbioMedicine*, **2021**, *75*, 103756. <https://doi.org/10.1016/j.EBIOM.2021.103756>
- Beroukhi, R., Mermel, C. H., Porter, D., Wei, G., Raychaudhuri, S., Donovan, J., Barretina, J., Boehm, J. S., Dobson, J., Urashima, M., McHenry, K. T., Pinchback, R. M., Ligon, A. H., Cho, Y. J., Haery, L., Greulich, H., Reich, M., Winckler, W., Lawrence, M. S., ... Meyerson, M. The landscape of somatic copy-number alteration across human cancers. *Nature*, **2010**, *463*(7283), 899–905. <https://doi.org/10.1038/NATURE08822>
- Mossafa, H., Damotte, D., Jenabian, A., Delarue, R., Vincenneau, A., Amouroux, I., Jeandel, R., Khoury, E., Martelli, J. M., Samson, T., Tapia, S., Flandrin, G., & Troussard, X. Non-Hodgkin’s lymphomas with Burkitt-like cells are associated with c-Myc amplification and poor prognosis. *Leukemia & Lymphoma*, **2006**, *47*(9), 1885–1893. <https://doi.org/10.1080/10428190600687547>



24. Vita, M., & Henriksson, M. The Myc oncoprotein as a therapeutic target for human cancer. *Seminars in Cancer Biology*, **2006**, *16*(4), 318–330. <https://doi.org/10.1016/j.semcancer.2006.07.015>
25. McCormick, F. KRAS as a Therapeutic Target. *Clinical Cancer Research: An Official Journal of the American Association for Cancer Research*, **2015**, *21*(8), 1797–1801. <https://doi.org/10.1158/1078-0432.CCR-14-2662>
26. Whitfield, J. R., Beaulieu, M. E., & Soucek, L. Strategies to inhibit Myc and their clinical applicability. *Frontiers in Cell and Developmental Biology*, **2017**, *5*(10), 1–13. <https://doi.org/10.3389/fcell.2017.00010>
27. Waters, A. M., Khatib, T. O., Papke, B., Goodwin, C. M., Hobbs, G. A., Diehl, J. N., Yang, R., Edwards, A. C., Walsh, K. H., Sulahian, R., McFarland, J. M., Kapner, K. S., Gilbert, T. S. K., Stalneck, C. A., Javaid, S., Barkovskaya, A., Grover, K. R., Hibshman, P. S., Blake, D. R., ... Der, C. J. Targeting p130Cas- and microtubule-dependent MYC regulation sensitizes pancreatic cancer to ERK MAPK inhibition. *Cell Reports*, **2021**, *35*(13), 109291. <https://doi.org/10.1016/j.celrep.2021.109291>
28. Hashimoto, A., Handa, H., Hata, S., Tsutaho, A., Yoshida, T., Hirano, S., Hashimoto, S., & Sabe, H. Inhibition of mutant KRAS-driven overexpression of ARF6 and MYC by an eIF4A inhibitor drug improves the effects of anti-PD-1 immunotherapy for pancreatic cancer. *Cell Communication and Signaling*, **2021**, *19*(54). <https://doi.org/10.1186/s12964-021-00733-Y/FIGURES/1>
29. Vaseva, A. V., Blake, D. R., Gilbert, T. S. K., Ng, S., Hostetter, G., Azam, S. H., Ozkan-Dagliyan, I., Gautam, P., Bryant, K. L., Pearce, K. H., Herring, L. E., Han, H., Graves, L. M., Witkiewicz, A. K., Knudsen, E. S., Pecot, C. V., Rashid, N., Houghton, P. J., Wennerberg, K., ... Der, C. J. KRAS Suppression-Induced Degradation of MYC Is Antagonized by a MEK5-ERK5 Compensatory Mechanism. *Cancer Cell*, **2018**, *34*(5), 807–822.e7. <https://doi.org/10.1016/j.ccell.2018.10.001>
30. Varshney, D., Spiegel, J., Zyner, K., Tannahill, D., & Balasubramanian, S. The regulation and functions of DNA and RNA G-quadruplexes. *Nature Reviews Molecular Cell Biology*, **2020**, *21*(8), 459–474. <https://doi.org/10.1038/s41580-020-0236-x>
31. Bochman, M. L., Paeschke, K., & Zakian, V. A. DNA secondary structures: stability and function of G-quadruplex structures. *Nature Reviews. Genetics*, **2012**, *13*(11), 770–780. <https://doi.org/10.1038/NRG3296>
32. Spiegel, J., Adhikari, S., & Balasubramanian, S. The Structure and Function of DNA G-Quadruplexes. *Trends in Chemistry*, **2020**, *2*(2), 123–136. <https://doi.org/10.1016/j.trechm.2019.07.002>
33. Huppert, J. L., & Balasubramanian, S. G-quadruplexes in promoters throughout the human genome. *Nucleic Acids Research*, **2007**, *35*(2), 406. <https://doi.org/10.1093/NAR/GKL1057>
34. Linke, R., Limmer, M., Juranek, S. A., Heine, A., & Paeschke, K. The Relevance of G-Quadruplexes for DNA Repair. *International Journal of Molecular Sciences*, **2021**, *22*(22), 12599. <https://doi.org/10.3390/ijms222212599>
35. Sarkies, P., Reams, C., Simpson, L. J., & Sale, J. E. Epigenetic instability due to defective replication of structured DNA. *Molecular Cell*, **2010**, *40*(5), 703–713. <https://doi.org/10.1016/j.molcel.2010.11.009>
36. Brooks, T. A., & Hurley, L. H. Targeting MYC Expression through G-Quadruplexes. *Genes & Cancer*, **2010**, *1*(6), 641–649. <https://doi.org/10.1177/1947601910377493>
37. Dexheimer, T. S., Sun, D., & Hurley, L. H. Deconvoluting the structural and drug-recognition complexity of the G-quadruplex-forming region upstream of the bcl-2 P1 promoter. *Journal of the American Chemical Society*, **2006**, *128*(16), 5404–5415. <https://doi.org/10.1021/JA0563861>
38. Cogoi, S., & Xodo, L. E. G-quadruplex formation within the promoter of the KRAS proto-oncogene and its effect on transcription. *Nucleic Acids Research*, **2006**, *34*(9), 2536–2549. <https://doi.org/10.1093/NAR/GKL286>
39. Coma, S., Noé, V., Eritja, R., & Ciudad, C. J. Strand Displacement of Double-Stranded DNA by Triplex-Forming Antiparallel Purine-Hairpins. *Oligonucleotides*, **2005**, *15*(4), 269–283. <https://doi.org/10.1089/oli.2005.15.269>
40. de Almagro, M. C., Coma, S., Noé, V., & Ciudad, C. J. Polypurine Hairpins Directed against the Template Strand of DNA Knock Down the Expression of Mammalian Genes. *The Journal of Biological Chemistry*, **2009**, *284*(17), 11579–11589. <https://doi.org/10.1074/jbc.M900981200>
41. Noé, V., Aubets, E., Félix, A. J., & Ciudad, C. J. Nucleic acids therapeutics using PolyPurine Reverse Hoogsteen hairpins. *Biochemical Pharmacology*, **2021**, *189*, 114371. <https://doi.org/10.1016/j.bcp.2020.114371>
42. Rodríguez, L., Villalobos, X., Solé, A., Liberós, C., Ciudad, C. J., & Noé, V. Improved design of PPRHs for gene silencing. *Molecular Pharmacology*, **2015**, *12*(3), 867–877. <https://doi.org/10.1021/mp5007008>
43. de Almagro, M. C., Mencia, N., Noé, V., & Ciudad, C. J. Coding polypurine hairpins cause target-induced cell death in breast cancer cells. *Human Gene Therapy*, **2011**, *22*(4), 451–463. <https://doi.org/10.1089/hum.2010.102>
44. Villalobos, X., Rodríguez, L., Solé, A., Liberós, C., Mencia, N., Ciudad, C. J., & Noé, V. Effect of Polypurine Reverse Hoogsteen Hairpins on Relevant Cancer Target Genes in Different Human Cell Lines. *Nucleic Acid Therapeutics*, **2015**, *25*(4), 198–208. <https://doi.org/10.1089/nat.2015.0531>
45. López-Aguilar, E., Fernández-Nogueira, P., Fuster, G., Carbó, N., Ciudad, C. J., & Noé, V. In Vitro and In Vivo Effects of the Combination of Polypurine Reverse Hoogsteen Hairpins against HER-2 and Trastuzumab in Breast Cancer Cells. *International Journal of Molecular Sciences*, **2023**, *24*(8), 7073. <https://doi.org/10.3390/ijms24087073>
46. Aubets, E., Félix, A. J., Garavís, M., Reyes, L., Aviñó, A., Eritja, R., Ciudad, C. J., & Noé, V. Detection of a G-Quadruplex as a Regulatory Element in Thymidylate synthase for Gene Silencing Using Polypurine Reverse Hoogsteen Hairpins. *International Journal of Molecular Sciences*, **2020**, *21*(14), 1–22. <https://doi.org/10.3390/ijms21145028>
47. Psaras, A. M., Valiuska, S., Noé, V., Ciudad, C. J., & Brooks, T. A. Targeting KRAS Regulation with PolyPurine Reverse Hoogsteen Oligonucleotides. *International journal of molecular sciences*, **2022**, *23*(4), 2097. <https://doi.org/10.3390/ijms23042097>
48. Valiuska, S., Psaras, A. M., Noé, V., Brooks, T. A., & Ciudad, C. J. Targeting MYC Regulation with Polypurine Reverse Hoogsteen Oligonucleotides. *International journal of molecular sciences*, **2022**, *24*(1), 378. <https://doi.org/10.3390/ijms24010378>

49. Phillips, P. C. Epistasis—the essential role of gene interactions in the structure and evolution of genetic systems. *Nature Reviews. Genetics*, **2008**, 9(11), 855–867. <https://doi.org/10.1038/NRG2452>
50. Eilers, M., & Eisenman, R. N. Myc's broad reach. *Genes & Development*, **2008**, 22(20), 2755–2766. <https://doi.org/10.1101/GAD.1712408>
51. Ischenko, I., Zhi, J., Hayman, M. J., & Petrenko, O. KRAS-dependent suppression of MYC enhances the sensitivity of cancer cells to cytotoxic agents. *Oncotarget*, **2017**, 8(11), 17995–18009. <https://doi.org/10.18632/ONCOTARGET.14929>
52. Lee, T., Yao, G., Nevins, J., & You, L. Sensing and integration of Erk and PI3K signals by Myc. *PLoS Computational Biology*, **2008**, 4(2), e1000013. <https://doi.org/10.1371/JOURNAL.PCBL1000013>
53. Shortt, J., & Johnstone, R. W. Oncogenes in cell survival and cell death. *Cold Spring Harbor Perspectives in Biology*, **2012**, 4(12), a009829. <https://doi.org/10.1101/CSHPERSPECT.A009829>
54. Chang, W. H., Liu, Y., Hammes, E. A., Bryant, K. L., Cerione, R. A., & Antonyak, M. A. Oncogenic RAS promotes MYC protein stability by upregulating the expression of the inhibitor of apoptosis protein family member Survivin. *The Journal of Biological Chemistry*, **2023**, 299(2). <https://doi.org/10.1016/j.jbc.2022.102842>
55. Donati, G., & Amati, B. (2022). MYC and therapy resistance in cancer: risks and opportunities. *Molecular Oncology*, 16(21), 3828–3854. <https://doi.org/10.1002/1878-0261.13319>
56. Walz, S., Lorenzin, F., Morton, J., Wiese, K. E., Von Eyss, B., Herold, S., Rycak, L., Dumay-Odelot, H., Karim, S., Bartkuhn, M., Roels, F., Wüstefeld, T., Fischer, M., Teichmann, M., Zender, L., Wei, C. L., Sansom, O., Wolf, E., & Eilers, M. Activation and repression by oncogenic MYC shape tumour-specific gene expression profiles. *Nature*, **2014**, 511, 483–487. <https://doi.org/10.1038/nature13473>
57. Psaras, A. M., Chang, K. T., Hao, T., & Brooks, T. A. Targeted Downregulation of MYC through G-quadruplex Stabilization by DNAI. *Molecules*, **2021**, 26(18), 5542. <https://doi.org/https://doi.org/10.3390/molecules26185542>
58. Chou, T. C. Theoretical basis, experimental design, and computerized simulation of synergism and antagonism in drug combination studies. *Pharmacol Reviews*. **2006**, 58 (3), 621–681 <https://doi.org/10.1124/pr.58.3.10>



### 4.3. ARTICLE IV

#### Detection of SARS-CoV-2 Virus by Triplex Enhanced Nucleic Acid Detection Assay (TENADA)

Anna Aviñó, Carlos Cuestas-Ayllón, Manuel Gutiérrez-Capitán, Lluïsa Vilaplana, Valeria Grazu, Véronique Noé, Eva Balada, Antonio Baldi, Alex J. Félix, Eva Aubets, Simonas Valiuska, Arnau Domínguez, Raimundo Gargallo, Ramon Eritja, M.-Pilar Marco, César Fernández-Sánchez, Jesús Martínez de la Fuente and Carlos J. Ciudad

International Journal of Molecular Sciences. 2022, 23(23), 15258 (Impact factor: 5.6)

**Background:** SARS-CoV-2, a member of the coronaviruses family, exhibits a high transmission rate and results in an elevated fatality rate (Jackson et al., 2021). The COVID-19 pandemics accelerated the rapid development and widespread adoption of various diagnostic techniques. The urgency to contain the viral spread and to rapidly detect cases drove researchers, scientists, and healthcare professionals worldwide to innovate and generate new diagnostic methods (Rong et al., 2023). Among these approaches, polymerase chain reaction (PCR)-based assays are considered as the gold standard for virus detection because of their exceptional sensitivity and specificity. However, it does have certain limitations, including the requirement for highly purified samples, an expensive laboratory equipment, the need for trained specialists, and extended processing times (Corman et al., 2020).

**Objectives:** We aimed to use the ability of PPRHs to form triplexes as a diagnostic tool for SARS-CoV-2. First, we wanted to design specific PPRHs against the viral RNA and to perform binding assays using the PPRHs as capture probes. Then we wanted to use these capture probes, immobilized in a biosensor, and combined with modified oligonucleotides reporter probes, to deliver optical and electrochemical transducer signals to the device which will be used for SARS-CoV-2 detection.

**Results:** We successfully designed three specific PPRHs targeting SARS-CoV-2: CC1-PPRH targeting *replicase*, CC2-PPRH directed to

the *N* gene, and CC3-PPRH targeting *spike*. The PPRHs followed our laboratory's established criteria for PPRH designing and were synthesized in two versions: one in their unmodified state and the second one extended with an aminohexyl group at the 5'-end, referred to as capture probes. This modification facilitated the anchoring of the PPRHs onto the biosensor surface. Next, a DNA oligonucleotide or reporter probe capable of forming a duplex with the viral RNA was designed and functionalized with biotin, fluorescent labels (Cy3, TAMRA), or peroxidase protein attached to its 3'-end to be used for the different biosensors.

We verified the specificity of the PPRHs to their corresponding SARS-CoV-2 ssRNA and ssDNA targets, achieving successful binding even at very low concentrations. The dissociation constant ( $K_d$ ) between the targets and PPRHs, which form triplex structures, was lower than for the probes forming duplexes. This indicates that triplex formation has the advantage of greater affinity and specificity compared to the complementary strand forming a duplex. The design and binding of the PPRHs allowed the development of the biosensors.

We also developed PPRHs targeting additional viruses to broaden the scope of diagnosis and detection. Specifically, we designed two PPRHs for the Influenza virus A (H1N1), one targeting the Polymerase PB1 and one against Nuclear Export protein (NEP), and two PPRHs for the Human respiratory syncytial virus (HRSV). All PPRHs exhibited strong binding to their respective targets at low concentrations.

**Conclusions:** The designed PPRHs targeting SARS-CoV-2, Influenza A and Human Respiratory syncytial virus can enhance diagnostic accuracy and enable precise treatments for patients with respiratory infections.



## Article

# Detection of SARS-CoV-2 Virus by Triplex Enhanced Nucleic Acid Detection Assay (TENADA)

Anna Aviñó <sup>1,2</sup>, Carlos Cuestas-Ayllón <sup>2,3</sup>, Manuel Gutiérrez-Capitán <sup>4</sup>, Lluïsa Vilaplana <sup>1,2</sup>, Valeria Grazu <sup>2,3</sup>, Véronique Noé <sup>5,6</sup>, Eva Balada <sup>1,2</sup>, Antonio Baldi <sup>4</sup>, Alex J. Félix <sup>5</sup>, Eva Aubets <sup>5</sup>, Simonas Valiuska <sup>5,6</sup>, Arnau Domínguez <sup>1,2</sup>, Raimundo Gargallo <sup>7</sup>, Ramon Eritja <sup>1,2,\*</sup>, M.—Pilar Marco <sup>1,2</sup>, César Fernández-Sánchez <sup>2,4</sup>, Jesús Martínez de la Fuente <sup>2,3</sup> and Carlos J. Ciudad <sup>5,6</sup>

- <sup>1</sup> Institute for Advanced Chemistry of Catalonia (IQAC), Consejo Superior de Investigaciones Científicas (CSIC), 08034 Barcelona, Spain
  - <sup>2</sup> Centro de Investigación Biomédica en Red de Bioingeniería, Biomateriales y Nanomedicina (CIBER-BBN), Instituto de Salud Carlos III, 28220 Madrid, Spain
  - <sup>3</sup> Instituto de Nanociencia y Materiales de Aragón (INMA), Consejo Superior de Investigaciones Científicas (CSIC), University of Zaragoza, 50009 Zaragoza, Spain
  - <sup>4</sup> Instituto de Microelectrónica de Barcelona (IMB-CNM). Consejo Superior de Investigaciones Científicas (CSIC), Campus UAB, 08193 Cerdanyola, Spain
  - <sup>5</sup> Department of Biochemistry and Physiology, School of Pharmacy and Food Sciences, University of Barcelona (UB), 08028 Barcelona, Spain
  - <sup>6</sup> Instituto de Nanociencia y Nanotecnología (IN2UB), University of Barcelona (UB), 08028 Barcelona, Spain
  - <sup>7</sup> Department of Chemical Engineering and Analytical Chemistry, University of Barcelona (UB), 08028 Barcelona, Spain
- \* Correspondence: recgma@cid.csic.es; Tel.: +34-934006145; Fax: +34-932045904



**Citation:** Aviñó, A.; Cuestas-Ayllón, C.; Gutiérrez-Capitán, M.; Vilaplana, L.; Grazu, V.; Noé, V.; Balada, E.; Baldi, A.; Félix, A.J.; Aubets, E.; et al. Detection of SARS-CoV-2 Virus by Triplex Enhanced Nucleic Acid Detection Assay (TENADA). *Int. J. Mol. Sci.* **2022**, *23*, 15258. <https://doi.org/10.3390/ijms232315258>

Academic Editors: Jussara Amato, Antonio Randazzo and Bruno Pandano

Received: 9 November 2022

Accepted: 29 November 2022

Published: 3 December 2022

**Publisher's Note:** MDPI stays neutral with regard to jurisdictional claims in published maps and institutional affiliations.



**Copyright:** © 2022 by the authors. Licensee MDPI, Basel, Switzerland. This article is an open access article distributed under the terms and conditions of the Creative Commons Attribution (CC BY) license (<https://creativecommons.org/licenses/by/4.0/>).

**Abstract:** SARS-CoV-2, a positive-strand RNA virus has caused devastating effects. The standard method for COVID diagnosis is based on polymerase chain reaction (PCR). The method needs expensive reagents and equipment and well-trained personnel and takes a few hours to be completed. The search for faster solutions has led to the development of immunological assays based on antibodies that recognize the viral proteins that are faster and do not require any special equipment. Here, we explore an innovative analytical approach based on the sandwich oligonucleotide hybridization which can be adapted to several biosensing devices including thermal lateral flow and electrochemical devices, as well as fluorescent microarrays. Polypurine reverse-Hoogsteen hairpins (PPRHs) oligonucleotides that form high-affinity triplexes with the polypyrimidine target sequences are used for the efficient capture of the viral genome. Then, a second labeled oligonucleotide is used to detect the formation of a trimolecular complex in a similar way to antigen tests. The reached limit of detection is around 0.01 nM (a few femtomoles) without the use of any amplification steps. The triplex enhanced nucleic acid detection assay (TENADA) can be readily adapted for the detection of any pathogen requiring only the knowledge of the pathogen genome sequence.

**Keywords:** Polypurine reverse-Hoogsteen hairpin; SARS-CoV-2 RNA detection; COVID diagnosis; thermal lateral flow; electrochemical magnetoassay; fluorescent microarray

## 1. Introduction

The COVID-19 pandemic has triggered the largest viral testing effort to monitor the spread of the infection and dictate the appropriate measures to prevent viral transmission [1]. This large testing effort has driven an extraordinary search for novel methods for the rapid detection of SARS-CoV-2 and other viral infections [2]. The reverse transcription quantitative polymerase chain reaction (RT-qPCR) method [3] provides a quantitative analysis of the viral genome, and it has been the gold standard method for the identification of infected individuals for the control of the pandemic. Although RT-qPCR can detect very small amounts of viral RNA it has been described that in the real clinical set-up it



has around 50–70% sensitivity [4]. In addition, this technique requires specialized personnel and instruments with the difficulty to be performed in low-income countries with a dispersed population. Many alternative methods avoiding the higher-temperature amplification steps have been described [2] including loop-mediated isothermal amplification (LAMP, [5]), nicking endonuclease amplification reaction, and recombinase polymerase amplification (RPA, [6]). The use of CRISPR for signal amplification (SHERLOCK, [7]), has also been described [8,9]. In addition, next-generation sequencing (NGS) has provided an excellent platform for the identification of the SARS-CoV-2 genome [10,11] as well as novel SARS-CoV-2 variants [12].

The development of highly specific monoclonal antibodies against viral proteins has produced several antibody tests in simple lateral flow formats that are able to detect the presence of the virus in nasopharyngeal samples in a short time [13]. The antibody tests are very popular despite having shown less sensitivity than assays based on nucleic acids [14].

Recently we have described that DNA hairpins that recognize nucleic acid targets by triplex formation can detect *Pneumocystis* in bronchoalveolar lavage, nasopharyngeal aspirates, and sputum samples using surface plasmon resonance (SPR) [15] or by using nanoporous anodic alumina scaffolds filled with a fluorescent dye reporter [16]. These successful strategies make us think that triplex-forming DNA hairpins could be used for the direct detection of viral RNA, concretely the detection of single-stranded SARS-CoV-2 RNA. To this end, we analyzed the SARS-CoV-2 genome, and we found a fair number of polypyrimidine stretches suitable for designing triplex-forming hairpins using the Polypurine reverse-Hoogsteen (PPRH) strategy [17].

PPRHs are single-stranded non-modified DNA hairpins formed by two antiparallel Polypurine mirror repeat domains linked by a thymidine loop and bound by intramolecular reverse-Hoogsteen bonds. They can bind in a sequence-specific manner to polypyrimidine sequences in either ssDNA, dsDNA, or RNA by Watson–Crick bonds, thus forming an antiparallel triplex and producing strand displacement on the DNA complex [18,19]. PPRHs have been described as gene silencing tools of several genes mainly involved in cancer with the capacity to produce strand displacement [17]. Additionally, they have been incorporated as probes in biosensors for the detection of miRNA-145 [20,21], to determine the DNA methylation status of the PAX-5 gene [22], and for the diagnosis of *Pneumocystis pneumonia* [15,16].

In the case of SARS-CoV-2, we decided to use the sandwich hybridization format [23] in several biosensing devices. This strategy uses two oligonucleotides: a triplex-forming PPRH hairpin [24] acting as a capture probe and a labeled duplex-forming DNA oligonucleotide acting as a detection probe (Figure 1). The triplex-forming PPRH hairpins were designed to bind to SARS-CoV-2 polypyrimidine sequences, and the detection probes were designed to be complementary to a region near the polypyrimidine target site. In this way, the presence of the SARS-CoV-2 RNA is detected by the formation of the ternary complex in a biosensor surface. We named this method after triplex enhanced nucleic acid detection assay (TENADA).

In this communication, we describe the simple and rapid detection of viral genome by TENADA in two different biosensing devices, once the TENADA is validated by a fluorescent DNA microarray chip. The first biosensing strategy is based on a thermal lateral flow system and the second one is on a compact electrochemical biosensor platform. The results demonstrate that TENADA is highly efficient for the detection of viral RNA obtaining high sensitivity and specificity with no need for amplification making possible direct detection in a lateral flow format in less than one hour.

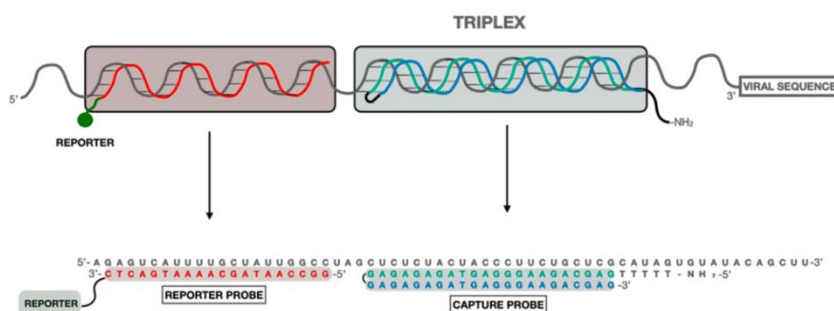


**Figure 1.** Design of the PPRH CC1 capture and reporter probes for the detection of the viral RNA.

## 2. Results and Discussion

### 2.1. Design and Synthesis of PPRH and Reporter Probes

Our goal, based on previous experiences in diagnosing biological materials, was to develop a technique for detecting directly (without the need for PCR) and very quickly (less than 1 h), the RNA of the SARS-CoV-2 virus. The method described here takes advantage of the property of a special kind of DNA hairpin, developed in our laboratory, and named PPRHs, to capture the viral RNA forming a triplex. We searched for triplex forming sequences in the SARS-CoV-2 genome (MN938384) with more than 15 nucleotides in length, a maximum of 3 pyrimidine interruptions and a minimum of 40% of G-C content as described [24]. The output of the search was given in the form of polypurine sequences that can be found in the forward or reverse orientation (Table S1).

We selected the three longest sequences in the reverse orientation and converted the polypurine sequence (20–21 nucleotides) to the complementary polypyrimidine generating the potential targets. These targets were named as CC1 (CTCTCTACTACCCCTCTGCTC, 21 bases) located at the replicase gene position 17,111; CC2 (CCTCTTCTCGTTCCTCATCAC, 21 bases), located at the N gene position 28,806 and CC3 (TCATCTTATGTCTCTCCCTC, 20 bases) located at the spike gene position 24,690. The selected target sequences contain three purine interruptions each (underlined).

Next, we prepared the corresponding PPRHs, as described in Materials and Methods (Supplementary Material), one for each potential target (CC1PPRH, CC2PPRH, and CC3PPRH, Tables S2 and S3) in two forms: unmodified for the binding assays and extended with a pentathymidine sequence followed by the addition of an aminohexyl group at the 5'-end that will be used for the immobilization of PPRH at the surface of the biosensors.

Once the PPRHs were designed, a second oligonucleotide or reporter probe was defined with the condition that the oligonucleotide is complementary to a nearby site avoiding steric factors (Tables S2 and S3 and Figure 1).

The reporter probes were functionalized at the 3'-end with either biotin, fluorescent labels (Cy3, TAMRA), or with peroxidase protein through a reactive thiol group to provide non-radioactive labeling systems to deliver optical or electrochemical transducer signals for three different biosensors. In addition, we prepared the complementary sequence of the target polypyrimidine sites (CC1duplex, CC2duplex, CC3duplex, Table S2) to be used for comparison purposes. Finally, several synthetic DNA and RNA oligonucleotides containing the viral polypyrimidine target sequences (Table S3) were prepared for binding assays or as artificial targets for the calculation of the limit of detection of the biosensors.

### 2.2. Gel Shift Binding Assays

As can be seen in Figure 2, increasing amounts of the PPRHs designed against the viral sequences for the replicase or spike were able to bind to 500 ng of their corresponding targets



in the SARS2 genome, either as ssDNA or ssRNA species. In both cases, a shifted band corresponding to the binding of the PPRH to its target, with lower mobility than the probe alone, can be observed. As a negative control, a PPRH with a scrambled sequence (HpSC6) was used that did not originate any shifted band in the presence of the specific probes.

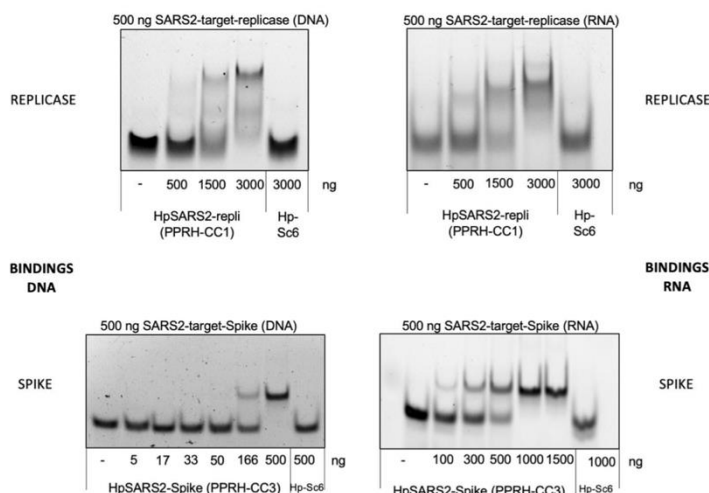


**Figure 2.** Binding of PPRHs CC1 and CC3 to DNA and RNA probes corresponding to SARS-CoV-2. Increasing amounts of PPRH-CC1 or PPRH-CC3 were incubated with 500 ng of 6-FAM-labeled ssDNA or ssRNA probes corresponding to replicase (top panel) or spike (bottom panel) sequences. Hp-Sc6 was included as a non-targeting control PPRH.

Gel shift assays on polyacrylamide gels allowed the measurement of the dissociation constant of the triplex-forming probes and the duplex-forming probes with their target sequence labeled with fluorescein. The dissociation constants ( $K_d$ ) have been determined for the formation of the triplex and the duplex, which are detailed in Figure S1 and Table S4. A control oligonucleotide (CC1-control) was added. This oligonucleotide can only form a duplex because the reverse Hoogsteen strand is scrambled. PPRH-CC1 and PPRH-CC3 present the highest affinity for their targets with dissociation constants of around  $3.8 \times 10^{-7}$  M. PPRH-CC2 presented the lower affinity PPRH ( $K_d$   $6.04 \times 10^{-7}$  M). As PPRH-CC1 and PPRH-CC2 have the same length (21 nt) and GC content (47.6%, Table S1) we believe that the reason for the lower affinity may be due to the relative position of the three interruptions (in CC2 the three interruptions are near the ends of the hairpins and this may debilitate the formation of the hairpin). However, all PPRHs have a higher affinity than the corresponding duplex-forming oligonucleotides (duplex-CC1, duplex-CC2, duplex-CC3, PPRH-CC1-control,  $K_d$  between  $4.79$  and  $10.5 \times 10^{-7}$  M). These data demonstrated a greater affinity of the triplex-forming probes for their target. (Figure S1 and Table S4).

### 2.3. CC Pair Validation with a Fluorescent DNA Microarray Chip

Since microarray analysis is a well-established and reliable methodology to study hybridization events between specific probes and the complementary targets, it has been used to validate the design and performance of the different probe pairs (CC capture and detection probes) in both formats: PPRH and duplex. With this aim, an array has been developed printing on a solid surface the different capture probes that hybridize selectively with the corresponding synthetic target sequences. This hybridization process is

reported to add specific labeled detection probes. More precisely, the capture probes (first oligonucleotide) have been chemically bound to a glass slide through the addition of a capture tag, which in this case is an amino group that reacts with the isothiocyanate groups of the previously biofunctionalized surface. These printed oligonucleotides bind to the corresponding target nucleotide sequences by complementarity base pairing events which are proved by adding specific detection probes (second oligonucleotide) labeled with a fluorophore (TAMRA or Cy3) (Figure 3). Finally, data acquisition is achieved by exciting the fluorophore with a laser beam of 532 nm. This readout signal is then scanned with a microarray scanner to visualize and quantify spot fluorescence.

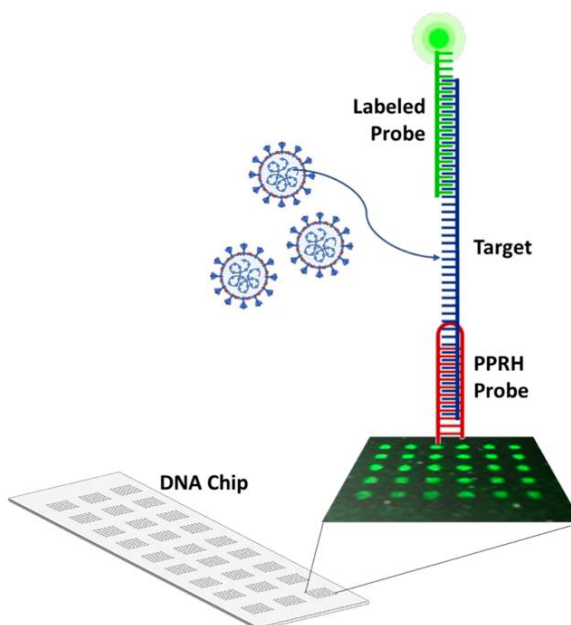


**Figure 3.** Scheme of the microarray system developed to validate the CC pairs designed for detecting SARS-CoV-2 viral RNA. It comprises a glass surface onto which DNA capture probes (PPRH or duplex) are chemically bounded. These capture probes printed on the glass slide hybridize selectively with the corresponding synthetic target and this binding is reported through the addition of a second probe, which allows the detection since it is coupled to a fluorophore. Thus, the principle of the system is based on the complementarity base pairing between the probes and the corresponding target nucleotide sequence.

To find out the optimal microarray working conditions, single oligonucleotide pair standard curves were performed printing six different concentrations (from 500 nM to 0 with a dilution factor of 2) of the capture probe (in PPRH and duplex format). Subsequently, eight serial dilutions of the corresponding target (ranging from 500 nM to 0 with a dilution factor of 5 and prepared in hybridization buffer) were added and let for hybridization during 5 min at RT. Finally, the detection probe was incorporated and incubated for 10 min at RT assaying two different concentrations of each one of them (500 and 250 nM also prepared in hybridization buffer). With the data obtained from these experiments, the analytical parameters of each CC pair microarray assay were determined. Afterward, matrix effect studies to assess the performance of the developed chip when diluting each

target with different universal transport media (UTM, i.e., the buffer used to collect the swabs) were also carried out. This study was needed since this sort of sample is usually collected in tubes that contain a UTM which, depending on the brand, can slightly vary its composition and either include the inactivation agent (usually guanidine isothiocyanate) or not. In our case, the matrix effect was studied by testing three different universal transport media (UTM) named buffers 1, 2, and 3. In all cases, good analytical features were obtained and even a slight improvement was observed when compared with the results obtained with the hybridization buffer prepared in the lab (see these data in Table S5).

Moreover, cross-reactivity studies were carried out to identify possible nonspecific hybridization events between oligonucleotides from different sets or among an oligonucleotide and a non-specific target. These experiments showed that neither targets nor CC oligonucleotides caused cross-hybridization artifacts, demonstrating that all hybridization processes that take place are specific (see Figure 4). These results also confirm the feasibility of developing a multiplex assay with the CC pairs studied. Finally, aiming at reproducing the conditions that will occur when testing real clinical samples, the synthetic CC1 DNA target used to develop the assay was replaced by the equivalent one but in an RNA format. The standard curve built in this case did not show significant differences with the ones obtained with DNA synthetic target confirming that the hybridization DNA: RNA is also optimal.

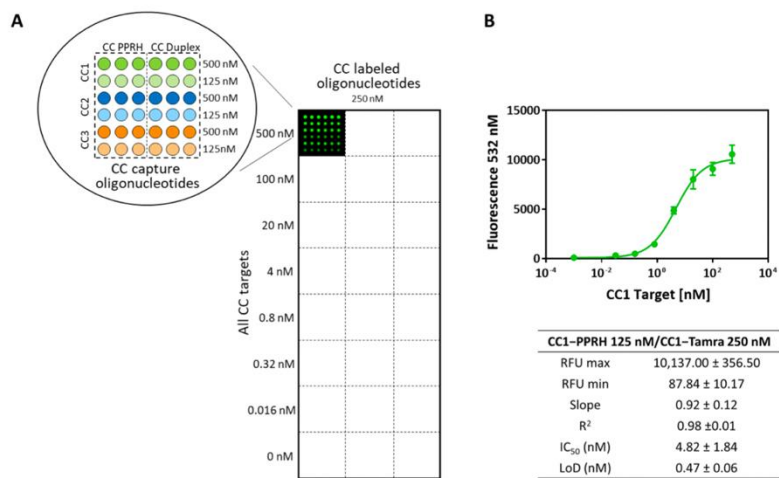


**Figure 4.** Microarray system designed to test simultaneously (multiplex) all three CC oligonucleotide pairs assayed in both formats (PPRH and duplex clamp). (A): Scheme of the chip organization and the concentrations used to build standard curves for each CC pair are shown together with a fluorescence image of a microarray well. (B): Calibration curve obtained for the CC1 pair and the corresponding analytical parameters of this sigmoidal curve obtained in a multiplex microarray assay (RFU: relative fluorescence units) are also plotted. All standard curves obtained were designed to record at least 3 spot replicates for each concentration value.

2.4. First Biosensor Device Thermal Lateral Flow System

The first technology developed to detect SARS-CoV-2 RNA is based on a commonly used lateral flow assay (Figure 5). Lateral flow technologies are based on the detection of different kinds of biomolecules by using a nitrocellulose membrane platform where a test line and a control line have been previously deposited. The test line is composed

of a protein solution (3 mg/mL) which recognize specifically the biotinylated capture probes after the interaction with the desired target. The control line is formed by a solution of a modified protein (2 mg/mL) with a particular oligonucleotide that recognizes the detection probe (first oligonucleotide) introduced in the gold nanoprisms (NPr). The detection probes or first oligonucleotides have been, previously to the biofunctionalization, modified by the introduction of a terminal amino group allowing the attachment onto the carboxylic derived gold nanoprisms. The concentration of detection oligonucleotide used in the biofunctionalization has been optimized at 1.36 pmol/ $\mu$ L. These probes hybridize selectively with the corresponding target and this binding was completed through the addition of a second capture probe. This second capture probe allowed the detection since it was labeled with biotin which reacts with the streptavidin introduced at the test line. The corresponding target was tested at eight different concentrations (ranging from 5 nM to 0). The LoD has been calculated after the membrane development by using a 1064 nm NIR laser; see Figure 6a. Visual detection has been performed in the back part of the strip by using a thermosensitive paper which changes from white to black when the local temperature increases as a consequence of plasmonic nanoparticles (gold nanoprisms, NPr) laser irradiation, see Figure 6b. No results are shown for PPRH-CC3 because nanoparticle aggregation was observed once the particles were introduced in the LF strip. The highest sensitivity was achieved with PPRH-CC1 and PPRH-CC2 with a limit of detection between 0.01 and 0.005 nM. The control duplex-CC1 and CC2 gave a limit of detection between 0.1 and 0.05 nM (one order of magnitude less sensitive). The matrix effect was studied testing one universal transport media (UTM) from Biocomma Limited (Guangdong, China) which has been selected due to the better compatibility with the TLF system. Similar results were obtained, even important improvements were observed when the results were compared with the corresponding in buffer media, as better LOD was obtained in all cases.

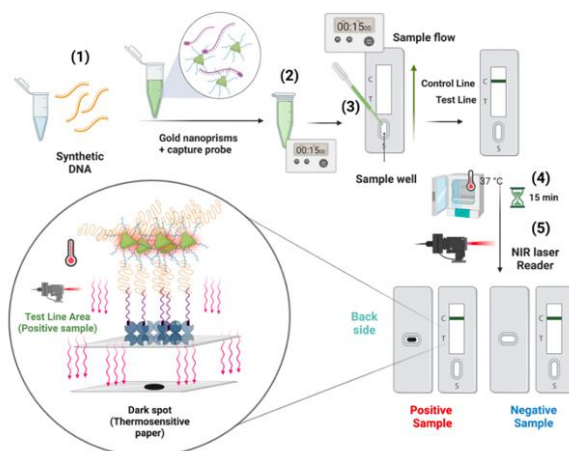


**Figure 5.** Scheme of the thermal lateral flow system and the analytical procedure. 1—Sample addition to a solution containing gold nanoprisms and the capture oligonucleotide labeled with biotin; 2—preincubation; 3—preincubated sample is added to the TLF strip, leaving the samples flow 15 min; 4—sample drying at 37 °C for 15 min; 5—test developing by NIR laser irradiation.



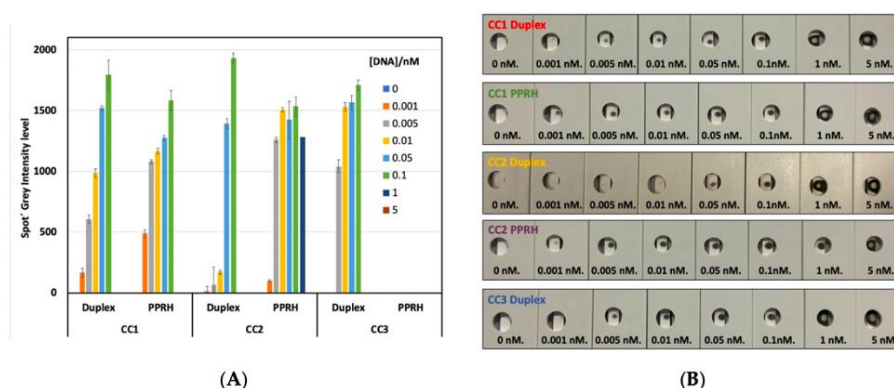


**Figure 6.** Results obtained with the thermal lateral flow system. (A): Profile of ipeak® (IUL S.A. commercial lateral flow reader) quantification of spiked samples with different concentrations of targets (from 0 to 5 nM) in UTM using capture sequences duplex-CC1, CC2, and CC3 duplex and PPRH-CC1 and CC2. Results with PPRH-CC3 sequence are not shown in this graph because NPRs aggregation was observed during the testing assay. Grey level intensity measurements were obtained from the LF reader to determine the value of LOD of the thermal lateral flow system. Standard deviation of three replicates carried out consecutively is drawn as error bars. (B): Image obtained from the back part of the LF strips (thermosensitive material) after the laser irradiation using a 1064 nm laser. The strips were loaded with spiked samples in UTM from Biocomma with different concentrations of DNA, from 0–5 nM, to determine the visual LOD of the system.

### 2.5. Second Biosensor Device Compact Electrochemical Biosensor Platform

Next, a compact fluidic electrochemical biosensor platform was developed (Figure 7) chronoamperometric responses to four different target sequence concentrations plus the blank signal in the hybridization buffer were recorded. As an example, Figure 8A depicts the signals obtained using the MNPs modified with PPRH-CC1. As expected, the cathodic currents increase with the target concentration, 0.01 nM (1 fmol) was the lowest concentration providing a signal that differed from the blank.

Figure 8B shows a bar graph comparing the analytical signals recorded with the six different capture sequences tested. In general terms, the PPRH—sequences present higher absolute current values and better sensitivities than the duplex ones. Then, the PPRH sequences were used to evaluate the electrochemical sensor performance in the UTM from Biocomma, as an approach to simulate the real conditions of analysis. Figure 8C shows bar graphs comparing the increase in the biosensor response with respect to the blank signal recorded in the UTM (in percentage) for PPRH-CC1, CC2, and CC3. Although a general decrease in the absolute current values was observed due to some possible matrix effects, the minimum concentration measured was also 0.01 nM in most cases. However, some important differences were observed among the different PPRH, CC2 showed a poor response. By contrast, the PPRH-CC1 appeared to keep a quite good response in the UTM with good proportionality with the target concentration and a wider linear range of response. Therefore, MNPs modified with PPRH-CC1 were used for the detection of SARS-CoV-2 RNA in clinically relevant samples.

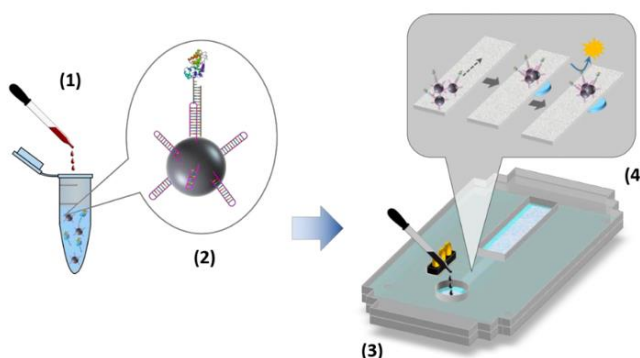


**Figure 7.** Scheme of the electrochemical biosensor platform and the analytical procedure: 1—sample addition to a solution containing functionalized MNPs and the detection oligonucleotide labeled with HRP enzyme; 2—hybridization assay on the MNP surface; 3—pretreated sample added to the electrochemical device; 4—steps taken place in the electrochemical device, including MNP flow, trapping and concentration, and electrochemical detection.

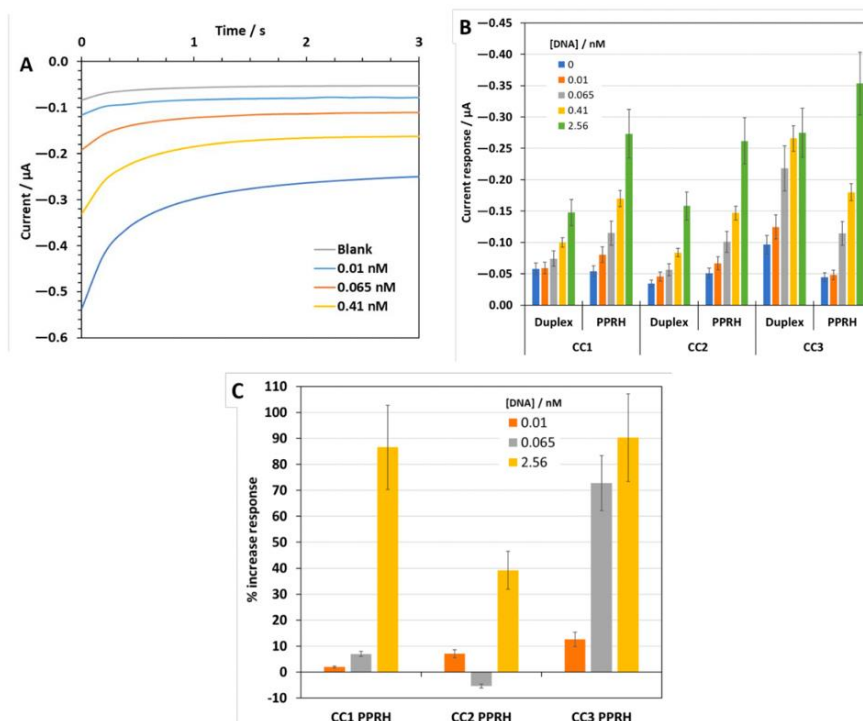


**Figure 8.** (A): Current response profiles to different concentrations of the target DNA CC1 sequence in hybridization buffer using the MNPs modified with PPRH—CC1. (B): Analytical signal values

recorded with the three different capture probes, CC1, CC2, and CC3, in a duplex and PPRH format for different concentrations of the corresponding oligonucleotide target DNA sequences in hybridization buffer. (C): Increase in response relative to the blank response (in %) recorded in the UTM from Biocomma with the PPRH—CC1, CC2, and CC3, respectively, for three of the tested oligonucleotide concentrations. Standard deviation of three replicates carried out consecutively is drawn as error bars.

## 2.6. Detection of SARS-CoV-2 RNA in Clinically Relevant Samples

To demonstrate the applicability of the two developed biosensor systems, a set of six clinical samples provided by the Biobank of the Aragon Health System (three positives and three negatives by PCR) were analyzed simultaneously. The samples were collected in the UTM from Biocomma. In the case of the TLF system evident dark spots were obtained in the back part of the LF strips, after being irradiated using NIR laser, for the three positive samples and no signals were obtained for the negatives ones (Figure 9A right side). A quantification profile was also performed using ipeak® (IUL S.A.) commercial lateral flow reader (Figure 9A left side) showing that the signal obtained for the positive 3 was higher than the signal obtained for positive 2 and this one higher than the obtained for positive 1. The graph also exposed that the signal obtained for the positive 1 was similar to the signal of the control of 0.001 nM and the values obtained for negative samples 1, 2, and 3 were very similar to the blank. In the electrochemical system, a clear increase in the analytical signal was observed for the three positive samples with respect to the negative ones (Figure 9B). In fact, the values for negatives 1 and 2 samples were very similar to the blank. The lower signal recorded for negative 3 compared with that of the blank is likely to be due to the sample matrix, collected by swabbing the patient's nasopharyngeal cavity. The biological material that is dissolved in the UTM could be very complex, and a matrix effect on the sensor response may take place, resulting in a signal that is lower than that of the blank signal recorded in a fresh UTM. Regarding the positives, the signal for the positive 3 samples was higher than the control of 0.41 nM. The Ct values for the three positive samples analyzed were 35 (sample #1), 19 (sample #2), and 30 (sample #3). Obviously, sample #2 with a Ct value of 19 was clearly positive, as it also was using our system. However, interestingly enough, the other two samples with much higher Ct values, and very especially sample #1 with Ct = 35, in the borderline between positive and negative in the PCR, gave a positive signal using the TENADA method. It should also be noted that the trend regarding the absolute signal values recorded for the three positive samples is the same for the two developed systems.

The two strategies described here especially using PPRHs as capture probes could be used as point-of-care screening for detecting SARS-CoV-2 and other viruses without the need of a pre-amplification step, as an alternative to other methods such as CRISPR-Cas13a [7–9], RPA [6], LAMP [5] and LAMP-Seq [25] developed recently. The limit of detection of TENADA was around 0.01 nM (a few femtomoles). Detection of the presence of the RNA of the SARS-CoV-2 virus in nasopharyngeal samples agreed with the results obtained by PCR. Alternative methods [5–9,25] may be more sensitive but the time required for the analysis in TENADA is less than 1 h, shorter than most of these alternative methods [5–9,25]. The detection limit, the analysis time, and the requirement of simple instrumentation are strong arguments for further development. During the two years of the pandemic, many mutations have been described. We have checked if any of the known mutations are in the selected target sequences and, until now, these mutations did not affect the target sequences, indicating that the selected polypyrimidine targets are well preserved.



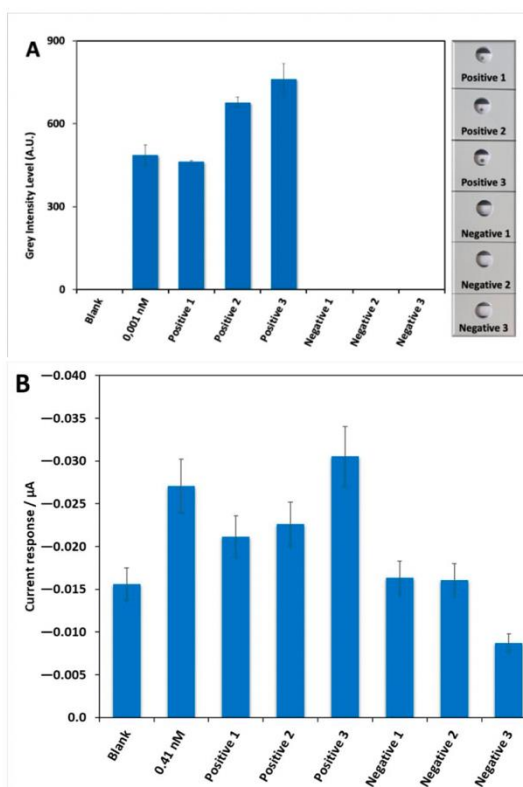


**Figure 9.** Testing of six real samples provided by the Biobank of the Aragon Health System (3 negatives and 3 positives by PCR: sample #1, Ct 35; sample #2, Ct 19 and sample #3, Ct 30) in UTM from Biocomma with the PPRH-CC1 as capture sequence using the two developed biosensor devices. (A): Profile of ipeak® (IUL S.A. commercial lateral flow reader) quantification (grey intensity level measurements, right side) of the results obtained with the TLF together with the signal obtained for the blank and control of 0.001 nM of target DNA CC1 sequence and the image obtained from the back part of the LF strips (thermosensitive material, left side) after the laser irradiation using a 1064 nm laser used. This image was used to measure the grey level intensity to develop the results of the thermal lateral flow assay. (B) Analytical signal values obtained by the electrochemical biosensor platform, together with the signal obtained for the blank and control of 0.41 nM of target DNA CC1 sequence. Standard deviation of three replicates carried out consecutively is drawn as error bars.

### 3. Materials and Methods

#### 3.1. Design of PPRH

The polypyrimidine sequences of SARS-CoV-2 genome were searched using the triplex-forming oligonucleotide Target Sequence Search software (Version V.1) from University of Texas, Austin, TX, USA (<http://utw10685.utweb.utexas.edu/tfo/>, accessed on 1 November 2022). The default parameters were set as (1) a minimum of 15 nucleotides in length; (2) a minimum of 40%GC content; and (3) a maximum allowable of 3 pyrimidine interruptions. In these conditions, we selected the longest three polypyrimidine sequences (20–21 nu-

cleotides) that were checked by BLAST +2.13.0 software to be not present in another virus or human genome ([https://blast.ncbi.nlm.nih.gov/Blast.cgi?PAGE\\_TYPE=BlastSearch](https://blast.ncbi.nlm.nih.gov/Blast.cgi?PAGE_TYPE=BlastSearch), accessed on 1 November 2022). The PPRH capture oligonucleotides were formed by the selected polypurine sequence followed by a 4-thymidine loop and a mirrored sequence to form a hairpin by intramolecular reverse-Hoogsteen bonds (see Tables S1 and S2). We designed three different hairpin oligonucleotides CC1, CC2, and CC3. For comparative purposes, purine duplex capture oligonucleotides were also prepared. The second oligonucleotide to perform the sandwich hybridization strategy was complementary to a 20-nucleotide sequence located near, usually 3 nucleotides 5', to the polypyrimidine target sequence (Figure 1).

### 3.2. Synthesis of Oligonucleotides

Oligonucleotide sequences were obtained either from commercial sources (Merck/Sigma, Haverhill, UK) or synthesized on an automatic Applied Biosystems 3400 DNA synthesizer on a 0.2  $\mu$ mol (LV200) scale using commercially available chemicals. Oligonucleotides were prepared using standard phosphoramidite solid-phase protocols. The introduction of amino groups at the 5'-position was performed by using *N*-trifluoroacetyl-6-aminoethyl 2-cyanoethylphosphoramidites. The introduction of the reporter groups such as biotin (biotin-TEG) or fluorescein (FAM) or Cy3 was performed using the appropriate phosphoramidite (if added 5'-end) or functionalized controlled-pore glass (CPG) (if added at the 3'-end). After the assembly of the sequences, oligonucleotide-supports were treated with 32% aqueous ammonia at 55 °C for 16 h. Ammonia solutions were concentrated to dryness and desalted by Sephadex G-25. Alternatively, the products were purified by cartridge oligonucleotide purification (COP) columns.

### 3.3. Gel-Binding Assays

Binding experiments were carried out by incubating the 6-FAM-labeled ss DNA or RNA probes corresponding to the SARS-CoV-2 targets with the corresponding PPRHs in a buffer containing 10 mM MgCl<sub>2</sub>, 100 mM NaCl, and 50 mM HEPES (pH 7.2), supplemented with 5% glycerol. Binding reactions (20  $\mu$ L) were incubated 30 min at 37 °C. A scrambled PPRH (HpSC6: AAGGAAGGAAGGAAGGAAGGTTTTTGAAGGAAGGAAGGAAGGAAGGAA) was used as negative control. Electrophoresis was performed on nondenaturing 8% polyacrylamide gels containing 10 mM MgCl<sub>2</sub>, 5% glycerol, and 50 mM HEPES (pH 7.2). Gels were run at a fixed voltage of 190 V (4 °C) using a running buffer containing 10 mM MgCl<sub>2</sub> and 50 mM HEPES (pH 7.2). Finally, gels were visualized using the Gel Doc™ EZ with the Image Lab Software, Version 6.0 (Bio-Rad, Barcelona, Spain). All reagents were obtained from Sigma-Aldrich (St. Louis, MO, USA).

### 3.4. Fluorescent DNA Microarray Chip

This protocol describes the chemical derivatization of the microarray slides, the spotting of the oligonucleotides, the hybridization reaction, and the fluorescence signal detection.

Slide derivatization: plain glass slides were first cleaned by immersing them in Piranha solution (H<sub>2</sub>SO<sub>4</sub>:H<sub>2</sub>O<sub>2</sub> 70:30 *v/v*) for 30 min. Subsequently, they were rinsed with Ultrapure water, activated with 10% NaOH for 2 h, and then rinsed again with ultrapure water and with ethanol 60% solution. After this cleaning step, they were dried with N<sub>2</sub>. Next, the chemical functionalization of the slides was achieved using a silane reagent. The protocol followed takes place in two steps: first, the aminopropyltrimethoxysilane (APTMS) reacts with the hydroxyl groups of the glass surface for 3 h at RT; and after, the amino groups of the silane react with the isocyanate groups of 1,4-phenylene diisothiocyanate during 2 h at RT in 10% pyridine. After this treatment, slides were serially washed with a 60% ethanol solution, methanol, and acetone, dried with N<sub>2</sub>, and stored in the desiccator until use.

DNA microarray chip manufacture: the first oligonucleotide solutions were prepared in printing buffer (150 nM sodium phosphate, 0.01% SDS) and subsequently filtered with 0.45  $\mu$ m PVDF syringe filters (Millipore). Afterward, they were spotted in defined positions

of the derivatized glass slides. This printing step was carried out using a sciFLEXARRAYER S3 (Scienion), under controlled temperature (20 °C) and humidity (65%). To perform the printing of each spot 5 drops were dispensed with a PDC70 piezo dispensing capillary (350 pL/drop). At the end of the whole printing process, slides were kept for 30 min inside the microarrayer chamber. The biofunctionalized slides were then stored at 4 °C until use. Up to 24 microarray chips could be printed in a single slide. Microarray chips for multiplex analysis consisted of a matrix of  $6 \times 6$  spots (3 different sets of oligonucleotides (first and second oligonucleotides) including the PPRH and duplex clamp format and 3 replicates of each). This scheme could be easily modified to allow the analysis of a higher number of samples.

**Hybridization assay:** the slides were placed on an Arrayit holder provided with a silicon gasket defining  $8 \times 3$  wells on each slide. Before starting the assay, the slides were washed (200  $\mu$ L/well) three times with PBST (0.01 M phosphate buffer in a 0.8% saline solution at pH 7.5 plus 0.005% Tween 20). Target standard solutions were prepared in Hybridization buffer (10 mM Tris, 1 mM EDTA, 1 M NaCl, adjusted at pH 7.2) or in the corresponding universal transport media used to collect the samples to be analyzed (7 concentration points plus zero: 0.032 nM–500 nM). Then, samples or standard solutions were added (50  $\mu$ L/well) and incubated at RT for 5 min. The next hybridization step included the addition of the second Cy3 labeled oligonucleotide (50  $\mu$ L/well). After 15 min at RT, the slides were washed again (200  $\mu$ L/well) three times with PBST and once with ultrapure water and finally dried with  $N_2$ .

**Fluorescence signal detection:** microarray fluorescence measurements were recorded on an InnoScan 710 (Innopsys) with an optical filter of 532 nm. The spots were measured by subtracting the mean of the corresponding fluorophore background intensity to the mean of the fluorophore foreground intensity using Mapix (Innopsys) software. The standard curves were analyzed with a four-parameter logistic equation using the software GraphPad Prism. Thus, the equation follows the formula:  $[(A - B)/(1 - (x/C)^D)] + B$  where A is the maximal fluorescence, B the minimum, C the concentration producing 50% of the difference between A and B ( $IC_{50}$  value), and D the slope at the inflection point of the sigmoid curve. The limit of detection (LoD) was defined as the concentration producing 10% of the maximal fluorescence ( $IC_{10}$  value).

### 3.5. Thermal Lateral Flow System Using PPRH as Biosensors Linked to Gold Nanoprisms

All reagents used in this biosensor's development were of high purity, analytical grade or equivalent and were purchased from Sigma-Aldrich (Madrid, Spain).

#### 3.5.1. Gold Nanoprisms (NPrs) Synthesis

Gold NPrs with a plasmon band between 1000 and 1200 nm have been prepared following a methodology previously reported by Pelaz et al. 2012 [26] prior to use, all glassware was washed with aqua regia and rinsed thoroughly with Milli-Q water.

To perform the synthesis, 140 mL of 0.5 mM  $Na_2S_2O_3$  (11 mg, 70  $\mu$ mol) aqueous solution (Milli-Q water) containing 10  $\mu$ L of 0.1 M KI (0.16 mg, 1  $\mu$ mol) was added slowly to 200 mL of aqueous  $HAuCl_4 \cdot H_2O_2$  mM (136 mg, 400  $\mu$ mol) in a slow but continuous way during 30 s. After 4 min, another 140 mL of  $Na_2S_2O_3$  0.5 mM (11 mg, 70  $\mu$ mol) containing 10  $\mu$ L of KI 0.1 M (0.16 mg, 1  $\mu$ mol) was added. After another undisturbed 4 min, 60 mL of  $Na_2S_2O_3$  0.5 mM (4.7 mg, 30  $\mu$ mol) were slowly added to the solution and the resulting mixture was left reacting for an hour at room temperature avoiding the light covering the mixture with aluminum foil.

UV-VIS (Cary-50, Variant) spectra revealed a strong absorbance peak at 1000 nm corresponding to gold nanoprisms as well as a minor absorption band at 536 nm corresponding with the by-product gold pseudospherical (polyhedral) nanoparticles. The concentration of NPrs was calculated using their LSPR peak absorbance at 1050 nm and applying a conversion factor ( $\epsilon$ ) 29 mL  $mg^{-1}$   $cm^{-1}$ . Note that  $\epsilon$  was obtained from combined UV-VIS spectroscopy / ICP analyses.

Gold NPrs were stabilized using heterobifunctional HS-PEG-COOH (Mercapto- $\omega$ -carboxy PEG MW. 5000 Dalton) by conjugation to the gold surface by the thiols (SH-) functional groups. For this purpose, a solution of HS-PEG5000-COOH (aq.) with a ratio PEG: Au NPrs of 2:1 (in mg) was added to the nanoprisms solution. HS-PEG5000-COOH was diluted in 1-mL Milli-Q and a determined volume of 10 mg/mL stock solution of NaBH<sub>4</sub> was then added to reach a 1:1 molar ratio of PEG: NaBH<sub>4</sub>. After that, the pH was raised to 12 with the addition of aqueous 2 M NaOH under mild mixing and the solution was sonicated for 30 min at 60 °C to complete the reaction with HS-PEG5000-COOH.

The resultant mix of gold nanoprisms and spheres was centrifuged at 5500 rcf for 15 min at room temperature to remove unreacted reagents and unwanted by-products. While the supernatant was discarded, the precipitate was resuspended in the same volume of water and two further washing steps were performed with Milli-Q water using the same conditions.

The aqueous dispersion of PEG derivatized gold nanoprisms and gold nanospheres (2 mL, 1.5 mg/mL) were loaded (mixed with loading buffer, i.e., TBE 0.5 $\times$ , 5% glycerol) in wells within an agarose gel (2.5%) immersed in an electrophoresis cuvette filled with TBE 0.5 $\times$ . Electrophoresis separation was run at 120 V for 40 min. The higher electrophoretic mobility and lower hydrodynamic diameter of nanospheres compared to nanoprisms, allows the nanospheres to enter in the gel and the nanoprisms stayed in the wells. The green nanoprisms solution was recovered from the wells carefully with a micropipette. The resultant dispersion of gold nanoprisms in TBE 0.5 $\times$  was centrifuged and washed with Milli-Q water (3 times in total) at 5500 rcf for 15 min at room temperature to remove the TBE buffer.

### 3.5.2. Nanoprisms Biofunctionalization

PEG derivatized gold nanoprisms were functionalized using amine-modified oligonucleotides able to recognize specific regions of COVID-19 viral RNA (PPRHs-CC1, CC2 or CC3 or duplex-CC1, CC2, or CC3). Briefly, 0.25 mg of PEG-derivatized gold nanoprisms were incubated with EDC (*N*-(3-dimethylaminopropyl)-*N*'-ethylcarbodiimide hydrochloride) 3 mM and Sulfo-NHS (*N*-Hydroxysulfosuccinimide sodium salt) 7 mM in 0.5 mL of filtered 10 mM MES (2-morpholinoethanesulfonic acid monohydrate) buffer pH 6 for 30 min at 37 °C; after that, the activated gold nanoprisms were centrifuged 9 min at 6500 rpm. After removal of the supernatant, the nanoprisms were incubated for 1.5 h at 37 °C with 0.68 nmol of amino-modified oligonucleotides (PPRHs-CC1, CC2, or CC3 or duplex-CC1, CC2, or CC3), 0.5 mL in filtered 50 mM MES buffer pH 6). Then, 0.5 mL of alpha-methoxy-omega-amino polyethylene glycol (MeO-PEG-NH<sub>2</sub>, 750 Da) in filtered 50 mM MES buffer pH 6 were added to the nanoprisms solution for 2 h at 37 °C added to derivatize the remaining activated carboxylic groups. Finally, biofunctionalized nanoprisms were washed out of ligand excess by centrifugation; nanoprisms were centrifuged three times for 9 min at 5500 rpm, and then pellets were resuspended in filtered 10 mM Hepes (4-(2-Hydroxyethyl)piperazine-1-ethanesulfonic acid) buffer pH 7.2 0.1% Tween 20, 0.1% BSA.

### 3.5.3. Capture Molecules (Test and Control Lines) Preparation

Test line's capture molecule was prepared by dissolving streptavidin (streptavidin from *Streptomyces avidinii*) at 1 mg/mL in Milli-Q water.

Control line's capture molecule was prepared by incubation of carboxylic acid-modified oligonucleotides able to recognize the nanoprisms biofunctionalized with first oligonucleotide (PPRHs-CC1, CC2, or CC3-amino or duplex-CC1, CC2 or CC3-amino) with EDC (*N*-(3-dimethylaminopropyl)-*N*'-ethylcarbodiimide hydrochloride) 1.5 mM and Sulfo-NHS (*N*-hydroxysulfosuccinimide sodium salt) 3 mM in 0.05 mL of filtered 10 mM MES (2-Morpholinoethanesulfonic acid monohydrate) buffer pH 6 for 30 min at 37 °C. After that, a solution of BSA (bovine serum albumin) 2 mg/mL (0.05 mL) in filtered 10 mM MES buffer pH 6 was added for 2 h at 37 °C. Then, the bioconjugate was centrifuged for 14 min



at 14,000 rpm using a 3 K Amicon Ultra tube to concentrate it. The final concentration is determined by UV spectrophotometer at 280 nm.

### 3.5.4. Preparation of Lateral Flow Test Strips

The TLF (thermal lateral flow) system was composed of 3 parts, held together in polyvinyl chloride (PVC) backing card sheet with a geometry of 80 mm × 300 mm: a glass fiber conjugate Pad (8964, Ahlstrom-Munksjö), which can be considered also as a sample pad), a nitrocellulose membrane (FF80HP, GE Healthcare Life Sciences, Little Chalfont, UK), and a cellulose wicking pad (222, Ahlstrom-Munksjö) which facilitates the liquid flow (Figure 5).

To prepare the capture and control regions, a solution of both capture and control molecules, at 1 and 3 mg/mL, respectively, in MilliQ water and PBS 10 mM (Pan Biotech, GmbH) were applied to the nitrocellulose membrane using a KinBio XYZ Platform Dispenser HM3030/HM3035 (Kinbio Tech.Co., Ltd. Shanghai, China). The nitrocellulose membrane was incubated after the test and control lines dispensing at 37 °C for 1 h in an incubator. After the test and control molecules solutions dried, the LFA strip parts were mounted onto the adhesive PVC backing card, and all the system was covered by a plastic film, which ensured correct contact between parts and avoided evaporation process during the assay. The final assembly was cut into 0.4 mm wide strips, and they were stored in a dry place.

### 3.5.5. Thermal Lateral Flow Assay (TLFA) Methodology

An amount of 25 µL of a spiked sample solutions containing increasing concentrations of the target DNA sequence complementary to the capture probes (0, 0.001, 0.005, 0.01, 0.05, 0.1, 1, and 5 nM) in Universal Transport Media (Biocomma Ltd., Shenzhen, China) were tested by mixing with 10 µg of nanoprisms functionalized with amino modified first (PPRH-CC1, CC2, or CC3-amino or duplex-CC1, CC2 or CC3) oligonucleotides, 0.0638 nmol (26.6 µL) of a biotinylated second oligonucleotide and 23.4 µL of running buffer. This mix was preincubated during 15 min at room temperature. Then, 0.1 mL of mix was loaded into the strip' cassette. The chromatography was performed for 15 min and after that the strip was dried at 37 °C for 15 min. The development of the stripes was performed by using a NIR laser (1064 nm, 1200 mW, 1 min). Positive samples will provide a dark brown spot after laser irradiation on the nitrocellulose strip when positive samples with high concentration of synthetic DNA were analyzed) and/or in the thermosensitive paper on the back side of the nitrocellulose which were included to increase the sensitivity of the sensor. A scheme of the process can be seen in Figure 5.

### 3.6. Electrochemical Biosensor

All reagents used in this approach were of high purity, analytical grade, or equivalent and were purchased from Sigma-Aldrich (Spain), unless stated otherwise. An amount of 200 nm diameter carboxylated magnetic nanoparticles (MNPs, fluidMAG-ARA, Chemically GmbH, Germany), 1-ethyl-3-(3-dimethylaminopropyl)carbodiimide hydrochloride (EDC), 0.1 M 2-(N-morpholino)ethanesulfonate (MES) buffer pH 5.0, phosphate-buffered saline (PBS) solution pH 7.4, 50 mM tris(hydroxymethyl)aminomethane (TRIS) buffer pH 7.2, 0.1 M citrate/acetate buffer pH 5.5, ferrocene-methanol and H<sub>2</sub>O<sub>2</sub> were utilized. The oligonucleotides used were: the capture sequences (PPRH-CC1, CC2, and CC3; duplex-CC1, CC2, and CC3), the target sequences CC1, CC2, and CC3, and the thiol-reported sequences (RP-CC1, CC2, and CC3), respectively. These three thiol-reported sequences were labeled with the horseradish peroxidase (HRP) enzyme using an HRP-oligo conjugation kit (thiol oligo) from CellMosaic, Inc. ([https://www.cellmosaic.com/content/Manual/DCM53402\\_HRP\\_Oligo\\_Kit\\_VB.pdf](https://www.cellmosaic.com/content/Manual/DCM53402_HRP_Oligo_Kit_VB.pdf); accessed on 23 April 2021, Woburn, MA, USA).

The compact fluidic electrochemical biosensor platform comprises the following main components. A scheme can be seen in Figure 7.

1. A reusable electrochemical cell of two gold thin-film electrodes fabricated by a standard photolithographic/lift-off process on 4-inch silicon wafers at the IMB-CNM Clean Room facilities [27]. Additionally,  $8 \times 8.3 \text{ mm}^2$  silicon chips, each one including a  $1 \times 1 \text{ mm}^2$  working electrode and a  $1.5 \times 1 \text{ mm}^2$  counter/reference electrode were manufactured.
2. A disposable fluidic channel made of Whatman® cellulose chromatography paper, Grade 1, cut using a custom-made die cutter (Tecnocut, Barcelona, Spain) sandwiched between two polyvinyl layers patterned using a blade plotter (CAMM-1 Servo Cutter, Roland DG, Barcelona, Spain) to expose the fluidic channels in the sample addition and detection areas.
3. A poly(methyl methacrylate) cartridge to integrate and align the cell and the fluidic channel, machined using a CO<sub>2</sub>-laser printer (Epilog Mini 24, Epilog Laser, Golden, CO, USA). The bottom part of the cartridge included an Nd magnet to trap MNPs inside the platform, as explained below.

The performance of the biosensor comprises the use of MNPs functionalized with the required capture sequences. The functionalization process was carried out as follows. An amount of 5 mg of MNPs were washed 2× with 1 mL MES buffer by using a magnetic separator and incubated with 5 mg of EDC in 250 µL of MES buffer for 10 min at RT and 750 rpm. After the activation, the MNPs were washed 2× with 1 mL MES buffer and resuspended in 125 µL of MES buffer. 0.17 nmol of capture sequence (PPRH-CC1, CC2 or CC3, and duplex-CC1, CC2, or CC3) were added and incubated for 2 h at 750 rpm. Then, the MNPs were again washed 3× with 1 mL of PBS and incubated in PBS containing 0.1% BSA for 2 h at 750 rpm. Finally, the solution was changed and the modified MNPs were resuspended in 1 mL PBS containing 0.05% sodium azide as preservative. Some 200 µL aliquots were prepared and stored in the fridge at 4 °C, until use.

The functionalized MNPs were used for sample pretreatment, which comprised the capture of the target sequence outside the biosensor device. An 83.3 µg/mL solution of MNPs modified with the capture sequence was prepared in TRIS buffer containing 1 mM EDTA and 1 M NaCl (hybridization buffer). To 300 µL of this suspension, 100 µL of a standard sample solution was added together with 100 µL of 83.3 nM HRP-conjugated reported sequence solution. Standard solutions containing increasing concentrations of the target DNA sequence (0, 0.01, 0.065, 0.41, and 2.56 nM) were tested. A first study was performed using the hybridization buffer to prepare the solutions. Thereafter, the evaluation was repeated but prepared the solutions of the target sequence in the Universal Transport Media from Biocomma Ltd., to simulate the real matrix of nasopharyngeal swab collected samples. In both studies, the mixture was incubated for 15 min at RT and 750 rpm. After this one-step incubation process, the MNPs were trapped with a magnet. The reaction solution was discarded and the MNPs were resuspended and concentrated in 100 µL PBS solution containing 0.05% Tween 20 (see Figure 7).

Once the sample was pretreated, some 7 µL of the MNP concentrated suspension was cast on the sample addition area of the fluidic channel in the electrochemical biosensor device and allowed to flow by capillary action. Solution took around 3 min to reach the area over the cartridge-inserted magnet where the MNPs were trapped. Then, a washing step was carried out by adding 7 µL citrate/acetate buffer solution and it was left to flow until all the solution disappeared from the sample addition area, taking around 6 min. Then, 7 µL of citrate/acetate buffer pH 5.5 containing 1.7 mM H<sub>2</sub>O<sub>2</sub> and 2 mM ferrocene-methanol was added to the fluidic channel, and it was left to flow for 5 min. At this time, a chronoamperometric measurement at −0.15 V vs. Au CRE was carried out recording the current every 200 ms for 3 s. For more experimental details on the performance of the two-electrode electrochemical cell see reference [27].

The HRP label catalyzed the reduction of H<sub>2</sub>O<sub>2</sub> using the ferrocene-methanol as electron donor, in situ generating its redox counterpart, that is ferrocenium methanol cation. This cation was reduced back to ferrocene-methanol at the electrode surface and the produced current signal was directly proportional to the concentration of the target



sequence in the solution (see Figure 8). The current responses at 1.6 s were used as the analytical signal.

### 3.7. Determination of SARS-CoV-2 RNA in Clinically Relevant Samples

Samples and data from patients included in this study were provided by the Biobank of the Aragon Health System (PT20/00112), integrated with the Spanish National Biobanks Network and they were processed following standard operating procedures with the appropriate approval of the Ethics and Scientific Committees.

Three positive and three negative samples confirmed by PCR were tested by using the thermal lateral flow and the electrochemical biosensor systems. The six samples come from nasopharyngeal swabs that were collected from patients during the first year of the pandemic situation (August 2020). The UTM from Biocomma was used for the collection, which contains an inactivating agent for the positive samples. The samples were kept at  $-80^{\circ}\text{C}$  to preserve the viral RNA until the moment of measurement.

For the TLF system, 25  $\mu\text{L}$  of sample either positive, negative, blank, or control, were tested by mixing the sample with 10  $\mu\text{g}$  of nanoprisms functionalized with amino-modified first oligonucleotide PPRHs-CC1, 0.0638 nmol (26.6  $\mu\text{L}$ ) of the specific biotinylated second oligonucleotide and 23.4  $\mu\text{L}$  of running buffer. 0.1 mL of this mixture was loaded directly into the strip cassette. The chromatography was performed for 15 min and after that, the strips were straightly irradiated by using a NIR laser (1064 nm, 1200 mW, 1 min). Positive samples provided a dark brown spot after laser irradiation in the back part of the strip, where the thermosensitive paper was included, and no signals were obtained for the negative ones.

For the electrochemical system, the samples were analyzed without any previous treatment, taking 100  $\mu\text{L}$  and performing the measurement procedure described in the previous Section 3.6.

## 4. Conclusions

We have described the design and preparation of three triplex-forming oligonucleotides PPRH-CC1, PPRH-CC2, and PPRH-CC3 with high affinity for polypyrimidine sequences for the efficient capture and detection of SARS-CoV-2 genome. These oligonucleotides together with the appropriate reporter probes have been adapted to three biosensing devices including glass microarrays, thermal lateral flow devices, and electrochemical devices. In the thermal lateral flow device, the PPRH or duplex oligonucleotides are used for the functionalization of gold nanoprisms. Using glass microarrays, capture oligonucleotides were used for the functionalization of the glass surface. The trimolecular complex was detected after the hybridization of a mixture of analyte and the fluorescently (TAMRA or Cy3) labeled reporter probe. Limits of detection also depended on the UTM used and, in this analytical platform, the differences between duplex and PPRH capture probes are not so evident as in the previous biosensors, but it is possible to achieve values close to the ones observed with the previous devices.

In the thermal lateral flow system, the trimolecular complex is captured by streptavidin and developed by irradiation of an IR laser-generated heat that is collected in a thermal paper. Detection limits are between 0.005 and 0.01 nM. The best results were found with the PPRH-CC1 system. The PPRH and duplex-CC3 were not possible to be studied due to the aggregation of the nanoparticles. The PPRH-CC1 gave a limit of sensitivity one order of magnitude higher than duplex-CC1 (0.01 nM versus 0.1 nM).

The data from the electrochemical sensor gave similar results to the thermal lateral flow test. The trimolecular complex is detected using a peroxidase label that is directly attached to the reporter probe. Limits of detection slightly varied depending on the universal transport media (UTM) used but they were clearly better for PPRH oligonucleotides CC1 and CC3. The PPRH-CC2 system generated a lower signal, as well as duplex oligonucleotides, did.



The limit of detection of TENADA using synthetic oligonucleotides was around 0.01 nM (a few femtomoles) without the use of amplification steps. Detection of the presence of the RNA of the SARS-CoV-2 virus in nasopharyngeal samples agreed with the results obtained by PCR. The time required for the analysis is less than 1 h. The detection limit, the analysis time, and the requirement of simple instrumentation are strong arguments for further development. In addition, the triplex-assisted assay can be readily adapted for the detection of any pathogen with either DNA or RNA genomes as PPRHs are able to produce strand displacement when targeting duplex DNA [15–18] and it only requires the knowledge of the pathogen genome sequence.

The high affinity of PPRHs towards viral RNA can also be used to inhibit viral replication. For this reason, we are also studying the antiviral properties of CC1 and CC3 by infecting with SARS-CoV-2 virions VeroE6 cells previously transfected with the PPRHs. Results will be published when completed. Taking all these results together we demonstrate that non-canonical DNA structures and especially triplex nucleic acids can open new and interesting routes for improving biomedical applications of oligonucleotides such as the diagnosis of viral diseases.

## 5. Patents

A patent application has been filed (EP21382818.9, priority date 13.09.2021).

**Supplementary Materials:** The following supporting information can be downloaded at: <https://www.mdpi.com/article/10.3390/ijms232315258/s1>.

**Author Contributions:** Conceptualization: V.G., V.N., R.E., M.–P.M., C.F.-S., J.M.d.l.F. and C.J.C.; Methodology: A.A., C.C.-A., M.G.-C., L.V., V.G., V.N., E.B., A.B., A.J.F., E.A., S.V., A.D., R.G., C.F.-S., J.M.d.l.F. and C.J.C.; Investigation: A.A., C.C.-A., M.G.-C., L.V., E.B., A.B., A.J.F., E.A., S.V., A.D. and R.G.; Data curation: A.A., C.C.-A., M.G.-C. and L.V.; Validation: A.A., C.C.-A., M.G.-C. and L.V.; Writing-review and editing: A.A., C.C.-A., M.G.-C., L.V., V.G., V.N., E.B., A.B., A.J.F., E.A., S.V., A.D., R.G., R.E., M.–P.M., C.F.-S., J.M.d.l.F. and C.J.C.; Conceptualization: V.G., V.N., R.E., M.–P.M., C.F.-S., J.M.d.l.F. and C.J.C.; Project administration: V.G., V.N., R.E., M.–P.M., C.F.-S. and J.M.d.l.F.; Supervision: R.E., M.–P.M., C.F.-S., J.M.d.l.F. and C.J.C. All authors have read and agreed to the published version of the manuscript.

**Funding:** This work was funded by Consejo Superior de Investigaciones Científicas (CSIC) (Project POC4CoV, CSIC-COV19-041), CHEST Foundation (040105-268-A1V), La Marató de TV3 Foundation (Project 202110-30-31-32-33 to R.E., C.C., V.N., V.G., J.M.), Spanish Ministry of Science and Innovation (MICINN) [PID2020-118145RB-I00 to R.E., PID2021-122271OB-I00 to V.N. and C.C.; PID2019-107158GB-I00 to R.G.] DGA and Fondos Feder (Bionanosurf E15\_17R) and CIBER-Consortio Centro de Investigación Biomédica en Red (CB06/01/0019 to R.E., CB06/01/0036 to P.M., CB16/01/00263 to J.M.), Instituto de Salud Carlos III (Spanish Ministry of Science and Innovation and European Commission, European Regional Development Fund). This research was also funded by the European Commission-NextGenerationEU (Regulation EU 2020/2094), through CSIC's Global Health Platform (PTI). We want to particularly acknowledge the patients and the Biobank of the Aragon Health System (PT20/00112), integrated in the Spanish National Biobanks Network for their collaboration.

**Institutional Review Board Statement:** Not applicable.

**Informed Consent Statement:** Not applicable.

**Data Availability Statement:** Data will be made available from the authors on request.

**Acknowledgments:** The work completed in this study has been supported by the following ICTS NANBIOIS units: U2. Customized Antibody Service (CAbS), and U29 Oligonucleotide Synthesis Platform (OSP). We thank Carme Fàbrega for helpful discussions. This work used the Spanish ICTS Network MICRONANOFABS which was partly supported by the Spanish Ministry of Science and Innovation.

**Conflicts of Interest:** The authors declare no conflict of interest.

## References

1. Mercer, T.R.; Salit, M. Testing at the scale during COVID-19 pandemics. *Nat. Genet. Rev.* **2021**, *22*, 415–426. [\[CrossRef\]](#) [\[PubMed\]](#)
2. Esbin, M.N.; Whitney, O.N.; Chong, S.; Maurer, A.; Darzacq, X.; Tjian, R. Overcoming the bottleneck to widespread testing: A rapid review of nucleic acid testing approaches for COVID-19 detection. *RNA* **2020**, *26*, 771–783. [\[CrossRef\]](#) [\[PubMed\]](#)
3. Corman, V.M.; Landt, O.; Kaiser, M.; Molenkamp, R.; Meijer, A.; Chu, D.K.W.; Bleickeret, T.; Brünink, S.; Schneider, J.; Schmidt, M.L.; et al. Detection of 2019 novel coronavirus (2019-nCoV) by real-time RT-PCR. *Eur. Surveill.* **2020**, *25*, 2000045. [\[CrossRef\]](#)
4. Wikramaratna, P.; Paton, R.; Ghafari, M.; Lourenco, J. Estimating false-negative detection rate of SARS-CoV-2 by RT-PCR 2020. *Eur. Surveill.* **2020**, *25*, 2000568.
5. Dao Thi, V.L.; Herbst, K.; Boerner, K.; Meurer, M.; Kremer, L.P.M.; Kirrmaier, D.; Freistaedter, A.; Papagiannidis, D.; Galmozzi, C.; Stanifer, M.L. A colorimetric RT-LAMP assay and LAMP-sequencing for detecting SARS-CoV-2 RNA in clinical samples. *Sci. Transl. Med.* **2020**, *12*, eabc7075. [\[CrossRef\]](#) [\[PubMed\]](#)
6. Piepenburg, O.; Williams, C.H.; Stemple, D.L.; Armes, N.A. A DNA detection using recombination proteins. *PLoS Biol.* **2006**, *4*, 1115–1121. [\[CrossRef\]](#)
7. Gootenberg, J.S.; Abudayyeh, O.O.; Lee, J.W.; Esslerzbichler, P.; Dy, A.J.; Joung, J.; Verdine, V.; Donghia, N.; Naringer, N.; Freije, C.A.; et al. Nucleic acid detection with CRISPR-Cas13a/C2c2. *Science* **2017**, *356*, 438–442. [\[CrossRef\]](#)
8. Broughton, J.P.; Deng, X.; Yu, G.; Fasching, C.L.; Servellita, V.; Singh, J.; Miao, X.; Streithorst, J.A.; Granados, A.; Sotomayor-Gonzalez, A.; et al. CRISPR-Cas12 based detection of SARS-CoV-2. *Nat. Biotechnol.* **2020**, *38*, 870–874. [\[CrossRef\]](#)
9. Fozouni, P.; Son, S.; Derby, M.D.L.; Knott, G.J.; Gray, C.N.; D'Ambrosio, M.V.; Zhao, C.; Switz, N.A.; Kumar, G.R.; Stephens, S.I.; et al. Amplification-free detection of SARS-CoV-2 with CRISPR-Cas13a and mobile phone microscopy. *Cell* **2021**, *184*, 323–333.e9. [\[CrossRef\]](#)
10. Zhou, P.; Yang, X.L.; Wang, X.G.; Hu, B.; Zhang, L.; Zhang, W.; Si, H.R.; Zhu, Y.; Li, B.; Huang, C.L.; et al. A pneumonia outbreak associated with a new coronavirus of probable bat origin. *Nature* **2020**, *579*, 270–273. [\[CrossRef\]](#)
11. Wu, F.; Zhao, S.; Yu, B.; Chen, Y.M.; Wang, W.; Song, Z.G.; Hu, Y.; Tao, Z.W.; Tian, J.H.; Pei, Y.Y.; et al. A new coronavirus associated with human respiratory disease in China. *Nature* **2020**, *579*, 265–269. [\[CrossRef\]](#) [\[PubMed\]](#)
12. Bloom, J.S.; Sathe, L.; Munugala, C.; Jones, E.M.; Gasperini, M.; Lubock, N.B.; Yarla, F.; Thompson, E.M.; Kovary, K.M.; Park, J.; et al. Massively scaled-up testing for SARS-CoV-2 RNA via next-generation sequencing of pooled and barcoded nasal and saliva samples. *Nat. Biomed. Eng.* **2021**, *5*, 657–665. [\[CrossRef\]](#) [\[PubMed\]](#)
13. Lambert-Niclot, S.; Cuffel, A.; Le Pape, S.; Vauloup-Fellous, C.; Morand-Joubert, L.; Roque-Afonso, A.M.; Le Goff, J.; Delaunay, C. Evaluation of a rapid diagnostic assay for detection of SARS-CoV-2 antigen in nasopharyngeal swabs. *J. Clin. Microbiol.* **2020**, *58*, e00977–e20. [\[CrossRef\]](#) [\[PubMed\]](#)
14. Scohy, A.; Anantharajah, A.; Bodéus, M.; Kabamba-Mukadi, B.; Verroken, A.; Rodriguez-Villalobos, H. Low performance of rapid detection test as frontline testing for COVID-19 diagnosis. *J. Clin. Virol.* **2020**, *129*, 104455. [\[CrossRef\]](#)
15. Calvo-Lozano, O.; Aviñó, A.; Friaza, V.; Medina-Escuela, A.; Huertas, C.S.; Calderón, E.J.; Eritja, R.; Lechuga, L.M. Fast and accurate *Pneumocystis pneumonia* diagnosis in human samples using a label-free plasmonic biosensor. *Nanomaterials* **2020**, *10*, 1246. [\[CrossRef\]](#)
16. Pla, L.; Aviñó, A.; Eritja, R.; Ruiz-Gaitán, A.; Pemán, J.; Friaza, V.; Calderón, E.J.; Aznar, E.; Martínez-Mañez, R.; Santiago-Felipe, S. Triplex hybridization-based nanosystem for the rapid screening of *Pneumocystis pneumonia* in clinical samples. *J. Fungi* **2020**, *6*, 292. [\[CrossRef\]](#)
17. Noé, V.; Aubets, E.; Félix, A.J.; Ciudad, C.J. Nucleic acids therapeutics using PolyPurine Reverse Hoogsteen hairpins. *Biochem. Pharm.* **2021**, *189*, 114371. [\[CrossRef\]](#)
18. Coma, S.; Noé, V.; Eritja, R.; Ciudad, C.J. Strand displacement of double-stranded DNA by triplex-forming antiparallel purine-hairpins. *Oligonucleotides* **2005**, *15*, 269–283. [\[CrossRef\]](#)
19. Aubets, E.; Chillon, M.; Ciudad, C.J.; Noe, V. PolyPurine Reverse Hoogsteen Hairpins work as RNA species for gene silencing. *Int. J. Mol. Sci.* **2021**, *22*, 10025. [\[CrossRef\]](#)
20. Aviñó, A.; Huertas, C.S.; Lechuga, L.M.; Eritja, R. Sensitive and label-free detection of miRNA-145 by triplex formation. *Anal. Bioanal. Chem.* **2016**, *408*, 885–893. [\[CrossRef\]](#)
21. Ribes, A.; Santiago-Felipe, S.; Aviñó, A.; Candela-Noguera, V.; Eritja, R.; Sancenón, F.; Martínez-Mañez, R.; Aznar, E. Design of oligonucleotide-capped mesoporous silica nanoparticles for the detection of miRNA-145 by duplex and triplex formation. *Sens. Actuators B. Chem.* **2018**, *277*, 598–603. [\[CrossRef\]](#)
22. Huertas, C.S.; Aviñó, A.; Kurachi, C.; Piqué, A.; Sandoval, J.; Eritja, R.; Esteller, M.; Lechuga, L.M. Label-free DNA-methylation detection by direct ds-DNA fragment screening using poly-purine hairpins. *Biosens. Bioelectr.* **2018**, *120*, 47–54. [\[CrossRef\]](#) [\[PubMed\]](#)
23. Ranki, M.; Palva, A.; Virtanen, M.; Laaksonen, M.; Soderlund, H. Sandwich hybridization as a convenient method for the detection of nucleic acids in crude samples. *Gene* **1983**, *21*, 77–85. [\[CrossRef\]](#)
24. Aviñó, A.; Eritja, R.; Ciudad, C.; Noé, V. Parallel clamps and polypurine hairpins (PPRH) for gene silencing and triplex-affinity capture: Design, synthesis and use. *Curr. Protoc. Nucleic Acid Chem.* **2019**, *77*, e78. [\[CrossRef\]](#) [\[PubMed\]](#)
25. Ludwig, K.U.; Schmithausen, R.M.; Li, D.; Max, L.; Jacobs, M.L.; Hollstein, R.; Blumenstock, K.; Liebing, J.; Ślabicki, M.; Ben-Shmuel, A.; et al. LAMP-Seq enables sensitive, multiplexed COVID-19 diagnostics using molecular barcoding. *Nat. Biotechnol.* **2021**, *39*, 1556–1562. [\[CrossRef\]](#) [\[PubMed\]](#)

26. Pelaz, B.; Grazil, V.; Ibarra, A.; Magen, C.; del Pino, P.; de la Fuente, J.M. Tailoring the synthesis and heating ability of gold nanoprisms for bioapplications. *Langmuir* **2012**, *28*, 8965–8970. [[CrossRef](#)]
27. Gutiérrez-Capitán, M.; Baldi, A.; Merlos, A.; Fernández-Sánchez, C. Array of individually addressable two-electrode electrochemical cells sharing a single counter/reference electrode for multiplexed enzyme activity measurements. *Biosens. Bioelectr.* **2022**, *201*, 113952. [[CrossRef](#)]

## Supplementary

**Table S1.** Results of TFO target sequences search in the SARS-CoV-2 genome.

Sequences (5'-3')	Length	%GC	Orientation	Position
AGATGAGGATGAAGAAGAAGGTGA	24	41.7	Forward	3031
GAGCAGAAGGGTAGTAGAGAG	21	47.6	Reverse	17128
GTGATGAGGAACGAGAAGAGG	21	47.6	Reverse	28823
GAGGGAAGGACATAAGATGA	20	40.0	Reverse	2470

**Table S2.** Sequences of the PPRH and reporter probes (RP) used in this study.

Oligonucleotide	Sequence (5'-3')
<b>PPRH-CC1</b>	<b>GAGCAGAAGGGTAGTAGAGAGTTTGGAGAGATGATGGGAAGACGAG</b>
<b>PPRH-CC2</b>	<b>GTGATGAGGAACGAGAAGAGGTTTGGAGAAGAGCAAGGAGTAGTG</b>
<b>PPRH-CC3</b>	<b>GAGGGAAGGACATAAGATGATTTAGTAGAATACAGGAAGGGAG</b>
<b>CC1-RP</b>	<b>GGCCAATAGCAAAATGACTC</b>
<b>CC2-RP</b>	<b>TGCGTAGAAGCCTTTTGCC</b>
<b>CC3-RP</b>	<b>CCCTTCCACAAAAATCAAC</b>

**Table S3.** Sequences of the oligonucleotides prepared in this work.

### CC1 SYSTEM:

CC1PPRH-amino

5'-NH<sub>2</sub>-TTTTGAGCAGAAGGGTAGTAGAGAGTTTGGAGAGATGATGGGAAGACGAG-3'

CC1PPRH

5'-GAGCAGAAGGGTAGTAGAGAGTTTGGAGAGATGATGGGAAGACGAG-3'

CC1PPRH-Control (reverse Hoogsteen strand scrambled)

5'-GAGCAGAAGGGTAGTAGAGAGTTTGGAGAGCAGGAATAGAGGAGT-3'

CC1duplex-amino

5'-NH<sub>2</sub>-TTTTGAGCAGAAGGGTAGTAGAGAG-3'

CC1biotineRP:

5'-GGCCAATAGCAAAATGACTC-BIOTINE-3'

CC1-TamraRP:

5'-GGCCAATAGCAAAATGACTC-Tamra-3'

CC1-Cy3RP:

5'-GGCCAATAGCAAAATGACTC-Cy3-3'

CC1-ThiolRP:

5'-GGCCAATAGCAAAATGACTC-Thiol-3'

CC1target:

5'-GAGTCATTTTGCTATTGGCCTAGCTCTACTACCTTCTGCTC-3'

CC1DNAtarget-FAM

5'-FAM-GCTATTGGCCTAGCTCTACTACCTTCTGCTCGCATAGTGTATAC-3'

CC1RNAtarget-FAM

5'-FAM-CUAGCUCUCUACUACCCUUCUGCUCGCAUA-3'



## Results

CC1DNAtargetLarge-FAM

5' FAM-GGTAAGAGTCATTTTGCTATTGGCCTAGCTCTCTACTACCTTCTGCTCGCATA 3'

### CC2 SYSTEM

CC2PPRH-amino:

5'-NH<sub>2</sub>-TTTTGTGATGAGGAACGAGAAGAGGTTTTGGAGAAGAGCAAGGAGTAGTG-3'

CC2PPRH:

5'-GTGATGAGGAACGAGAAGAGGTTTTGGAGAAGAGCAAGGAGTAGTG-3'

CC2duplex-amino:

5'-NH<sub>2</sub>-TTTTGTGATGAGGAACGAGAAGAGG-3'

CC2-biotineRP:

5'- TGCGTAGAAGCCTTTTGGC-biotine-3'

CC2-Cy3RP:

5'- TGCGTAGAAGCCTTTTGGC-Cy3-3'

CC2-ThiolRP:

5'- TGCGTAGAAGCCTTTTGGC-thiol-3'

CC2-biotineRPNew:

5'-CCTTCTGCGTAGAAGCCTTT -biotine-3'

CC2DNATarget:

5'-GCCAAAAGGCTTCTACGCAGAAGGGAGCAGAGGCGGCAGTCAAGCCTCTTCTCGTTCCTCATCAC-3'

CC2NewTarget:

5'-AAAGGCTTCTACGCAGAAGGGAGCAGAGGCGGCAGTCAAGCCTCTTCTCGTTCCTCATCAC-3'

CC2DNAtarget-FAM

FAM-5'- TCAAGCCTCTTCTCGTTCCTCATCACGTAGT-3'

### CC3 SYSTEM

CC3PPRH-amino:

5'-NH<sub>2</sub>-TTTTGAGGGAAGGACATAAGATGATTTTAGTAGAATACAGGAAGGGAG-3'

CC3PPRH:

5'-GAGGGAAGGACATAAGATGATTTTAGTAGAATACAGGAAGGGAG-3'

CC3duplex-amino:

5'-NH<sub>2</sub>-TTTTGAGGGAAGGACATAAGATGA-3'

CC3-biotineRPnew1:

5'-CCCTTTCCACAAAAATCAAC-BIOTINE-3'

CC3-biotineRP:

5'- CCCTTTCCACAAAAATCAAC-biotine-3'

CC3-Cy3RP:

5'- CCCTTTCCACAAAAATCAAC-Cy3-3'

CC3-thiolRP:

5'- CCCTTTCCACAAAAATCAAC-thiol-3'

CC3DNATarget:

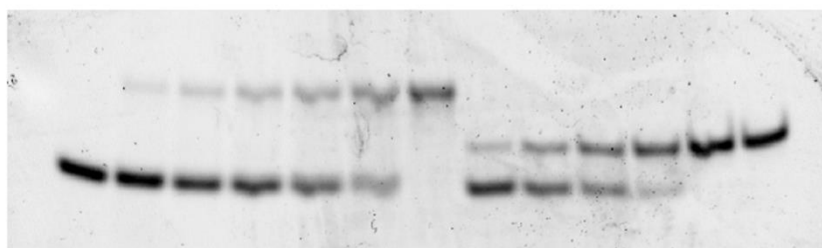
5'-GTTGATTTTGTGGAAAGGGCTATCATCTTATGTCCTTCCTC-3'

CC3DNAtarget-FAM

FAM-5'-GTGGAAAGGGCTATCATCTTATGTCCTTCCTCAGTCAGCACCTCAT-3'

CC3RNAtarget-FAM

FAM-5'-GGCUAUCAUCUUAUGUCCUCCUCAGUCA-3'

**Figure S1.** Binding of CC2-DNA-target with NH<sub>2</sub>-PPRH-CC2 and NH<sub>2</sub>-CC2 duplex

$$K_d \text{ PPRH} = 6.04 \cdot 10^{-7} \text{ M}$$

$$K_d \text{ duplex} = 7.47 \cdot 10^{-7} \text{ M}$$

**Table S4.** Dissociation constants of PPRH-CC1, CC2, CC3 and PPRH-CC1-control and duplex-CC1, CC2 and CC3.

Oligonucleotide	$K_d (10^{-7}), \text{ M}$
PPRH-CC1 <sup>#</sup>	3.88
Duplex-CC1 <sup>#</sup>	4.79
PPRH-CC2 <sup>&amp;</sup>	6.04
Duplex-CC2 <sup>&amp;</sup>	7.47
PPRH-CC3 <sup>*</sup>	3.86
Duplex-CC3 <sup>*</sup>	10.5
PPRH-CC1Control <sup>#</sup>	6.24

<sup>#</sup>Target oligonucleotide used: CC1DNAtargetLarge-FAM;

<sup>&</sup>Target oligonucleotide used: CC2DNAtarget-FAM;

<sup>\*</sup>Target oligonucleotide used: CC3DNAtarget-FAM;

**Table S5.** Limit of detection values (LoD, expressed in nanomolar, nM) corresponding to the CC pairs calibration curves obtained in a multiplex assay. The table shows the data obtained when diluting the corresponding targets in different Universal Transport media (UTMs 1-3) compared with the values achieved when using hybridization buffer. In this case, the first oligonucleotides (PPRH and duplex format) were printed on the glass slide at a concentration of 125 nM. Subsequently, serial target dilutions were added (ranging from 500 nM to 0 with a dilution factor of 5). Finally, the labelled second oligonucleotides were added at an optimized concentration of 250 nM.

Buffer/UTM	CC1		CC2		CC3	
	PPRH	Duplex	PPRH	Duplex	PPRH	Duplex
Hybridization buffer	1.01	0.64	3.16	4.67	1.56	3.49
UTM 1	0.47	0.61	2.53	2.60	2.58	3.76
UTM 2	0.01	0.06	2.03	1.23	0.72	0.33
UTM 3	0.03	0.02	0.89	0.71	1.50	1.17





4.3.1 Additional results to Article IV

In addition to SARS-CoV-2, we targeted the H1N1 and HRSV viruses. Two PPRHs were designed for each viral sequence and binding assays were carried out (Figures 15 and 16) to determine the specific binding of each PPRH with its corresponding target. PPRHs bound specifically to their targets since we observed shifted bands in the experiments for both viruses. No binding was detected when the negative control HpSc9 was combined with H1N1 and HRSV viral probes.

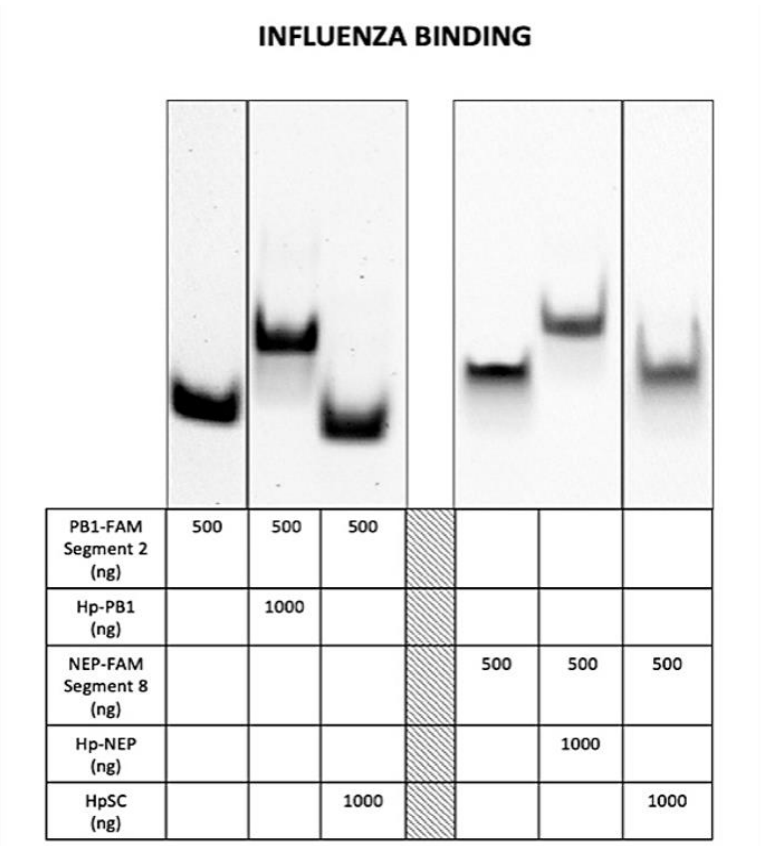


**Figure 15.** PPRHs binding to their target sequences in the Influenza A virus (H1N1). The binding of HpPB1, and Hp-NEP and HpSc9 (1000 ng) to the complementary FAM-labeled polypyrimidine target sequence dsDNA (500 ng) is shown. Image is representative of a minimum of three independent EMSA experiments.

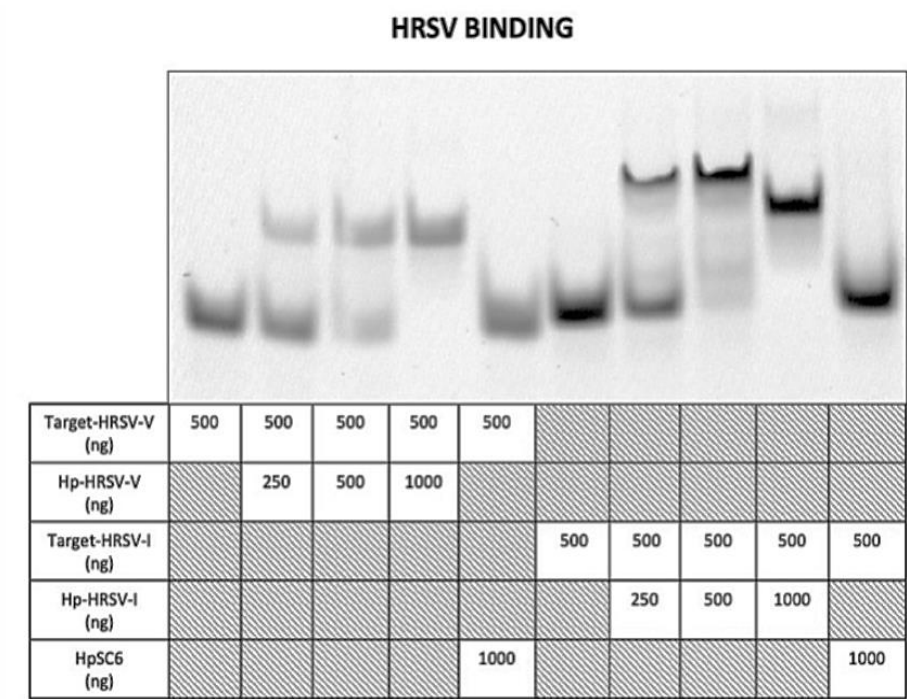


**Figure 16.** PPRH Binding to their target sequences in the Human respiratory syncytial virus (HRSV). The binding of Hp-HRSV-V, Hp-HRSV-I (from 250 to 1000 ng) and HpSc9 (1000 ng) to the complementary FAM-labeled polypyrimidine target sequence dsDNA (500 ng) is depicted. This image is representative of a minimum of three independent EMSA experiments.

#### 4.5. ARTICLE V (Manuscript in preparation)

##### Polypurine Reverse Hoogsten hairpins as a therapeutic tool for SARS-CoV-2

**Background:** During COVID-19 pandemic, the main objective of the scientific community was to develop an effective and wide-scale producible vaccine to prevent the spreading of SARS-CoV-2, the symptoms of the disease and its impact in public health (Gupta et al., 2021). Alternative therapeutic approaches to treat and mitigate the symptoms of COVID-19 have also been explored (Scavone et al., 2020). Many of those were antiviral drugs targeting SARS-CoV-2 to (Qiao et al., 2023) inhibit its replication, which can be achieved by aiming different viral regions (Babalola et al., 2023). Other strategies were based on the development of therapeutic oligonucleotides such as antisense oligonucleotides (ASOs) (Qiao et al., 2023) small interfering RNAs (siRNA) (Y. R. Lee et al., 2023), (CRISPR)-based systems (Nguyen et al., 2020), or microRNAs (miRNA) (Ergün et al., 2023). These therapeutic oligonucleotides could be used to target SARS-CoV-2 sequences to potentially repress virus replication. In this direction, we wanted to explore the protective and therapeutic capabilities of PPRHs against this virus.

**Objectives:** To evaluate the efficacy of PPRHs as a therapeutic approach for suppressing SARS-CoV-2 replication both *in vitro* and *in vivo*.

**Results:** We used two previously designed PPRHs, named CC1 and CC3, directed against replicase and spike regions of SARS-Cov-2, respectively. Each PPRH interacted in a sequence-specific manner with their corresponding ssRNA and ssDNA targets at very low concentrations.

*In vitro*, PPRHs showed a high transfection rate in VERO-E6 monkey kidney cells that express ACE2 receptor (Beyerstedt et al., 2021), with an optimal concentration of 300 nM complexed with 30  $\mu$ M DOTAP. At this nM concentration, CC1 and CC3 PPRHs were able to inhibit SARS-CoV-2 proliferation as compared to a scramble PPRH. CC1

and CC3 ASOs and parallel orientation (PO) PPRHs showed no inhibitory effect.

Furthermore, we analyzed the effects of these PPRHs *in vivo* in K18-hACE2 transgenic mice which express the human ACE2 receptor (Dong et al., 2022; McCray et al., 2007). Mice treated with CC1-PPRH survived the viral infection, with no significant weight loss and clinical signs. Scramble and 80% of CC3-treated mice presented drastic weight loss as well as increasing clinical signs and had to be euthanized seven days after infection with SARS-CoV-2.

**Conclusions:** In this work we validated both *in vitro* and *in vivo* the protective and therapeutic ability of PPRHs against SARS-CoV-2. While both CC1 and CC3 PPRHs demonstrated to be efficacious at inhibiting SARS-CoV-2 proliferation *in vitro*, only CC1 showed potent effects *in vivo*. CC1-PPRH holds promise as a valuable candidate for further investigations against viral infection.



## Article

# Polypurine Reverse Hoogsteen hairpins as a therapeutic tool for SARS-CoV-2 infection

**Abstract:** Although COVID-19 pandemic was declared no longer a global emergency by World Health Organization in May 2023, SARS-CoV-2 is still infecting people across the world. Many therapeutic oligonucleotides such as ASOs, siRNAs or CRISPR-based systems emerged as promising antiviral strategies for the treatment of SARS-CoV-2. In this work we explored the inhibitory potential on SARS-CoV-2 replication of Polypurine Reverse Hoogsteen Hairpins (PPRHs), CC1-PPRH and CC3-PPRH, previously validated for COVID-19 diagnosis. Both PPRHs were tested *in vitro*, exhibiting promising efficacy in impeding viral replication. Further evaluation in an *in vivo* model revealed that intranasal administration of CC1-PPRH provided significant protection in mice infected with SARS-CoV-2. The properties of PPRHs positions them as promising candidates for the development of novel therapeutics against SARS-CoV-2 and other viral infections for the development of novel therapeutics against SARS-CoV-2 and other viral infections.

**Keywords:** PPRH; SARS-CoV-2; Therapy; Virology

## 1. Introduction

Severe Acute Respiratory Syndrome Coronavirus 2 (SARS-CoV-2) belongs to the family of coronaviruses, which are enveloped, positive and single stranded viruses. This family includes viruses responsible for common colds as well as severe pathogens such as SARS-CoV and MERS-CoV [1,2]. SARS-CoV-2 is responsible for the COVID-19 outbreak originated in Wuhan, China in late 2019, and declared as a global pandemic in March 2020 for its rapid spread and high fatality rate [3]. In May 2023, the World Health Organization (WHO) declared that COVID-19 was no longer classified as a public health emergency of international concern. SARS-CoV-2 infected over 769.3 million individuals and had caused more than 6.95 million deaths worldwide by August 2023 [4]. However, these numbers might be underestimated due to many non-detected asymptomatic cases.

The genetic material of SARS-CoV-2, whose RNA is about 30kb, carries instructions for the synthesis of both structural and non-structural proteins. The non-structural proteins include two open reading frames (ORF), including ORF 1a and ORF 1b, that are translated into two polypeptides, pp1a and pp1ab [5]. Structural proteins consist of spike (S), membrane (M), envelope (E), and nucleocapsid (N) along with accessory proteins. Spike interacts with the human ACE2 receptor, allowing viral attachment and fusion with the membrane. Then, the viral genome is transcribed and translated by the host machinery, and the newly synthesized viral RNA and proteins are assembled in the host cells cytoplasm. Finally, viral particles are enclosed in vesicles, transported to the cell surface, and released. This process frequently results in programmed cell death of the infected cells [1,6].

During the pandemics, the scientific community worked intensively to develop a wide array of therapies against SARS-CoV-2. The primary approach was to develop an effective and large-scale producible vaccine. While the development of traditional vaccines typically spans a period of 10 to 15 years, COVID-19 vaccines were generated and authorized for their emergency use within a remarkably short timeframe, ranging from 12 to 16 months [7]. While vaccines were under development, other options were considered to treat and reduce COVID-19 symptoms [8,9]. One approach was the usage of

**Citation:** To be added by editorial staff during production.

Academic Editor: Firstname Last-name

Received: date

Revised: date

Accepted: date

Published: date



**Copyright:** © 2023 by the authors. Submitted for possible open access publication under the terms and conditions of the Creative Commons Attribution (CC BY) license (<https://creativecommons.org/licenses/by/4.0/>).

antiviral drugs such as polymerase or protease inhibitors, immune modulators, viral entry inhibitors, neuraminidase inhibitors, which target various stages of the viral life cycle by interfering with specific viral proteins or enzymes [10, 11]. Another approach was based on monoclonal antibodies specific against the SARS-CoV-2 spike protein [12]. Other therapies include convalescent plasma therapy that uses, as a temporary protection, recovered plasma from previously infected patients, which provides antibodies against the virus [13] or corticoids as anti-inflammatory drugs to modulate the immune system in critically ill patients [14].

Alternative strategies to potentially repress viral replication involved the development of therapeutic oligonucleotides to target SARS-CoV-2 sequences. Some of the strategies include antisense oligonucleotides (ASOs) [15,16], microRNAs (miRNA) [17], small interfering RNAs (siRNA) [18–21] or CRISPR-based systems [22,23]. In this work, we used Polypurine Reverse Hoogsteen (PPRH) hairpins targeting specific SARS-CoV-2 regions for therapeutic and protective purposes against the viral infection and its spread. PPRHs are non-modified single-stranded DNA molecules made of two polypurine strands, linked by a four-thymidine loop, that run in antiparallel orientation and interact with each other by Hoogsteen bonds. These molecules are designed to specifically bind by Watson-Crick bonds to a DNA or RNA sequence rich in polypyrimidines and form a triplex structure, displacing the complementary strand in the case of dsDNA [24–27]. The target sequence does not have to be a pure polypyrimidine stretch and can present up to three purine interruptions. Thus, PPRHs can be designed to target practically any gene in the genome [28]. Our research group has previously designed PPRHs directed towards SARS-CoV-2 for diagnostical purposes, namely CC1-PPRH, CC2-PPRH and CC3-PPRH, targeting *replicase*, *N gene*, and *spike* of the SARS-CoV-2 genome, respectively [29]. In this study, we focused on CC1 and CC3 PPRHs to evaluate their potential therapeutic effect against the virus.

## 2. Results

### 2.1. PPRH Target Selection and Sequence Design

CC1-PPRH (CC1) and CC3-PPRH (CC3) target replicase (CTCTC-TACTACCCTTCTGCTC), and spike (TCATCTTATGTCCTCCCTC) regions in the SARS-CoV-2 genome, located at 17111 and 24690 positions, respectively [29] (Figure 1). These designs were obtained by combining the Triplex-Forming Oligonucleotide (TFO) search tool and the following PPRH design criteria: no more than three pyrimidine interruptions [30], a minimum of 40% GC content and a minimum length of 20 nucleotides. As a negative control, we designed a scrambled PPRH with similar length, GC content, and number of interruptions as CC1 and CC3 PPRHs (Table 1).

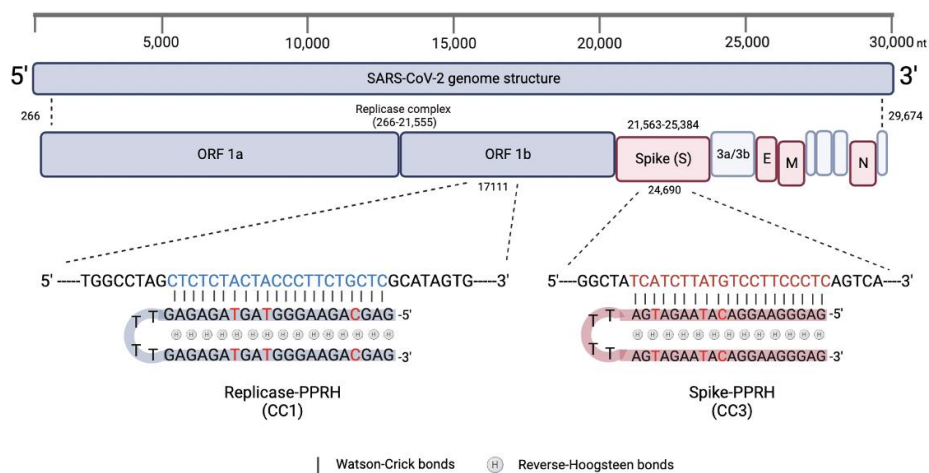


**Figure 1.** Schematic representation of the SARS-CoV-2 genome and the corresponding CC1 and CC3 targeting PPRHs. In blue, the target of CC1-PPRH in the replicase complex, ORF1b; in red the target of CC3-PPRH in the *spike* gene. (Figure created with biorender.com).

PPRH Name (Location)	Gene location	Target length	% GC Content	Target (5'-3') PPRH
CC1-PPRH (Replicase)	17111	21	47.62	5'- CTCTCT <u>ACT</u> ACCCCTCTGCTC -3' 4T $\left\{ \begin{array}{l} \text{GAGAGATGATGGGAAGACGAG-5'} \\ \text{GAGAGATGATGGGAAGACGAG-3'} \end{array} \right.$
CC3-PPRH (Spike)	24690	20	40	5'- TCATCTTATGTCCTCCCTC -3' 4T $\left\{ \begin{array}{l} \text{AGTAGAATACAGGAAGGGAG-5'} \\ \text{AGTAGAATACAGGAAGGGAG-3'} \end{array} \right.$
SCR (Negative Control)	-	21	47.62	5'-AGAGAGGTTAGGAGGACAAGG 3'-AGAGAGGTTAGGAGGACAAGG $\right\}$ 4T

**Table 1.** Name, location, length, GC content and sequence of the two PPRHs targeting specific SARS-CoV-2 genome regions (CC1 and CC3) and the scrambled PPRH (SCR) used as a negative control. Interruptions are marked in red in the PPRHs and underlined in the target sequence.



## 2.2. PPRHs Binding to SARS-CoV-2 target sequences.

To study the interactions between the designed PPRHs and their target regions in SARS-CoV-2, we conducted electrophoretic mobility shift assays (EMSAs) on native gels (Figure 2). A fixed amount of each target, either as single stranded (ss) DNA or RNA sequences, was incubated with increasing amounts of the specific PPRH. In all cases, we observed a shifted band corresponding to the triplex structure, which increased in intensity with increasing amount of PPRH (Figure 2A). Binding curves were obtained from the quantification of the bands corresponding to the triplex and the corresponding concentration of PPRH (Figure 2B) and the calculated values for dissociation constants ( $K_d$ ) are indicated below each binding image (Figure 2A). All RNA-PPRH and DNA-PPRH interactions were very strong and highly specific since all  $K_d$  values were in the order of nanomolar. PPRHs targeting ssRNA showed a lower  $K_d$ , interacting with higher affinity as compared to ssDNA. CC1-ssRNA had a lower  $K_d$  value than CC3-ssRNA but CC3-ssDNA  $K_d$  was lower than CC1-ssDNA.

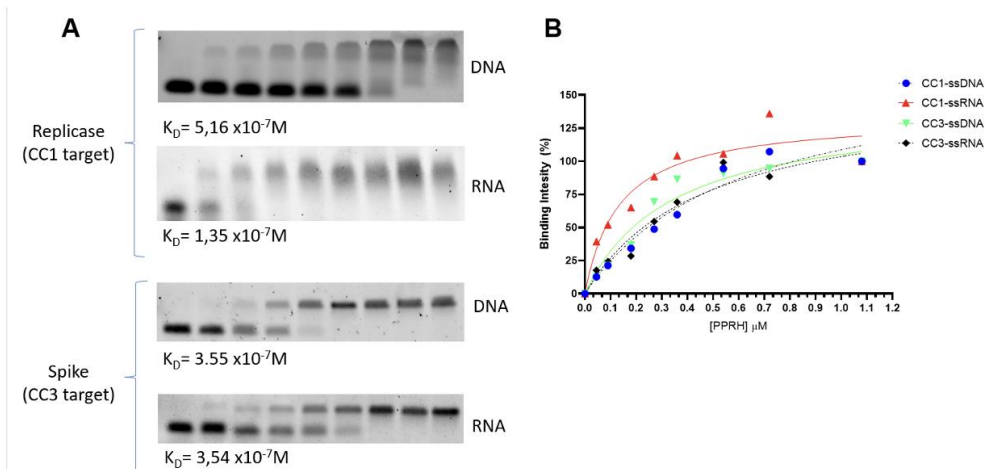


**Figure 2. CC1 and CC3 PPRH binding to their corresponding SARS-CoV-2 genome target sequences (A)** Representative images of the binding assays of CC1 and CC3 PPRHs targeting replicase and spike regions of SARS-CoV-2 with their corresponding constants of dissociation ( $K_d$ ). **(B)** Binding curves of RNA-PPRH and DNA-PPRH triplex formations. Graphics and  $K_d$ s values were obtained using GraphPad one-site specific binding analyses.

## 2.3. CC1-PPRH internalization in VERO-E6 cells

We wanted to evaluate the uptake of PPRHs complexed with DOTAP in cells that express the ACE2 receptor. As a model, we used the VERO-E6 cell line, since these monkey kidney cells do express the receptor [31]. Cells were incubated for 24 hours with FAM-labeled CC1-PPRH and its internalization was evaluated by flow cytometry. As shown in Figure 3A, 70% of the cells were transfected at the minimum amount of PPRH tested (100 nM) with a fluorescence x-mean value of 10. Optimal internalization occurred in cells transfected with 300 nM of PPRH. At this concentration, 95% of cells showed PPRH internalization with a x-mean value of 87.3 (Figure 3B).

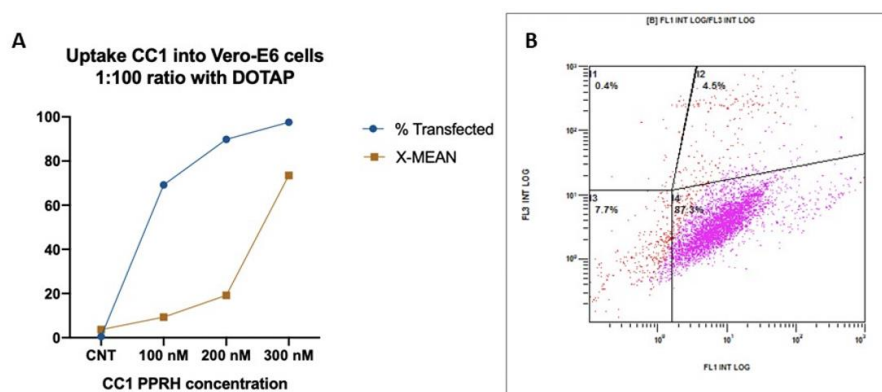


**Figure 3. Cellular uptake of CC1-PPRH in VERO-E6 cells.** (A) Uptake of increasing concentrations of FAM labeled CC1-PPRH in VERO-E6 cells determined by flow cytometry. In blue, the percentage of transfected cells; in orange the fluorescence x-mean. (B) Fluorescent intensity of CC1 (300 nM) transfected with DOTAP (30  $\mu$ M) in VERO-E6. I1 represents non-fluorescent living cells, I2 non-fluorescent dead cells, I3 fluorescent dead cells and I4 fluorescent living cells.

#### 2.4. SARS-CoV-2 mRNA proliferation inhibition by CC1 and CC3 PPRHs

Next, we wanted to study the protective effect of the PPRHs upon viral infection. VERO-E6 cells were transfected with different oligonucleotides 24 hours before viral infection, and SARS-CoV-2 RNA levels were determined 48 hours after infection. In this approach, CC1 and CC3 targeting PPRHs, antisense oligonucleotides (ASO), parallel orientation PPRHs (PO) which are PPRHs with the same orientation as the target, and a scrambled PPRH (SCR-CNT) as a negative control, were used at a concentration of 300 nM, complexed with 30  $\mu$ M of DOTAP (Figure 4). CC1 and CC3 PPRHs reduced SARS-CoV-2 expression by 93 and 92%, respectively. Since PO-PPRH were expected to not affect SARS-CoV-2 replication because they are not able to bind to their target, their corresponding SARS-CoV-2 RNA values were similar to SCR-CNT (Figure 4). Previous studies reported the successful inhibition of SARS-CoV-2 infection *in vitro* using ASOs [15,16]. However, these results were not reflected when we used ASOs targeting the same regions as PPRHs since these showed similar non-inhibitory results as PO-PPRHs. All together, these results revealed that PPRHs were much more efficient than ASOs to target SARS-CoV-2.

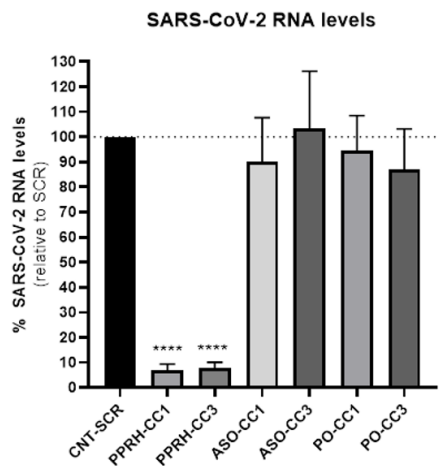


**Figure 4.** Levels of viral RNA in VERO-E6 cells infected with SARS-CoV-2. Cells were transfected with either PPRHs, ASOs, POs or a negative control SCR at a concentration of 300 nM and 30  $\mu$ M of DOTAP, 24 hours before SARS-CoV-2 infection. Levels of SARS-CoV-2 RNA were determined 48 h upon infection by Real Time PCR. Results are the mean of three separate experiments with internal duplicates. Statistical significance was analyzed by one-way ANOVA with a post hoc Dunnett test comparing groups with the CNT-SCR; \*\*\*\*  $p < 0.0001$ .

2.5. Internalization of CC1 and CC3 PPRHs in K18-hACE2 mouse lung cells.

Once we demonstrated the efficacy of PPRHs directed against SARS-Cov-2 *in vitro*, we wanted to explore their effects *in vivo* in K18-hACE2 transgenic mice which express the human ACE2 receptor under the control of the human keratin 18 promoter in the epithelia, including airway epithelia, where infections begin [32-33]. Firstly, we explored the internalization of SARS-CoV-2 targeting PPRHs in mouse lung cells. The following oligonucleotides VP7, a non-fluorescent oligonucleotide, and FAM-labeled PPRHs CC1 and CC3 were applied intranasally mixed with *in vivo*-JET-PEI. Six hours after administration, lungs were snap-frozen, and sections were prepared. As shown in Figure 5A, mice lung cells were successfully transfected with both CC1 and CC3 PPRHs. The mean of CC1 and CC3 FAM-positive lung cells was 4.5 and 7 %, respectively (Figure 5B). On the other hand, control cells, treated with VP7, displayed minimal or no fluorescence (Figure 5A and 5B).

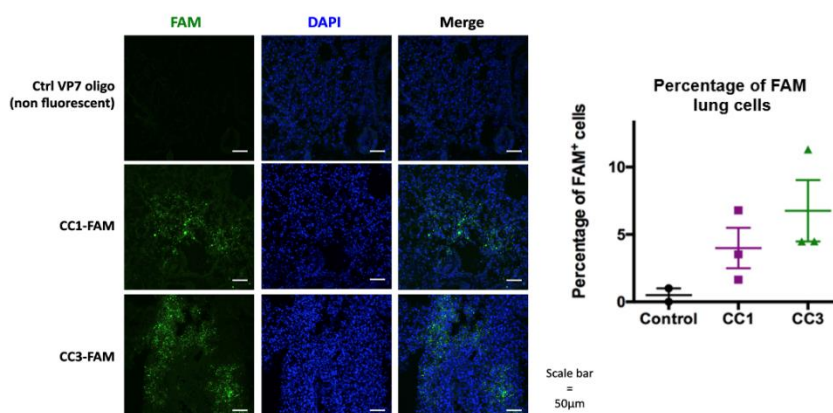


**Figure 5. PPRH internalization in mouse lung cells.** (A) VP7, a control non-fluorescent oligonucleotide and fluorescein, FAM-labeled, CC1 and CC3 PPRHs were administered intranasally to K18-hACE2 mice lung cells. Cell fluorescence was evaluated six hours after oligonucleotide administration. Images were obtained by confocal microscopy. In green, FAM-positive cells; in blue, cells nuclei counterstained with DAPI (B) Quantification of FAM-positive positive lung cells upon CC1 or CC3 intranasal administration. Experiments were performed in triplicate.

## 2.6. SARS-CoV-2 proliferation inhibition by CC1 and CC3 PPRHs in K18-hACE2 mice

To evaluate the therapeutic effects of PPRHs against SARS-CoV-2 infection *in vivo*, CC1, CC3, and SCR PPRHs were delivered intranasally using *in vivo*-JET-PEI. The administration was performed twice at 20 μg and 10 μg, respectively, 24 and 4 hours prior to SARS-CoV-2 infection. Then, mice were infected with the viral MAD6 strain, and additional doses of 10 μg of PPRH were administered on days 2, 4, 6, and 8 after infection (Figure 6A). Mice were weighed daily and monitored for 14 days. Since the beginning of the infection, mice treated with the scrambled control PPRH showed severe body weight loss (15%), and the highest severity rating, with a clinical score of 75 (Figures 6B, 6C and 6D). In cases where the animals lost 20% or more body weight or presented signs of severe suffering with clinical scores higher than 50 [34], euthanasia was performed seven days after infection. In comparison, all mice treated with CC1 PPRH survived the infection (Figure 6B), showing no significant body weight lost (less than 5%) (Figure 6C), and only mild or no clinical signs over the 14 days period of monitorization (Figure 6D). In the case of CC3, 20 % of mice survived the infection (Figure 6B). The other 80% presented an increasing weight loss and evident clinical signs over the period of monitorization, reaching a weight loss of 25% and a clinical score of 79, thus being sacrificed seven days post-infection (dpi) (Figures 6B, 6C and 6D). After 14 dpi, mice that survived the infection regained their lost weight (Figure 6B).

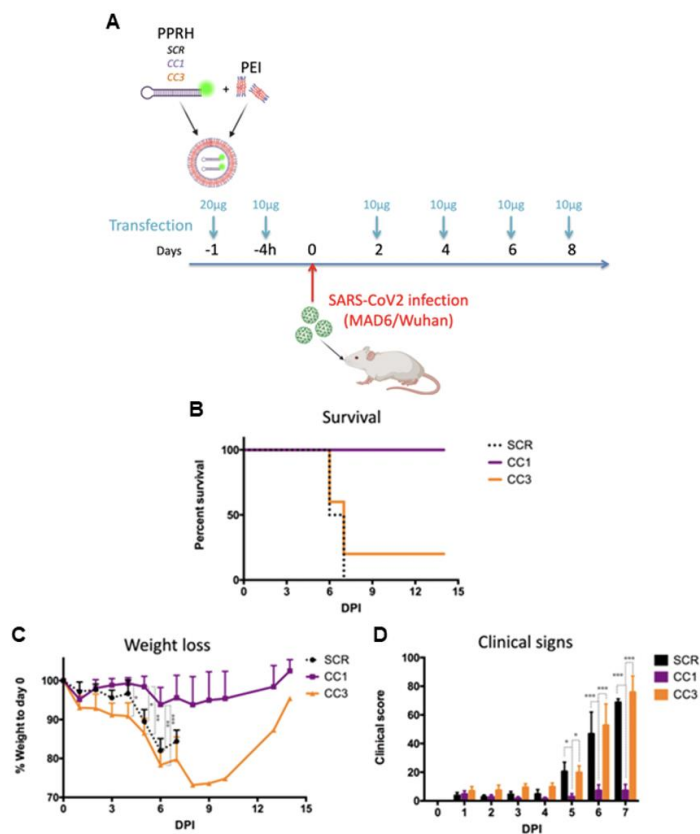


**Figure 6.** Effect of CC1, CC3 and SCR PPRH intranasal administration in K18-hACE2 mice infected with SARS-CoV-2 **(A)** Design of the treatment of K18-hACE2 mice with CC1 and CC3, complexed with *in vivo*-JET-PEI. The red arrow indicates the intranasal inoculation of SARS-CoV-2 ( $1 \times 10^5$  PFU/mouse). **(B)** Rate of survival of K18-hACE2 mice infected with SARS-CoV-2 and treated with PPRHs (SCR, CC1 or CC3). In black dots, the SCR; in purple, the CC1-PPRH; in orange, the CC3-PPRH. **(C)** Mice body weight as assessed daily. Data correspond to weight loss normalized to day 0. **(D)** Clinical signs in infected mice. Mice were monitored daily and scored. Statistical significance was analyzed by two-way ANOVA with FISHER's LSD post-test. \*  $p < 0.05$ ; \*\* $p < 0.01$ ; \*\*\* $p < 0.001$ .

**3. Discussion**

In the current project, we utilized PPRHs as a therapeutic and protective tool against SARS-CoV-2 *in vitro* and *in vivo* models expressing ACE2 receptors, to prevent its proliferation upon infection, disease symptoms and spread. We used two PPRHs, CC1 and CC3 PPRH targeting replicase and spike SARS-CoV-2 regions, previously designed for diagnosis of SARS-CoV-2 in human samples [18]. PPRH hairpins have already demonstrated their therapeutic properties as gene silencing tool both *in vitro* and *in vivo* [35-38]. Previously, therapeutic oligonucleotides such as siRNAs [18-21], ASOs [15,16] and CRISPR-based systems [22,23] have shown their ability to suppress SARS-CoV-2 replication.



However, some therapeutic strategies explored against SARS-CoV-2 involve invasive systemic delivery by intravenous administration [19]. Other strategies considered, especially for respiratory diseases, are inhaled treatments which can ensure a high drug concentration in lung and blood at low doses [40]. In 2022, Zhu, C. et. al [16] demonstrated that daily intranasal administration of ASOs targeting SARS-CoV-2 in K18-hACE2 mice presented high antiviral efficacy with no immunogenicity. Similar studies by Supramaniam, A. et. al, in 2023, showed SARS-CoV-2 replication inhibition by administrating siRNAs intranasally [21].

The designed PPRHs bound specifically to their intended targets showing higher affinity to ssRNA targets than ssDNA. The stability of RNA-PPRH interactions can be conditioned by multiple factors, such as the site-specific binding, buffer conditions, and thermodynamics of the binding process [41]. RNA-PPRH interactions may exhibit a lower *K<sub>d</sub>* due to a strong and specific base pairing, presenting higher affinity. This high specificity led to inhibition of SARS-CoV-2 proliferation both *in vitro* and *in vivo*.

Strategies using chemically modified and stabilized siRNAs against SARS-CoV-2 in VERO-E6 cells showed inhibition of up to 70% of different SARS-CoV-2 at a concentration of 30 nM [21]. A similar strategy was implemented by transfecting locked nucleic acid (LNA) ASOs that targeted SARS-CoV-2 Nucleocapsid and Spike regions in Huh-7 cells, which showed a reduction of more than 99% of SARS-CoV-2 expression at 100 nM [16]. In our work, PPRHs demonstrated to have a great effect at 300 nM, preventing viral replication *in vitro*. However, the ASO versions of CC1 and CC3 PPRHs did not prevent viral replication thus demonstrating a higher efficacy for PPRHs. These results agree with previous studies that demonstrated that PPRHs have inhibitory effects at concentrations ten times lower than those needed for ASOs, and at similar concentrations as siRNAs [25]. It is worth mentioning that, in our study, cells were transfected with 300 nM based on the maximum transfection rate observed by flow cytometry. While further studies are needed, lower concentrations might also show an effective inhibition of viral replication.

Here we explored the effects of PPRHs *in vivo* by the non-invasive intranasal administration. Out of the two PPRHs tested, CC1-PPRH strongly protected mice from virus spread and disease development when administered at very low amounts, 20 and 10 µg, assuring the survival of mice with low clinical signs and weight loss. Other studies administering intranasally LNA ASOs, demonstrated that these can be efficacious as either prophylactic or post-infection treatments. Zhu, C. et. al, [16] found that mice treated with daily intranasal administration of 400 µg of naked LNA ASOs presented no weight loss until 4 days post-infection (dpi). After 4 dpi, mice weight loss was significant and only a small group of mice survived viral infection [35]. Similar studies with daily intranasal administration of modified siRNAs (40 µg) showed low but significant decrease of viral proliferation in lungs at 7 dpi [21]. The intravenous administration 20 µg of siRNA with lipid nanoparticles achieved 20% of mice survival seven days post-infection [19]. Both ASOs [16] and siRNAs [19] strategies showed low or no significant immune stimulatory effects. Previous *in vitro* studies comparing the immunogenicity induced by PPRHs and siRNAs demonstrated that PPRHs did not generate an immune response, while the transfection of siRNAs induced unintended immune reactions [42]. Additionally, studies in mice showed that intranasal administration of *in vivo*-JET-PEI alone showed no significant immunogenic response [43]. Given the low immune response provoked by ASOs [35] and siRNAs [34] and the low impact of CC1-PPRH on mice weight and clinical symptoms, we could conclude that PPRHs may not induce severe toxic effects. Altogether, it suggests us that the intranasal administration of PPRHs complexed with *in vivo*-JET-PEI in mice may not produce noticeable immune response. However, further studies analyzing mice immune response are needed to confirm this statement.

When the COVID-19 pandemic started over three years ago, the development and deployment of therapies emerged as main strategies to mitigate the impact of the virus. Here we explored the PPRHs as a protective barrier against SARS-CoV-2 infection. Although vaccines are usually the priority agents to prevent the spreading of infectious diseases, their development is time-consuming and undergo through many steps before being approved and commercialized. Out of 273 vaccine candidates, to date, 108 have entered the human clinical phase and just 4 got to phase 4 [45]. In the case of SARS-CoV-2, the vaccines used during the COVID-19 pandemic did not prevent the infection nor the symptoms. Since other oligonucleotide-based strategies have showed effective inhibitory effect against SARS-CoV-2, we considered our laboratory-developed molecules, PPRHs as a potential therapeutic tool for viral infection. While additional research with a higher sample size is necessary, our *in vitro* and *in vivo* findings present promising outcomes, suggesting CC1-PPRH as a potential candidate against SARS-CoV-2. This PPRH demonstrates the ability to protect from infection and the spread of the virus. PPRHs present many advantages among some of their therapeutic oligonucleotide competitors, such as their efficacy at very low doses and they are very economical to synthesize given their non-modified nature [42]. This could make PPRHs producible and implementable at a large-scale in a scenario such as a new viral pandemic. Although further studies are needed before implementing PPRH in clinical assays, our technology could be used to protect patients at risk of developing SARS-CoV-2 infection and, they could be used as a treatment in patients upon infection. Altogether, our findings indicate that PPRHs offer promising approaches to improve the use of oligonucleotides in biomedical applications, particularly in the field of viral disease treatment.

#### 4. Materials and Methods

##### 4.1. Polypurine Reverse Hoogsteen hairpins

We used previously two designed PPRHs against SARS-CoV-2 replicase and spike regions, named CC1 and CC3, respectively [29]. Additionally, we designed a scrambled PPRH (SCR) as a negative control. The designed PPRHs were synthesized as non-modified oligodeoxynucleotides by Sigma-Aldrich (Haverhill, UK), resuspended in sterile Tris-EDTA buffer (10 mM Tris and 1 mM EDTA, pH 8.0) from Sigma-Aldrich (Madrid, Spain), and stored at -20 °C. For SCR PPRH, we performed BLAST analyses to avoid unintended mismatches.

##### 4.2. Cell Culture

Vero E6 cells, derived from the African green monkey kidney, were grown as described in [45], in Dulbecco's Modified Eagle Medium (DMEM) (Sigma Aldrich, Boston, MA, USA) supplemented with 5% fetal bovine serum (FBS) (Logan, UT, USA) or in Ham's F12 medium supplemented with 10% FBS (GIBCO, Invitrogen, Barcelona, Spain).

##### 4.3. PPRHs transfection

Cells were plated in 6-well dishes in 900 µL of Ham's F12 medium supplemented with 10% FBS. For transfection we used a mixture of 1,2-Dioleoyl-3-trimethylammonium propane (DOTAP; Biontex, Germany) with variable quantities of PPRHs always maintaining a molar 1:100 ratio of PPRH:DOTAP in serum-free medium up to 100 µL. After a 20-



minute incubation at room temperature, the mixture was added to the cells to reach a final volume of 1 mL.

#### 4.4. Fluorescent Microscopy and Flow Cytometry

Cells (100,000) were plated in Ham's F12 medium in 6-well dishes and transfected the following day with 10–30  $\mu$ M of DOTAP and 100–300 nM of CC1 PPRH labeled with fluorescein (6-FAM) in its 5'-end. Twenty-four hours following transfection, cells were harvested through trypsinization, resuspended in PBS, and then centrifugated at 800 $\times$ g at 4 °C for 5 minutes. The resulting pellet was resuspended in 400  $\mu$ L of cold PBS. Prior to flow cytometry analyses, propidium iodide (Merck, Madrid, Spain) was added to a final concentration of 5  $\mu$ g/mL. Flow cytometry analyses were conducted in a Gallios flow cytometer (Beckman Coulter, Inc. Barcelona, Spain) to detected green and orange fluorescences of both control and treated cells.

#### 4.5. Electrophoretic Mobility Shift Assay (EMSA)

Electrophoretic mobility shift assays (EMSA) were performed with 6-FAM-labeled single-stranded DNA (ssDNA) or RNA probes corresponding to the SARS-CoV-2 targets and their corresponding PPRHs, in a buffer containing 10 mM MgCl<sub>2</sub>, 100 mM NaCl, and 50 mM HEPES (pH 7.2), supplemented with 5% glycerol. Binding reactions were performed with increasing amounts of CC1 and CC3 PPRHs, from 0 to 300 ng combined with a fixed amount, 100 ng, of 6-FAM labeled probes. As a negative control, 100 ng of a scrambled PPRH (SCR: AGAGAGGTTAGGAGGACAAGGTTTTGGAACAGGAGGATTGGAGAGA) was used. The binding reactions (20  $\mu$ L) were incubated for 30 minutes at 37°C. Electrophoreses were carried out on non-denaturing 8% polyacrylamide gels containing 10 mM MgCl<sub>2</sub>, 5% glycerol, and 50 mM HEPES (pH 7.2), at a constant voltage of 190 V at 4°C, using a running buffer of 10 mM MgCl<sub>2</sub> and 50 mM HEPES (pH 7.2). Bands were visualized using the Gel Doc™EZ with Image Lab Software, Version 6.0 (Bio-Rad, Barcelona, Spain). All reagents were purchased from Sigma-Aldrich (St. Louis, MO, USA).

#### 4.6. Virus Infection and Quantification

After 24 hours of transfection with PPRH:DOTAP complexes, Vero E6 cells were infected with 200 plaque-forming units (PFU) of the SARS-CoV-2 strain hCoV-19/Spain/VH000001133/2020 (EPI\_ISL\_418860). After 48 hours, RNA was extracted from the supernatants using the Quick-RNA Viral Kit from Zymo Research (Irvine, CA, USA). Quantification of SARS-CoV-2 production was performed by qPCR using the qScript XLT One-Step RT-qPCR ToughMix with ROX (Quanta Biosciences, Beverly, USA). This included the specific probe 2019-nCoV\_N1-P (5'-FAM-ACCCCGCATTACGTTTGTTG-TGACC-BHQ1-3'), as well as primers 2019-nCoV\_N1-F (5'-GACCCCAAAATCAGCGAAAT-3') and 2019-nCoV\_N1-R (5'-TCTGGTTACTGCCAG-TTGAATCTG-3') obtained from Biomers (Ulm, Germany).

#### 4.7. Biosafety

All aspects of this study were approved by the office of Environmental Health and Safety at CISA-CSIC, Madrid, Spain before initiation of this study. Work with SARS-CoV-2 was performed in a biosafety level 3 laboratory by personnel equipped with powered air-purifying respirators.

#### 4.8. Animals

B6Cg-Tg(K18-hACE2)2PrImn/J mice (Jackson ImmunoResearch, West Grove, PA) were employed in protection experiments. The animals were generally lodged in groups of five, always following the space requirements specified in legislation (EU Directive 2010/63 and Spain regulation RD53/2013, modified by RD1386/2018). Experimentation with infected mice was carried out in BSL3+ laboratories (CISA-INIA-CSIC). All animals received food and water *ad libitum*. Animal welfare measures were applied, considering replacement, reduction, and refinement. Environmental enrichment was implemented. Animals were anesthetized with isoflurane (3% for induction, 1.5% for maintenance) before the intranasal administration of PPRHs. The same anesthesia was administered upon sacrifice by intracardiac puncture. The endpoint criterion was adopted when appropriate. In the specific case of the K18-hACE2 mice after the viral challenge, euthanasia was immediately applied when animal weight decreased 20% or more and when any incipient sign of suffering (clinical score higher than 50) was detected. The procedures applied in challenge experiments were then subject to retrospective evaluation.

#### 4.9. SARS-CoV-2 infectious challenge

Mice were challenged with  $10^5$  PFU of MAD6 SARS-CoV-2 by the intranasal route after two doses of PPRH, 24 and 4 hours before the viral infection. Body weight and clinical scores were followed daily in five K18-hACE2 mice per group (SCR control, CC1 and CC3) for each experiment. The clinical score was calculated as explained below (section 4.10).

#### 4.10. Clinical Score Evaluation

Mice were observed and weighed daily post-challenge, and clinical signs were scored according to [34]. The sum score in clinical signs (based on body weight, appearance, motility, and respiration) was used to evaluate disease severity. A humane endpoint was implemented when this score reached >50 to reduce animal suffering.

#### 4.11. Statistical Analyses

Statistical analyses were carried out using GraphPad Prism 6 (GraphPad Software, CA, USA). Data represented the mean value and the standard error of the mean (SEM) from at least three separate experiments. Levels of statistical significance are indicated as follows:  $p < 0.05$  (),  $p < 0.01$  (),  $p < 0.001$  (), or  $p < 0.0001$  (\*\*\*\*).

## References

1. Wu, C. rong, Yin, W. chao, Jiang, Y., & Xu, H. E. Structure genomics of SARS-CoV-2 and its Omicron variant: drug design templates for COVID-19. *Acta Pharmacologica Sinica*, **2022**, 43(12), 3021–3033. <https://doi.org/10.1038/s41401-021-00851-w>
2. Harrison, A. G., Lin, T., & Wang, P. Mechanisms of SARS-CoV-2 Transmission and Pathogenesis. *Trends in Immunology*, **2020** 41(12), 1100–1115. <https://doi.org/10.1016/j.IT.2020.10.004>
3. Jackson, C. B., Farzan, M., Chen, B., & Choe, H. Mechanisms of SARS-CoV-2 entry into cells. *Nature Reviews Molecular Cell Biology*, **2021**, 23(1), 3–20. <https://doi.org/10.1038/s41580-021-00418-x>
4. WHO Coronavirus disease (COVID-19) pandemic. World Health Organization, Geneva. COVID Live - Coronavirus Statistics - Worldometer (worldometers.info). **2022**. (Accessed Date: August 16, 2023)
5. Michel, C. J., Mayer, C., Poch, O., & Thompson, J. D. Characterization of accessory genes in coronavirus genomes. *Virology Journal*, **2020**, 17(1), 131. <https://doi.org/10.1186/S12985-020-01402-1>

6. Jamison, D. A., Anand Narayanan, S., Trovão, N. S., Guarnieri, J. W., Topper, M. J., Moraes-Vieira, P. M., Zaksas, V., Singh, K. K., Wurtele, E. S., & Beheshti, A. A comprehensive SARS-CoV-2 and COVID-19 review, Part 1: Intracellular overdrive for SARS-CoV-2 infection. *European Journal of Human Genetics*, **2022**, 30(8), 889–898. <https://doi.org/10.1038/s41431-022-01108-8>
7. Kashte, S., Gulbake, A., El-Amin, S. F., & Gupta, A. COVID-19 vaccines: rapid development, implications, challenges and future prospects. *Human Cell*, **2021**, 34(3), 711–733. <https://doi.org/10.1007/S13577-021-00512-4/TABLES/3>
8. Scavone, C., Brusco, S., Bertini, M., Sportiello, L., Rafaniello, C., Zoccoli, A., Berrino, L., Racagni, G., Rossi, F., & Capuano, A. Current pharmacological treatments for COVID-19: What's next? *British Journal of Pharmacology*, **2020**, 177(21), 4813–4824. <https://doi.org/10.1111/BPH.15072>
9. Gupta, A., Pradhan, A., Maurya, V. K., Kumar, S., Theengh, A., Puri, B., & Saxena, S. K. Therapeutic approaches for SARS-CoV-2 infection. *Methods*, **2021**, 195, 29–43. <https://doi.org/10.1016/j.YMETH.2021.04.026>
10. Tao, K., Tzou, P. L., Nouhin, J., Bonilla, H., Jagannathan, P., & Shafer, R. W. SARS-CoV-2 Antiviral Therapy. *Clinical Microbiology Reviews*, **2021**, 34(4), e0010921. <https://doi.org/10.1128/CMR.00109-21>
11. Babalola, B. A., Akinsuyi, O. S., Folajimi, E. O., Olujimi, F., Otunba, A. A., Chikere, B., Adewumagun, I. A., & Adetobi, T. E. Exploring the future of SARS-CoV-2 treatment after the first two years of the pandemic: A comparative study of alternative therapeutics. *Biomedicine & Pharmacotherapy*, **2023**, 165, 115099. <https://doi.org/10.1016/j.BIOPHA.2023.115099>
12. Baum, A., Fulton, B. O., Wloga, E., Copin, R., Pascal, K. E., Russo, V., Giordano, S., Lanza, K., Negron, N., Ni, M., Wei, Y., Atwal, G. S., Murphy, A. J., Stahl, N., Yancopoulos, G. D., & Kyratsous, C. A. Antibody cocktail to SARS-CoV-2 spike protein prevents rapid mutational escape seen with individual antibodies. *Science (New York, N.Y.)*, **2020**, 369(6506), 1014–1018. <https://doi.org/10.1126/SCIENCE.ABD0831>
13. Ye, M., Fu, D., Ren, Y., Wang, F., Wang, D., Zhang, F., Xia, X., & Lv, T. Treatment with convalescent plasma for COVID-19 patients in Wuhan, China. *Journal of Medical Virology*, **2020**, 92(10), 1890–1901. <https://doi.org/10.1002/JMV.25882>
14. Fardet, L., & Fève, B. Systemic glucocorticoid therapy: a review of its metabolic and cardiovascular adverse events. *Drugs*, **2014**, 74(15), 1731–1745. <https://doi.org/10.1007/S40265-014-0282-9>
15. Qiao, Y., Wotring, J. W., Zhang, C. J., Jiang, X., Xiao, L., Watt, A., Gattis, D., Scandalis, E., Freier, S., Zheng, Y., Pretto, C. D., Ellison, S. J., Swayze, E. E., Guo, S., Sexton, J. Z., & Chinnaiyan, A. M. Antisense oligonucleotides to therapeutically target SARS-CoV-2 infection. *PLoS ONE*, **2023**, 18(2), e0281281. <https://doi.org/10.1371/JOURNAL.PONE.0281281>
16. Zhu, C., Lee, J. Y., Woo, J. Z., Xu, L., Nguyenla, X., Yamashiro, L. H., Ji, F., Biering, S. B., Van Dis, E., Gonzalez, F., Fox, D., Wehri, E., Rustagi, A., Pinsky, B. A., Schaletzky, J., Blish, C. A., Chiu, C., Harris, E., Sadreyev, R. I., ... Näär, A. M. An intranasal ASO therapeutic targeting SARS-CoV-2. *Nature Communications*, **2022**, 13(1), 4503. <https://doi.org/10.1038/S41467-022-32216-0>
17. Ergün, S., Sankaranarayanan, R., & Petrović, N. Clinically informative microRNAs for SARS-CoV-2 infection. *Epigenomics*, **2023**, 15(13), 705–716. <https://doi.org/10.2217/EPI-2023-0179>
18. Traube, F. R., Stern, M., Tölke, A. J., Rudelius, M., Mejías-Pérez, E., Raddaoui, N., Kümmerer, B. M., Douat, C., Streshnev, F., Albanese, M., Wratil, P. R., Gärtner, Y. V., Nainytė, M., Giorgio, G., Michalakis, S., Schneider, S., Streeck, H., Müller, M., Keppler, O. T., & Carell, T. Suppression of SARS-CoV-2 Replication with Stabilized and Click-Chemistry Modified siRNAs. *Angewandte Chemie (International Ed. in English)*, **2022**, 61(38), e202204556. <https://doi.org/10.1002/ANIE.202204556>
19. Idris, A., Davis, A., Supramaniam, A., Acharya, D., Kelly, G., Tayyar, Y., West, N., Zhang, P., McMillan, C. L. D., Soemardy, C., Ray, R., O'Meally, D., Scott, T. A., McMillan, N. A. J., & Morris, K. V. A SARS-CoV-2 targeted siRNA-nanoparticle therapy for COVID-19. *Molecular Therapy*, **2021**, 29(7), 2219–2226. <https://doi.org/10.1016/j.YMTHE.2021.05.004>
20. Lee, Y. R., Tsai, H. P., Yeh, C. S., Fang, C. Y., Chan, M. W. Y., Wu, T. Y., & Shen, C. H. RNA Interference Approach Is a Good Strategy against SARS-CoV-2. **2023**, *Viruses*, 15(1), 100. <https://doi.org/10.3390/V15010100>
21. Supramaniam, A., Tayyar, Y., Clarke, D. T. W., Kelly, G., Acharya, D., Morris, K. V., McMillan, N. A. J., & Idris, A. Prophylactic intranasal administration of lipid nanoparticle formulated siRNAs reduce SARS-CoV-2 and RSV lung infection. *Journal of Microbiology, Immunology and Infection*, **2023**, 56(3), 516–525. <https://doi.org/10.1016/j.jmii.2023.02.010>
22. Nguyen, T. M., Zhang, Y., & Pandolfi, P. P. Virus against virus: a potential treatment for 2019-nCov (SARS-CoV-2) and other RNA viruses. *Cell Research*, **2020**, 30(3), 189–190. <https://doi.org/10.1038/s41422-020-0290-0>
23. Cui, Z., Zeng, C., Huang, F., Yuan, F., Yan, J., Zhao, Y., Zhou, Y., Hankey, W., Jin, V. X., Huang, J., Staats, H. F., Everitt, J. I., Sempowski, G. D., Wang, H., Dong, Y., Liu, S. L., & Wang, Q. Cas13d knockdown of lung protease Ctsl prevents and treats SARS-CoV-2 infection. *Nature Chemical Biology*, **2022**, 18(10), 1056–1064. <https://doi.org/10.1038/S41589-022-01094-4>
24. Coma, S., Noé, V., Eritja, R., & Ciudad, C. J. Strand Displacement of Double-Stranded DNA by Triplex-Forming Antiparallel Purine-Hairpins. *Oligonucleotides*, **2005**, 15(4), 269–283. <https://doi.org/10.1089/oli.2005.15.269>
25. de Almagro, M. C., Coma, S., Noé, V., & Ciudad, C. J. Polypurine Hairpins Directed against the Template Strand of DNA Knock Down the Expression of Mammalian Genes. *The Journal of Biological Chemistry*, **2009**, 284(17), 11579–11589. <https://doi.org/10.1074/jbc.M900981200>
26. Noé, V., Aubets, E., Félix, A. J., & Ciudad, C. J. Nucleic acids therapeutics using PolyPurine Reverse Hoogsteen hairpins. *Biochemical Pharmacology*, **2021**, 189, 114371. <https://doi.org/10.1016/j.bcp.2020.114371>
27. de Almagro, M. C., Mencia, N., Noé, V., & Ciudad, C. J. Coding polypurine hairpins cause target-induced cell death in breast cancer cells. *Human Gene Therapy*, **2011**, 22(4), 451–463. <https://doi.org/10.1089/hum.2010.102>
28. Rodríguez, L., Villalobos, X., Solé, A., Lliberós, C., Ciudad, C. J., & Noé, V. Improved design of PPRHs for gene silencing. *Molecular Pharmaceutics*, **2015**, 12(3), 867–877. <https://doi.org/10.1021/mp5007008>

29. Aviñó, A., Cuestas-Ayllón, C., Gutiérrez-Capitán, M., Vilaplana, L., Grazu, V., Noé, V., Balada, E., Baldi, A., Félix, A. J., Aubets, E., Valiuska, S., Domínguez, A., Gargallo, R., Eritja, R., Marco, M. P., Fernández-Sánchez, C., Martínez de la Fuente, J., & Ciudad, C. J. Detection of SARS-CoV-2 Virus by Triplex Enhanced Nucleic Acid Detection Assay (TENADA). *International Journal of Molecular Sciences*, **2022**, 23(23), 15258. <https://doi.org/10.3390/IJMS232315258/S1>
30. Rodríguez, L., Villalobos, X., Solé, A., Lliberós, C., Ciudad, C. J., & Noé, V. Improved design of PPRHs for gene silencing. *Molecular Pharmaceutics*, **2015**, 12(3), 867–877. <https://doi.org/10.1021/mp5007008>
31. Beyerstedt, S., Casaro, E. B., & Rangel, É. B. COVID-19: angiotensin-converting enzyme 2 (ACE2) expression and tissue susceptibility to SARS-CoV-2 infection. *European Journal of Clinical Microbiology & Infectious Diseases*, **2021**, 40(5), 905–918. <https://doi.org/10.1007/S10096-020-04138-6>
32. McCray, P. B., Pewe, L., Wohlford-Lenane, C., Hickey, M., Manzel, L., Shi, L., Netland, J., Jia, H. P., Halabi, C., Sigmund, C. D., Meyerholz, D. K., Kirby, P., Look, D. C., & Perlman, S. Lethal infection of K18-hACE2 mice infected with severe acute respiratory syndrome coronavirus. *Journal of Virology*, **2007**, 81(2), 813–821. <https://doi.org/10.1128/JVI.02012-06>
33. Dong, W., Mead, H., Tian, L., Park, J.-G., Garcia, J. I., Jaramillo, S., Barr, T., Kollath, D. S., Coyne, V. K., Stone, N. E., Jones, A., Zhang, J., Li, A., Wang, L.-S., Milanes-Yearsley, M., Torrelles, J. B., Martínez-Sobrido, L., Keim, P. S., Barker, B. M., ... Yu, J. The K18-Human ACE2 Transgenic Mouse Model Recapitulates Non-severe and Severe COVID-19 in Response to an Infectious Dose of the SARS-CoV-2 Virus. *Journal of Virology*, **2022**, 96(1), e0096421. <https://doi.org/10.1128/JVI.00964-21>
34. Alcolea, P. J., Larraga, J., Rodríguez-Martin, D., Alonso, A., Loayza, F. J., Rojas, J. M., Ruiz-García, S., Louloutes-Lázaro, A., Carlón, A. B., Sánchez-Cordón, P. J., Nogales-Altozano, P., Redondo, N., Manzano, M., Lozano, D., Palomero, J., Montoya, M., Vallet-Regí, M., Martín, V., Sevilla, N., & Larraga, V. Non-replicative antibiotic resistance-free DNA vaccine encoding S and N proteins induces full protection in mice against SARS-CoV-2. *Frontiers in Immunology*, **2022**, 13, 1023255. <https://doi.org/10.3389/fimmu.2022.1023255>
35. Rodríguez, L., Villalobos, X., Dakhel, S., Padilla, L., Hervás, R., Hernández, J. L., Ciudad, C. J., & Noé, V. Polypurine reverse Hoogsteen hairpins as a gene therapy tool against survivin in human prostate cancer PC3 cells in vitro and in vivo. *Biochemical Pharmacology*, **2013**, 86(11), 1541–1554. <https://doi.org/10.1016/j.bcp.2013.09.013>
36. López-Aguilar, E., Fernández-Nogueira, P., Fuster, G., Carbó, N., Ciudad, C. J., & Noé, V. In Vitro and In Vivo Effects of the Combination of Polypurine Reverse Hoogsteen Hairpins against HER-2 and Trastuzumab in Breast Cancer Cells. *International Journal of Molecular Sciences*, **2023**, 24(8), 7073. <https://doi.org/10.3390/IJMS24087073>
37. Villalobos, X., Rodríguez, L., Solé, A., Lliberós, C., Mencía, N., Ciudad, C. J., & Noé, V. Effect of Polypurine Reverse Hoogsteen Hairpins on Relevant Cancer Target Genes in Different Human Cell Lines. *Nucleic Acid Therapeutics*, **2015**, 25(4), 198–208. <https://doi.org/10.1089/NAT.2015.0531>
38. Psaras, A. M., Valiuska, S., Noé, V., Ciudad, C. J., & Brooks, T. A. Targeting KRAS Regulation with PolyPurine Reverse Hoogsteen Oligonucleotides. *International Journal of Molecular Sciences*, **2022**, 23(4). <https://doi.org/10.3390/IJMS23042097/S1>
39. Valiuska, S., Psaras, A. M., Noé, V., Brooks, T. A., & Ciudad, C. J. Targeting MYC Regulation with Polypurine Reverse Hoogsteen Oligonucleotides. *International Journal of Molecular Sciences*, **2022**, 24(1). <https://doi.org/10.3390/IJMS24010378>
40. Khadka, P., Sinha, S., Tucker, I. G., Dummer, J., Hill, P. C., Katare, R., & Das, S. C. Studies on the safety and the tissue distribution of inhaled high-dose amorphous and crystalline rifampicin in a rat model. *International Journal of Pharmaceutics*, **2021**, 597, 120345. <https://doi.org/10.1016/j.ijpharm.2021.120345>
41. Andrzejewska, A., Zawadzka, M., & Pachulska-Wieczorek, K. On the Way to Understanding the Interplay between the RNA Structure and Functions in Cells: A Genome-Wide Perspective. *International Journal of Molecular Sciences*, **2020**, 21(18). <https://doi.org/10.3390/IJMS21186770>
42. Villalobos, X.; Rodríguez, L.; Prevot, J.; Oleaga, C.; Ciudad, C.J.; Noe, V. Stability and immunogenicity properties of the gene-silencing polypurine reverse Hoogsteen hairpins. *Mol. Pharm.* **2014**, 11, 254–264.
43. Cao, W., Mishina, M., Amoah, S., Mboko, W. P., Bohannon, C., McCoy, J., Mittal, S. K., Gangappa, S., & Sambhara, S. Nasal delivery of H5N1 avian influenza vaccine formulated with genjet<sup>TM</sup> or in vivo-JetPEI<sup>®</sup> induces enhanced serological, cellular and protective immune responses. *Drug Delivery*, **2018**, 25(1), 773–779. <https://doi.org/10.1080/10717544.2018.1450909>
44. Panahi, Y., Gorabi, A. M., Talaie, S., Beiraghdar, F., Akbarzadeh, A., Tarhriz, V., & Mellatayr, H. An overview on the treatments and prevention against COVID-19. *Virology Journal*, **2023**, 20(1), 23. <https://doi.org/10.1186/S12985-023-01973-9>
45. Yao, X., Ye, F., Zhang, M., Cui, C., Huang, B., Niu, P., Liu, X., Zhao, L., Dong, E., Song, C., Zhan, S., Lu, R., Li, H., Tan, W., & Liu, D. In vitro antiviral activity and projection of optimized dosing design of hydroxychloroquine for the treatment of severe acute respiratory syndrome coronavirus 2 (SARS-CoV-2). *Clinical Infectious Diseases*, **2020**, 71(15), 732–739. <https://doi.org/10.1093/cid/ciaa237>





## **5. DISCUSSION**





Our research group is committed to continuously progress in the development of PolyPurine Reverse Hoogsteen (PPRH) hairpins. One of our primary goals is to advance in their potential for applications in the field of gene therapy. We explored the utilization of PPRHs as alternative gene silencing tools against G-quadruplexes of undruggable *KRAS* and *MYC* cancer targets. Furthermore, our plans included investigating the properties of PPRHs to evaluate their potential utility as diagnostic and therapeutic tools to target SARS-CoV-2.

## 5.1 PPRHs as gene silencing tools

PPRH hairpins are a promising class of therapeutic oligonucleotides with distinctive advantages, including high binding specificity and stability. Their ability to target DNA directly sets them apart from other oligonucleotide therapies, such as TFOs, ASOs or siRNAs, making them a valuable tool for various gene therapy applications. PPRHs have been used for different purposes such as gene editing, gene repair, for diagnostic/detection purposes and especially as a gene silencing tool (Noé et al., 2021).

Recently, our research group showed special interest in G-quadruplex (G4), a G-rich secondary structure widely present in the genome. These structures have multiple functions such as modulating gene transcription, blocking DNA synthesis, participating in DNA repair and telomere homeostasis (Huppert & Balasubramanian, 2007; Sarkies et al., 2010; Sharma et al., 2021). Our group has previously used PPRHs against the complementary strand of *thymidylate synthase* (*TYMS*) G4 forming sequence (G4FS) to facilitate the formation of these secondary structures and enhance gene silencing. More specifically, PPRHs targeted the complementary strand of a G4FS in the 5'UTR region of the *TYMS* and proved effectiveness in reducing cell viability, mRNA, and protein levels in PC-3 and HeLa cells (Aubets, Félix, et al., 2020).

### 5.1.1 PPRHs targeting *KRAS*

*KRAS* gene silencing has been validated as a therapeutic approach to treat cancer that relies on abnormal *KRAS* signaling (Adjei, 2001; Hu et al., 2012). Since it is highly present in many cancers including pancreatic, colorectal,

lung, neuroblastoma, and ovarian cancers (Deramaudt & Rustgi, 2005; Ostrem & Shokat, 2016; Parikh et al., 2022; Y. Wang et al., 2013), we wanted to study the effects upon PPRH treatment. More specifically, our objective was to create an innovative approach for modifying the expression and/or activity of *KRAS* by utilizing PPRHs targeting the complementary strand of G4FS in several *KRAS*-dependent cell lines, especially focusing on pancreatic and ovarian cancer cell lines.

Many studies support the idea that G4s formed in promoter sequences are involved in the regulation of gene expression (Amato et al., 2018; Tian et al., 2018). The *KRAS* gene sequence is rich in guanines and cytosines, especially its promoter. Some of these G/C stretches can form G4s that may regulate *KRAS* expression (D'Aria et al., 2020). We designed a set of five PPRHs, four coding and one template, directed against polypyrimidine tracts containing putative G4FS using QGRS mapper (Kikin et al., 2006). We have conducted a search for higher-order DNA structures within three previously unexplored regions of *KRAS*: one located in the distal promoter, another within an intron, and the third in an exon. Among these three regions, it was observed that the exon region had the capability to form inter-strand G4 structures. Furthermore, we designed PPRH molecules to target these three newly detected G-rich DNA regions, in addition to the previously identified G4-forming region known as G4<sub>mid</sub> within the proximal promoter (Morgan et al., 2016).

We confirmed the sequence-specific interaction of the PPRHs with their target DNA by performing DNA-binding analyses and determined their high affinity by melting temperatures. The scrambled PPRH showed no specificity in binding assays with the different targets and very low interaction in melting temperatures. When coding- and template-PPRHs bind to their target, they induce strand displacement. Coding-PPRHs can bind directly to the mRNA, and template-PPRHs can disrupt RNA polymerase transcription (de Almagro et al., 2009, 2011). When a PPRH targets the complementary strand of a G4FS, it could promote G4 formation leading to a downregulation of gene expression. Previous studies have identified the presence of several transcription factor (TF) binding sites within the core region of the *KRAS* promoter, spanning from +50 to -510 base pairs from the transcription start site (TSS), such as Sp1, E2F-1, STAT4, MAZ, WT1, or P53. Importantly, the target sequences of the PPRHs include binding sites for TFs like Sp1 and E2F-1. Therefore, it is feasible that the PPRHs have the potential to disrupt the interaction between these TFs and the

promoter sequence, independently of G4 formation and thus leading to a reduction in transcription (Morgan et al., 2016). Whether it promotes G4 formation or disruption of transcription factor binding, PPRH targeting would result in a decreased proliferation of KRAS-dependent cancer cells.

Here we analyzed the effects of the PPRHs mainly on pancreatic and ovarian cancer cells lines, but also in KRAS-deregulated prostate, colorectal, neuroblastoma and breast cancer cell lines, observing variations in their effectiveness. Nevertheless, consistent results were obtained when targeting the promoter region (HpKRAS-Pr-C, PPRH 1 and PPRH 2), which caused the highest reduction in cell viability and growth confluence. PPRH 2 targeting the known G4<sub>mid</sub> region was the most effective PPRH in all pancreatic and ovarian cell lines tested, whereas HpKRAS-Pr-C was the most potent in prostate, breast, neuroblastoma, and colorectal cancer cell lines. Remarkably, we found a synergistic effect on viability when PPRHs were combined in pancreatic AsPc-1 cells and an additive effect in ovarian SKOV-3 cancer cells. No effect was observed when the scrambled PPRH, alone or in combination with KRAS-targeting PPRHs, were incubated in KRAS-dependent cancer cells. These results prove the therapeutic value of KRAS-targeting PPRHs *in vitro*, especially the promoter-targeting PPRHs, which can decrease transcription and the binding of TF thus leading to a decreased *KRAS* expression.

Focusing on selectively stabilizing specific G4s as a potential anti-cancer strategy is currently an active area of research. Many molecules have been used as G4-ligands and stabilizers to repress gene expression (Awadasseid et al., 2021; D'Aria et al., 2020; Tian et al., 2018; T. Y. Wu et al., 2020). We had previously observed synergistic effects with PPRHs combined with other molecules such as Fluorouracil (5-FU) (Aubets, Félix, et al., 2020) or Trastuzumab (López-Aguilar et al., 2023). In this study we explored the effects of a G4<sub>mid</sub>-selective small molecule, NSC 317605 (Psaras et al., 2022), in combination with PPRHs. NSC 317605 binds to the *KRAS* promoter G4<sub>mid</sub> stabilizing the G4 structure, that leads to a downregulation of *KRAS* transcription which correlates with a decrease in cell viability in the KRAS-dependent AsPc-1 pancreatic cancer cell line. The reduction in transcription was also observed with promoter-targeting PPRHs individually and in combination with NSC 317605 which acted in a synergistic manner. Luciferase experiments provide supporting evidence for these transcriptional decreases.

In this work, we successfully identified novel G4 structures in the *KRAS* sequence, designed new PPRHs against this oncogene and validated a small molecule to enhance G4 stability to modulate oncogene expression in *KRAS*-dependent cancer cell lines. We demonstrated the individual and combinatorial potential of PPRHs and *KRAS*-localized G4s stabilizing molecules in different *KRAS*-mutated cancer cell lines. The combination of G4 stabilizing molecules with G4 targeting PPRHs emerged as a potential alternative for gene silencing of undruggable cancer targets.

### 5.1.2 PPRHs targeting *MYC*

For many years, *MYC* has been considered a challenging target for drug development, primarily due to several factors. These include its absence of an enzymatic active site, its location within the nuclear compartment, and its strong protein-protein interactions with partners like MAX. Although to this date, no specific drugs directly inhibiting *MYC* have been clinically-approved (C. Wang et al., 2021), the research is getting closer by the development of molecules like Omomyc (Massó-Vallés & Soucek, 2020). This molecule interacts with *MYC* protein network inducing apoptosis in cancer but not in healthy cells, blocking proliferation and invasion and recruiting immune cells to the tumor (Massó-Vallés & Soucek, 2020). While approaches like Omomyc are under development, parallelly, alternative strategies focusing on key elements involved in transcription, translation, stability, and activation have been explored to modulate *MYC* expression (H. Chen et al., 2018). *MYC* contains well-known G4 structures with silencing properties (Brown et al., 2011). We considered that targeting these G4s with PPRHs as a powerful approach for *MYC* gene silencing and cell death in *MYC*-dependent cancer cells. Our laboratory had previously designed a PPRH targeting *MYC* intron 1 and tested its effects in different breast cancer cell lines, with a reduction of cell viability and mRNA expression of 80 and 50%, respectively (Villalobos et al., 2015). In the present work we focused on the development and evaluation of a set of PPRH oligonucleotides designed to target the *MYC* gene and its associated regulatory regions.

We designed a total of six PPRHs to target various regions of the *MYC* gene, encompassing the promoter and intronic regions, both the coding (C) and template (T) strands, sequences complementary to G4FS, and additional regulatory regions. We identified putative G4FS with the QGRS mapper (Kikin et al., 2006). Among the PPRHs, *MYC*-G4-PR-C and *MYC*-I2-C were directed

towards coding strand regions that are complementary to G4 formation, whereas the remaining four were designed to target template strands within non-G4-forming regions, named HpMYC-PR-Distal-T, HpMYC-PR-Prox-T HpMYC-I1-T and HpMYC-I1-short-T. MYC-G4-PR-C targets a complementary sequence of a major promoter G4 structure, called nuclease hypersensitive element (NHEIII<sub>1</sub>) located in the 5'UTR, (Brooks & Hurley, 2010). HpMYC-I2-C, which targets a newly identified G4 structure with parallel formation, is present in the coding strand and thus in the mRNA, and it may have a role in splicing and pre-mRNA processing (Dumas et al., 2021). Additional research is needed to investigate its biological significance. However, such investigations were outside the scope and objectives of the present study.

All PPRHs successfully established triplex structures with their respective target sequences, displacing their complementary strands. PPRH interaction and affinity with their targets were validated by determining melting temperatures. The scrambled PPRH showed no interaction with the different MYC targets. The PPRHs strong interaction with their targets exhibited the ability to modulate *MYC* promoter activity and demonstrated significant antiproliferative effects across breast, neuroblastoma, colorectal, and prostate cancer cell lines. We observed consistent dose- and time-dependent impacts on cell viability and growth in PC-3 prostate cancer cells and, in previously identified PPRH-sensitive, AsPc-1 pancreatic cancer cells. Two lead PPRHs, HpMYC-G4-PR-C and HpMYC-I1-T, had a higher impact on MYC-dependent cancer cells. HpMYC-I1-T targets the template sequence of *MYC*, and thus directly interferes with RNA polymerase that will interrupt transcription and mRNA elongation. On the other hand, HpMYC-G4-PR-C targets the complementary strand of a G4FS, located in the promoter and containing binding sites for TF such as Sp1, CNBP, KLF4, KLF5 or MZF1, and/or MZF1 (Guo et al., 2009; Morales-Martinez et al., 2019; Tsai et al., 2015), as determined by JASPAR transcription database (Castro-Mondragon et al., 2022). Therefore, HpMYC-G4-PR-C potentially promotes G4 formation and disrupts the binding of transcription factors like Sp1 and CNBP, thereby resulting in a transcription reduction as demonstrated by the work of Brown and Brooks in 2011 with the G4-stabilizing compound GQC-05 (NSC338258) (Brown et al., 2011). HpMYC-I1-T and HpMYC-G4-PR-C caused the inhibition of *MYC* transcription and translation at concentrations as low as 25 nM. These PPRHs impacted MYC downstream Cyclin D1, reducing its protein levels. Cyclin D1 overexpression is related to the formation, progression, and

maintenance of cancer, its downregulation could be a useful strategy for cancer treatment (Alao, 2007; Choi et al., 2012).

Our findings validate PPRHs as a potential strategy to directly target and silence *MYC*. As we continue to unlock the full potential of PPRH-mediated *MYC* regulation in advancing this technology, future research should explore the potential of *MYC* promoter G4-stabilizing compounds and investigate other chemotherapeutic approaches to enhance *MYC* downregulation.

### 5.1.3 Combinatorial effects of PPRHs against *KRAS* and *MYC*

Single therapy for cancer treatment can be challenging and may carry the risk of incomplete eradication, since this disease can be originated from mutations in multiple genes. Combination therapy has demonstrated a higher rate of success in cancer treatment compared to monotherapies. It involves two different therapies such as a combination of radio and immunotherapy (Bhatia et al., 2020; Yu et al., 2022) or the combination of therapeutic oligonucleotides (Xiong et al., 2021). Some combinations of therapeutic oligonucleotides against one single target can compete for target binding, leading to reduced activity (Tanudji et al., 2010). In 2023, Yanagidaira et al. observed that combinations of ASOs against one single target, the human superoxide dismutase 1 pre-mRNA, maintained their potency. One of the first clinical trials involved targeting two different targets, Kinesin Spindle Protein (KSP) and Vascular Endothelial Growth Factor (VEGF) in cancer patients, administering a combination of two different siRNA against (Tabernero et al., 2013). Here we explored the effects of a combination of two different PPRHs targeting two oncogenes, *MYC* and *KRAS*.

In this work, we considered combining the most efficient PPRHs previously validated against *KRAS* and *MYC* to target both oncogenes in PC-3 prostate cancer cells that showed to be sensitive and dependent on those oncogenes. We selected four of the best PPRHs, two targeting *MYC* (I1-T and G4-C) and two against *KRAS* (PR-C and PPRH2). Combinations of these PPRHs had a more potent effect on cell viability compared to individual treatments, showing a synergistic effect, except for the combos of I1-T and PR-C which presented slight synergism. PPRHs showed an interesting modulatory effect in *KRAS* and *MYC* mRNA levels over time, observing an increase at early times followed by a decrease that reaches the lowest mRNA levels at five days post-transfection. We observed similar fluctuations in mRNA levels of both



oncogenes where MYC mRNA expression was more sensitive to PPRH transfection. Our general hypothesis is that cells try to compensate the effect of PPRHs at early hours increasing the transcription which increases mRNA levels. This mechanism starts to be counteracted three days post-transfection and the subsequent decrease is exceeded by the PPRHs reducing both *KRAS* and *MYC* mRNA levels.

In the same conditions, five days post-transfection, a similar pattern is observed in translation, where MYC protein expression was lower than *KRAS*. Like in viability experiments, combinations of MYC and *KRAS*-targeting PPRHs showed a greater effect in decreasing protein levels. Both *KRAS* and *MYC* intrinsically collaborate, as oncogenic *KRAS* makes *MYC* constitutively expressed and stabilized, making cells susceptible to apoptosis (Hashimoto et al., 2021; T. Lee et al., 2008; Waters et al., 2021). Some studies have reported that *MYC* is required for the initiation and progression of *KRAS*-mutated tumors and its silencing affects the growth of pancreatic cancer (Vaseva et al., 2018; Walz et al., 2014). This might be one possible explanation for the observed reduction on *KRAS* mRNA and protein levels upon MYC-targeting PPRH transfection in PC-3 cells. Although combinations of MYC and *KRAS*-targeting PPRHs have a synergic effect on cell viability, it seems that the main driving force for the modulation of both oncogenes are the PPRHs targeting *MYC*, while the effect of *KRAS* PPRHs seems less effective. Of the two MYC PPRHs used, G4-C was the most effective, especially on cell viability and protein reduction. This PPRH targets a complementary sequence of a G4FS, allowing G-quadruplex formation when it binds to its target. This G4 formation has gene-silencing properties (Psaras et al., 2021). Additionally, it has the potential to disrupt the binding of TF, Sp1, and CNBP. This makes G4-C able to trigger gene silencing either by displacing the complementary sequence, by allowing the G4 formation or by disrupting the binding of TF.

From our results, we hypothesize that although the reduction in mRNA levels might influence, the main driving force in decreasing cell viability is caused by translation downregulation provoked by PPRHs. The synergic effect of the combination of PPRH is confirmed to be a potent approach against the deregulated *KRAS* and *MYC*-dependent PC-3 prostate cancer cells. Future studies in different *KRAS*-*MYC*-dependent cancer cells are needed to validate these PPRHs. It would be interesting to perform combination therapy using different PPRHs against *MYC* to see if there is a similar synergistic effect leading

to lethal outcomes in cells overexpressing a single target as observed with combinations KRAS-targeting PPRHs. It would be also worth trying these PPRH combinations with G4 stabilizing molecules to enhance gene silencing of both oncogenes. The next step would be to try these combinations *in vivo*, in genetically engineered mice models expressing mutated *MYC* or *KRAS* (McFadden et al., 2016).

## 5.2 Detection of SARS-CoV-2 using PPRH as a diagnostic tool

The COVID-19 pandemic had an unprecedented impact on global health, economies, and society. The generation and application of precise and easily accessible diagnostic instruments for detecting SARS-CoV-2 served as a fundamental pillar in fighting the pandemic (Alhamid et al., 2022; Rong et al., 2023). In this study, we investigated the potential of PPRHs as a rapid diagnostic tool for detecting SARS-CoV-2 RNA, eliminating the necessity for PCR and obtaining results in less than an hour.

The capability of PPRHs to selectively bind to specific targets has been previously examined and validated for diagnostic applications. More specifically, PPRHs have been employed in the development of biosensors for cancer detection, where they analyze the hypermethylation status of PAX-5, as well as in microbiological detection for the diagnosis of *Pneumocystis pneumonia* in human samples (Calvo-Lozano et al., 2020; Huertas et al., 2018). Using a similar approach, our laboratory collaborated with other research groups to develop a system based on the concept of “sandwich oligonucleotide hybridization” in several biosensing devices (Ranki et al., 1983). This system utilizes specially designed PPRH hairpins that form high-affinity triplexes with polypyrimidine targets from the SARS-CoV-2 genome, effectively capturing the viral genetic material. We named the method Triplex enhanced nucleic acid detection assay (TENADA).

Three PPRHs denoted as CC1-PPRH, CC2-PPRH, and CC3-PPRH, were designed to selectively bind to the *replicase*, *N gene*, or the *spike* sequences in the SARS-CoV-2 genome, respectively. They were synthesized in two forms: unmodified and modified PPRHs, the latter called capture probes that had an aminohexyl group at the 5'-end. Additionally, duplex-forming DNA oligonucleotides, called reporter probes, were designed close to the binding site of the PPRHs, avoiding interactions between oligonucleotides. PPRHs

demonstrated a remarkable ability to bind specifically to their corresponding single stranded (ss) targets, ssRNA, and ssDNA, achieving successful binding at very low concentrations. The constant of dissociation ( $K_d$ ) between targets and PPRHs forming a triplex, was lower compared to the duplex-forming probes. This suggests that the triplex formation is characterized by higher affinity and specificity compared to the complementary strand forming a duplex. Triplex structures can be more stable than duplex structures under certain conditions, especially when the target DNA contains pyrimidine-rich regions favorable for Hoogsteen bonding (Dalla Pozza et al., 2022). The design of the PPRHs, capture probes, and reporter probes, and their posterior successful bindings served as the foundation for the development of the biosensors.

Capture probes were adapted to be immobilized at the surface of the biosensors, and reporter probes were functionalized with biotin, fluorescent labels (Cy3, TAMRA), or peroxidase protein attached to their 3'-ends, enabling the delivery of optical and electrochemical transducer signals in the biosensors. The PPRHs were used for different methods including a Fluorescent DNA Microarray Chip and the biosensor devices: Thermal Lateral Flow System and Compact Electrochemical Biosensor Platform.

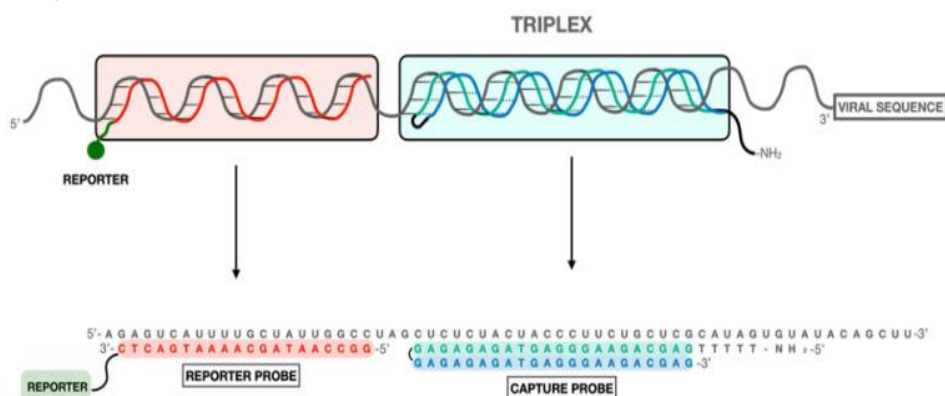


**Figure 17:** Schematic representation of the development of the PPRH CC1 capturing and reporter probes for the identification of SARS-CoV-2 viral RNA.

We also designed PPRHs targeting other viruses to extend the virus diagnosis or detection. Specifically, we designed two PPRHs targeting Influenza virus A (H1N1), one targeting the Polymerase PB1 and the Nuclear Export protein (NEP) and two PPRHs targeting the Human respiratory syncytial virus (HRSV). All PPRHs bound to their corresponding targets at low concentrations.

These PPRHs can be used to improve diagnosis in patients with respiratory infections.

### 5.3 PPRHs therapeutic properties for SARS-CoV-2

When the COVID-19 pandemic started, the development and deployment of therapies emerged as pivotal strategies to mitigate the impact of the virus. Although vaccines are usually the most used agents to prevent the spreading of infectious diseases, their development is time-consuming and undergoes many strict steps before being approved and commercialized. Out of 273 vaccine candidates, only 108 entered the human clinical phase and just four of them entered phase 4 (Panahi et al., 2023). It is important to mention that the vaccines used during the COVID-19 pandemic did not prevent the infection of the disease or the onset of symptoms. Before the development of vaccines, many strategies were considered and used with the goal of preventing the transmission of SARS-CoV-2 and reducing public health impact (Gupta et al., 2021). Therapeutic oligonucleotides such as siRNA, ASOs and CRISPR-Cas systems, showed the ability to suppress SARS-CoV-2 proliferation (Cui et al., 2022; Qiao et al., 2023; Traube et al., 2022). In this work, we explored the possible usage of PPRHs as a protective and therapeutic tool against SARS-CoV-2. We selected the most successful PPRHs used for the diagnostic of SARS-CoV-2, CC1, and CC3 PPRHs targeting replicase and spike regions of the virus, respectively. We performed improved binding assays and determined the  $K_d$ s for PPRHs with ssRNA and ssDNA targets finding that PPRHs bound to ssRNA with lower  $K_d$ s than to ssDNA. This higher affinity of RNA-PPRH interactions can be influenced by various factors, including the specific binding site, buffer conditions, and the thermodynamics of the binding process (Andrzejewska et al., 2020). Both PPRHs exhibited low nanomolar affinity demonstrating strong interaction with their targets.

When transfected 24 hours before the infection, 300 nM of CC1 and CC3 PPRHs reduced drastically SARS-CoV-2 proliferation *in vitro* in monkey kidney VERO-E6 cells that express ACE2 receptors which is the viral entry point (Beyerstedt et al., 2021). Interestingly, no protective effect was seen using CC1 and CC3 ASO, proving that the PPRHs are more effective than ASOs. These differences could be related to previous studies in our laboratory, demonstrating that PPRHs have an inhibitory effect ten times higher than ASOs (De Almagro et al., 2011). Studies using modified ASOs showed a decrease in SARS-CoV-2 proliferation using 100 nM. It is worth mentioning that we used a concentration

of 300 nM, based on the maximum transfection rate observed in VERO-E6 cells, and lower concentrations might significantly reduce SARS-CoV-2 proliferation. Studies using modified siRNA showed a high decrease of viral proliferation in VERO-E6 using concentrations lower than 30 nM (Supramaniam et al., 2023). Parallel orientation (PO) PPRHs, which are PPRHs that have the same orientation as their target and thus are not supposed to bind to it, had no protective effect, leading to SARS-CoV-2 proliferation in VERO-E6 cells.

Given that the disease provoked by SARS-CoV-2 affects especially the respiratory system, we explored the effects *in vivo* by administrating the PPRHs by the non-invasive intranasal method. CC1-PPRH protected K18-hACE2 mice from viral replication, showing no significant weight variation and clinical signs ensuring total survival. PPRHs were effective at very low quantities, 20 and 10 µg, one day and four hours before the infection, respectively, followed by administrations of 10 µg every two days. Scramble-treated and 80% of CC3-treated mice showed severe weight loss and increasing clinical over time. Similar studies using modified ASOs administrating 400 µg per dose, showed no variance in weight four days post-infection. After four days, only a small group of mice treated with ASOs survived showing no immunogenic response (C. Zhu et al., 2022). study following similar strategies, administrating 40 µg of modified siRNAs, showed a decrease of viral proliferation in mice lung seven days post-infection, although long-term survival was not reported (Supramaniam et al., 2023). Previous studies comparing the immune response of siRNA and PPRHs demonstrated that siRNA induced immunogenicity while PPRHs produced none (Villalobos et al., 2014). Considering the minimal immune response triggered by ASOs (C. Zhu et al., 2022) and siRNAs (Supramaniam et al., 2023) along with the negligible impact of CC1-PPRH on mice weight and clinical symptoms, PPRHs might not have a high impact in mice immune response. Nevertheless, additional studies focusing on the immunogenic response in mice are necessary to validate this suggestion.

PPRHs offer numerous advantages over certain therapeutic oligonucleotide competitors, demonstrating effectiveness at low doses. Additionally, they are cost-effective to synthesize due to their non-modified nature (De Almagro et al., 2011). This could facilitate the large-scale production and implementation of PPRHs in scenarios like the COVID-19 pandemic. In this work, CC1-PPRH showed to be a promising candidate against SARS-CoV-2 for this purpose. Future studies are presently underway using a higher number of animals (N=10) to confirm this PPRH as a therapeutic tool with protective

properties towards SARS-CoV-2 infection before considering it for clinical trials. PPRHs could be used as a measure to prevent patients at risk of developing SARS-CoV-2 infection and as a treatment in patients developing the disease.

## 5.4 Conclusion remarks

For many decades, patients had limited choices for cancer treatment, including chemotherapy, radiotherapy, or surgery as single treatments or in combination (Arruebo et al., 2011). Cancer therapy has witnessed significant advancements over the years, driven by extensive research and innovative strategies aimed at improving treatment efficacy and reducing adverse effects. Among the modern advancements are hormone therapy, anti-angiogenic treatments, stem cell therapies, immunotherapy, and immunotherapy based on dendritic cells (Charmsaz et al., 2019). Therapeutic oligonucleotides represent a promising frontier in cancer therapy, offering precision, adaptability, and potential synergy with existing treatments (Debela et al., 2021). PPRH hairpins represent a novel tool contributing to the ongoing quest for more effective and personalized cancer treatments.

Presently, we extend the utility of PPRHs as a gene-silencing tool, focusing on the undruggable genes *MYC* and *KRAS* targeting both established and newly identified G4 structures within their genomes. We analyzed the effect of different PPRHs in both oncogenes. Furthermore, we combined the most efficient PPRH hairpins and found promising results. We believe that the PPRH combination against one or two interacting oncogenes could be a potent solution for future cancer therapy.

We also expanded PPRHs applications not only for gene silencing but also as diagnostic tool for SARS-CoV-2. The biosensor devices used for SARS-CoV-2 detection by PPRH technology could be expanded for other infections or diseases when pathogens like viruses, bacterium, fungus, or parasites are implicated. Additionally, we demonstrated the protective effect of SARS-CoV-2-targeting PPRH *in vitro* and *in vivo* prior to the viral infection. In the experiments with mice infected with the SARS-Cov-2 virus, we also demonstrated that PPRHs can be administered as a regular treatment to stop virus progression. This approach could be complemented with other therapeutic drugs to reduce viral spread and symptoms.







## **6. CONCLUSIONS**



1. PPRHs directed against *KRAS* induce the formation of secondary structures, including G4<sub>mid</sub> and a newly discovered G4 located in exon 5.
2. PPRHs targeting the *KRAS* promoter together with NSC 317605 resulted in a significant reduction in *KRAS* expression and cell survival in cancer cell lines. The observed synergy between PPRHs and NSC 317605 accentuates their potential in combinatorial therapeutic strategies.
3. PPRHs targeting *MYC* facilitate the formation of secondary structures including a newly discovered G4 located in Intron 2 and a known G4 in the *MYC* promoter.
4. *MYC*-targeting PPRHs have the potential to reduce growth and viability of cancer cells with mutated *MYC*. HpMYC-G4-PR-C and HpMYC-I1-T are the most potent PPRHs provoking cell death by downregulation of *MYC* expression.
5. PPRHs can be used in combination therapies against *MYC* and *KRAS*. PPRHs combination reduce *KRAS* and *MYC* expression provoking cell death in a synergistic manner in PC-3 prostate cancer cells.
6. Given the high sensitivity of binding of PPRHs to RNA, specific PPRHs against SARS-CoV-2 can be used for the diagnosis of the virus using different biosensor methodologies.
7. PPRHs have antiviral efficacy against SARS-CoV-2 *in vitro*. CC1-PPRH can protect mice *in vivo* from the infection and disease symptoms caused by SARS-CoV-2.



## **7. BIBLIOGRAPHY**





## A

- Adhikary, S., & Eilers, M. (2005). Transcriptional regulation and transformation by Myc proteins. *Nature Reviews. Molecular Cell Biology*, 6(8), 635–645.
- Adjei, A. A. (2001). Blocking oncogenic Ras signaling for cancer therapy. *Journal of the National Cancer Institute*, 93(14), 1062–1074.
- Ala, M. (2022). Target c-Myc to treat pancreatic cancer. *Cancer Biology & Therapy*, 23(1), 34–50.
- Alao, J. P. (2007). The regulation of cyclin D1 degradation: Roles in cancer development and the potential for therapeutic invention. In *Molecular Cancer*, 6(1), 1-24.
- Alhamid, G., Tombuloglu, H., Rabaan, A. A., & Al-Suhaimi, E. (2022). SARS-CoV-2 detection methods: A comprehensive review. *Saudi Journal of Biological Sciences*, 29(11), 103465.
- Ali, S., Ahmad, A., Aboukameel, A., Bao, B., Padhye, S., Philip, P. A., & Sarkar, F. H. (2012). Increased Ras GTPase activity is regulated by miRNAs that can be attenuated by CDF treatment in pancreatic cancer cells. *Cancer Letters*, 319(2), 173–181.
- Amato, J., Madanayake, T. W., Iaccarino, N., Novellino, E., Randazzo, A., Hurley, L. H., & Pagano, B. (2018). HMGB1 binds to the KRAS promoter G-quadruplex: A new player in oncogene transcriptional regulation? *Chemical Communications*, 54(68), 9442–9445.
- Amini, R., Zhang, Z., Li, J., Gu, J., Brennan, J. D., & Li, Y. (2022). Aptamers for SARS-CoV-2: Isolation, Characterization, and Diagnostic and Therapeutic Developments. *Analysis & Sensing*, 2(5), e202200012.
- Andrzejewska, A., Zawadzka, M., & Pachulska-Wieczorek, K. (2020). On the Way to Understanding the Interplay between the RNA Structure and Functions in Cells: A Genome-Wide Perspective. *International Journal of Molecular Sciences*, 21(18), 6770.
- Armelin, H. A., Armelin, M. C. S., Kelly, ..., Stiles, C. D. (1984). Functional role for c-myc in mitogenic response to platelet-derived growth factor. *Nature*, 310(5979), 655–660.
- Arruebo, M., Vilaboa, N., Sáez-Gutierrez, B., Lambea, J., Tres, A., Valladares, M., & González-Fernández, Á. (2011). Assessment of the evolution of cancer treatment therapies. *Cancers*, 3(3), 3279–3330.
- Aubets, E., Félix, A. J., Garavís, M., Reyes, L., Aviñó, A., Eritja, R., Ciudad, C. J., & Noé, V. (2020). Detection of a G-Quadruplex as a Regulatory Element in Thymidylate synthase for Gene Silencing Using Polypurine Reverse Hoogsteen Hairpins. *International Journal of Molecular Sciences*, 21(14), 1–22.
- Aubets, E., Grier, R., Felix, A. J., Rigol, G., Sikorski, C., Limón, D., Mastroso, C., Busquets, M. A., Pérez-García, L., Noé, V., & Ciudad, C. J. (2021). Synthesis and validation of DOPY: A new gemini

dioleilylbispyridinium based amphiphile for nucleic acid transfection. *European Journal of Pharmaceutics and Biopharmaceutics*, 165(February), 279–292.

- Aubets, E., Noé, V., & Ciudad, C. J. (2020). Targeting replication stress response using polypurine reverse Hoogsteen hairpins directed against WEE1 and CHK1 genes in human cancer cells. *Biochemical Pharmacology*, 175, 113911.
- Awadasseid, A., Ma, X., Wu, Y., & Zhang, W. (2021). G-quadruplex stabilization via small-molecules as a potential anti-cancer strategy. *Biomedicine & Pharmacotherapy*, 139, 111550.

## B

- Babalola, B. A., Akinsuyi, O. S., Folajimi, E. O., Olujimi, F., Otunba, A. A., Chikere, B., Adewumagun, I. A., & Adetobi, T. E. (2023). Exploring the future of SARS-CoV-2 treatment after the first two years of the pandemic: A comparative study of alternative therapeutics. *Biomedicine & Pharmacotherapy*, 165, 115099.
- Baud, V., & Karin, M. (2009). Is NF-kappaB a good target for cancer therapy? Hopes and pitfalls. *Nature Reviews. Drug Discovery*, 8(1), 33–40.
- Baum, A., Fulton, B. O., Wloga, E., Copin, R., ..., Kyratsous, C. A. (2020). Antibody cocktail to SARS-CoV-2 spike protein prevents rapid mutational escape seen with individual antibodies. *Science (New York, N.Y.)*, 369(6506), 1014–1018.
- Beaulieu, M. E., Castillo, F., & Soucek, L. (2020). Structural and Biophysical Insights into the Function of the Intrinsically Disordered Myc Oncoprotein. *Cells*, 9(4), 1038.
- Bener, G., Félix, A. J., Sánchez de Diego, C., Pascual Fabregat, I., Ciudad, C. J., & Noé, V. (2016). Silencing of CD47 and SIRPα by Polypurine reverse Hoogsteen hairpins to promote MCF-7 breast cancer cells death by PMA-differentiated THP-1 cells. *BMC Immunology*, 17(1), 1–12.
- Benizri, S., Gissot, A., Martin, A., Vialet, B., Grinstaff, M. W., & Barthélémy, P. (2019). Bioconjugated Oligonucleotides: Recent Developments and Therapeutic Applications. *Bioconjugate Chemistry*, 30(2), 366–383.
- Bernheim, A., Mei, X., Huang, M., Yang, Y., Fayad, Z. A., ... Chung, M. (2020). Chest CT Findings in Coronavirus Disease-19 (COVID-19): Relationship to Duration of Infection. *Radiology*, 295(3), 200463.
- Beroukhi, R., Mermel, C. H., Porter, D., Wei, G., Raychaudhuri, ... Meyerson, M. (2010). The landscape of somatic copy-number alteration across human cancers. *Nature*, 463(7283), 899–905.
- Besch, R., Giovannangeli, C., & Degitz, K. (2004). Triplex-forming oligonucleotides - sequence-specific DNA ligands as tools for gene

- inhibition and for modulation of DNA-associated functions. *Current Drug Targets*, 5(8), 691–703.
- Beyerstedt, S., Casaro, E. B., & Rangel, É. B. (2021). COVID-19: angiotensin-converting enzyme 2 (ACE2) expression and tissue susceptibility to SARS-CoV-2 infection. *European Journal of Clinical Microbiology & Infectious Diseases*, 40(5), 905–918.
- Bhatia, K., Bhumika, & Das, A. (2020). Combinatorial drug therapy in cancer - New insights. *Life Sciences*, 258 (118134).
- Bochman, M. L., Paeschke, K., & Zakian, V. A. (2012). DNA secondary structures: stability and function of G-quadruplex structures. *Nature Reviews. Genetics*, 13(11), 770–780.
- Brahmachari, S. K., Sarkar, P. S., Raghavan, S., Narayan, M., & Maiti, A. K. (1997). Polypurine/polypyrimidine sequences as cis-acting transcriptional regulators. *Gene*, 190(1), 17–26.
- Brooks, T. A., & Hurley, L. H. (2010). Targeting MYC Expression through G-Quadruplexes. *Genes & Cancer*, 1(6), 641–649.
- Brown, R. V., Danford, F. L., Gokhale, V., Hurley, L. H., & Brooks, T. A. (2011). Demonstration that Drug-targeted Down-regulation of MYC in Non-Hodgkins Lymphoma Is Directly Mediated through the Promoter G-quadruplex. *Journal of Biological Chemistry*, 286(47), 41018–41027.
- Bryan, T. M. (2020). G-Quadruplexes at Telomeres: Friend or Foe? *Molecules*, 25(16), 3686.
- Butreddy, A., Kommineni, N., & Dudhipala, N. (2021). Exosomes as naturally occurring vehicles for delivery of biopharmaceuticals: Insights from drug delivery to clinical perspectives. *Nanomaterials*, 11(6), 1481.

## C

- Calvo-Lozano, O., Aviñó, A., Friaza, V., Medina-Escuela, A., Huertas, C. S., Calderón, E. J., Eritja, R., & Lechuga, L. M. (2020). Fast and Accurate Pneumocystis Pneumonia Diagnosis in Human Samples Using a Label-Free Plasmonic Biosensor. *Nanomaterials*, 10(6), 1246.
- Castro-Mondragon, J. A., Riudavets-Puig, R., Rauluseviciute, ... Mathelier, A. (2022). JASPAR 2022: the 9th release of the open-access database of transcription factor binding profiles. *Nucleic Acids Research*, 50(D1), D165–D173.
- Charmsaz, S., Collins, D. M., Perry, A. S., & Prencipe, M. (2019). Novel Strategies for Cancer Treatment: Highlights from the 55th IACR Annual Conference. *Cancers*, 11(8), 1125.
- Chen, H., Liu, H., & Qing, G. (2018). Targeting oncogenic Myc as a strategy for cancer treatment. *Signal Transduction and Targeted Therapy*, 3(5).

- Chen, Q., Li, J., Deng, Z., Xiong, W., Wang, Q., & Hu, Y. Q. (2010). Comprehensive detection and identification of seven animal coronaviruses and human respiratory coronavirus 229E with a microarray hybridization assay. *Intervirology*, 53(2), 95–104.
- Chinta, S., Rodriguez-Guerra, M., Shaban, M., Pandey, N., Jaquez-Duran, M., & Vittorio, T. J. (2023). COVID-19 therapy and vaccination: a clinical narrative review. *Drugs in Context*, 12, 2022-7–2.
- Chitsike, L., & Duerksen-Hughes, P. (2021). Keep out! SARS-CoV-2 entry inhibitors: their role and utility as COVID-19 therapeutics. *Virology Journal*, 18(154), 1–17.
- Choi, Y. J., Li, X., Hydbring, P., Sanda, T., Stefano, J., ... Sicinski, P. (2012). The Requirement for Cyclin D Function in Tumor Maintenance. *Cancer Cell*, 22(4), 438–451.
- Ciudad, C. J., Medina Enriquez, M. M., Félix, A. J., Bener, G., & Noé, V. (2019). Silencing PD-1 and PD-L1: the potential of PolyPurine Reverse Hoogsteen hairpins for the elimination of tumor cells. *Immunotherapy*, 11, 369–372.
- Cogoi, S., & Xodo, L. E. (2006). G-quadruplex formation within the promoter of the KRAS proto-oncogene and its effect on transcription. *Nucleic Acids Research*, 34(9), 2536–2549.
- Colicelli, J. (2004). Human RAS Superfamily Proteins and Related GTPases. *Science's STKE: Signal Transduction Knowledge Environment*, 2004(250), RE13.
- Coma, S., Noé, V., Eritja, R., & Ciudad, C. J. (2005). Strand Displacement of Double- Stranded DNA by Triplex-Forming Antiparallel Purine-Hairpins. *Oligonucleotides*, 15(4), 269–283.
- Conacci-Sorrell, M., McFerrin, L., & Eisenman, R. N. (2014). An overview of MYC and its interactome. *Cold Spring Harbor Perspectives in Medicine*, 4(1), 1–24.
- Corman, V. M., Landt, O., Kaiser, M., Molenkamp, R., ... Drosten, C. (2020). Detection of 2019 novel coronavirus (2019-nCoV) by real-time RT-PCR. *Euro Surveillance: Bulletin European Sur Les Maladies Transmissibles* 25(3).
- Cox, A. D., & Der, C. J. (2010). Ras history: The saga continues. *Small GTPases*, 1(1), 2–27.
- Cox, A. D., Fesik, S. W., Kimmelman, A. C., Luo, J., & Der, C. J. (2014). Drugging the undruggable RAS: Mission possible? *Nature Reviews. Drug Discovery*, 13(11), 828–851.
- Crooke, S. T. (2017). Molecular Mechanisms of Antisense Oligonucleotides. *Nucleic Acid Therapeutics*, 27(2), 70–77.
- Cui, Z., Zeng, C., Huang, F., Yuan, F., Yan, J., Zhao, Y., Zhou, Y., ... Wang, Q. (2022). Cas13d knockdown of lung protease Ctsl prevents and treats SARS-CoV-2 infection. *Nature Chemical Biology*, 18(10), 1056–1064.

## D

- Dalla Pozza, M., Abdullrahman, A., Cardin, C. J., Gasser, G., & Hall, J. P. (2022). Three's a crowd – stabilisation, structure, and applications of DNA triplexes. *Chemical Science*, 13(35), 10193–10215.
- Dang, C. V. (2012). MYC on the Path to Cancer. *Cell*, 149(1), 22–35.
- Dang, C. V., Reddy, E. P., Shokat, K. M., & Soucek, L. (2017). Drugging the “undruggable” cancer targets. *Nature Reviews Cancer*, 17(8), 502–508.
- D'Aria, F., D'Amore, V. M., Di Leva, F. S., Amato, J., ... & Giancola, C. (2020). Targeting the KRAS oncogene: Synthesis, physicochemical and biological evaluation of novel G-Quadruplex DNA binders. *European Journal of Pharmaceutical Sciences*, 149, 105337.
- de Almagro, M. C., Coma, S., Noé, V., & Ciudad, C. J. (2009). Polypurine Hairpins Directed against the Template Strand of DNA Knock Down the Expression of Mammalian Genes. *The Journal of Biological Chemistry*, 284(17), 11579–11589.
- De Almagro, M. C., Mencia, N., Noé, V., & Ciudad, C. J. (2011). Coding polypurine hairpins cause target-induced cell death in breast cancer cells. *Human Gene Therapy*, 22(4), 451–463.
- Debela, D. T., Muzazu, S. G. Y., Heraro, K. D., Ndalama, M. T., Mesele, B. W., Haile, D. C., Kitui, S. K., & Manyazewal, T. (2021). New approaches and procedures for cancer treatment: Current perspectives. *SAGE Open Medicine*, 9.
- Delgado, A., Grier, R., Llor, N., López-Aguilar, E., Busquets, M. A., Noé, V., & Ciudad, C. J. (2023). Trioleyl Pyridinium, a Cationic Transfection Agent for the Lipofection of Therapeutic Oligonucleotides into Mammalian Cells. *Pharmaceutics*, 15(2).
- Deramaut, T., & Rustgi, A. K. (2005). Mutant KRAS in the initiation of pancreatic cancer. *Biochimica et Biophysica Acta*, 1756(2), 97–101.
- Deshpande, G. R., Yadav, P. D., Abraham, P., ... Bhargava, B. (2022). Booster dose of the inactivated COVID-19 vaccine BBV152 (Covaxin) enhances the neutralizing antibody response against Alpha, Beta, Delta and Omicron variants of concern. *Journal of Travel Medicine*, 29(3).
- Dexheimer, T. S., Sun, D., & Hurley, L. H. (2006). Deconvoluting the structural and drug-recognition complexity of the G-quadruplex-forming region upstream of the bcl-2 P1 promoter. *Journal of the American Chemical Society*, 128(16), 5404–5415.
- Donati, G., & Amati, B. (2022). MYC and therapy resistance in cancer: risks and opportunities. *Molecular Oncology*, 16(21), 3828–3854.
- Dong, W., Mead, H., Tian, L., Park, J.-G., Garcia, J. I., ... Yu, J. (2022). The K18-Human ACE2 Transgenic Mouse Model Recapitulates Non-

- severe and Severe COVID-19 in Response to an Infectious Dose of the SARS-CoV-2 Virus. *Journal of Virology*, 96(1), e0096421.
- Duca, M., Vekhoff, P., Oussedik, K., Halby, L., & Arimondo, P. B. (2008). The triple helix: 50 years later, the outcome. *Nucleic Acids Research*, 36(16), 5123–5138.
- Duffy, M. J., O'Grady, S., Tang, M., & Crown, J. (2021). MYC as a target for cancer treatment. *Cancer Treatment Reviews*, 94, 102154.
- Dumas, L., Herviou, P., Dassi, E., Cammas, A., & Millevoi, S. (2021). G-Quadruplexes in RNA Biology: Recent Advances and Future Directions. *Trends in Biochemical Sciences*, 46(4), 270–283.
- Dunbar, C. E., High, K. A., Joung, J. K., Kohn, D. B., Ozawa, K., & Sadelain, M. (2018). Gene therapy comes of age. *Science*, 359(6372).
- Duvall, C. L., Prokop, A., Gersbach, C. A., & Davidson, J. M. (2014). Gene Delivery into Cells and Tissues. *Principles of Tissue Engineering: Fourth Edition*, 687–723.

## E

- Eddy, J., Vallur, A. C., Varma, S., Liu, H., Reinhold, W. C., Pommier, Y., & Maizels, N. (2011). G4 motifs correlate with promoter-proximal transcriptional pausing in human genes. *Nucleic Acids Research*, 39(12), 4975–4983.
- Eftekhari, A., Alipour, M., Chodari, L., Dizaj, S. M., Ardalani, M. R., Samiei, M., Sharifi, S., Vahed, S. Z., Huseynova, I., Khalilov, R., Ahmadian, E., & Cucchiari, M. (2021). A Comprehensive Review of Detection Methods for SARS-CoV-2. *Microorganisms*, 9(2), 232.
- Eilers, M., & Eisenman, R. N. (2008). Myc's broad reach. *Genes & Development*, 22(20), 2755–2766.
- Elsharkasy, O. M., Nordin, J. Z., Hagey, D. W., de Jong, O. G., Schiffelers, R. M., Andaloussi, S. EL, & Vader, P. (2020). Extracellular vesicles as drug delivery systems: Why and how? *Advanced Drug Delivery Reviews*, 159, 332–343.
- Elzahhar, P., Belal, A. S. F., Elamrawy, F., Helal, N. A., & Nounou, M. I. (2019). Bioconjugation in Drug Delivery: Practical Perspectives and Future Perceptions. *Methods in Molecular Biology (Clifton, N.J.)*, 2000, 125–182.
- EMA (2020) European Medicines Agency. *EMA recommends first COVID-19 vaccine for authorisation in the EU* | Retrieved November 22, 2023 from <https://www.ema.europa.eu/en/news/ema-recommends-first-covid-19-vaccine-authorisation-eu>
- Enríquez, M. M. M., Félix, A. J., Ciudad, C. J., & Noé, V. (2018). Cancer immunotherapy using PolyPurine Reverse Hoogsteen hairpins targeting the PD-1/PD-L1 pathway in human tumor cells. *PLoS ONE*, 13(11)

- Ergün, S., Sankaranarayanan, R., & Petrović, N. (2023). Clinically informative microRNAs for SARS-CoV-2 infection. *Epigenomics*, 15(13), 705–716.

## F

- Fardet, L., & Fève, B. (2014). Systemic glucocorticoid therapy: a review of its metabolic and cardiovascular adverse events. *Drugs*, 74(15), 1731–1745.
- Faria, M., & Giovannangeli, C. (2001). Triplex-forming molecules: From concepts to applications. *Journal of Gene Medicine*, 3(4), 299–310.
- FDA. (2019). *FDA approves venetoclax for CLL and SLL* | Food and Drug Administration. Retrieved August 20, 2023 from <https://www.fda.gov/drugs/resources-information-approved-drugs/fda-approves-venetoclax-cll-and-sll>
- FDA. (2020). *FDA Approves First Treatment for COVID-19* | FDA. Retrieved August 24, 2023 from <https://www.fda.gov/news-events/press-announcements/fda-approves-first-treatment-covid-19>
- FDA. (2021). *FDA Approves First COVID-19 Vaccine* | FDA. Retrieved August 24, 2023 from <https://www.fda.gov/news-events/press-announcements/fda-approves-first-covid-19-vaccine>
- Félix, A. J., Ciudad, C. J., & Noé, V. (2020). Correction of the aprt Gene Using Repair-Polypurine Reverse Hoogsteen Hairpins in Mammalian Cells. *Molecular Therapy - Nucleic Acids*, 19, 683–695.
- Fortner, A., & Schumacher, D. (2021). First COVID-19 Vaccines Receiving the US FDA and EMA Emergency Use Authorization. *Discoveries*, 9(1), e122.
- Frank-Kamenetskii, M. D., & Mirkin, S. M. (1995). Triplex DNA structures. *Annual Review of Biochemistry*, 64, 65–95.
- Frenzel, A., Loven, J., & Henriksson, M. A. (2010). Targeting MYC-Regulated miRNAs to Combat Cancer. *Genes & Cancer*, 1(6), 660–667.
- Friday, B. B., & Adjei, A. A. (2005). K-ras as a target for cancer therapy. *Biochimica et Biophysica Acta*, 1756(2), 127–144.

## G

- Gaddis, S. S., Wu, Q., Thames, H. D., Digiovanni, J., Walborg, E. F., Macleod, M. C., & Vasquez, K. M. (2006). A web-based search engine for triplex-forming oligonucleotide target sequences. *Oligonucleotides*, 16(2), 196–201.
- Gardlík, R., Pálffy, R., Hodosy, J., Lukács, J., Turňa, J., & Celec, P. (2005). Vectors and delivery systems in gene therapy. *Medical Science Monitor*, 11(4), 110–121.



- Goñi, J. R., de la Cruz, X., & Orozco, M. (2004). Triplex-forming oligonucleotide target sequences in the human genome. *Nucleic Acids Research*, 32(1), 354–360.
- Goñi, J. R., Vaquerizas, J. M., Dopazo, J., & Orozco, M. (2006). Exploring the reasons for the large density of triplex-forming oligonucleotide target sequences in the human regulatory regions. *BMC Genomics*, 7, 1–10.
- Gowers, D. M., & Fox, K. R. (1999). Towards mixed sequence recognition by triple helix formation. *Nucleic Acids Research*, 27(7), 1569–1577.
- Guo, P., Dong, X. Y., Zhao, K., Sun, X., Li, Q., & Dong, J. T. (2009). Opposing effects of KLF5 on the transcription of MYC in epithelial proliferation in the context of transforming growth factor beta. *The Journal of Biological Chemistry*, 284(41), 28243–28252.
- Gupta, A., Pradhan, A., Maurya, V. K., Kumar, S., Theengh, A., Puri, B., & Saxena, S. K. (2021). Therapeutic approaches for SARS-CoV-2 infection. *Methods*, 195, 29–43.

## H

- Hammad, H. M., Nauman, H. M. F., Abbas, F., Jawad, R., Farhad, W., Shahid, M., Bakhat, H. F., Farooque, A. A., Mubeen, M., Fahad, S., & Cerda, A. (2023). Impacts of COVID-19 pandemic on environment, society, and food security. *Environmental Science and Pollution Research*, 1, 1–12.
- Hashimoto, A., Handa, H., Hata, S., Tsutaho, A., Yoshida, T., Hirano, S., Hashimoto, S., & Sabe, H. (2021). Inhibition of mutant KRAS-driven overexpression of ARF6 and MYC by an eIF4A inhibitor drug improves the effects of anti-PD-1 immunotherapy for pancreatic cancer. *Cell Communication and Signaling*, 19(54).
- Herrick, D. J., & Ross, J. (1994). The half-life of c-myc mRNA in growing and serum-stimulated cells: influence of the coding and 3' untranslated regions and role of ribosome translocation. *Molecular and Cellular Biology*, 14(3), 2119–2128.
- Hirai, H., Satoh, E., Osawa, M., Inaba, T., Shimazaki, C., Kinoshita, S., Nakagawa, M., Mazda, O., & Imanishi, J. (1997). Use of EBV-based Vector/HVJ-liposome complex vector for targeted gene therapy of EBV-associated neoplasms. *Biochemical and Biophysical Research Communications*, 241(1), 112–118.
- Hu, Y., Ou, Y., Wu, K., Chen, Y., & Sun, W. (2012). miR-143 inhibits the metastasis of pancreatic cancer and an associated signaling pathway. *Tumour Biology: The Journal of the International Society for Oncodevelopmental Biology and Medicine*, 33(6), 1863–1870.

- Huang, L., Guo, Z., Wang, F., & Fu, L. (2021). KRAS mutation: from undruggable to druggable in cancer. *Signal Transduction and Targeted Therapy*, 6(1), 1–20.
- Huang, Y., Liu, X., Dong, L., Liu, Z., He, X., & Liu, W. (2011). Development of viral vectors for gene therapy for chronic pain. *Pain Research and Treatment*, 2011.
- Huertas, C. S., Aviñó, A., Kurachi, C., Piqué, A., Sandoval, J., Eritja, R., Esteller, M., & Lechuga, L. M. (2018). Label-free DNA-methylation detection by direct ds-DNA fragment screening using poly-purine hairpins. *Biosensors and Bioelectronics*, 120, 47–54.
- Huff, S., Kummetha, I. R., Tiwari, S. K., Huante, M. B., Clark, A. E., Wang, S., Bray, W., Smith, D., Carlin, A. F., Endsley, M., & Rana, T. M. (2022). Discovery and Mechanism of SARS-CoV-2 Main Protease Inhibitors. *Journal of Medicinal Chemistry*, 65(4), 2866–2879.
- Huppert, J. L., & Balasubramanian, S. (2007). G-quadruplexes in promoters throughout the human genome. *Nucleic Acids Research*, 35(2), 406–413.

## I

- Idris, A., Davis, A., Supramaniam, A., Acharya, D., Kelly, G., ... Morris, K. V. (2021). A SARS-CoV-2 targeted siRNA-nanoparticle therapy for COVID-19. *Molecular Therapy*, 29(7), 2219–2226.
- Immordino, M. L., Dosio, F., & Cattell, L. (2006). Stealth liposomes: review of the basic science, rationale, and clinical applications, existing and potential. *International Journal of Nanomedicine*, 1(3), 297.
- Izda, V., Jeffries, M. A., & Sawalha, A. H. (2021). COVID-19: A review of therapeutic strategies and vaccine candidates. *Clinical Immunology (Orlando, Fla.)*, 222, 108634.

## J

- Jackson, C. B., Farzan, M., Chen, B., & Choe, H. (2021). Mechanisms of SARS-CoV-2 entry into cells. *Nature Reviews Molecular Cell Biology*, 23(1), 3–20.
- James, A. S., & Alwneh, J. I. (2020). COVID-19 Infection Diagnosis: Potential Impact of Isothermal Amplification Technology to Reduce Community Transmission of SARS-CoV-2. *Diagnostics (Basel, Switzerland)*, 10(6), 399.
- Jamison, D. A., Anand Narayanan, S., Trovão, N. S., ... Beheshti, A. (2022). A comprehensive SARS-CoV-2 and COVID-19 review, Part 1: Intracellular overdrive for SARS-CoV-2 infection. *European Journal of Human Genetics*, 30(8), 889–898.

- Jayamohan, H., Lambert, C. J., Sant, H. J., Jafek, A., Patel, D., Feng, H., Beeman, M., Mahmood, T., Nze, U., & Gale, B. K. (2021). SARS-CoV-2 pandemic: a review of molecular diagnostic tools including sample collection and commercial response with associated advantages and limitations. *Analytical and Bioanalytical Chemistry*, 413(1), 49–71.
- Judge, A. D., Sood, V., Shaw, J. R., Fang, D., McClintock, K., & MacLachlan, I. (2005). Sequence-dependent stimulation of the mammalian innate immune response by synthetic siRNA. *Nature Biotechnology* 2005 23:4, 23(4), 457–462.

## K

- Karsisiotis, A. I., O’Kane, C., & Webba da Silva, M. (2013). DNA quadruplex folding formalism--a tutorial on quadruplex topologies. *Methods (San Diego, Calif.)*, 64(1), 28–35.
- Kashte, S., Gulbake, A., El-Amin, S. F., & Gupta, A. (2021). COVID-19 vaccines: rapid development, implications, challenges and future prospects. *Human Cell*, 34(3), 711–733.
- Kaushik, M., Kaushik, S., Roy, K., Singh, A., Mahendru, S., Kumar, M., Chaudhary, S., Ahmed, S., & Kukreti, S. (2016). A bouquet of DNA structures: Emerging diversity. *Biochemistry and Biophysics Reports*, 5, 388–395.
- Kerkhoff, E., Houben, R., Löffler, S., Troppmair, J., Lee, J. E., & Rapp, U. R. (1998). Regulation of c-myc expression by Ras/Raf signalling. *Oncogene*, 16(2), 211–216.
- Kikin, O., D’Antonio, L., & Bagga, P. S. (2006). QGRS Mapper: a web-based server for predicting G-quadruplexes in nucleotide sequences. *Nucleic Acids Research*, 34(Web Serv. iss.), W676-682.
- Kosiol, N., Juranek, S., Brossart, P., Heine, A., & Paeschke, K. (2021). G-quadruplexes: a promising target for cancer therapy. *Molecular Cancer*, 20(1), 1–18.

## L

- Lam, T. T. Y., Jia, N., Zhang, Y. W., Shum, M. H. H., ... Cao, W. C. (2020). Identifying SARS-CoV-2-related coronaviruses in Malayan pangolins. *Nature*, 583(7815), 282–285.
- Land, H., Parada, L. F., & Weinberg, R. A. (1983). Tumorigenic conversion of primary embryo fibroblasts requires at least two cooperating oncogenes. *Nature*, 304(5927), 596–602.
- Lee, E. Y. P., Ng, M. Y., & Khong, P. L. (2020). COVID-19 pneumonia: what has CT taught us? *The Lancet. Infectious Diseases*, 20(4), 384–385.

- Lee, T., Yao, G., Nevins, J., & You, L. (2008). Sensing and integration of Erk and PI3K signals by Myc. *PLoS Computational Biology*, 4(2), e1000013.
- Lee, Y. R., Tsai, H. P., Yeh, C. S., Fang, C. Y., Chan, M. W. Y., Wu, T. Y., & Shen, C. H. (2023). RNA Interference Approach Is a Good Strategy against SARS-CoV-2. *Viruses*, 15(1), 100.
- Levens, D. L. (2008). How the c-myc Promoter Works and Why It Sometimes Does Not. *Journal of the National Cancer Institute. Monographs*, 39, 41–43.
- Li, Y., Liu, L., & Liu, G. (2019). CRISPR/Cas Multiplexed Biosensing: A Challenge or an Insurmountable Obstacle? *Trends in Biotechnology*, 37(8), 792–795.
- Lin, M., & Qi, X. (2023). Advances and Challenges of Stimuli-Responsive Nucleic Acids Delivery System in Gene Therapy. *Pharmaceutics*, 15(5), 1–26.
- Linke, R., Limmer, M., Juranek, S. A., Heine, A., & Paeschke, K. (2021). The Relevance of G-Quadruplexes for DNA Repair. *International Journal of Molecular Sciences*, 22(22), 12599.
- Liu, W., Liu, L., Kou, G., Zheng, Y., Ding, Y., Ni, W., Wang, Q., Tan, L., Wu, W., Tang, S., Xiong, Z., & Zheng, S. (2020). Evaluation of Nucleocapsid and Spike Protein-Based Enzyme-Linked Immunosorbent Assays for Detecting Antibodies against SARS-CoV-2. *Journal of Clinical Microbiology*, 58(6), e00461-20.
- Liu, Y., Li, D., Liu, Z., Zhou, Y., Chu, D., ... Zhang, C. Y. (2015). Targeted exosome-mediated delivery of opioid receptor Mu siRNA for the treatment of morphine relapse. *Scientific Reports*, 5(November), 1–10.
- Llombart, V., & Mansour, M. R. (2021). Review Therapeutic targeting of “undruggable” MYC. *EBioMedicine*, 75, 103756.
- López-Aguilar, E., Fernández-Nogueira, P., Fuster, G., Carbó, N., Ciudad, C. J., & Noé, V. (2023). In Vitro and In Vivo Effects of the Combination of Polypurine Reverse Hoogsteen Hairpins against HER-2 and Trastuzumab in Breast Cancer Cells. *International Journal of Molecular Sciences*, 24(8), 7073.
- Luther, D. C., Huang, R., Jeon, T., Zhang, X., Lee, Y. W., Nagaraj, H., & Rotello, V. M. (2020). Delivery of drugs, proteins, and nucleic acids using inorganic nanoparticles. *Advanced Drug Delivery Reviews*, 156, 188–213.
- Lv, H., Wu, N. C., Tsang, O. T. Y., Yuan, M., ... Mok, C. K. P. (2020). Cross-reactive Antibody Response between SARS-CoV-2 and SARS-CoV Infections. *Cell Reports*, 31(9), 107725.

## M

- Madden, S. K., de Araujo, A. D., Gerhardt, M., Fairlie, D. P., & Mason, J. M. (2021). Taking the Myc out of cancer: toward therapeutic strategies to directly inhibit c-Myc. *Molecular Cancer*, 20(1).
- Marquevielle, J., Robert, C., Lagrabette, O., Wahid, M., Bourdoncle, A., Xodo, L. E., Mergny, J. L., & Salgado, G. F. (2020). Structure of two G-quadruplexes in equilibrium in the KRAS promoter. *Nucleic Acids Research*, 48(16), 9336–9345.
- Massó-Vallés, D., & Soucek, L. (2020). Blocking Myc to Treat Cancer: Reflecting on Two Decades of Omomyc. In *Cells* 9(4), 883. Multidisciplinary Digital Publishing Institute.
- McCormick, F. (2015). KRAS as a Therapeutic Target. *Clinical Cancer Research: An Official Journal of the American Association for Cancer Research*, 21(8), 1797–1801.
- McCray, P. B., Pewe, L., Wohlford-Lenane, C., Hickey, M., ... Perlman, S. (2007). Lethal infection of K18-hACE2 mice infected with severe acute respiratory syndrome coronavirus. *Journal of Virology*, 81(2), 813–821.
- McFadden, D. G., Politi, K., Bhutkar, A., Chen, F. K., Song, X., ... Varmus, H. (2016). Mutational landscape of EGFR-, MYC-, and Kras-driven genetically engineered mouse models of lung adenocarcinoma. *Proceedings of the National Academy of Sciences of the United States of America*, 113(42), E6409–E6417.
- Meyer, N., & Penn, L. Z. (2008). Reflecting on 25 years with MYC. *Nature Reviews Cancer*, 8(12), 976–990.
- Michel, C. J., Mayer, C., Poch, O., & Thompson, J. D. (2020). Characterization of accessory genes in coronavirus genomes. *Virology Journal*, 17(1), 131.
- Morales-Martinez, M., Valencia-Hipolito, A., Vega, G. G., Neri, N., ... Vega, M. I. (2019). Regulation of Krüppel-Like Factor 4 (KLF4) expression through the transcription factor Yin-Yang 1 (YY1) in non-Hodgkin B-cell lymphoma. *Oncotarget*, 10(22), 2173–2188.
- Morgan, R. K., Batra, H., Gaerig, V. C., Hockings, J., & Brooks, T. A. (2016). Identification and characterization of a new G-quadruplex forming region within the kRAS promoter as a transcriptional regulator. *Biochimica et Biophysica Acta (BBA) - Gene Regulatory Mechanisms*, 1859(2), 235–245.
- Mossafa, H., Damotte, D., Jenabian, A., Delarue, R., ... Troussard, X. (2006). Non-Hodgkin's lymphomas with Burkitt-like cells are associated with c-Myc amplification and poor prognosis. *Leukemia & Lymphoma*, 47(9), 1885–1893.
- Nakajima, E. C., Drezner, N., Li, X., Mishra-Kalyani, P. S., Liu, Y., ...Singh, H. (2022). FDA Approval Summary: Sotorasib for KRAS G12C Mutated Metastatic NSCLC. *Clinical Cancer Research: An Official*

*Journal of the American Association for Cancer Research*, 28(8), 1482–1486.

## N

- Navya, P. N., Kaphle, A., Srinivas, S. P., Bhargava, S. K., Rotello, V. M., & Daima, H. K. (2019). Current trends and challenges in cancer management and therapy using designer nanomaterials. *Nano Convergence* 2019 6:1, 6(1), 1–30.
- Nayerossadat, N., Maedeh, T., & Ali, P. A. (2012). Viral and nonviral delivery systems for gene delivery. *Advanced Biomedical Research*, 1(1), 27.
- Nelson, C. E., Kintzing, J. R., Hanna, A., Shannon, J. M., Gupta, M. K., & Duvall, C. L. (2013). Balancing cationic and hydrophobic content of PEGylated siRNA polyplexes enhances endosome escape, stability, blood circulation time, and bioactivity in vivo. *ACS Nano*, 7(10), 8870–8880.
- Neumann, J., Zeindl-Eberhart, E., Kirchner, T., & Jung, A. (2009). Frequency and type of KRAS mutations in routine diagnostic analysis of metastatic colorectal cancer. *Pathology, Research and Practice*, 205(12), 858–862.
- Nguyen, T. M., Zhang, Y., & Pandolfi, P. P. (2020). Virus against virus: a potential treatment for 2019-nCov (SARS-CoV-2) and other RNA viruses. *Cell Research*, 30(3), 189–190.
- Nie, Z., Guo, C., Das, S. K., Chow, C. C., Batchelor, E., Simons Jnr, S. S., & Levens, D. (2020). Dissecting transcriptional amplification by MYC. *ELife*, 9, e52483.
- Noé, V., Aubets, E., Félix, A. J., & Ciudad, C. J. (2021). Nucleic acids therapeutics using PolyPurine Reverse Hoogsteen hairpins. *Biochemical Pharmacology*, 189, 114371.
- Noé, V., & Ciudad, C. J. (2021). Polypurine reverse-hoogsteen hairpins as a tool for exon skipping at the genomic level in mammalian cells. *International Journal of Molecular Sciences*, 22(7), 3784.
- Nouri, R., Tang, Z., Dong, M., Liu, T., Kshirsagar, A., & Guan, W. (2021). CRISPR-based detection of SARS-CoV-2: A review from sample to result. *Biosensors & Bioelectronics*, 178, 113012.

## O

- Orkin, S. H., & Reilly, P. (2016). Paying for future success in gene therapy. *Science*, 352(6289), 1059–1061.
- Oster, M. E., Shay, D. K., Su, J. R., Gee, J., Creech, C. B., ... Shimabukuro, T. T. (2022). Myocarditis Cases Reported After mRNA-Based COVID-

19 Vaccination in the US From December 2020 to August 2021. *JAMA*, 327(4), 331–340.

Ostrem, J. M. L., & Shokat, K. M. (2016). Direct small-molecule inhibitors of KRAS: from structural insights to mechanism-based design. *Nature Reviews Drug Discovery* 2016 15:11, 15(11), 771–785.

## P

Panahi, Y., Gorabi, A. M., Talaei, S., Beiraghdar, F., Akbarzadeh, A., Tarhriz, V., & Mellatyar, H. (2023). An overview on the treatments and prevention against COVID-19. *Virology Journal*, 20(1), 23.

Pandey, P. S., Raghuwanshi, S. K., Shadab, A., Ansari, M. T. I., Tiwari, U. K., & Kumar, S. (2022). SPR Based Biosensing Chip for COVID-19 Diagnosis - A Review. *IEEE Sensors Journal*, 22(14), 13800–13810.

Papachristos, A., Pippa, N., Demetzos, C., & Sivolapenko, G. (2016). Antibody-drug conjugates: a mini-review. The synopsis of two approved medicines. *Drug Delivery*, 23(5), 1662–1666.

Parikh, K., Banna, G., Liu, S. V., Friedlaender, A., Desai, A., Subbiah, V., & Addeo, A. (2022). Drugging KRAS: current perspectives and state-of-art review. *Journal of Hematology & Oncology*, 15(152), 1–22.

Peeling, R. W., Oliaro, P. L., Boeras, D. I., & Fongwen, N. (2021). Scaling up COVID-19 rapid antigen tests: promises and challenges. *The Lancet Infectious Diseases*, 21(9), e290–e295.

Piotrowski-Daspiet, A. S., Kauffman, A. C., Bracaglia, L. G., & Saltzman, W. M. (2020). Polymeric vehicles for nucleic acid delivery. *Advanced Drug Delivery Reviews*, 156, 119–132.

Prior, I. a, Lewis, P. D., & Mattos, C. (2012). A comprehensive survey of Ras mutations in cancer. *Cancer Research*, 72(10), 2457–2467.

Psaras, A. M., Carty, R. K., Miller, J. T., Tumey, L. N., & Brooks, T. A. (2022). Indoloquinoline-Mediated Targeted Downregulation of KRAS through Selective Stabilization of the Mid-Promoter G-Quadruplex Structure. *Genes*, 13(8), 1440.

Psaras, A. M., Chang, K. T., Hao, T., & Brooks, T. A. (2021). Targeted Downregulation of MYC through G-quadruplex Stabilization by DNAi. *Molecules*, 26(18), 5542.

Pylayeva-Gupta, Y., Grabocka, E., & Bar-Sagi, D. (2011). RAS oncogenes: weaving a tumorigenic web. *Nature Reviews. Cancer*, 11(11), 761.

## Q

Qiao, Y., Wotring, J. W., Zhang, C. J., Jiang, X., Xiao, L., ... Chinnaiyan, A. M. (2023). Antisense oligonucleotides to therapeutically target SARS-CoV-2 infection. *PLoS ONE*, 18(2), e0281281.



- Qiu, G., Gai, Z., Tao, Y., Schmitt, J., Kullak-Ublick, G. A., & Wang, J. (2020). Dual-Functional Plasmonic Photothermal Biosensors for Highly Accurate Severe Acute Respiratory Syndrome Coronavirus 2 Detection. *ACS Nano*, 14(5), 5268–5277.
- Qiu, X., Boufaied, N., Hallal, T., Feit, A., de Polo, A., ... Labbé, D. P. (2022). MYC drives aggressive prostate cancer by disrupting transcriptional pause release at androgen receptor targets. *Nature Communications*, 13(1).

## R

- Ranki, M., Palva, A., Virtanen, M., Laaksonen, M., & Söderlund, H. (1983). Sandwich hybridization as a convenient method for the detection of nucleic acids in crude samples. *Gene*, 21(1–2), 77–85.
- Ren, L. L., Wang, Y. M., Wu, Z. Q., Xiang, Z. C., ... Wang, J. W. (2020). Identification of a novel coronavirus causing severe pneumonia in human: a descriptive study. *Chinese Medical Journal*, 133(9), 1015–1024.
- Roberts, T. C., Langer, R., & Wood, M. J. A. (2020). Advances in oligonucleotide drug delivery. *Nature Reviews Drug Discovery*, 19(10), 673–694.
- Robertson, E. S., Ooka, T., & Kieff, E. D. (1996). Epstein-Barr virus vectors for gene delivery to B lymphocytes. *Proceedings of the National Academy of Sciences of the United States of America*, 93(21), 11334–11340.
- Rodríguez, L., Villalobos, X., Dakhel, S., Padilla, L., Hervas, R., Hernández, J. L., Ciudad, C. J., & Noé, V. (2013). Polypurine reverse Hoogsteen hairpins as a gene therapy tool against survivin in human prostate cancer PC3 cells in vitro and in vivo. *Biochemical Pharmacology*, 86(11), 1541–1554.
- Rodríguez, L., Villalobos, X., Solé, A., Lliberós, C., Ciudad, C. J., & Noé, V. (2015). Improved design of PPRHs for gene silencing. *Molecular Pharmaceutics*, 12(3), 867–877.
- Rong, G., Zheng, Y., Chen, Y., Zhang, Y., Zhu, P., & Sawan, M. (2023). COVID-19 Diagnostic Methods and Detection Techniques. *Encyclopedia of Sensors and Biosensors*, 17–32.

## S

- Sadoff, J., Gray, G., Vandebosch, A., Cárdenas, V., ... Douoguih, M. (2021). Safety and Efficacy of Single-Dose Ad26.COV2.S Vaccine against Covid-19. *The New England Journal of Medicine*, 384(23), 2187–2201.

- Sahay, G., Querbes, W., Alabi, C., Eltoukhy, A., ... Anderson, D. G. (2013). Efficiency of siRNA delivery by lipid nanoparticles is limited by endocytic recycling. *Nature Biotechnology*, 31(7), 653–658.
- Salem, M. E., El-Refai, S. M., Sha, W., Puccini, A., ... Tie, J. (2022). Landscape of KRASG12C, Associated Genomic Alterations, and Interrelation With Immuno-Oncology Biomarkers in KRAS-Mutated Cancers. *JCO Precision Oncology*, 6, e2100245.
- Salvati, E., Leonetti, C., Rizzo, A., Scarsella, M., ... Biroccio, A. (2007). Telomere damage induced by the G-quadruplex ligand RHPS4 has an antitumor effect. *The Journal of Clinical Investigation*, 117(11), 3236–3247.
- Sarkies, P., Reams, C., Simpson, L. J., & Sale, J. E. (2010). Epigenetic instability due to defective replication of structured DNA. *Molecular Cell*, 40(5), 703–713.
- Scavone, C., Brusco, S., Bertini, M., Sportiello, L., ... Capuano, A. (2020). Current pharmacological treatments for COVID-19: What's next? *British Journal of Pharmacology*, 177(21), 4813–4824.
- Scherer, F., Anton, M., Schillinger, U., Henke, ... J., Plank, C. (2002). Magnetofection: enhancing and targeting gene delivery by magnetic force in vitro and in vivo. *Gene Therapy*, 9(2), 102–109.
- Schirmacher, V. (2019). From chemotherapy to biological therapy: A review of novel concepts to reduce the side effects of systemic cancer treatment (Review). *International Journal of Oncology*, 54(2), 407–419.
- Seliger, B. (2005). Strategies of tumor immune evasion. *BioDrugs: Clinical Immunotherapeutics, Biopharmaceuticals and Gene Therapy*, 19(6), 347–354.
- Seo, G., Lee, G., Kim, M. J., Baek, S. H., ... Kim, S. II. (2020). Rapid Detection of COVID-19 Causative Virus (SARS-CoV-2) in Human Nasopharyngeal Swab Specimens Using Field-Effect Transistor-Based Biosensor. *ACS Nano*, 14(4), 5135–5142.
- Shalaby, T., Fiaschetti, G., Nagasawa, K., Shin-Ya, K., Baumgartner, M., & Grotzer, M. (2013). G-Quadruplexes as Potential Therapeutic Targets for Embryonal Tumors. *Molecules*, 18(10), 12500–12537.
- Sharifian-Dorche, M., Bahmanyar, M., Sharifian-Dorche, A., Mohammadi, P., Nomovi, M., & Mowla, A. (2021). Vaccine-induced immune thrombotic thrombocytopenia and cerebral venous sinus thrombosis post COVID-19 vaccination; a systematic review. *Journal of the Neurological Sciences*, 428, 117607.
- Sharma, S., Mukherjee, A. K., Roy, S. S., Bagri, S., ... Chowdhury, S. (2021). Human telomerase is directly regulated by non-telomeric TRF2-G-quadruplex interaction. *Cell Reports*, 35(7), 109154.
- Shen, L., O'Shea, J. M., Kaadige, M. R., Cunha, S., Wilde, B. R., Cohen, A. L., Welm, A. L., & Ayer, D. E. (2015). Metabolic reprogramming in

- triple-negative breast cancer through Myc suppression of TXNIP. *Proceedings of the National Academy of Sciences of the United States of America*, 112(17), 5425–5430.
- Shen, M., Zhou, Y., Ye, J., Abdullah AL-maskri, A. A., Kang, Y., Zeng, S., & Cai, S. (2020). Recent advances and perspectives of nucleic acid detection for coronavirus. *Journal of Pharmaceutical Analysis*, 10(2), 97–101.
- Shortt, J., & Johnstone, R. W. (2012). Oncogenes in cell survival and cell death. *Cold Spring Harbor Perspectives in Biology*, 4(12), a009829.
- Simonovich, V. A., Burgos Pratx, L. D., Scibona, P., Beruto, M. V., ... Belloso, W. H. (2021). A Randomized Trial of Convalescent Plasma in Covid-19 Severe Pneumonia. *The New England Journal of Medicine*, 384(7), 619–629.
- Singh, A., Greninger, P., Rhodes, D., Koopman, L., Violette, S., Bardeesy, N., & Settleman, J. (2009). A gene expression signature associated with “K-Ras addiction” reveals regulators of EMT and tumor cell survival. *Cancer Cell*, 15(6), 489–500.
- Solé, A., Ciudad, C. J., Chasin, L. A., & Noé, V. (2016). Correction of point mutations at the endogenous locus of the dihydrofolate reductase gene using repair-PolyPurine Reverse Hoogsteen hairpins in mammalian cells. *Biochemical Pharmacology*, 110–111, 16–24.
- Soucek, L., Whitfield, J. R., Sodir, N. M., Massó-Vallés, D., Serrano, E., Karnezis, A. N., Swigart, L. B., & Evan, G. I. (2013). Inhibition of Myc family proteins eradicates KRas-driven lung cancer in mice. *Genes & Development*, 27(5), 504–513.
- Spiegel, J., Adhikari, S., & Balasubramanian, S. (2020). The Structure and Function of DNA G-Quadruplexes. *Trends in Chemistry*, 2(2), 123–136.
- Springer, A. D., & Dowdy, S. F. (2018). GalNAc-siRNA Conjugates: Leading the Way for Delivery of RNAi Therapeutics. *Nucleic Acid Therapeutics*, 28(3), 109–118.
- Suda, T., & Liu, D. (2007). Hydrodynamic gene delivery: its principles and applications. *Molecular Therapy: The Journal of the American Society of Gene Therapy*, 15(12), 2063–2069.
- Supramaniam, A., Tayyar, Y., Clarke, D. T. W., Kelly, G., Acharya, D., Morris, K. V., McMillan, N. A. J., & Idris, A. (2023). Prophylactic intranasal administration of lipid nanoparticle formulated siRNAs reduce SARS-CoV-2 and RSV lung infection. *Journal of Microbiology, Immunology and Infection*, 56(3), 516–525.

## T

- Tabernero, J., Shapiro, G. I., LoRusso, P. M., Cervantes, A., ... Burris, H. A. (2013). First-in-humans trial of an RNA interference therapeutic

- targeting VEGF and KSP in cancer patients with liver involvement. *Cancer Discovery*, 3(4), 406–417.
- Tanudji, M., MacHalek, D., Arndt, G. M., & Rivory, L. (2010). Competition between siRNA duplexes: impact of RNA-induced silencing complex loading efficiency and comparison between conventional-21 bp and Dicer-substrate siRNAs. *Oligonucleotides*, 20(1), 27–32.
- Tao, K., Tzou, P. L., Nouhin, J., Bonilla, H., Jagannathan, P., & Shafer, R. W. (2021). SARS-CoV-2 Antiviral Therapy. *Clinical Microbiology Reviews*, 34(4), e0010921.
- Tenchov, R., Bird, R., Curtze, A. E., & Zhou, Q. (2021). Lipid Nanoparticles from Liposomes to mRNA Vaccine Delivery, a Landscape of Research Diversity and Advancement. *ACS Nano*, 15(11), 16982–17015.
- Thompson, M. G., Stenehjem, E., Grannis, S., Ball, S. W., ... Klein, N. P. (2021). Effectiveness of Covid-19 Vaccines in Ambulatory and Inpatient Care Settings. *The New England Journal of Medicine*, 385(15), 1355–1371.
- Tian, T., Chen, Y. Q., Wang, S. R., & Zhou, X. (2018). G-Quadruplex: A Regulator of Gene Expression and Its Chemical Targeting. *Chem*, 4(6), 1314–1344.
- Tong, B. C.-K., & Benjamin Chun-Kit Tong. (2017). Bioconjugates for Targeted Delivery of Therapeutic Oligonucleotides. *Physiology & Behavior*, 176(5), 139–148.
- Torres-Vanegas, J. D., Cruz, J. C., & Reyes, L. H. (2021). Delivery Systems for Nucleic Acids and Proteins: Barriers, Cell Capture Pathways and Nanocarriers. *Pharmaceutics*, 13(3), 428.
- Traube, F. R., Stern, M., Tölke, A. J., Rudelius, M., ... Carell, T. (2022). Suppression of SARS-CoV-2 Replication with Stabilized and Click-Chemistry Modified siRNAs. *Angewandte Chemie (International Ed. in English)*, 61(38), e202204556.
- Tsai, L. H., Wu, J. Y., Cheng, Y. W., Chen, C. Y., Sheu, G. T., Wu, T. C., & Lee, H. (2015). The MZF1/c-MYC axis mediates lung adenocarcinoma progression caused by wild-type lkb1 loss. *Oncogene*, 34(13), 1641–1649.

## V

- Varshney, D., Spiegel, J., Zyner, K., Tannahill, D., & Balasubramanian, S. (2020). The regulation and functions of DNA and RNA G-quadruplexes. *Nature Reviews Molecular Cell Biology*, 21(8), 459–474.
- Vaseva, A. V., Blake, D. R., Gilbert, T. S. K., Ng, S., Hostetter, G., ... Der, C. J. (2018). KRAS Suppression-Induced Degradation of MYC Is Antagonized by a MEK5-ERK5 Compensatory Mechanism. *Cancer Cell*, 34(5), 807–822.e7.

- Villalobos, X., Rodríguez, L., Prévot, J., Oleaga, C., Ciudad, C. J., & Noé, V. (2014). Stability and immunogenicity properties of the gene-silencing polypurine reverse Hoogsteen hairpins. *Molecular Pharmaceutics*, 11(1), 254–264.
- Villalobos, X., Rodríguez, L., Solé, A., Lliberós, C., Mencia, N., Ciudad, C. J., & Noé, V. (2015). Effect of Polypurine Reverse Hoogsteen Hairpins on Relevant Cancer Target Genes in Different Human Cell Lines. *Nucleic Acid Therapeutics*, 25(4), 198–208.
- Voysey, M., Costa Clemens, S. A., Madhi, S. A., ... Zuidewind, P. (2021). Single-dose administration and the influence of the timing of the booster dose on immunogenicity and efficacy of ChAdOx1 nCoV-19 (AZD1222) vaccine: a pooled analysis of four randomised trials. *Lancet (London, England)*, 397(10277), 881–891.

## W

- Walz, S., Lorenzin, F., Morton, J., Wiese, K. E., ... Eilers, M. (2014). Activation and repression by oncogenic MYC shape tumour-specific gene expression profiles. *Nature*, 511, 483–487.
- Wang, C., Zhang, J., Yin, J., Gan, Y., Xu, S., Gu, Y., & Huang, W. (2021). Alternative approaches to target Myc for cancer treatment. *Signal Transduction and Targeted Therapy*, 6(117).
- Wang, G., Seidman, M. M., & Glazer, P. M. (1996). Mutagenesis in mammalian cells induced by triple helix formation and transcription-coupled repair. *Science (New York, N.Y.)*, 271(5250), 802–805.
- Wang, G., & Vasquez, K. M. (2014). Impact of alternative DNA structures on DNA damage, DNA repair, and genetic instability. *DNA Repair*, 19, 143–151.
- Wang, Y., Kaiser, C. E., Frett, B., & Li, H. Y. (2013). Targeting mutant KRAS for anticancer therapeutics: A review of novel small molecule modulators. *Journal of Medicinal Chemistry*, 56(13), 5219–5230.
- Waters, A. M., Khatib, T. O., Papke, B., Goodwin, C. M., ... Der, C. J. (2021). Targeting p130Cas- and microtubule-dependent MYC regulation sensitizes pancreatic cancer to ERK MAPK inhibition. *Cell Reports*, 35(13), 109291.
- Watson, J. D., & Crick, F. H. C. (1953). Molecular structure of nucleic acids; a structure for deoxyribose nucleic acid. *Nature*, 171(4356), 737–738.
- Whitfield, J. R., Beaulieu, M. E., & Soucek, L. (2017). Strategies to inhibit Myc and their clinical applicability. *Frontiers in Cell and Developmental Biology*, 5(10), 1–13.
- WHO (2023) - WHO | Coronavirus Statistic World Health Organization, Geneva. Retrieved August 16, 2023 from <https://covid19.who.int/>
- Wu, C. rong, Yin, W. chao, Jiang, Y., & Xu, H. E. (2022). Structure genomics of SARS-CoV-2 and its Omicron variant: drug design

templates for COVID-19. *Acta Pharmacologica Sinica*, 43(12), 3021–3033.

Wu, L., Zhou, W., Lin, L., Chen, A., Feng, J., Qu, X., Zhang, H., & Yue, J. (2022). Delivery of therapeutic oligonucleotides in nanoscale. *Bioactive Materials*, 7, 292–323.

Wu, T. Y., Huang, Q., Huang, Z. S., Hu, M. H., & Tan, J. H. (2020). A drug-like imidazole-benzothiazole conjugate inhibits malignant melanoma by stabilizing the c-MYC G-quadruplex. *Bioorganic Chemistry*, 99, 103866.

Xiong, H., Veedu, R. N., & Diermeier, S. D. (2021). Recent advances in oligonucleotide therapeutics in oncology. In *International Journal of Molecular Sciences* 22(7), 3295

## Y

Yadav, T., Kumar, S., Mishra, G., & Saxena, S. K. (2023). Tracking the COVID-19 vaccines: The global landscape. *Human Vaccines & Immunotherapeutics*, 19(1), 2191577.

Yanagidaira, M., Yoshioka, K., Nagata, T., Nakao, S., Miyata, K., & Yokota, T. (2023). Effects of combinations of gapmer antisense oligonucleotides on the target reduction. *Molecular Biology Reports*, 50(4), 3539–3546.

Ye, M., Fu, D., Ren, Y., Wang, F., Wang, D., Zhang, F., Xia, X., & Lv, T. (2020). Treatment with convalescent plasma for COVID-19 patients in Wuhan, China. *Journal of Medical Virology*, 92(10), 1890–1901.

Yu, S., Wang, Y., He, P., Shao, B., Liu, F., Xiang, Z., Yang, T., Zeng, Y., He, T., Ma, J., Wang, X., & Liu, L. (2022). Effective Combinations of Immunotherapy and Radiotherapy for Cancer Treatment. In *Frontiers in Oncology*, 12

## Z

Zhang, W., Du, R. H., Li, B., Zheng, X. S., ... Zhou, P. (2020). Molecular and serological investigation of 2019-nCoV infected patients: implication of multiple shedding routes. *Emerging Microbes & Infections*, 9(1), 386–389.

Zhu, C., Lee, J. Y., Woo, J. Z., Xu, L., ... Näär, A. M. (2022). An intranasal ASO therapeutic targeting SARS-CoV-2. *Nature Communications*, 13(1), 4503.

Zhu, L., & Mahato, R. I. (2010). Lipid and polymeric carrier-mediated nucleic acid delivery. *Expert Opinion on Drug Delivery*, 7(10), 1209–1226.

Zyner, K. G., Mulhearn, D. S., Adhikari, S., Cuesta, S. M., ... Balasubramanian, S. (2019). Genetic interactions of G-quadruplexes in humans. *ELife*, 8, e46793.

